Understanding the Role of Amphiphilic Chemical Additives in Enhanced Oil Recovery from Molecular Perspectives

by

Yiling Nan

A thesis submitted in partial fulfillment of the requirements for the degree of

Doctor of Philosophy

in

Petroleum Engineering

Department of Civil and Environmental Engineering
University of Alberta

Abstract

Carefully designed chemical formulas are often applied in the enhanced oil recovery (EOR) process. Understanding the molecular distribution and working mechanism of each component can provide theoretical guidance in designing chemical formulas with desired functionalities. In this dissertation, we employ the molecular dynamics (MD) simulation to study the atomic distribution as well as the working mechanism of the amphiphilic chemical additives (surfactant, co-surfactant) applied in the petroleum industry, especially during the chemical flooding and gas injection process.

In chemical flooding, surfactant formulas are injected into the reservoir to reduce the interfacial tension (IFT) between oil and brine. The injected surfactant should be stable and effective under reservoir conditions, generally associated with high-pressure high-temperature, and formation water (omnipresent in the reservoir, contains various salt ions with its salinity can be up to 35 *wt.*%). We first explore the effect of ion valency and concentration on sodium dodecyl sulfate (SDS) surfactant arrangement and efficiency. Two different cations (Na^+ and Ca^{2+}) with a wide range of ion concentrations (up to 3.96 M) are employed to simulate reservoir conditions. We demonstrate that ion valency has a significant effect on molecular configurations. Ca^{2+} ions can form unique pentagon-like SDS-Ca^{2+} complexes through SDS-Ca^{2+}-SDS cation bridging. Monovalent Na^+ can also generate SDS-Na^+-SDS cation bridgings, while their concentration is much lower than that of SDS-Ca^{2+}-SDS. The non-ionic (propanol) and cationic [cetrimonium bromide (CTAB)] surfactants with a wide range of concentrations are introduced to the primary SDS formula, to study the effect of chemical additives. We find that CTAB can disaggregate the cation bridging when their concentration is above a certain threshold. The cation bridging density is maintained at a low level when the sum of surfactants and cosurfactant interface charges is

neutral or positive. On the other hand, propanol barely disaggregates the cation bridging. Both propanol and CTAB can further decrease the oil-brine IFT while having different efficacies. More rapid IFT decrement is observed when cation bridging is disaggregated. Propanol, as a cosurfactant, can be transported through oil and brine phases; such a dislocation of propanol in the system is a dynamic process. In the meantime, the introduction of propanol does not always increase the local fluidity of surfactants at the interface. A local maximum fluidity was observed when the SDSs are more perpendicular to the interface. These works should guide surfactant formula design in the chemical flooding process.

Alcohol blending is often employed in the super critical CO_2 ($scCO_2$) gas injection. Ethanol can increase the sodium bis(2-Ethylhexyl) sulfosuccinate (AOT) solubility in $scCO_2$ during the gas injection, while their working mechanism is not well established yet. Spontaneous aggregation processes in two systems (one consists of AOT and $scCO_2$; the other consists of AOT, $scCO_2$, and 10 *wt*.% ethanol) are conducted under a typical tight oil reservoir condition (333 K and 200 bar) to investigate the working mechanism of ethanol. After 600-ns runs, the AOT molecules aggregate together and form rod-like reversed micelles (RMs) in the System without ethanol, while forming several small sphere-like RMs by introducing the ethanol to the system. We propose that the ethanol molecules can better solvate and surround Na^+ ions, preventing the further aggregation of AOT clusters. Other than increasing surfactant solubility, as an amphiphilic molecule, alcohols can also distribute at the interface region and further affect the water/$scCO_2$ (foam interface) interfacial properties. Alcohols with varying tail lengths (C_2OH-$C_{16}OH$) under a wide range of concentrations are introduced to water/AOT/$scCO_2$ interface systems to study their effects. We demonstrate that alcohol can distribute in water, interface region, and $scCO_2$ phases, and their participation in phases is affected by the alcohol tail length. Alcohols' tail length has a negligible

effect on alcohol distribution at the interface when their concentration in the $scCO_2$ phase is fixed. On the other hand, alcohol concentration in the water phase increase as tail length decrease. The ability in decreasing IFT is similar for different tail length alcohols when alcohol concentration is relatively low (before reaching the inflection point). However, the lowest available IFT (inflection point) increases as alcohol chain length increases. The mean-squared displacement (MSD) of AOT decreases as alcohol concentration increases, and such a decrement trend is more significant in systems with long-chain alcohols. These works should provide important insights into designing chemical formulas for gas injection.

Preface

All the contents (except Introduction and Conclusion Chapters) have been published or are under submission in peer-reviewed journals or eBook. Chapter 2 is published in *J. Phys. Chem. B*. (Nan *et al*., 125, 33, 9610-9620, 2021). Chapter 3 is published in *Langmuir* (Nan *et al.*, in press, 2022). Chapter 4 is published in *Langmuir* (Nan *et al*., 36, 19, 5198-5207, 2020). Chapter 5 is published in *J. Phys. Chem. B*. (Nan *et al*., 125, 33, 9621-9628, 2021). Chapter 6 is to be submitted to *ACS Symposium Series* (Nan and Jin, 2022).

I was responsible for conceptualizing, building simulation systems, running simulations, analyzing data, and preparing and revising the draft of manuscripts. My supervisor was responsible for conceptualizing, insightful discussions, providing computing resources, and reviewing and revising manuscript drafts. My co-authors were responsible for insightful discussions, essential technical support in building systems and data analysis, and reviewing and revising manuscript drafts. The necessary approvals to include the journal papers as chapters in this work are provided in sequential order in the Copyright Permissions section.

Dedication

This dissertation is dedicated to my beloved parents.

Acknowledgements

I would like to express my gratitude to my supervisor, Dr. Zhehui (Charlie) Jin, who provided me a chance to study statistical mechanics and further apply them in interesting research on petroleum engineering. Weekly individual discussions were especially helpful in the contemplation of day-to-day works and in promoting research progress. Special thanks to his patient guidance and support throughout the program. In addition, I also would like to extend my thank to the supervisor committee (Dr. Huazhou Li and Dr. Nobuo Maeda), Dr. Hao Zhang, and Dr. Alberto Striolo for their insightful suggestions and comments to improve this work.

I would like to acknowledge current or previous group members (Dr. Wenhui Li, Dr. Wanying Pang, Dr. Yinuo Zhao, Dr. Chang Lu, Mingshan Zhang, Yingnan Wang, and Haoxiang Wang) and visiting scholars (Dr. Dengke Liu, Dr. Shiyuan Zhan, and Wei Zhang) for their insightful discussions, support, and friendships.

I would like to thank my parents (Zhenshu Cui and Chengzhu Nan) and grandparents (Huazhi Li, Zhengxiong Nan, Chunyue Jin, and Longzhe Cui). You are my source of love, courage, and power. I also would like to thank my boyfriend Dr. Wenhui Li, who accompanied me throughout the journey. Thank you for brightening and enriching my Ph.D. life with love and positive energy.

I feel very lucky to be surrounded and received a lot of love and help from enthusiastic and talented people. I faithfully hope some of my efforts can also bring some warmth and inspiration to others.

Table of Contents

List of Tables

List of Figures

Chapter 1 : INTRODUCTION

1.1 Research Background

As the global energy demand gradually increases[1], the tertiary recovery[2], the so-called enhanced oil recovery (EOR) becomes increasingly important. It has been reported that only 20~40% of the original oil in place (OOIP) can be generally extracted by the primary recovery (oil produced by natural forces) and the secondary recovery (water flooding)[3], while the residual oil can be extracted by an appropriate EOR method. The EOR method can further be classified as chemical flooding, gas injection, and thermal recovery, based on the mechanism. In chemical flooding and gas injection carefully designed chemical formulas are often employed to achieve desired functionalities.

The main mechanism of the chemical flooding process is to reduce the interfacial tension between oil and brine in the reservoir thereby recovering the residual oils trapped by capillary forces[4-6]. In some cases, the polymers are employed to improve sweep efficiency. An ideal chemical solution for chemical flooding should meet two basic requirements: First, it should be able to decrease the interfacial tension (IFT) of brine-oil interfaces. Second, the surfactant formula should be stable and effective under reservoir conditions, generally associated with high pressure and high temperature[7-9]. In particular, the formation of water (so-called brine), which is omnipresent in oil reservoirs, contains various salt ions (*e.g.*, Na^+, K^+, Ca^{2+}, Mg^{2+}, Cl^-, SO_4^{2-}, CO_3^{2-}, *etc*.)[10], while its salinity can be up to 35 *wt*.%[11, 12]. One of the commonly used surfactants in the chemical flooding processes is anionic surfactants[13]. The strong electrostatic interactions between salt ions and ionic surfactants are imperative to the efficacy and functionality of the surfactant formula in EOR. In addition to surfactants, in actual oil fields, cosurfactants (or

cosolvent), defined as a chemical used in combination with the primary surfactant, are also injected to improve the effectiveness of surfactant solutions[14-18].

The gas injection accounts for nearly 60% of the EOR process in the United States[19]. Injecting gas such as natural gas, carbon dioxide, and nitrogen instead of water not only can supply the reservoir energy but also can lower the oil viscosity as the gas dissolution in the oil. Supercritical CO_2 ($scCO_2$), as an environmentally friendly and inexpensive chemical having moderate critical constants (T_c= 304.1 K, P_c=7.38 MPa)[20] with sterling miscibility with oil [21-24] is an excellent candidate for the gas injection. In addition, as one of several geological carbon sequestrations (GCS) schemes[25-28], CO_2 injection into formations can help mitigate carbon emissions. However, CO_2 flooding is subject to gas channeling which can adversely impact the efficacy of EOR[29]. Therefore, surfactants are usually added to $scCO_2$ injection to facilitate CO_2 foam formation[22, 29] which can eliminate the early breakthrough and viscous fingering due to the heterogeneous pore distributions[30]. Furthermore, surfactants can further decrease the minimum miscible pressure (MMP) of the oil which is favorable for EOR[31, 32]. Unfortunately, in general, commonly used surfactants in oil reservoirs (*e.g.*, sodium bis(2-Ethylhexyl) sulfosuccinate (AOT) and sodium dodecyl sulfate (SDS)) have limited solubility in $scCO_2$[32]. Namely, surfactants precipitate in $scCO_2$, which significantly limits their delivery efficiency to the target zone. Therefore, extensive efforts have been dedicated to improving surfactant solubility and dispersity in $scCO_2$. These efforts can be generally classified into two approaches: the first one is to optimize surfactant structures to form relatively stable reverse micelles (RMs)[33-38], in which the head groups of surfactants distribute in the core with their tail groups immersed in the solvent. The second method is to introduce some chemical additives (such as alcohols) to the solvent to improve the RM dispersity[29, 32, 38-42]. The latter approach can be conveniently

applied in actual oil fields. Alcohols are originally introduced to increase the surfactant solubility, while they can also distribute at interface and further affects water/$scCO_2$ interface properties.

1.2 Problem Statement

Though many interesting and suggestive studies have been reported, to our best knowledge, the roles of chemical additives in the petroleum industry during the EOR process, especially at the brine-oil or water/$scCO_2$ interfaces as well as in the surfactant solubility increment in $scCO_2$ are remaining elusive.

- The distribution and roles of the chemical additives as chemical additives during the chemical flooding process are still not clear.
- Whether these alcohol distributions and roles are affected by the ion valency and concentration, which drastically varies by reservoirs is doubtful.
- How and why can the alcohols increase the solubility of the surfactant in $scCO_2$ is not well explained from molecular perspectives.
- The effect of alcohols on water/$scCO_2$ interface properties (foam interface) is not well studied.

1.3 Research Objectives

Objective of this research is to investigate the role of chemical additives in the EOR process from molecular perspectives.

- To study the ion valency and concentration effect on the surfactant distribution and efficacy.
- To investigate the propanol distribution and their roles at the oil-brine interface with the existence of surfactant SDS.

- To study how nonionic and cationic surfactants as chemical additives affect the surfactant distribution and efficacy at the brine-oil interface.
- To study the working mechanism of alcohol on the surfactant solubility increment.
- To study the effect of alcohols on the water/$scCO_2$ interface properties.

1.4 Simulation Methods

1.4.1 Molecular Simulation

To study the molecular distribution and behaviors at the atomic level, the molecular simulation[43] method is employed throughout the study. The commonly used molecular simulation includes Monte Carlo (MC) and Molecular Dynamics (MD) simulation. Both methods are based on the statistical mechanics and ergodic hypothesis, while the algorithm to explore the phase space is different. We employ the MD simulation, in which the time evolution of coordinates and the momentum of atoms and molecules in the systems are determined by Newton's second law at every timestep (around 2 fs = 2×10^{-15} s). In MD simulation, thermodynamic and structural properties including temperature, pressure, density, free energy, orientation parameter, H-bond density, *etc*. are calculated from the trajectories generated from above stated time "evolution" of molecular movements.

1.4.2 Force Fields

The forces between the atoms and molecules are determined by certain formulas so-called "force fields". These forcefields are developed semi-empirically by adjusting the form and corresponding parameters of *inter- intra-* molecular interactions to match important thermodynamic properties like density, the heat of vaporization, diffusion coefficient, ionic

conductivity, *etc*. Different forcefields are developed for different purposes and possess their application conditions. Therefore, careful calibration of the forcefield validity on object systems is of great importance. Commonly used force field developed for the organic compounds includes OPLS-AA[44], OPLS-UA[45, 46], TraPPE[47], GROMOS[48, 49], CHARMM[50]. Commonly used water forcefield includes SPC[51], SPC/E[52], TIP3P[53], TIP4P[54], and TIP5P[55].

In general, the forces between the molecules are classified into non-bonded and bonded interactions, while interactions are defined differently in different forcefields. The most commonly used form of non-bonded interaction includes electrostatic and van der Waals (vdW) interactions, which is shown as,

$$U_{non-bonded} = \sum_{non-bonded} \left(4\varepsilon_{ij} \left[\left(\frac{\sigma_{ij}}{r_{ij}} \right)^{12} - \left(\frac{\sigma_{ij}}{r_{ij}} \right)^{6} \right] + \frac{q_i q_j}{4\pi\varepsilon_0 r_{ij}} \right) \tag{1-1}$$

Where ε_{ij} and σ_{ij} are the Lennard-Jones (LJ) energy and size parameters, respectively; r_{ij} is the site-site separation distance, q_i and q_j are the partial charges on sites i , and j , and ε_0 is the dielectric permittivity in a vacuum. The cross LJ parameters between unlike molecules are described by combining rules (*e.g*., geometric average or Lorentz-Berthelot rules) based on the corresponding force field.

Bonded interactions include bond stretching (2-body), angle bending (3-body), proper dihedrals, and improper dihedrals (4-body). More varied forms are used in the bonded interactions. Take bond stretching potential, for example, it can be described in the form of harmonic potential, fourth power potential, morse potential bond stretching, cubic bond stretching potential, and finitely extensible nonlinear elastic (FENE) bond stretching potential, *etc*. Here we list the bonded

potentials used in the CHARMM forcefield for we employ the CHARMM forcefield in most of our works. The bonded interaction is described as,

$$U_{bonded} = \sum_{bonds} K_b\left(b-b_0\right)^2 + \sum_{angles} K_\theta\left(\theta-\theta_0\right)^2 + \sum_{dihedrals} K_\varphi\left(1+\cos\left(n\varphi-\delta\right)\right) + \sum_{improper\,dihedrals} K_\phi\left(\phi-\phi_0\right)^2 + \sum_{Urey-Bradley} K_{UB}\left(r_{1,3}-r_{1,3_0}\right)^2 \quad (1\text{-}2)$$

Where b_0, θ_0, ϕ_0, and $r_{1,3_0}$ are the bond, angle, improper, and Urey_Bradley equilibrium terms respectively, n and δ are the bond, are the dihedral multiplicity and phase and K's are the respective force constants.

1.4.3 Simulation Systems and Techniques

Throughout the thesis, three different systems are employed.

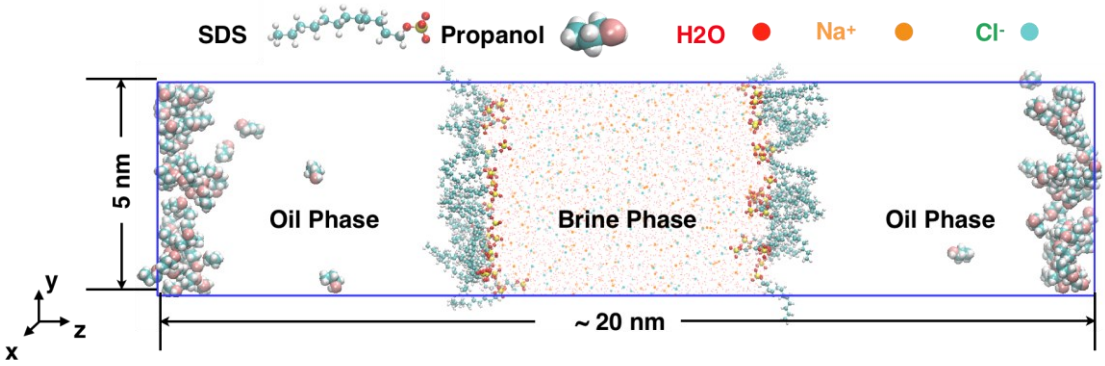

Figure 1-1 Schematic diagram of the initial configuration. n-decane molecules and hydrogen atoms in water molecules are omitted here for a better observation. The periodic boundaries are depicted by blue lines[56].

One is the bilayer system, with one phase (brine) sandwiched in between two symmetrically distributed identical phases (oil or $scCO_2$), as shown in **Figure 1-1**. This system is designed to study the fluid-fluid interfacial properties, which is employed in **Chapters 2**, **3**, **4**, and **6**. Periodic

boundary conditions (PBC) are applied in the *x*-, *y*-, and *z*-directions. The simulation box sizes are 5 nm, 5 nm, and about 20 nm for systems in **Chapters 2**, **3**, and **4** (about 40 nm in **Chapter 6**), in *x*-, *y*-, and *z*-directions, respectively.

The spontaneous aggregation of the surfactants AOT in $scCO_2$ with and without chemical additive (**Chapter 5**) is studied by starting the simulation from the randomly distributed initial configurations (surfactant, chemical additive, CO_2). Different replicas are constructed to study the initial configuration effect. The initial simulation box size for both systems is $11\times11\times11$ nm^3.

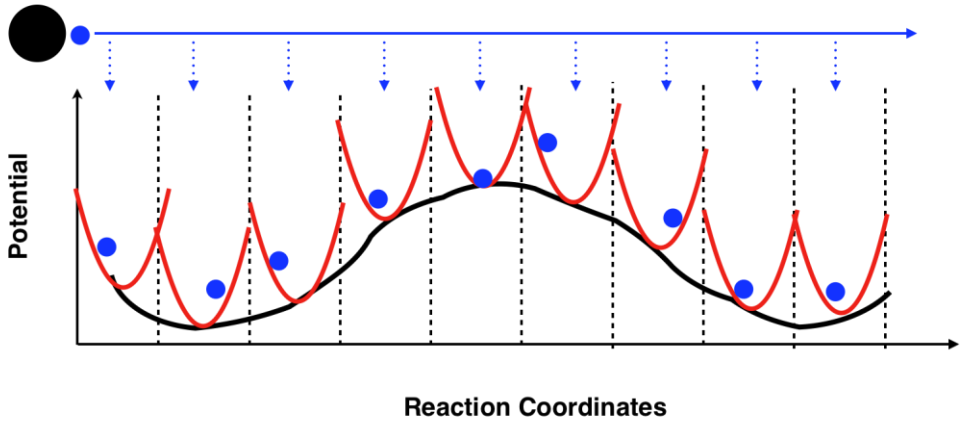

Figure 1-2 Schematic diagram of the initial configuration generation for umbrella sampling.

The free energy profile of AOT self-aggregation (**Chapter 5**) is calculated using umbrella sampling. We first generate initial configurations for umbrella sampling windows with the center of mass (COM) of desired molecules sequentially moving 0.1-0.2 nm between adjacent windows, as shown in **Figure 1-2**. The weighted histogram analysis method[57] is used to obtain PMF curves among the sampled windows. The resulting PMF curves are adjusted by subtracting the entropic contribution of increased accessible phase space due to the volume increment[58], which is given as

$$V_{PMF}(r) = -(n_c - 1)k_B T \log(r) \tag{1-3}$$

Where $n_c = 3$ is the number of dimensions in the reaction coordinate r. The PMF curves are further adjusted by a parallel movement in the *y*-axis to ensure their values vanish at the place where the reaction coordinate is large (2 nm).

The potential of mean force (PMF) can also be calculated from density profile or RDFs when molecular diffusion can overcome the energy barrier in the energy profile. The formula to calculate PMF is given as [59]

$$W(z) = -k_B T \ln \frac{\rho(z)}{\rho_{bulk}}, \tag{1-4}$$

where k_B is the Boltzman constant and T is the system temperature; $\rho(z)$ and ρ_{bulk} are the local density and bulk density, respectively.

1.4.4 Key Formulas and Concepts in Analysis

1.4.4.1 Radial Distribution Functions/Densities

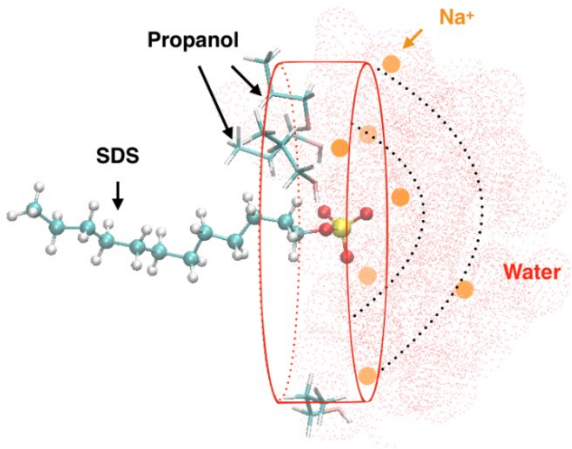

Figure 1-3 Snapshot of propanol, Na^+ ion, and the water molecules around the SDS[56].

The radial distribution functions/densities (RDFs/RDDs) describe how density varies as a function of distance from a reference particle. In the bilayer system we used, the molecular distribution is heterogeneous. Therefore, modified RDFs/RDDs are used to study the molecular distribution around reference particles. Two different formulas are used to calculate the radial distribution densities of the molecules mainly distributed in the interface region (*i.e.*, propanol in **Figure 1-3**), where the shape of the iso-density of the molecules is cylindrical (**Equation 1-5**); and in bulk(*i.e.*, Na^+ and water in **Figure 1-3**), where the shape of iso-density of the molecules are the hemisphere(**Equation 1-6**).

$$\rho_{\mathrm{d,i}}(r) = \frac{\langle N(r) \rangle}{2\pi r \Delta r} \tag{1-5}$$

$$\rho_{\mathrm{d,b}}(r) = \frac{\langle N(r) \rangle}{4\pi r^2 \Delta r} \tag{1-6}$$

where $N(r)$ is the number of the molecules placed in the distance of r to $r + \Delta r$. $\langle ... \rangle$ implies averaging over time and molecules.

Two different formulas are used to calculate the radial distribution functions of the molecules mainly distributed in the interface (**Equation 1-7**) and the bulk (**Equation 1-8**).

$$\rho_i(r) = \frac{\langle N(r) \rangle}{2\pi r \Delta r \rho_{\mathrm{d,i,2\text{-}2.5}}(r)} \tag{1-7}$$

$$\rho_{\mathrm{b}}(r) = \frac{\langle N(r) \rangle}{4\pi r^2 \Delta r \rho_{\mathrm{d,b,2\text{-}2.5}}(r)} \tag{1-8}$$

Where $\rho_{\mathrm{d,i,2\text{-}2.5}}(r)$ and $\rho_{\mathrm{d,b,2\text{-}2.5}}(r)$ are the average of $\rho_{\mathrm{d,i}}(r)$ and $\rho_{\mathrm{d,b}}(r)$ when $2 \le r \le 2.5\,\mathrm{nm}$, where the number density converges to a constant value.

1.4.4.2 Spatial Distribution Functions (SDFs)

SDFs depict the iso-density distribution of target molecules in the three-dimensional space, which can provide a more intuitive observation of the molecular distributions. SDFs can overcome the limitation of the RDFs on can not showing spatial molecular distribution.

1.4.4.3 Interfacial Tension (IFT)

The IFT between two phases γ is obtained from Kirkwood and Buff [60],

$$\gamma = \frac{L_z}{2}\left(\langle P_{zz} \rangle - \frac{\langle P_{xx} \rangle + \langle P_{yy} \rangle}{2} \right) \tag{1-9}$$

Where L_z is the average length of the simulation box in the z-direction, and $\langle P_{\alpha\alpha} \rangle$ (α=x, y, z) is the diagonal element of pressure tensor averaged over time and position. This formula is applied in the bilayer systems.

1.4.4.4 Orientation Parameter

The orientation parameter to quantify the molecular configurations, which is given as [61-63],

$$S_z = \frac{3}{2}\langle \cos^2 \theta_z \rangle - \frac{1}{2} \tag{1-10}$$

where the θ_z is the angle between the z-axis and the molecular axis; $\langle \cdots \rangle$ implies averaging over time and molecules. The value of the orientation parameter can vary from -0.5 to 1. When the molecules are completely parallel to the plane, the calculated orientation parameter is -0.5; the orientation parameter of 1 indicates that the molecules are fully perpendicular to the *x*-*y* plane; the value of the orientation parameter is zero when the molecules are randomly distributed.

1.4.4.5 H-bonds

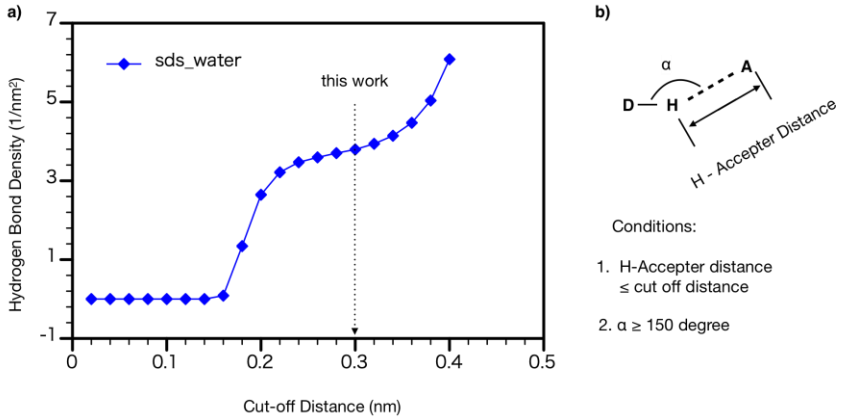

Figure 1-4 Criteria for hydrogen bonding[64].

Further increase in the hydrogen bond density between SDS and water was observed when the cut-off distance is large. This increment is contributed by the water molecules from the second shell[65], which should not be counted as the hydrogen bond.

1.4.4.6 Diffusion Coefficient

The diffusion coefficient is a proportionality factor in Fick's Law. The diffusion coefficient can be measured and calculated using several methods. In this dissertation, D_A, (in the x-y plane and the *z*-direction) are calculated by the Einstein relation[66]:

$$\lim_{t\to\infty}\left\langle \left|x_i(\mathrm{t})-x_i(0)\right|^2+\left|y_i(\mathrm{t})-y_i(0)\right|^2 \right\rangle = 2n\times D_{A,x-y}\times t\,, \tag{1-11}$$

$$\lim_{t\to\infty}\left\langle \left|z_i(\mathrm{t})-z_i(0)\right|^2 \right\rangle = 2n\times D_{A,z}\times t\,, \tag{1-12}$$

where $x_i(\mathrm{t})$, $y_i(\mathrm{t})$, and $z_i(\mathrm{t})$ is the center of mass position of molecule *i* at time *t* in the *x*-, *y*-, and *z*-directions, respectively. *n* is number of dimensions (*n*=2 for *x*-*y* plane, *n*=1 for *z*-direction). $\langle ... \rangle$ implies averaging over time and molecules.

1.5 Organization of Thesis

This dissertation is divided into 7 chapters. **Chapters 2** to **5** have been published in peer-reviewed journals, **Chapter 6** is under submission to a peer-reviewed eBook.

Chapter 1 gives a general introduction of theoretical background, motivation, objectives, and a brief explanation of the simulation methods. **Chapter 2** to **4** explores the chemical additive (co-surfactant) effect on the chemical flooding process. **Chapter 2** probes the effect of ion valency and concentration on the surfactant SDS efficacy at the brine-water interface. **Chapter 3** introduced nonionic alcohols and cationic CTAB surfactants in the systems studied in **Chapter 2**, investigating how different cosurfactants affect the SDS interfacial behaviors with the systems containing divalent ion Ca^{2+}. **Chapter 4** investigates the alcohol distribution and effect on the brine-oil interfacial properties in the systems with only monovalent ions. **Chapters 5** and **6** studied the chemical additive (alcohol) effect on the $scCO_2$ foam flooding process. **Chapter 5** interprets the working mechanism of ethanol in increasing surfactant AOT solubility in $scCO_2$. **Chapter 6** explores the alcohol chain length effect on the foam interfacial properties (*i.e.*, water/$scCO_2$ interface). **Chapter 7** summarizes the key findings and discusses the limitations of this study. Some recommendations for future works are discussed as well.

Chapter 2 : ION VALENCY AND CONCENTRATION EFFECT ON THE STRUCTURAL AND THERMODYNAMIC PROPERTIES OF BRINE-DECANE INTERFACES WITH ANIONIC SURFACTANT (SDS)

A version of this chapter has been published in *J. Phys. Chem. B*. (Nan *et al*.,2021) [64]

2.1 Introduction

Surfactants play an indispensable role in daily lives, from shampoos and detergents to pharmaceuticals and industrial applications (*e.g.*, chemical flooding in enhanced oil recovery (EOR))[5]. The requirement for the surfactant formula varies depending on their applications. For example, pharmaceuticals should be non-toxic and effective in physiological conditions. On the other hand, in EOR processes, the surfactant formula should be stable and effective under reservoir conditions, generally associated with high pressure and high temperature[7-9]. In particular, the formation water (so-called brine), which is omnipresent in oil reservoirs, contains various salt ions (*e.g.*, Na^+, K^+, Ca^{2+}, Mg^{2+}, Cl^-, SO_4^{2-}, CO_3^{2-}, *etc*.)[10], while its salinity can be up to 35 *wt.*%[11, 12]. The strong electrostatic interactions between salt ions and ionic surfactants are imperative to the efficacy and functionality of surfactant formula in EOR.

The main working mechanism of surfactants at the brine-oil interfaces is to decrease the interfacial tension (IFT) so that the residual oils trapped by the capillary forces can be recovered[4-

6, 67]. In the EOR processes, IFT is often used as an important indicator to quantify the efficiency of surfactant formula, while in general a lower IFT is favored[5]. Therefore, the effect of salt ions including salt types and concentrations on IFT (when surfactants are involved) is an important topic in oil exploitations. A number of experimental studies proved that the ion valency and concentration not only affect the morphology and stability of brine-oil interfaces but also have a significant impact on the brine-oil IFT. Taylor *et al.* reported that a significant reduction in IFT is observed by introducing Ca^{2+} ions to the water/n-heptane/naphthenic acid system, while the effect of Na^{+} ions is negligible[68]. Another study on the system with water/oil/linear alkylbenzene sulfonates (LAS) by Anachkov *et al.* also reported that the effect of Ca^{2+} ions is much more significant than that of Na^{+} on the IFT due to the stronger binding between Ca^{2+} ions and surfactants[69]. On the other hand, Yadali *et al.*[70] reported that the IFT of the dilute petroleum sulfonates increases by adding Ca^{2+} ions. Similar results were observed by Kumar *et al*.[71] and Roberson *et al*.[72]. On the other hand, Badakhshan *et al*.[73] reported that the salt concentration (NaCl solution) effect hinges on surfactant and oil component types. They reported that IFT increases as salinity increases for most systems except those with ionic surfactants, which shows a decreasing trend at a high salinity. Theoretical and simulational studies have also been conducted to explore the ion effects in brine-oil systems. A molecular dynamics (MD) simulation study by Sedghi *et al.*[74] reported that the IFT between brine-oil increases with increasing brine salinity. Similar phenomena were also observed by Lara *et. al.*[75], Li *et al*.[76], and Alejandre *et al.*[77]. Nevertheless, non-monotonic changes are also reported[78, 79].

From a molecular perspective, the IFT changes are related to the molecular configurations and their structural properties at the interfaces. There have been studies on the ion effect on structural properties at brine-oil interfaces either containing non-ionic surfactants[76] or without surfactants[78-81], while their effect on the systems containing ionic surfactants[82] (one of the most commonly-used surfactants in the chemical flooding[83]) are scarce. The ions are depleted from the brine-oil interface without the surface active components[84-86], however, the introduction of the ionic surfactants makes the story different. Yan *et al*.[87] observed in-plane aggregations consisting of three-to-four sodium dodecyl sulfate (SDS) surfactants at brine (1.0 M salinity)-vapor interfaces in the presence of Ca^{2+} ions. The in-plane aggregations of SDSs are induced by the SDS-Ca^{2+}-SDS cation bridging. On the other hand, Chen *et al.*[88] reported that divalent ions such as Mg^{2+} and Ca^{2+} barely penetrate into the hydration shell of the SDS sulfate group, resulting in less cation bridging at the brine (1.0 M salinity)/SDS/vapor interface than Na^{+} only systems. Recently, Müller *et al*.[89] reported that the ionic surfactant distributions at the brine-oil and water-vapor interfaces are different due to the cooperative/competitive behaviors of the oil and surfactants. While these works shed light on the structural and thermodynamic properties of water-oil and water-vapor interfaces with anionic surfactants, a comprehensive understanding of the effect of salt ion valency and concentrations on brine-oil interfaces with anionic surfactants is still lacking.

Therefore, in this work, we use MD simulations to study the effect of salt ion valency and concentration on the structural and thermodynamic properties of brine-oil interfaces with anionic surfactants. The temperature and pressure are set as 353 K and 200 bar, respectively[76], to

represent a typical reservoir condition. Crude oil is composed of thousands of components, which is hardly reproducible in the molecular simulation with the exact formula and fraction of each component[90-92]. For simplicity, we chose n-Decane[93], which contains the same carbon number as the recommended crude (light) oil equivalent alkane carbon number (EACN)[94-97], to represent the oil phase. We design a series of brine phases with varying salt concentrations (0 ~ 25 *wt*.% and cation valency (Na^+ and Ca^{2+})). We use SDS as an anionic surfactant, which is commonly used in chemical flooding. The Gibbs surface excess[98] of the surfactant is fixed as 1 nm^{-2}, within the practical range during chemical flooding[83]. We find that ion valency has a significant effect on the structural properties of SDS at the brine-decane interfaces. Due to strong electrostatic interactions, SDS and Ca^{2+} ions can form SDS-Ca^{2+} complexes with a pentagon-like structure through SDS-Ca^{2+}-SDS cation bridging. The cation bridging induces a non-uniform surfactant distribution at the brine-oil interfaces and further increases the brine-oil IFT. This work should provide important insights into the design and optimization of anionic surfactant formula for effective EOR processes.

The remainder of this paper is organized as follows. In **Computational Methodology**, we introduce the simulation methods and define molecular models. In **Result and Discussion**, we first investigate the salt ion effect (valency and concentration) on the structural properties (*i.e.*, in-plane aggregation and hydrogen bonding). Then, we discuss the relationship between structural properties and IFT. In **Conclusion**, we summarize key findings and discuss potential implications.

2.2 Computational Methodology

2.2.1 Molecular Model and Simulation

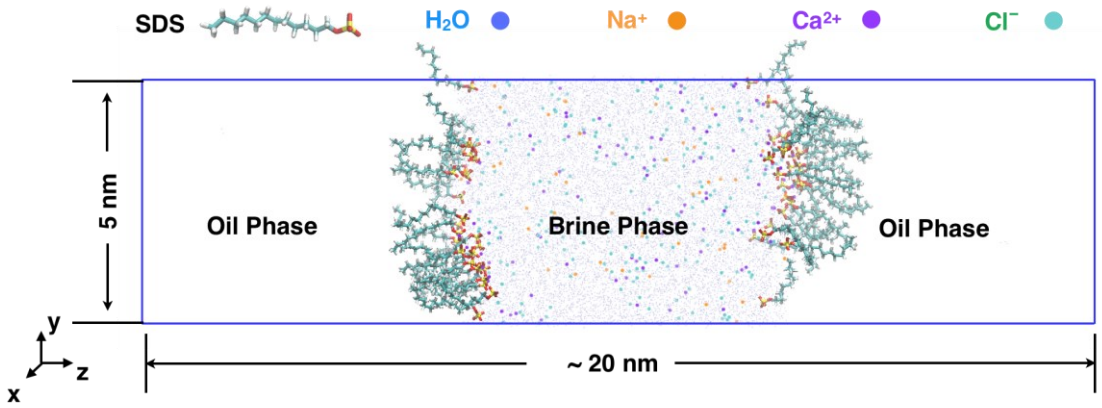

Figure 2-1 System configuration at equilibrium (system IV_Ca). Oil phase is represented by n-decane molecules, which are not shown for clarity. The periodic boundaries are depicted by the blue rectangular.

The system design in this study is similar to our previous work[56]: a brine phase is sandwiched between two decane phases as shown in **Figure 2-1**. The simulation box sizes are 5 nm, 5 nm, and ~20 nm in the *x*-, *y*-, and *z*-directions, respectively. The lengths of decane and brine slabs in the *z*-direction are about 6 nm and 8 nm, respectively. Such a dimension is large enough to overcome the finite size effect[76]. A series of systems (denoted as I, II, III, IV, and V) over a wide range of salt concentrations (from 0 to 25 *wt*.%) are designed to study the ion concentration effect. The ion valency effect is studied by replacing Na^+ ions with Ca^{2+} ions while keeping the number of Cl^- ions the same (denoted as II_Ca, III_Ca, IV_Ca, and V_Ca). The concentration of

SDS in most systems at the brine-decane interface is 1 nm^{-2}, within the practical range during chemical flooding[83]. We note that SDS concentration at the pure water- decane interface at the critical micelle concentration (CMC) point is around 3.18 nm^{-2} (see **Appendix A.1**). The number of molecules and the corresponding bulk brine salt concentrations in various systems are listed in **Table 2-1**. The same number of SDS molecules are located at the two brine-oil interfaces. Three-dimensional (3-D) periodic boundary conditions (PBCs) are applied in all cases.

Table 2-1 System settings in each simulation run.

System	SDS	Water	Na^+	Cl^-	Ca^{2+}	n-Decane	Bulk Brine Concentration (*wt.* %)	Bulk Brine Concentration Cl^- (M)
I	50	5200	50	0	0	874	0.233	0.000
II	50	5200	100	50	0	874	4.149	0.690
III	50	5200	152	102	0	874	7.943	1.311
IV	50	5200	270	220	0	874	16.107	2.601
V	50	5200	402	352	0	874	25.220	3.960
II_Ca	50	5200	50	50	25	874	3.331	0.559
III_Ca	50	5200	50	102	51	874	5.883	0.999
IV_Ca	50	5200	50	220	110	874	13.319	2.243
V_Ca	50	5200	50	352	176	874	22.416	3.694

We employ the CHARMM36[50] (an all-atom force field) combined with the modified TIP3P[99] forcefield as well as TIP3P compatible ions in the present work, as it has been reported as the best forcefield to study the structural properties of SDS among the commonly used forcefields (OPLS-AA[44], OPLS-UA[45, 46], and GROMOS[48, 49] force field). A series of calibrations are conducted by comparing various physical properties (densities (pure n-Decane and

brine) and IFT (pure water-decane)) to the experimental results (see **Appendix A.1**). Our simulation generally shows a good agreement with experimental data in terms of densities[100] and IFT[101, 102].

2.2.2 Simulation Details

All simulations are conducted by GROMACS (version 2019.1)[103] software package. The equations of motions are integrated by the Leap-Frog algorithm[104] with a time step of 2 fs. The system energy is first minimized until the maximum force is less than $1000\,kJ\,mol^{-1}nm^{-1}$ using the steepest descent algorithm. An equilibration run of 20 ns (*i.e.,* 0-20 ns) followed by a production run of 70 ns (*i.e.,* 20-90 ns) in NP_zT (*i.e.*, a fixed number of molecules, a constant pressure in the *z*-direction normal to the interfaces, and a constant temperature) ensemble is carried out at a constant pressure of 200 bar and temperature of 353 K. Velocity rescaling[105] and Nose-Hoover[106] thermostats with a relaxation time of 0.1 ps is employed to control the system temperature for the equilibration and production processes, respectively. Berendsen[107] and Parrinello-Rahman[108] barostats with a time interval of 0.2 ps are used to control the *z*-direction pressure for the equilibration and production processes, respectively. The atomic and molecular trajectories in the production stage are saved every 100 steps (200 fs) for data analysis.

The particle-mesh Ewald (PME) method[109] with a Fourier spacing of 0.12 nm and a 1.2 nm real-space cut-off is used to calculate the electrostatic interactions. Lennard Jones (LJ) forces are modified to decay smoothly to zero between 1.0 nm and 1.2 nm[103]. LJ interactions between the unlike atoms are obtained from the conventional Lorentz-Berthelot[110, 111] mixing rules. The SETTLE algorithm[112] is used to constrain the bond length and angle of water molecules,

while the LINCS algorithm[113] is used to constrain the bond length for other molecules. The snapshots are presented by the Visual Molecular Dynamics (VMD) package[114].

2.3 Results and Discussion

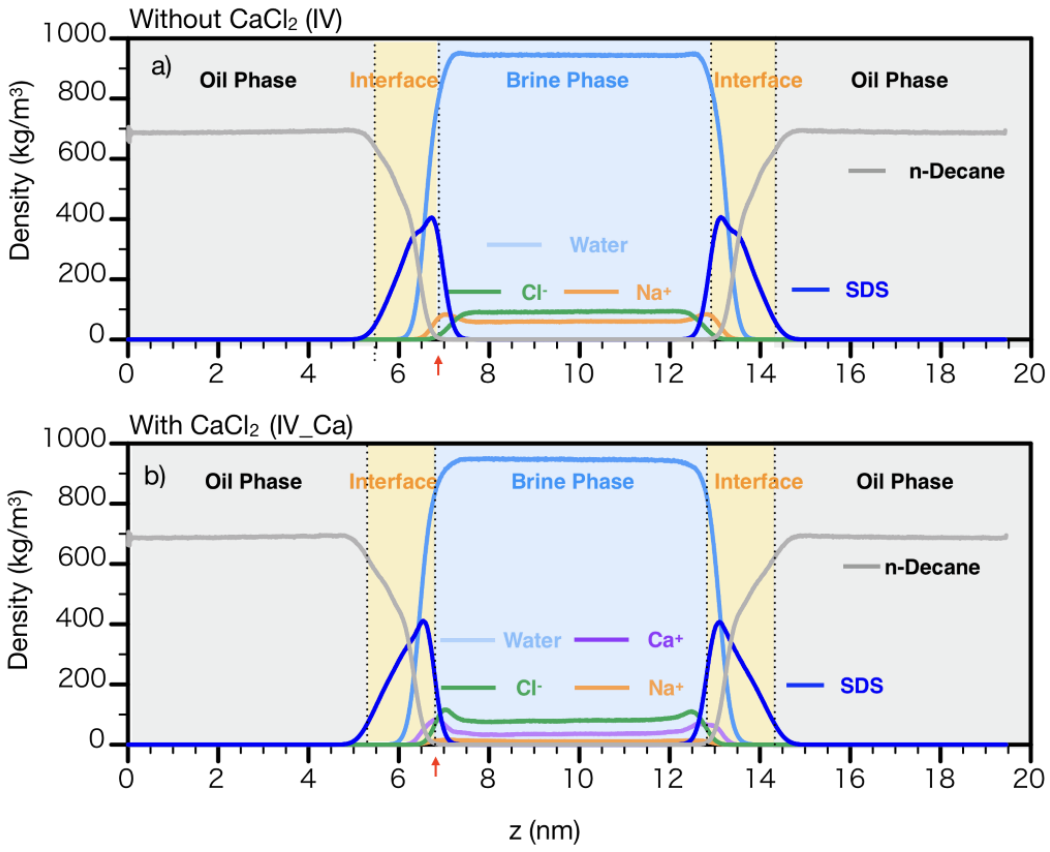

Figure 2-2 Mass density distribution of each component in a) system IV; b) system IV_Ca. The oil phase, interface region, and brine phase are represented by gray, yellow, and blue colors, respectively. The boundaries of the interface region are depicted by dotted lines.

In **Figure 2-2**, we present fluid density distributions in the *z*-direction in system IV (**Figure 2-2 a**) and system IV_Ca (**Figure 2-2 b**). The density distributions in other systems are similar, which are depicted in **Appendix A.2**. We use the "90-90" criterion[115] to define the brine-oil

interface regions, where the interfacial boundaries are 90% of oil and water bulk density values. For both systems, all SDS molecules distribute in the brine-oil interface region. Both n-decane and water densities converge to their respective bulk values far away from the interface region. For system IV, Na^+ ions are enriched at the interface, while Cl^- ions are depleted. On the other hand, in system IV_Ca, Ca^{2+} ions are preferably adsorbed at the interface, followed by Cl^- adsorption, which is in line with the previous simulation observation in a water-SDS-vapor system[87]. The enrichment of Cl^- ions at the interface in system IV_Ca is due to the strong Ca^{2+} adsorption forming a layering structure[116]. The positive adsorption of the counterions (Na^+ and Ca^{2+}) is due to the existence of the anionic SDS. With the absence of the SDS, all the ions are depleted from the brine-decane interface, as shown in **Appendix A.3**. We note that ion densities converge to constant values in the middle of the brine phase in both systems, representing their salt concentrations in **Table 2-1** (columns 9 and 10). Although the total numbers of Cl^- ions in systems IV and IV_Ca are equal, Cl^- concentrations in the bulk brine are not the same due to the drastically different Cl^- distributions at the interface as shown in **Figure 2-2**.

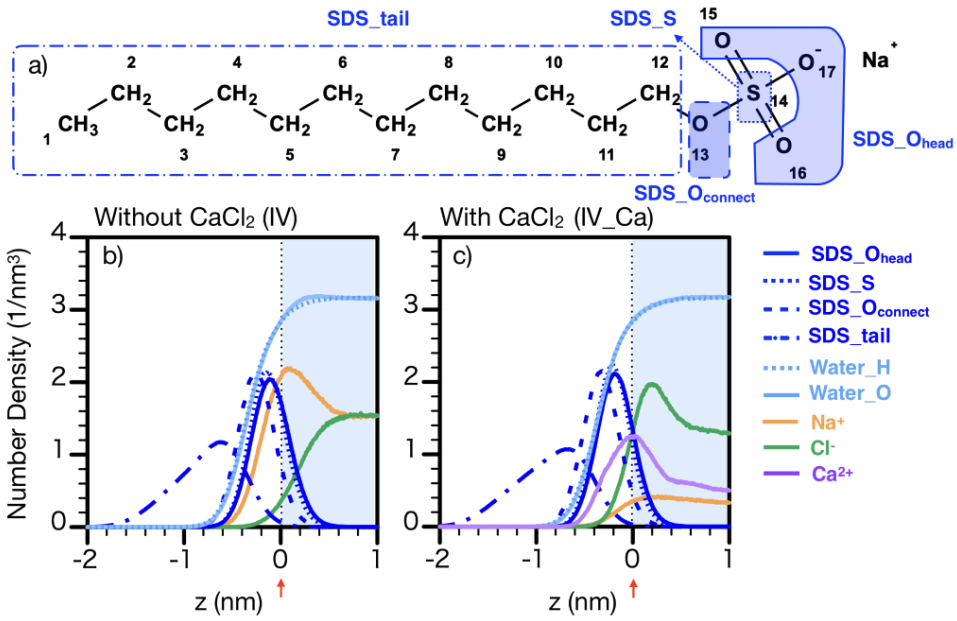

Figure 2-3 a) Molecular structure of SDS; b) number density distributions of functional groups in system IV in the interface region; c) same as b) but for system IV_Ca. In b) and c), Water_H and Water_O density distributions are scaled down by 20 and 10 times for a better comparison, respectively, for clarity; the entire functional group is counted as one unit; the black dotted lines represent the contact of the brine phase and the interface region.

We classify SDS molecules into four distinct functional groups (SDS_O_{head}, SDS_S, SDS_$O_{connect}$, and SDS_tail) as shown in **Figure 2-3 a** to investigate detailed molecular distributions. The number density distributions of each functional group for systems IV and IV_Ca in the interface region are presented in **Figures 2-3 b** and **2-3c**, respectively. For a better comparison, the origin of the *z*-axis is set at the contact of the interface region and brine phase highlighted by a red arrow in **Figure 2-2**. In addition, the water hydrogen and oxygen (Water_H and Water_O) densities are reduced by 20 and 10 times, respectively, for a better observation. For both cases, the peak in SDS_O_{head} distributions is the closest to the brine phase, and the peaks in

SDS_S, SDS_$O_{connect,}$ and SDS_tail subsequently shift away from the brine phase. SDS_O_{head}, SDS_$O_{connect}$, and SDS_S have similar distributions, while their peak positions have subtle differences. Thus, for simplicity, we use the SDS_S density distributions to represent the entire SDS head group distributions in the following discussion.

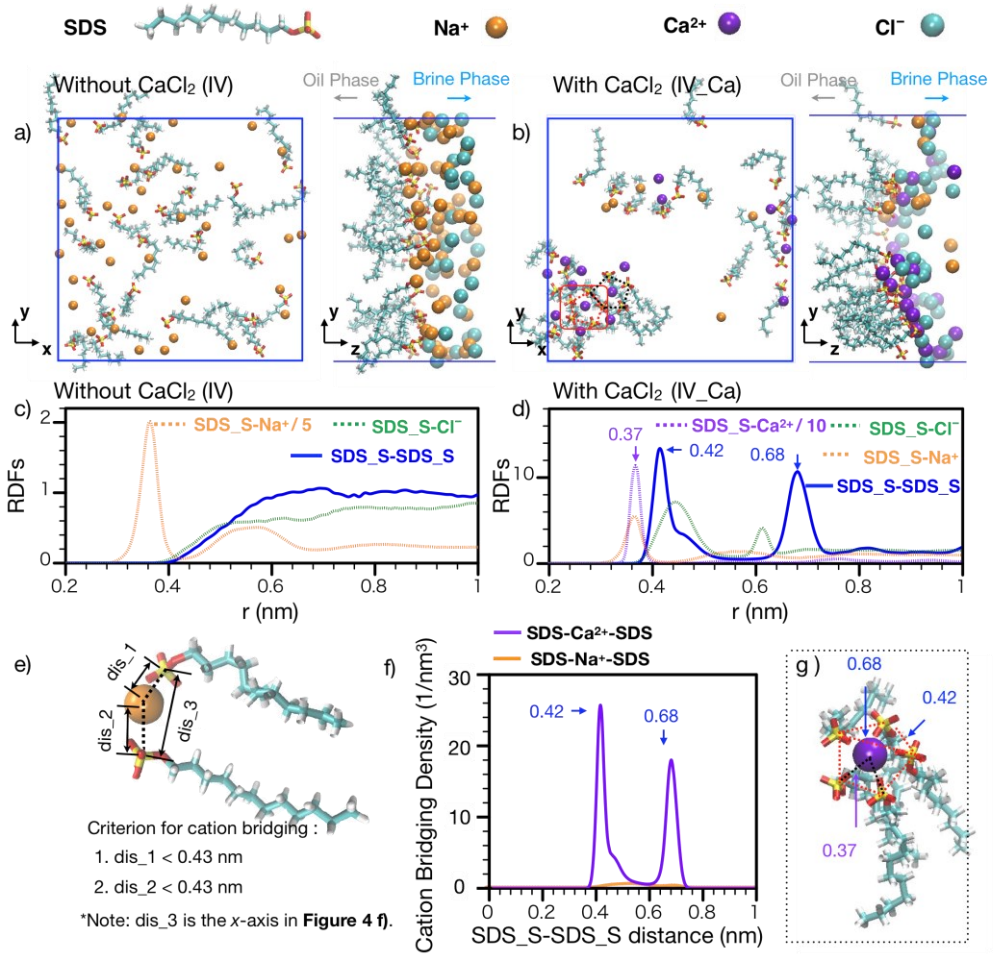

Figure 2-4 Snapshots in the *x*-*y* and *y*-*z* planes for a) system IV; b) system IV_Ca. Snapshots in the *x*-*y* plane are obtained in the region of z < 0.4 nm shown in Figures 2-3 b and c. Cl^- ions are omitted in the snapshots in the *x*-*y* plane for clarity. The red rectangle highlights the formation of pentagon-like SDS-Ca^{2+} complexes. The black dashed lines enclose the structures satisfying Pentagon_C1 but not qualifying as Pentagon_C2. The red dashed lines enclose the structures

satisfying Pentagon_C2. RDFs of SDS_S and ions around SDS_S in c) system IV; d) system IV_Ca. e) Criteria of cation bridging. f) Cation bridging distributions of SDS-Na^+-SDS and SDS-Ca^{2+}-SDS in systems IV and IV_Ca, respectively. g) The Pentagon_C2 structure is highlighted in the red rectangle in Figure 2-4 b.

To better understand the structural properties of SDS at the brine-oil interfaces, the snapshots of systems IV and IV_Ca in the interface region in the *x-y* and *y-z* planes are presented in **Figures 2-4 a** and **2-4 b**, respectively. In system IV (**Figure 2-4 a**), SDS molecules are well dispersed at the *x-y* interface plane. Meanwhile, Cl^- ions rarely penetrate into the SDS and Na^+ ion layers in the *y-z* plane, which is also revealed in **Figure 2-2 b** (Cl^- ions are depleted at the brine-oil interfaces). On the other hand, aggregation of SDS molecules in the *x-y* plane and penetration of Cl^- ions into SDS and cation (Na^+ and Ca^{2+}) layers in the *y-z* plane are observed for system IV_Ca (see **Figure 2-4 b**), in line with **Figure 2-2 c** (Cl^- ions are enriched at the brine-oil interfaces). The radial distribution functions (RDFs) of SDS_S and salt ions around SDS_S are depicted in **Figures 2-4 c** and **2-4 d** (details about RDF calculations can be referred to **Chapter 1 Section 1.4.4.1**). For better visualization, the Na^+-SDS_S RDF in **Figure 2-4 c**, and the Ca^{2+}-SDS_S RDF in **Figure 2-4d** are reduced by 5 and 10 times, respectively. In **Figure 2-4 c**, Na^+ and Cl^- ions, as counterions and coions for SDS molecules, show accumulation and depletion around SDS_S, respectively. No distinct peak is observed in the SDS_S-SDS_S RDF. However, in **Figure 2-4 d**, in the presence of Ca^{2+} ions, all the salt ions (including Na^+, Ca^{2+}, and Cl^-) show strong adsorptions around SDS_S. Besides, two distinguishable peaks at $r = 0.42$ nm and $r = 0.68$ nm are observed in the SDS_S-SDS_S RDF. The peaks in the SDS_S-SDS_S RDF induced by Ca^{2+} ions are due to the cation

bridging defined as two SDS molecules bridged by a cation (Ca^{2+} ion here) with the separation distance between the cation and SDS_S less than 0.43 nm (see **Figure 2-4 e**). The distance criterion (0.43 nm) is obtained from the first local minimum position in the SDS_S-Na^{+} and SDS_S-Ca^{2+} RDFs (see **Appendix A.4**). All the structures satisfying the cation bridging criteria are further classified to obtain the cation bridging distributions (see **Appendix A.4**) as shown in **Figure 2-4 f**. The orange and purple lines in **Figure 2-4 f** represent the cation bridging distributions of SDS-Na^{+}-SDS in system IV and SDS-Ca^{2+}-SDS in system IV_Ca, respectively. SDS-Na^{+}-SDS cation bridging is negligible compared to that of SDS-Ca^{2+}-SDS, which is in line with the results shown in **Figures 2-4 a**-**d**. We note that the peak positions in the cation bridging distributions in SDS-Ca^{2+}-SDS in system IV_Ca (**Figure 2-4 f**) are the same as those in the SDS_S-SDS_S RDF (**Figure 2-4 d**), indicating that the SDS aggregation is dominated by the SDS-Ca^{2+}-SDS cation bridging.

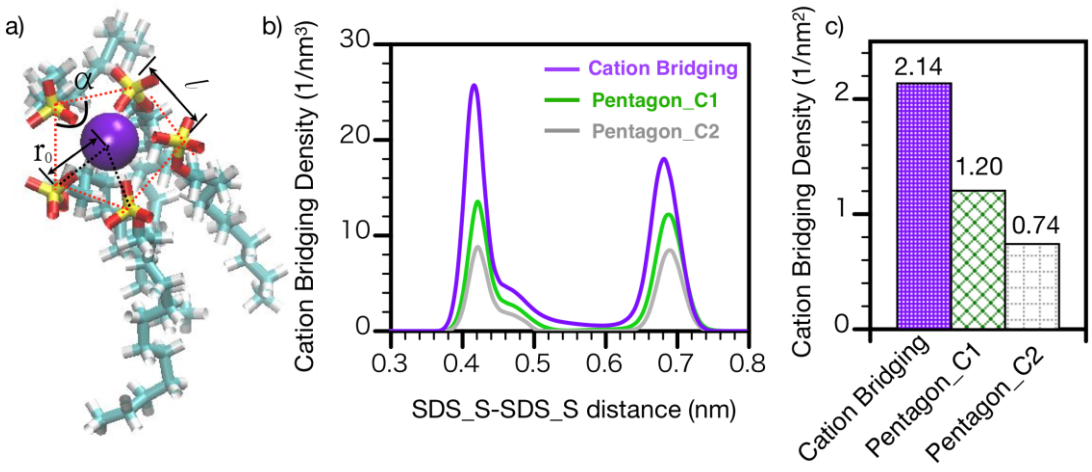

Figure 2-5 a) Characterization of the pentagon-like structures; b) cation bridging distributions in different scenarios in system IV_Ca; c) cation bridging densities in different scenarios in system IV_Ca.

In addition, we also observe the formation of unique SDS-Ca^{2+} complexes with a pentagon-like structure highlighted in the red rectangle in **Figure 2-4 b**, where the head groups of five SDS molecules are bounded by one Ca^{2+} ion. The pentagon-like structures can be classified based on two different criteria: The **Criterion I** is that there are exactly five SDS_Ss around a Ca^{2+} ion with the SDS_S-Ca^{2+} separation distance r_0 less than 0.43 nm; The **Criterion II** is that the angle formed by three neighboring SDS_Ss, α, is within 108°±10° and the distance between two adjacent SDS_Ss, l, is within 0.4 nm±0.1 nm (see **Figure 2-5 a**). The pentagon-like structures satisfying **Criterion I** are classified as "Pentagon_C1" and those satisfying both **Criterion I** and **Criterion II** are denoted as "Pentagon_C2". In other words, Pentagon_C2 is the subsect of Pentagon_C1. It is possible that the five SDS_Ss and one Ca^{2+} ion consisting Pentagon_C1 or Pentagon_C2 are not on the same plane. We present the standard deviation distances from SDS_S and Ca^{2+} ion to the

optimized plane in the Pentagon_C1 and Pentagon_C2 structures in **Appendix A.6**. The deviations are generally small (less than 0.05 nm), indicating that the SDS_Ss and Ca^{2+} ion in Pentagon_C1 and Pentagon_C2 structures almost perfectly align in the same plane. In other words, the Pentagon_C1 and Pentagon_C2 structures represent the in-plane aggregation of SDSs around Ca^{2+} ions arising from the cation bridging. In fact, the pentagon-like structure highlighted in the red rectangle in **Figure 2-4 b** qualifies as Pentagon_C2, with typical SDS_S-SDS_S and SDS_S-Ca^{2+} separation distances shown in **Figure 2-4 g** concede with the peak positions in SDS_S-SDS_S and SDS_S-Ca^{2+} RDFs shown in **Figure 2-4 d**.

Figure 2-5 b presents the cation bridging distributions in the structures satisfying the criteria "Cation Bridging", "Pentagon_C1", and "Pentagon_C2" in system IV_Ca. The peak values in the cation bridging distributions gradually decrease as more restrictions are applied. The integration of the cation bridging distributions along the SDS_S-SDS_S distance provides the cation bridging density in different scenarios as shown in **Figure 2-5 c**. Around 56.3% of total cation bridgings are contributed by Pentagon_C1 (1.20 nm^{-2} out of 2.14 nm^{-2}) with about 34.6% of them arising from Pentagon_C2 (0.74 nm^{-2} out of 2.14 nm^{-2}). We also checked the dependence of this pentagon-like structure on the forcefield (CHARMM36, OPLS-AA, and OPLS-UA) in **Appendix A.5**. The pentagon-like structure is still observed in the results from OPLS-AA[44] and OPLS-UA[45, 46] forcefield. All the results shown in the main text are results from the CHARMM36[50] forcefield.

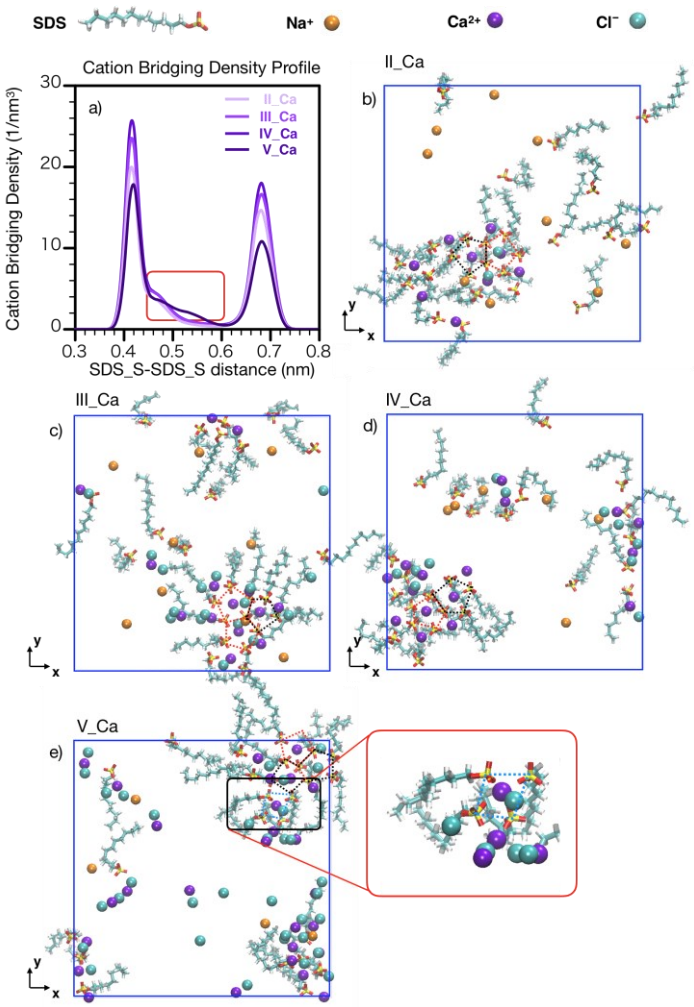

Figure 2-6 a) Cation bridging distributions for the systems containing Ca^{2+} ions (II_Ca, III_Ca, IV_Ca, V_Ca). The darker color indicates a higher salinity. The difference in distribution shape is highlighted by a red rectangle. The snapshots in the *x*-*y* plane for b) system II_Ca; c) system III_Ca; d) system IV_Ca; e) system V_Ca. The black dashed lines enclose the structures satisfying Pentagon_C1 but not qualifying as Pentagon_C2. The red dashed lines enclose the structures satisfying Pentagon_C2. The snapshots in the *x*-*y* plane are obtained by the same method in Figure 2-4.

Table 2-2 Total cation bridging density and those from Pentagon_C1 and Pentagon_C2 in systems containing Ca^{2+} ions.

System	Total Cation Bridging Density (nm^{-2})	Cation Bridging Density From Pentagon_C1 (nm^{-2})	Cation Bridging Density From Pentagon_C2 (nm^{-2})
II_Ca	1.76	0.91	0.53
III_Ca	2.00	1.17	0.71
IV_Ca	2.14	1.20	0.74
V_Ca	1.57	0.74	0.46

The Pentagon_C1 and Pentagon_C2 structures are observed in all the systems containing Ca^{2+} ions (II_Ca, III_Ca, IV_Ca, and V_Ca) as shown in **Figure 2-6**. The *x-y* plane snapshots for these systems can be found in **Figures 2-6 b-e**. **Figure 2-6 a** depicts the cation bridging distributions in different systems. Overall, the shapes of the cation bridging distributions for systems II_Ca, III_Ca, and IV_Ca are similar except that their peak values are different. The peak values first increase and then decrease as salinity increases. In addition, as shown in **Table 2-2**, the total cation bridging density and those from Pentagon_C1 and Pentagon_C2 gradually increase. The increment trend in systems II_Ca, III_Ca, and IV_Ca can be attributed to the increase in the Ca^{2+} distributions at the brine-decane interfaces which enhances the cation bridging possibility (see **Appendix A.7**). However, when the salinity further increases (*e.g.*, system V_Ca), the peak values at 0.42 nm and 0.68 nm are lower than those in system IV_Ca. It is probably because as salinity increases, Cl^- ions are enriched at the brine-decane interfaces due to the double layer[116] (see **Appendix A.7**), which can disturb the formation of cation bridging. This strong adsorption of Cl^- ions around SDS_S interferes with other SDS_Ss, especially with the second peak in cation bridging distributions at

$r = 0.68$ nm as shown in **Appendix A.9** (*i.e.*, the radial distribution density of Cl^- ions around SDS_S increment as salinity increases). We also note that, in system V_Ca, the shape of cation bridging distribution is slightly different from the rest as highlighted by the red rectangular box in **Figure 2-6 a**. **Figure 2-6 e** highlights the disturbance of a pentagon-like structure (rather than forming a quadrilateral structure), where one Cl^- ion penetrates into the SDS-Ca^{2+} complex. A more detailed analysis is conducted on the pentagon-like structure disturbance in systems IV_Ca and V_Ca, as shown in **Appendix A.8**. The reduction in the cation bridging density from Pentagon_C1 (from 1.20 nm^{-2} to 0.74 nm^{-2}) accounts for more than 80% of the total cation bridging density decrement (from 2.14 nm^{-2} to 1.57 nm^{-2}), highlighting the pentagon-like structure melting by Cl^- ions. As a result, the contribution of Pentagon_C1 to the total cation bridging density drops from 56.3% (1.20 nm^{-2} out of 2.14 nm^{-2}) in system IV_Ca to 47.1% (0.74 nm^{-2} out of 1.57 nm^{-2}) in system V_Ca as shown in **Table 2-2**.

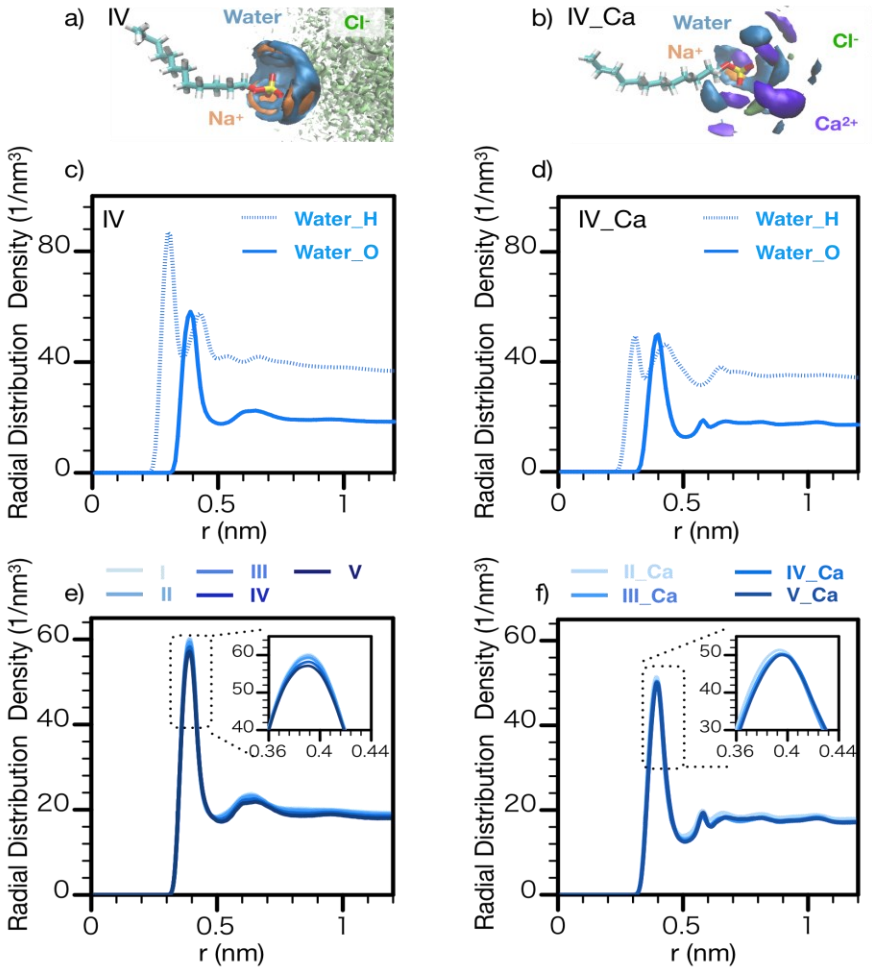

Figure 2-7 Spatial distribution functions (SDFs) of a) water (102/nm^3), Na^+ (5/nm^3), and Cl^- (3/nm^3) around the SDS head group in system IV; b) water (102/nm^3), Na^+ (5/nm^3), Ca^{2+} (31/nm^3), and Cl^- (3/nm^3) around SDS head group in system IV_Ca; radial distribution density of water_O and water_H around SDS_S in c) system IV; d) system IV_Ca; radial distribution density of water_O around SDS_S at various salinities in e) systems without Ca^{2+} ions (*i.e.*, I, II, III, IV, and V); f) systems with Ca^{2+} ions (*i.e.*, II_Ca, III_Ca, IV_Ca, and V_Ca). The darker color indicates a higher salt concentration.

Ion valency and concentration not only affect the cation bridging and the formation of pentagon-like structures but also influence the SDS head group hydration structures. **Figures 2-7**

a and **b** illustrate the spatial distribution functions (SDFs) of the water and salt ions around the SDS head groups in system IV and system IV_Ca, respectively. SDFs are the three-dimensional (3D) iso-density distributions of the selected components around a specific group, which can intuitively display the molecular configurations in the 3D space. In system IV, the SDS head group is almost fully solvated by water molecules except for the locations around the SDS_O_{head}, which is surrounded by Na^+ ions. In addition, Cl^- ions are largely depleted from the SDS head group, which is in line with **Figure 2-4 c**. On the other hand, in system IV_Ca, the water hydration structure is greatly disturbed by salt ions as shown in **Figure 2-7 b**. Radial density distributions of Water_H and Water_O around SDS_S in **Figures 2-7 c** and **d** also reveal significant decrements in the hydration structures due to Ca^{2+} ions. The salinity effect on the hydration structures is also revealed in **Figures 2-7 e** and **f**. It can be seen that the peak value decreases as salinity increases in all the systems, indicating weaker water solvation around SDS. The hydration structure influences the hydrogen bonding (H-bonding) between SDS and water and ultimately affects the SDS efficacy (*e.g.*, IFT reduction). The H-bond density between SDS and water is recognized and the calculation details can be found in **Chapter 1**, **Section 1.4.4.5**.

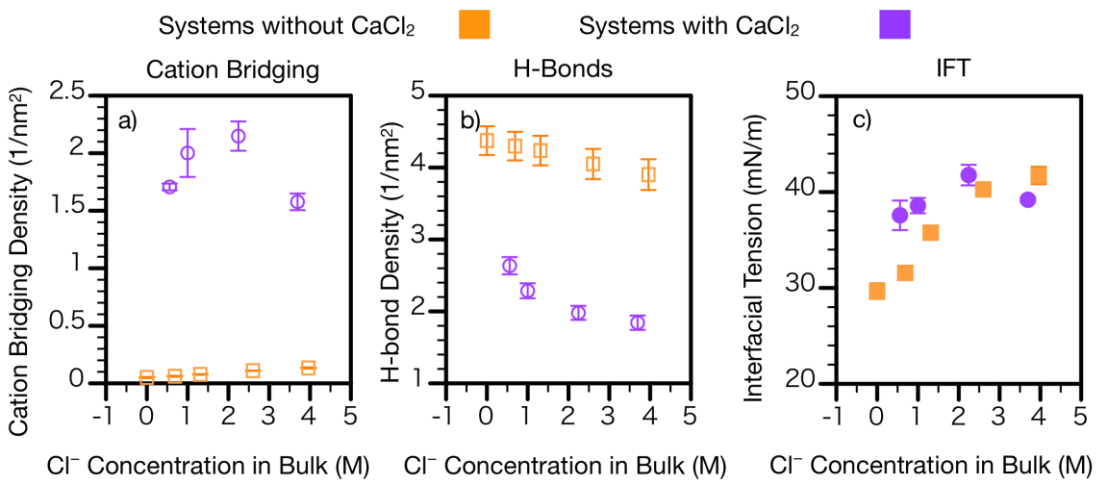

Figure 2-8 a) Cation bridging densities for all the systems; b) H-bond densities between SDS and water of SDS for the systems for all the systems; c) interfacial tension for all the systems

All the above discussion focuses on the structural properties of SDS at the brine-decane interfaces. On the other hand, the main mechanism of SDS in the EOR process is the brine-decane IFT reduction. **Figure 2-8** summarizes the effect of ion valency and concentration on cation bridging density, H-bond density between SDS and water, as well as brine-decane IFT. **Figure 2-8 a** compares the cation bridging capability in all the systems. It can be seen that Na^+ ion has a negligible capability to form SDS-Na^+-SDS cation bridging, while Ca^{2+} ion could form a significant number of SDS-Ca^{2+}-SDS cation bridging. This result is in line with previous studies[65, 117], which reported that the divalent ions can induce strong cation bridging. Besides, as salt concentration increases, the SDS-Na^+-SDS cation bridging density gradually increases, but that in SDS-Ca^{2+}-SDS shows an increasing trend until Cl^- concentration reaches 2.24 M and then decreases afterward. **Figure 2-8 b** presents the H-bond density between SDS and water in all the systems. When the system contains Ca^{2+} ions, H-bond density dramatically decreases compared

to those systems that only contain Na^+ ions. This can be explained by the hydration structure differences in **Figures 2-7 a-d**. H-bond density decreases as the ion concentration increases for both cations (Na^+ and Ca^{2+}), which can be seen in **Figures 2-7 e** and **f**, where SDS_S is increasingly less hydrated by water as salinity increases. **Figure 2-8 c** plots the brine-decane IFTs in all the systems. The IFT calculation is shown in **Chapter 1**, **Section 1.4.4.3**. We find that in the system without Ca^{2+} ions, brine-decane IFT monotonically increases, whereas, in the systems with Ca^{2+} ions, brine-decane IFT first increases and then decreases, showing a similar trend to the cation bridging density shown in **Figure 2-8 a**. Collectively, we find that brine-decane IFT depends on the surfactant structural properties such as cation bridging and H-bond. In the systems without Ca^{2+} ions, SDS molecules are more uniformly distributed at the interface than those containing Ca^{2+} ions (see **Figure 2-4 a**). Their brine-decane IFT has a negative correlation with H-bond (*i.e.*, increases as salinity increases), which is unfavorable for effective chemical flooding[83]. On the other hand, SDS molecules render a non-uniform distribution in the systems containing Ca^{2+} ions (see **Figure 2-4 b**), in which the SDS distribution pattern is the determining factor for IFT. Therefore, brine-decane IFT has a synchronous change with cation bridging density. This result is in line with the previous theoretical study which suggested that the in-plane aggregation of surfactants at the interface can not be overlooked[118]. Meanwhile, the salt concentration also shows a non-monotonic relation with IFT in the systems with Ca^{2+} ions. This result suggests that extensive attention should be paid during the chemical flooding process with ionic surfactants when there exist divalent ions in the formation water. On the other hand, it also implies that designing the surfactant formula with a better dispersity or co-surfactant blending to disturb in-

plane surfactant aggregations might improve the chemical flooding efficiency. We note that the current work does not consider the surface excess change (usually increases with adding Ca^{2+} ions due to tighter packing) of surfactants at the interface, which might have a significant effect on the IFT of the brine-decane interface[68, 89, 119]. This limitation is also the possible reason for the deviation of the IFT trend from the experimental reports[69]. On the other hand, fixing the surface excess of surfactant has advantages in exclusively studying the in-plane aggregation effect on the thermodynamic properties at the interface, which is important from a theoretical perspective.

2.4 Summary

In this chapter, we use MD simulations to study the effect of salt ion valency and concentration on the structural and thermodynamic properties of SDS at the brine-decane interfaces under typical reservoir conditions. We find that ion valency has a significant effect on the molecular configurations due to the strong adsorption of Ca^{2+} ions at the interface, which can induce the SDS-Ca^{2+}-SDS cation bridging, forming SDS-Ca^{2+} complexes. Such a structure renders a non-uniform distribution of SDS at the interfaces, which can probably hamper the efficiency of the chemical flooding[120]. We also highlight that the SDS-Ca^{2+} complexes with a pentagon-like structure are observed in the systems with Ca^{2+} ions at all salinity conditions. It is also noted that these pentagon-like structures are also observed under ambient conditions (298.15 K, 1 bar), which might have a significant effect on SDS efficiency as surface-active components applied in the industries conducted under mild conditions (see **Appendix A.11**).

For the systems without Ca^{2+} ions, the cation bridging density between SDS and Na^{+} monotonically increases as ion concentration increases. Salt ions also reduce the H-bond density between SDS and water. As a result, brine-decane IFT increases as salt concentration increases for the systems without Ca^{2+} ions. In systems with Ca^{2+} ions, the cation bridging density between SDS and Ca^{2+} ions first increases, then decreases, as ion concentration increases. The decrease in cation bridging density under high salinity conditions is due to the accumulation of Cl^{-} ions at the interface, disturbing the formation of SDS-Ca^{2+} complexes. Similar to the systems without Ca^{2+} ions, the H-bond density between SDS and water decreases as ion concentration increases for the systems with Ca^{2+} ions.

Collectively, we find that the presence of divalent ions can greatly influence the interactions between SDS and salt ions as well as those between SDS and water, thus further altering the functionalities of anionic surfactants at the brine-decane interfaces, which cannot be overlooked when applying chemical flooding. Our work provides important insights into the structural and thermodynamic properties of anionic surfactant, water, oil, and salt ions at the brine-oil interfaces which play an imperative role in the design and optimization of chemical flooding processes.

Current study is limited in studying the ion valency and concentration effect using Na^{+} and Ca^{2+} ions as cations, which have similar ion sizes (see **Appendix A.12**). The size of the ions might also have a significant effect on the molecular arrangement at the interface. Our preliminary result on the different ion sizes (Na^{+}, K^{+}, Mg^{2+}, and Ca^{2+}) also shows that the cation bridging density and H-bond density are also affected by the ion size (see **Appendix A.12**). In our future works, we

would study the ion size effect on the surface molecular arrangement and thermodynamic properties.

Chapter 3 : MOLECULAR DYNAMICS STUDIES ON EFFECTIVE SURFACE-ACTIE ADDITIVES: TOWARDS HARD WATER RESISTANT CHEMICAL FLOODING FOR ENHANCED OIL RECOVERY

A version of this chapter has been published in *Langmuir*. (Nan *et al*.,2022) [121]

3.1 Introduction

Chemical flooding, in which chemical formulas are injected into oil reservoirs, is an important enhanced oil recovery (EOR) approach. Either pure or mixtures of surface-active additives (surfactants and/or co-surfactants) are injected into oil reservoirs to further recover residual oils during the chemical flooding process[14-18]. This process usually lasts months or years under high temperature and pressure conditions, with injected chemicals exposed to the omnipresent formation water (so-called brine) containing mono- and multi-valent salt ions (*e.g.*, Na^+, K^+, Ca^{2+}, Mg^{2+}, Cl^-, SO_4^{2-}, and CO_3^{2-}, *etc.*)[10]. These salt ions can strongly interact with ionic surfactants due to electrostatic interactions. The divalent cations (such as Ca^{2+} and Mg^{2+}), in particular, can form cation bridging with anionic surfactants, *i.e.*, negatively charged surfactants connected by one cation, thereby triggering unfavorable precipitations or in-plane aggregations[64]. Detailed literature review of the study on the cation bridging formed by anionic surfactants and divalent cations is listed in **Appendix B.1**. Surfactant precipitation can not only cause its retention but also block small pores which can severely hinder further oil production[122]. Theoretical[118] and

simulation[89] studies suggest that such in-plane aggregations hinder surfactant pressure build-up at the interface region, thereby increasing IFT. On the other hand, high oil-brine interfacial tension (IFT) is unfavorable during chemical flooding[4-6, 67]. An experimental study by Yadali *et al.*[70] reported that the IFT of oil/petroleum sulfonate/brine system increases by adding Ca^{2+} ions. Our previous study also reported that the oil-brine IFT is positively related to cation bridging density[64].

Enormous efforts have been dedicated to improving the hard water (water containing a high concentration of multi-valent ions) resistance of surfactant formulas during chemical flooding[7-9, 123], which can be classified into either removing divalent ions using ion capturing agents[124-126] (chelating agents or ion exchanger) or inhibiting cation bridging formation[122, 127] (Gemini surfactant and surfactant blend). Surfactant blending is an economically friendly and convenient approach without expensive and time-consuming chemical synthesis. Anionic surfactant (such as Sodium dodecyl sulfate (SDS)) and non-ionic cosurfactant are one of the most common combinations in chemical flooding[56]. Alcohols are often employed as cosurfactant[128] due to their ability to further decrease oil-brine IFT[56, 129], and their possible roles in increasing surfactant solubility[130] and disaggregating liquid crystalline structures[131]. Though theoretical studies have suggested that alcohols can disaggregate the liquid crystalline structures[131], direct observation of such an effect is reported in neither experiment nor simulation studies. On the other hand, blending cationic and anionic surfactants has received extensive attention nowadays[132], thanks to their superior synergic effect compared to other surfactant mixtures[133]. Experimental studies reported that the mixtures of SDS and cetrimonium bromide (CTAB) can not only work

effectively without precipitation but also greatly reduce air-brine IFT[134]. While these works hinted the potential applications of surfactant mixtures in chemical flooding process, the understanding about their collective roles against cation bridging induced by divalent ions at oil-brine interfaces under reservoir conditions still remains elusive.

Herein, we use molecular dynamics (MD) simulations to study the structural properties of surfactant mixtures at oil-brine interfaces. We study two different combinations of surfactant and cosurfactant systems. SDS with propanol, a commonly used surfactant formula in the petroleum industry[56], is used to represent the anionic surfactant and non-ionic cosurfactant (ASNC) blend. On the other hand, SDS with CTAB is employed to represent the anionic surfactant and cationic surfactant (ASCS) blend. In both systems, SDS interface concentration is fixed, while those of propanol and CTAB are altered. Although it is well known that various salt ions exist in reservoir brine[10], a pure $CaCl_2$ solution is employed in this work for simplicity. Crude oil consists of thousands of components, which can be hardly explicitly represented in molecular simulation with the exact formula and fraction of each component[90-92]. Therefore, we use pure n-decane (nC_{10}), which has the same carbon number as the recommended light oil equivalent alkane carbon number (EACN)[94-97] to represent the oil phase. The temperature and pressure are set as a typical reservoir condition (*i.e.*, 353 K and 200 bar, respectively[76]). We demonstrate that the introduction of CTAB in the SDS surfactant formula can disaggregate the in-plane aggregation thanks to its ability to neutralize the oil-brine interface charge. On the other hand, propanol can barely disaggregate cation bridging. Our work should provide the theoretical foundation and guidance to surfactant formula design for its applications in hard-water resistant chemical flooding.

The remainder of this paper is organized as follows. In **Computational Methodology**, we introduce simulation methods and define molecular models. In **Result and Discussion**, we first discuss the molecular configurations of different surfactant mixtures in the interface region. Then, we discuss the potential of using cosurfactants to increase hard-water resistance, as well as their working mechanisms. In **Conclusion**, we summarize key findings and discuss potential implications.

3.2 Computational Methodology

3.2.1 Molecular Model and Simulation

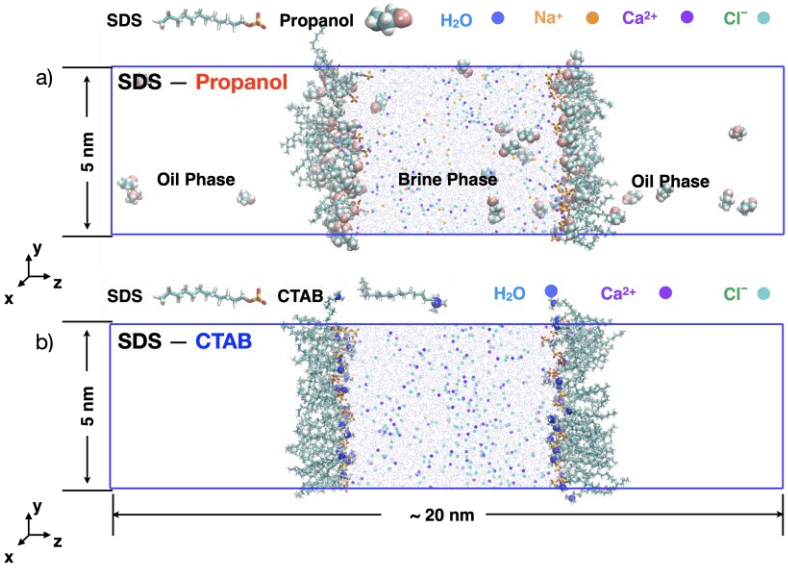

Figure 3-1 Molecular configurations at equilibrium in a) system SDS50_Prop50; b) system SDS50_CTAB50. Oil phases are not shown for clarity. The periodic boundaries are depicted by the blue rectangular.

We employ a similar system design as in our previous studies[56, 64]: one ~8 nm brine slab sandwiched between two ~ 6 nm oil slabs, as shown in **Figure 3-1**. Such a dimension is large enough to overcome the finite size effect[76]. The simulation box lengths in the *x*- and *y*-directions are set as 5 nm, while the dimension in the *z*-directions varies from 20 ~ 22 nm depending on the systems. We use a relatively high $CaCl_2$ concentration (~13 *wt*.%) in the brine phase to study the hard-water resistance of the surfactant formula. SDS concentration is fixed as $1/nm^2$, within the practical range during chemical flooding[83]. A series of systems with various propanol and CTAB concentrations are designed to study their effect on the interfacial properties. Cl^- ions instead of their original counterion, Br^- ions, are used as the CTAB counterions for simplicity. The number of fluid molecules in various systems is listed in **Table 3-1**. We separate SDS and CTAB, which barely relocate during simulation, into two interfaces for the initial configuration. On the other hand, propanol, which can transport from the oil phase to the brine phase[56], is originally set in the oil phase. We place the same number of propanol molecules randomly on the left and right oil phases. Initial configurations for SDS50_Prop50 and SDS50_CTAB50 are presented in **Appendix B.2**, as representatives. Three-dimensional (3-D) periodic boundary conditions (PBCs) are applied in all cases. CHARMM36[50] forcefield with modified TIP3P[99] and TIP3P compatible ion forcefields are employed in the current study. Detailed calibration on the forcefields in terms of density and IFT can be referred to in our previous works[56, 64]**.**

Table 3-1 Number of fluid molecules in each system

Name	System	SDS	Propanol	CTAB	H_2O	Na^+	Cl^-	Ca^{2+}	nC_{10}
SDS50	-	50	0	0	5200	0	220	110	874
SDS50_Prop50		50	50	0	5200	50	220	110	874
SDS50_Prop100		50	100	0	5200	50	220	110	874
SDS50_Prop150		50	150	0	5200	50	220	110	874
SDS50_Prop200	ASNC	50	200	0	5200	50	220	110	874
SDS50_Prop250		50	250	0	5200	50	220	110	874
SDS50_Prop400		50	400	0	5200	50	220	110	874
SDS50_Prop600		50	600	0	5200	50	220	110	874
SDS50_CTAB10		50	0	10	5200	0	180	110	874
SDS50_CTAB20		50	0	20	5200	0	190	110	874
SDS50_CTAB30		50	0	30	5200	0	200	110	874
SDS50_CTAB50	ASCS	50	0	50	5200	0	220	110	874
SDS50_CTAB70		50	0	70	5200	0	240	110	874
SDS50_CTAB90		50	0	90	5200	0	260	110	874
SDS50_CTAB100		50	0	100	5200	0	270	110	874

3.2.2 Simulation Details

All simulations are conducted using GROMACS (version 2019.1) software package[135]. We first minimize the system energy using the steepest descent algorithm until the maximum force between any of two atoms is less than $1000\,\mathrm{kJ\cdot mol^{-1}\cdot nm^{-1}}$. The systems are equilibrated for 20 ns with NP_zT (*i.e.*, a fixed number of molecules, a constant pressure in the z-direction normal to the interfaces, and a constant temperature) ensemble using the velocity rescaling[105] thermostat and the Berendsen[107] barostats with the time interval of 0.1 and 0.2 ps, respectively. Then, production runs are conducted for 150 ns in NP_zT ensemble using the Nose-Hoover[106] thermostats and the Parrinello-Rahman[108] barostats with a relaxation time of 0.1 and 0.2 ps, respectively. Velocity rescaling is an efficient method of controlling temperature. On the other

hand, the Nose-Hoover thermostat abstracts away the thermal bath from the previous thermostats and condenses it into a single additional degree of freedom. We first use the velocity rescaling to equilibrate the system and then employ the Nose-Hoover for production. In addition, we also run a production run using the velocity rescaling and find that the IFT and the cation bridging density are similar in using two different thermostats, as shown in **Appendix B.13**. The equations of motions are integrated by the Leap-Frog algorithm[104] with a time step of 2 fs. Trajectories in the production runs are saved every 100 steps (200 fs) for further data analysis.

Electrostatic and Lennard Jones (LJ) potentials are calculated using the algorithms suggested by the CHARMM forcefield[50]. Namely, the electrostatic interactions are calculated using the particle-mesh Ewald (PME) method[109] with the Fourier spacing of 0.12 nm and 1.2 nm real-space cut-off. LJ forces are modified to decay smoothly to 0 between 1.0 nm and 1.2 nm. LJ interactions between the unlike atoms are obtained from the conventional Lorentz-Berthelot mixing rules. We use the SETTLE[112] and LINCS[113] algorithms to constrain the bond length and angle of H_2O and other molecules. The snapshots are depicted using the Visual Molecular Dynamics (VMD) package[114].

3.3 Results and Discussion

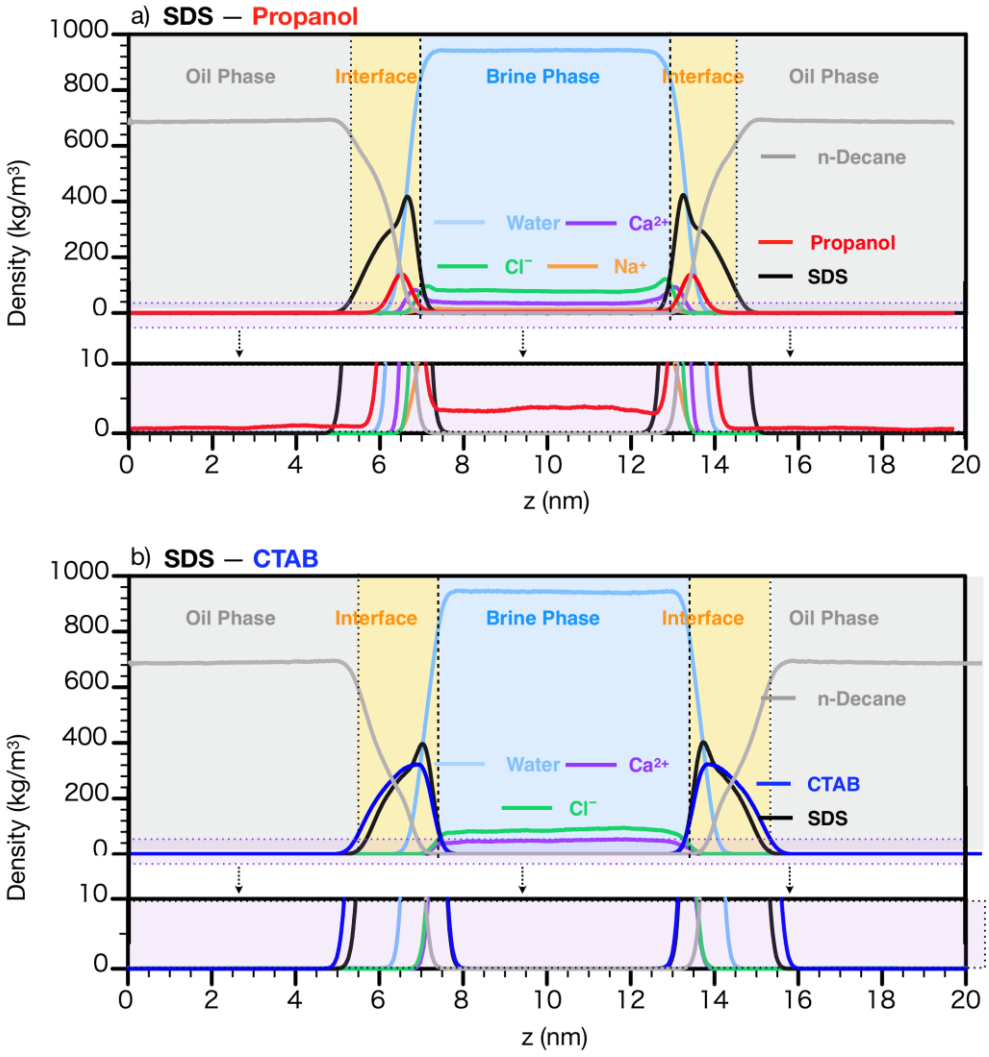

Figure 3-2 Mass density distribution and enlargements in a) system SDS50_Prop50; b) system SDS50_CTAB50. The oil phase, interface region, and brine phase are represented by gray, yellow, and blue colors, respectively. The boundaries of the brine phase and interface region, as well as the interface and oil phase, are depicted by black dashed and dashed lines, respectively.

Figure 3-2 depicts the density distributions of each component in systems SDS50_Prop50 (**Figure 3-2 a**) and SDS50_CTAB50 (**Figure 3-2 b**). For a better interpretation, we employ the "90-90" criterion[115], where interfacial boundaries are 90% of H_2O and nC_{10} densities to define the brine, oil, and interface region. Surface active chemicals (SDS, propanol, and CTAB) are mainly distributed in the interface regions in both systems. The only difference is that some propanol molecules distribute in the brine and oil phase, while all SDS and CTAB molecules are located in the interface regions. nC_{10} and H_2O molecules are depleted from the interface region with their respective densities converging to their bulk values away from the interface region. Due to the symmetry in both systems, we only depict the left-hand side of the system in the rest of the discussion. To clarify, we set the origin of the *z*-axis as the contact of the brine phase and interface region hereafter.

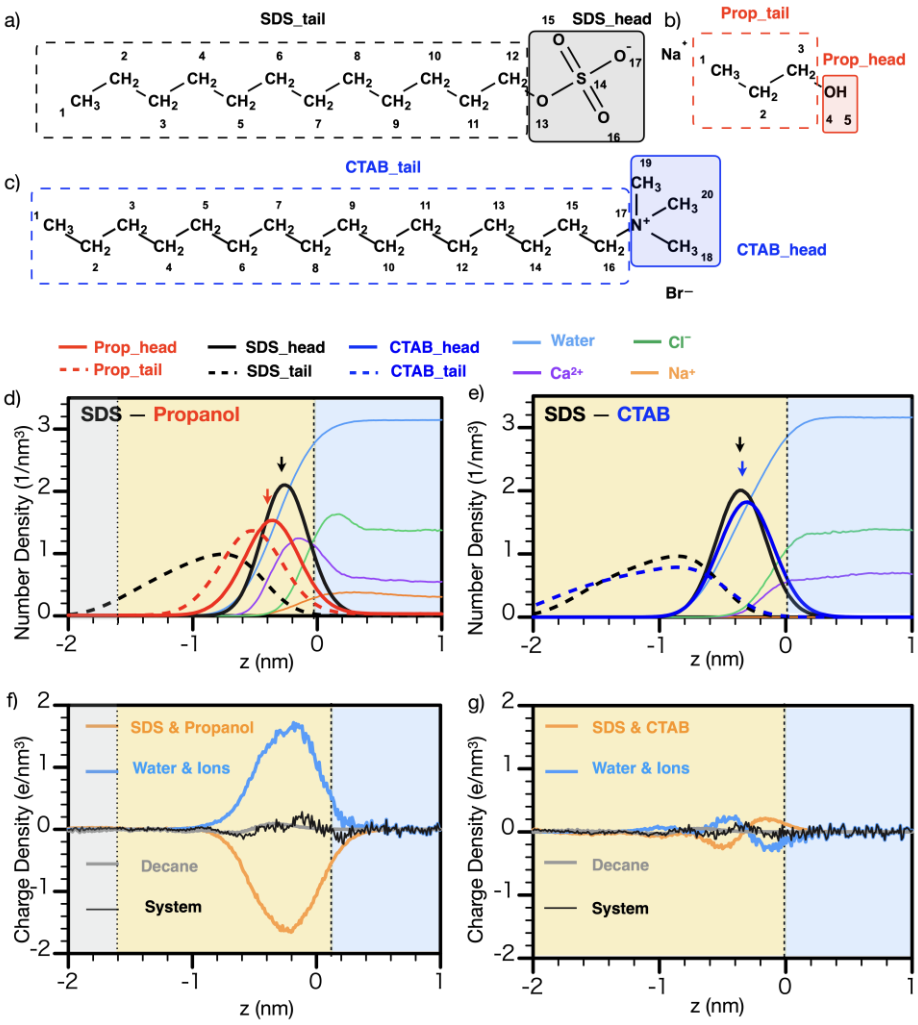

Figure 3-3 Molecular structures of a) SDS; b) propanol; c) CTAB. Number density distributions of functional groups in the interface region in d) system SDS50_Prop50; e) system SDS50_CTAB50. Charge density distributions in interface region in f) system SDS50_Prop50; g) SDS50_CTAB50. In b) and c), water density distributions are scaled-down by 10 times for a better comparison; the entire functional group is counted as one unit; The oil phase, interface region, and brine phase are represented by gray, yellow, and blue colors, respectively. The boundaries of the brine phase and interface region, as well as the interface and oil phase, are depicted by black dashed and gray dotted lines, respectively.

We present the corresponding surfactant and cosurfactant functional group distributions in **Figure 3-3**. SDS, propanol, and CTAB molecules are classified into head and tail groups based on their affinity to H_2O as shown in **Figures 3-3 a**, **b**, and **c**. For clarity, H_2O number density is reduced by 10 times for a better comparison. It can be seen that the SDS head group is closer to the brine phase than that of propanol, similar to the case without divalent ions[56, 136]. Such a distribution can be caused by various factors including geometric size difference, ability to form H-bonds, and formation of ion pairing. SDS has a stronger affinity to the brine phase (forms more H-bonds, while it can also strongly interact with cations in brine) than propanol. In addition, it has a larger head group than propanol. Interestingly, we find that the hydrophobic groups connected to the head group of SDS and propanol are distributed at almost the same plane, as shown in **Appendix B.12**. On the other hand, the CTAB head group distributes at almost the same position in the *z*-direction as the SDS head group. Ca^{2+} and Cl^- ions have enrichment in the interface region in system SDS50_Prop50, while they are depleted in system SDS50_CTAB50. The positive adsorption of Ca^{2+} ions in the interface region in system SDS50_Prop50 is mainly due to the electrostatic attraction[116] from the negatively charged SDS at the interface (see **Figures 3-3 d** and **f**). These Ca^{2+} ions can further attract negatively charged Cl^- ions[64] from the brine phase, as shown in **Figure 3-3 d**. Snapshots in **Figure 3-4 a** also clearly indicate the enrichment of Ca^{2+} and Cl^- ions at the interface around SDS molecules. On the other hand, the negative charges of SDS are drastically neutralized by the positively-charged CTAB at the interface in system SDS50_CTAB50 (see **Figure 3-3 g**). As a result, salt ion accumulation at the interface is largely suppressed even showing depletion[137].

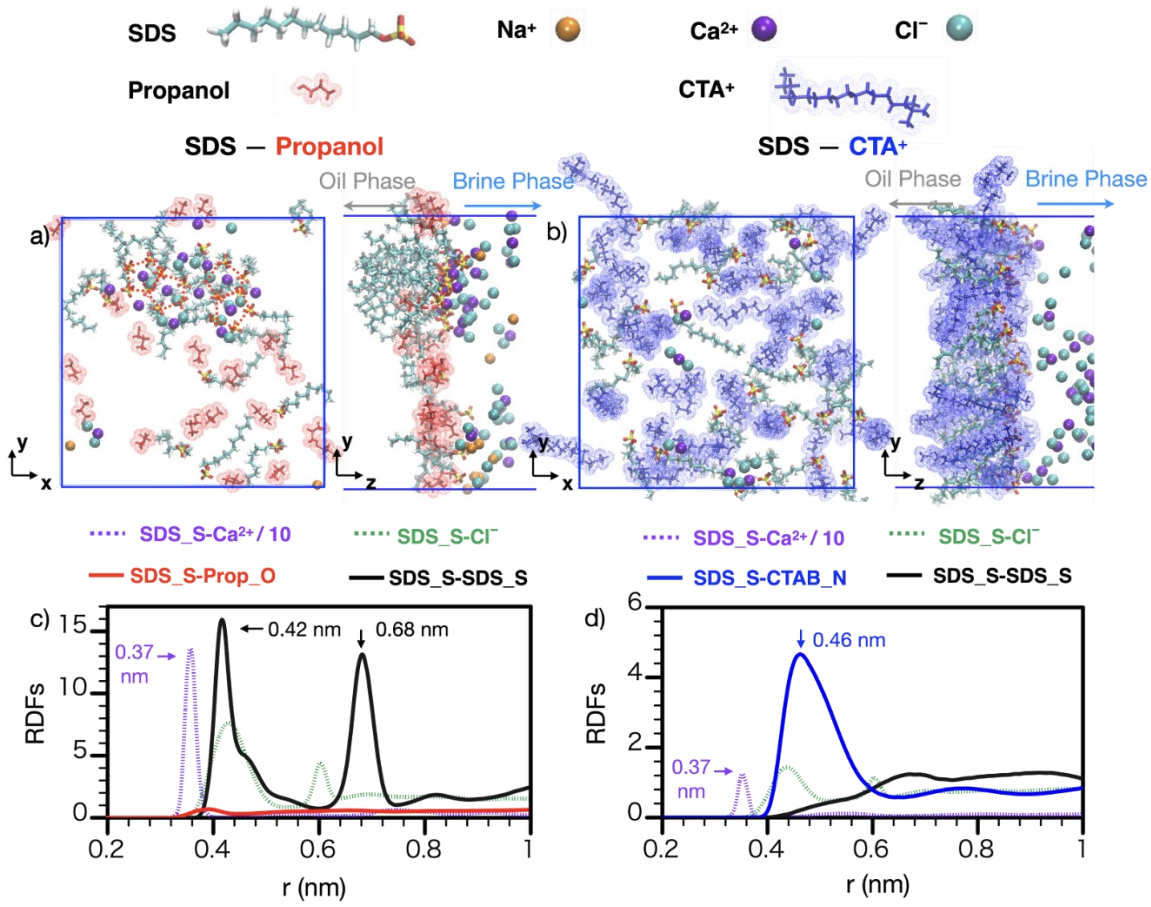

Figure 3-4 Molecular configurations in the *x-y* and *y-z* planes for a) system SDS50_Prop50; b) system SDS50_CTAB50. The snapshots in the *x-y* plane are obtained in the region of $-2 < z < 0.4$ nm shown in Figures 3-3 d and e. The red dotted lines highlight the formation of pentagon-like SDS-Ca^{2+} complexes[64]. RDFs of SDS_S (*i.e.*, S atom in SDS), Prop_O (*i.e.*, O atom in propanol), CTAB_N (*i.e.*, N atom in CTAB), and salt ions around SDS_S in c) system SDS50_Prop50; d) system SDS50_CTAB50. To clarify, SDS_S-Ca^{2+} RDFs in Figures 3-4 c and d are scaled down by 10 times for a better observation.

To better understand molecular configurations at the interfaces, in **Figure 3-4**, we present the *x-y* plane and *y-z* plane views in the interface region. In-plane aggregations and pentagon-like complexes formed by SDS molecules and Ca^{2+} ions[64] are observed in SDS50_Prop50. Propanol

molecules tend to distribute in spaces where there are no SDS molecules. Accumulation of Ca^{2+} ions around SDS molecules shown in the snapshot in the *x*-*y* plane indicates that their enrichment at the interface is mainly due to the attraction from SDS molecules, in line with **Figure 3-3**. Two distinct peaks at 0.42 nm and 0.68 nm in the radial distribution function (RDF) of the SDS_S (*i.e.*, S atom in SDS)-SDS_S (see **Figure 3-4 c**) reveals the formation of the pentagon-like complex (one Ca^{2+} ion surrounded by five SDS molecules)[64]. Detailed definitions and quantification for such a pentagon-like structure are discussed below. In contrast, SDS molecules are well dispersed in the *x*-*y* plane in system SDS50_CTAB50, as shown in **Figure 3-4 b**. Both Ca^{2+} and Cl^- ions are depleted from the interface region, in line with **Figures 3-2 b** and **3-3 e**. The disappearance of peaks in SDS_S-SDS_S RDF (see **Figure 3-4 d**) indicates the disaggregation of SDS in-plane aggregation. The peak value in SDS_S-Ca^{2+} RDF at 0.37 nm in system SDS50_CTAB50 is lower than that in system SDS50_Prop50, indicating weaker Ca^{2+} ion accumulation around SDS in system SDS50_CTAB50. RDFs of ions and fluid molecules around CTAB_N (*i.e.*, N atom in CTAB) are depicted in **Appendix B.3**. Water molecules enrich at the closest place around CTAB_N, followed by SDS, Cl^- and Ca^{2+} ions. A detailed discussion of the water solvation structures around SDS_S and CTAB_N will be discussed along with H-bond densities in **Figure 3-9**. Unlike **Figure 3-4 d**, CTAB is mainly neutralized by SDS thanks to their stabilization at the interface (see **Figure 3-2 b**) stemming from both hydrophobic and electrostatic interactions. In addition, the counterion of CTAB is a monovalent Cl^- ion, while the divalent Ca^{2+} ions have a stronger interaction than the Na^+ ion which is the counterion of SDS. No distinct peak in CTAB_N-CTAB_N RDF indicates that there is no in-plane aggregation of CTABs. It is noted that we only

show a limited region (0.2 nm - 1 nm) in RDF curves for a better observation in **Figures 3-4 c** and **d**. The full range (0 - 2.5 nm) RDFs are shown in **Appendix B.4**. In addition, molecular spatial distribution functions (SDFs) are illustrated in **Appendix B.5** for a more intuitive understanding of molecular configurations in three-dimensional space.

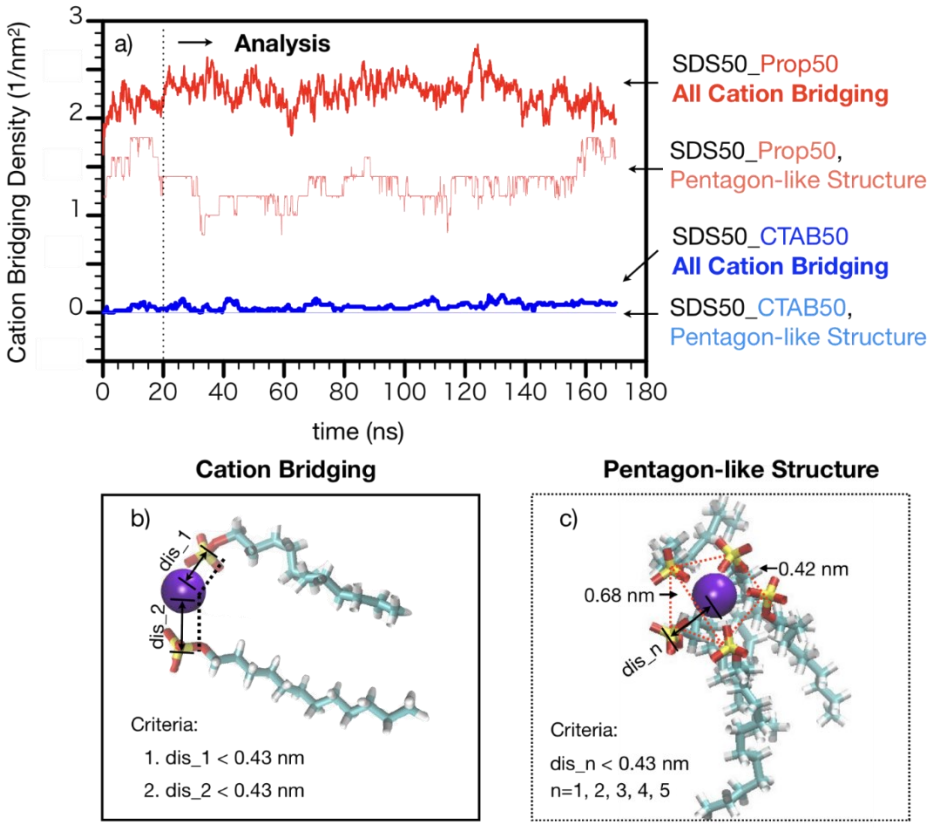

Figure 3-5 a) Cation bridging density in system SDS50_Prop50 and system SDS50_CTAB50. b) Criteria for cation bridging. c) Pentagon-like structure configuration[64].

In-plane aggregation of SDSs is further investigated by using cation bridging density as shown in **Figure 3-5 a**. The criteria for SDS cation bridging are given in **Figure 3-5 b**: *i.e.*, a

complex consisting of two SDS molecules connected by one Ca^{2+} ion with SDS_S-Ca^{2+} ion separation distances less than 0.43 nm. We note that 0.43 nm is selected based on the first local minimum value in SDS_S-Ca^{2+} RDFs shown in **Appendix B.6**. As shown in **Figure 3-4 a**, such a cation bridging can be further classified based on their structures, which are simple cation bridging (**Figures 3-4 a i** and **3-5 b**) and pentagon-like complexes (**Figures 3-4 a ii** and **3-5 c**). We note that unique pentagon-like complexes are observed in systems containing Ca^{2+} ions (hard water) without cosurfactant at the oil-brine interface[64]. To better understand the disaggregation effect of propanol and CTAB on this unique structure, we explicitly characterize cation bridging originated from the pentagon-like complex. One complex having exactly five SDS_Ss around one Ca^{2+} ion with SDS_S and Ca^{2+} separation distances less than 0.43 nm is defined as one pentagon-like structure[64]. Based on the criteria depicted in **Figure 3-5 b** and **Figure 3-5 c**, one pentagon-like complex contains 10 simple cation bridging structures. **Figure 3-5 a** depicts the evolution of cation bridging density (total and that from the pentagon-like structure) in system SDS50_Prop50 and system SDS50_CTAB50. Formation and disaggregation of cation bridging structures are a dynamic process, resulting in fluctuations in cation bridging density. In system SDS50_Prop50, both total cation bridging density and that from pentagon-like structures are high. On the other hand, the cation bridging and pentagon-like structures are barely observed in system SDS50_CTAB50, indicating disaggregation of the cation bridging structure. It is because SDS and CTAB can have a strong pairing between their headgroups, while their hydrophobic tails stabilize them at the oil-brine interfaces. As a result, the interaction between SDS and Ca^{2+} ions is largely screened as shown in **Figure 3-4 d**, and Ca^{2+} ions are depleted from the interface (**Figure 3-3 e**).

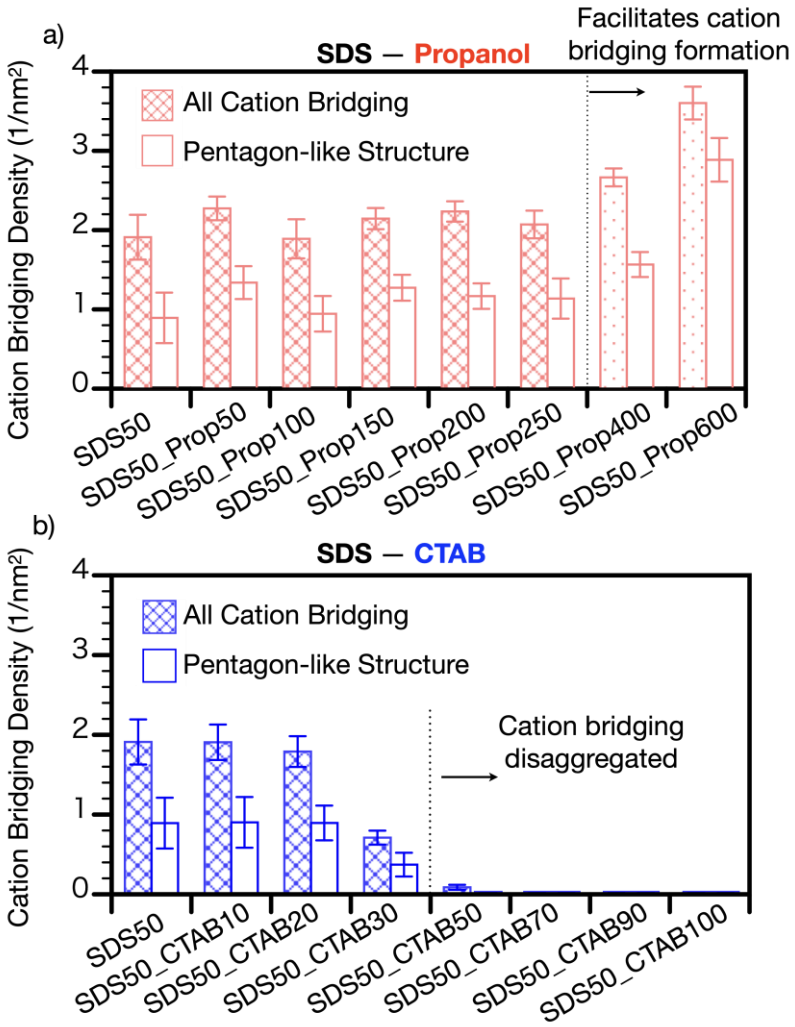

Figure 3-6 Cation bridging densities in a) ASNC systems; b) ASCS systems.

We further study the effect of the propanol and CTAB concentrations on the cation bridging density as shown in **Figure 3-6**. It shows that propanol can neither disaggregate the cation bridging nor the pentagon-like structure. At high propanol interface concentrations (*i.e.*, in systems SDS50_Prop400 and SDS50_Prop600), propanol even facilitates the formation of cation bridging. On the other hand, introducing CTAB can effectively disaggregate the cation bridging and

pentagon-like structures when its interface concentration is above 1 nm^{-2} (*i.e.*, in systems SDS50_CTAB50, SDS50_CTAB70, SDS50_CTAB90, and SDS50_CTAB100). The cation bridging disaggregation effect is not significant in the systems where CTAB concentration is low (< ~ 0.4 nm^{-2}), *i.e.*, system SDS50_CTAB10 and system SDS50_CTAB20. In addition, the concentration of propanol and CTAB has a negligible effect on the fraction of the cation bridging originated from the pentagon-like structure in all cation bridging, as shown in **Appendix B.7**.

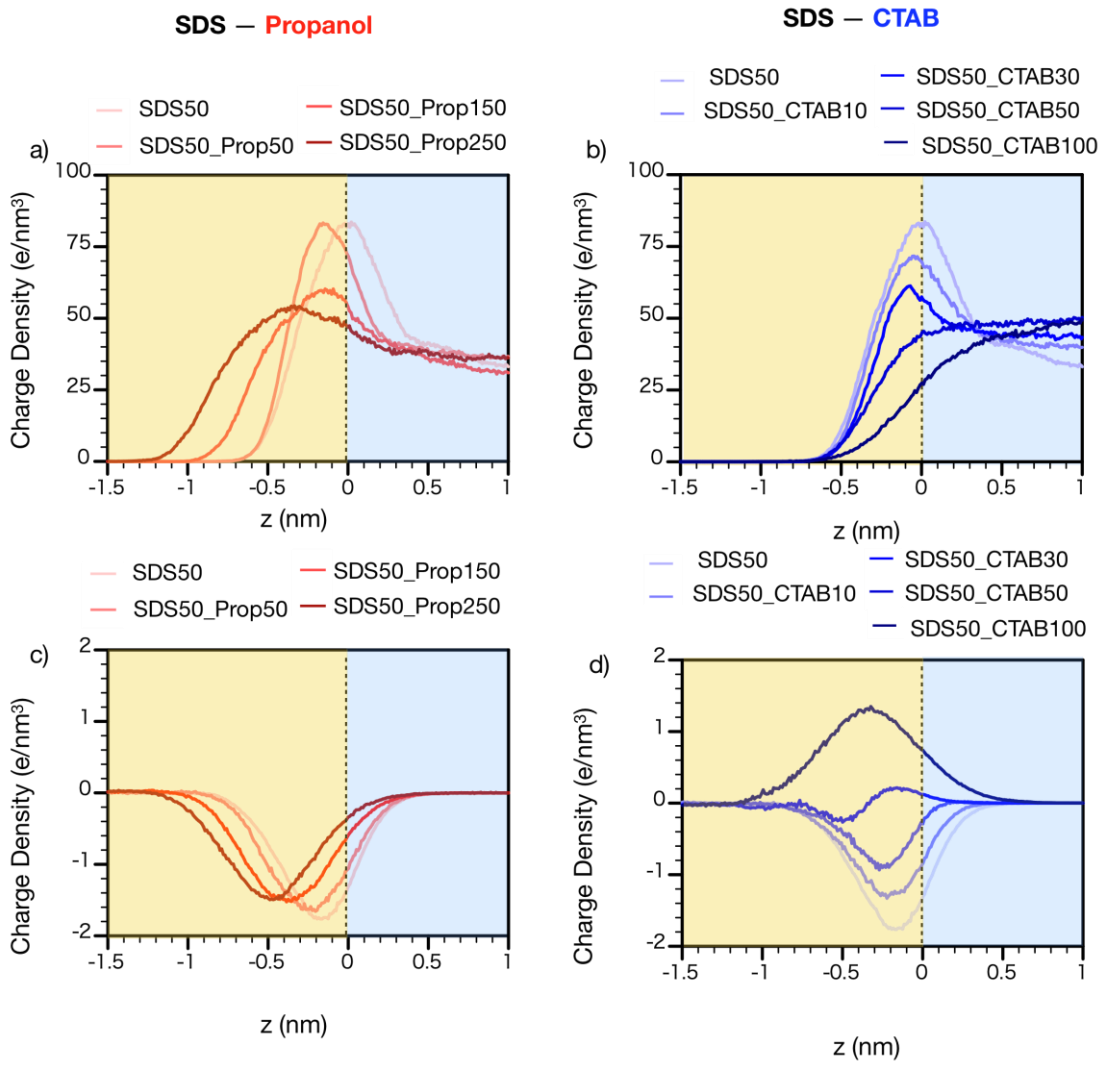

Figure 3-7 Ca^{2+} density distribution in interface region in a) select ASNC systems; b) select ASCS systems. The corresponding charge density distribution of surfactants and cosurfactant in the interface region in c) select ASNC systems; d) select ASCS systems. The black dashed lines represent the contact between the brine phase and the interface region. The brine phase and interface region are represented by blue and yellow colors.

Why CTAB can disaggregate cation bridging, but propanol cannot? How is the threshold CTAB concentration on the cation bridging disaggregation determined? **Figures 3-7 a** and **b** depict

the Ca^{2+} distribution of selected systems in the interface region. The deeper color indicates the higher cosurfactant concentration. Ca^{2+} ions show adsorption at the interface in ASNC systems. Similarly, Ca^{2+} ions are adsorbed at the interface in the systems SDS50, SDS50_CTAB10, and SDS50_CTAB30, where the cation bridging still exists. In contrast, Ca^{2+} ions are depleted from the interface in system SDS50_CTAB50 and system SDS50_CTAB100. The different Ca^{2+} ion density distributions can be attributed to the surface-active chemical distributions, as shown in **Figures 3-3 f** and **g**. **Figures 3-7 c** and **d** depict the charge density distribution of the surface-active chemicals at the interface. SDS and propanol lead to a negative surface charge at the interface, resulting in Ca^{2+} ion adsorption. Similar phenomena are also observed in systems SDS50_CTAB10 and SDS50_CTAB30. On the other hand, systems SDS50_CTAB50 and SDS50_CTAB100 lead to neutral and positive surface charges, respectively, depleting Ca^{2+} ions from the interface.

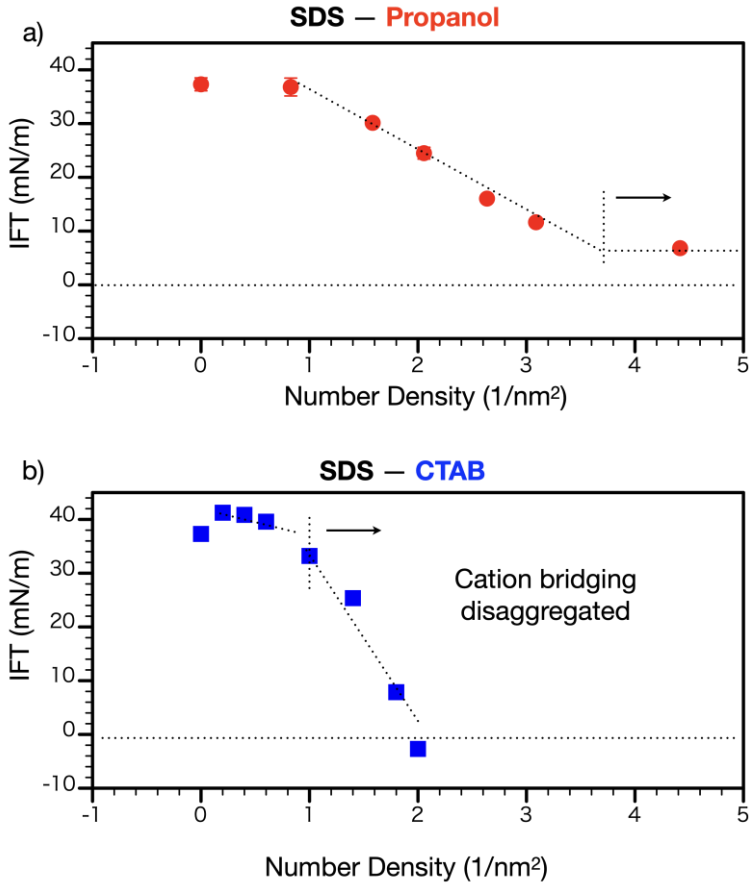

Figure 3-8 Oil-brine IFT in a) ASNC systems; b) ASCS systems. The dotted lines are for eye guidance.

Oil-brine IFT, as an important indicator for effective chemical flooding, is depicted in **Figure 3-8.** The formula used for IFT calculations is described in **Chapter 1**, **Section 1.4.4.3**. In both systems, IFT decreases as propanol and CTAB concentration increase. The slope of the IFT in ASNC systems is constant as propanol concentration further increases as shown in **Figure 3-8 a**. Considering that cation bridging density is almost identical in SDS-Propanol systems (propanol concentration 0 ~ 4 /nm^2), as discussed in **Figure 3-6 a**, this decrement trend in IFT is mainly

contributed from the propanol adsorption in the interface region[56]. On the other hand, the slope can be divided into with and without cation bridging regions in SDS-CTAB systems, as shown in **Figure 3-8 b**. This trend is in line with previous experimental observations[134]. A steeper trend in the IFT decrement is observed in the systems without cation bridging when compared to those with cation bridging. The decrement of the IFT in the first region is mainly contributed by the adsorption of CTAB. On the other hand, both CTAB adsorption and cation bridging disaggregation contribute to decreasing the IFT in the second region. This result agrees well with the previous simulation study which suggested that the in-plane aggregation of surfactants is detrimental to decreasing IFT[89]. In addition, a slight increment in IFT is observed in SDS50_CTAB10 compared to SDS50, as shown in **Figure 3-8 b**, which might be caused by the slight decrement in H-bond density (**Figure 3-9 b**) between SDS and water.

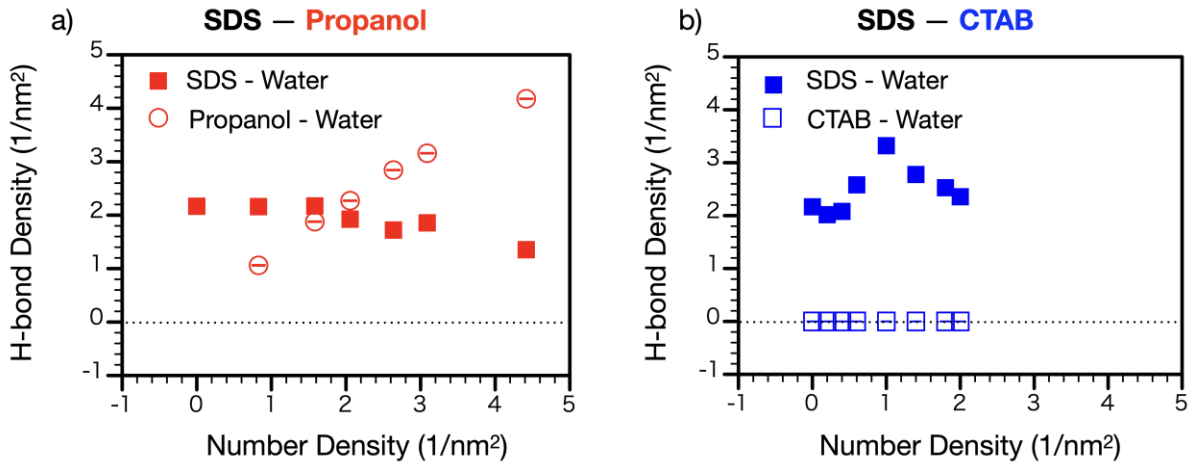

Figure 3-9 H-bond densities between surfactants/cosurfactant and H_2O in a) ASNC systems; b) ASCS systems.

Propanol and CTAB not only affect the cation bridging formation but also impact the H-bond formation by affecting SDS hydration structures. In this work, we did not calculate the H-bond interaction energies, which can be obtained from the quantum mechanical density functional theory (DFT) calculations. However, we note that the H-bond formation is also affected by the surrounding hydration structures and the presence of surfactant and cosurfactant molecules as well as their configurations, which cannot be fully captured by DFT due to excessively-high computational cost. Instead, based on the hydration structures around surfactant and cosurfactant molecules as well as the H-bond number, we can infer how H-bond formation is affected by the concentrations of propanol and CTAB. Detailed criteria for the H-bonds are defined in **Appendix B.8**. **Figures 3-9 a** and **b** depict the H-bond density of surfactant-water and cosurfactant-water in ASNC and ASCS systems, respectively. Increasing propanol concentration slightly decreases the SDS-H_2O H-bond formations. In the meantime, the propanol-H_2O H-bond density increases gradually. The negligible influence of propanol on SDS-H_2O H-bond density can be explained by low propanol distribution around SDS, as shown in **Figure 3-4 c**. On the other hand, CTAB has a more significant effect on the SDS-H_2O H-bond density, though itself barely forms H-bond with H_2O, as shown in **Figure 3-9 b**. The low H-bond density between CTAB and H_2O is mainly due to the steric hindrance from its tri-methyl group, resulting in weaker H_2O solvation around N atom in CTAB, as shown in **Appendix B.10**. In addition, the separation distance between H_2O and CTAB_N is larger than that between H_2O and SDS_S. Overall, the H-bond density between SDS and H_2O first increases and then decreases as CTAB concentration increases, as shown in **Figure 3-9 b**. The increment trend of H-bond density between SDS and water under lower CTAB

concentration might be caused by the disaggregation of cation bridging, releasing SDS from strong SDS-Ca^{2+} binding (see **Appendix B.10** for water solvation structures with and without SDS-Ca^{2+} binding). We note that the SDS molecules from pentagon-like structures can only form ~1 H-bonds per SDS, while those not the part of pentagon-like structures (pentagon-like structure-free) can form ~ 3 H-bonds per SDS as shown in **Appendix B.14**. Radial distribution densities of water distribution around SDS in **Appendix B.10** also indicate the Water_H density around SDS increases CTAB concentration increases in systems (SDS50, SDS50_CTAB10, SDS50_CTAB30, SDS50_CTAB50). As CTAB concentration further increases, CTAB distribution around SDS increases (**Appendix B.15**). In addition, SDS molecules are gradually repelled from the brine phase as shown in **Appendix B.11**. As a result, the H-bond density between SDS and water decreases. Water radial distribution densities in ASCS systems depicted in **Appendix B.10** also reveal the weaker water solvation around SDS under high CTAB concentration conditions.

3.4 Summary

In this work, we use MD simulations to study the structural and thermodynamic properties of oil-brine interfaces with the combinations of anionic surfactant and cationic/non-ionic chemical additives in relation to hard-water resistant chemical flooding. Both propanol and CTAB molecules are distributed at the interface region and decrease oil-brine IFT, which is favorable for chemical flooding. Propanol, as a non-ionic surfactant, is distributed in the spaces where there is no SDS, thereby barely disaggregating the cation bridging formed between SDS and Ca^{2+} ion. On the other hand, CTAB can bind with SDS and subsequently disaggregate the cation bridging. Its

disaggregation mechanism is to neutralize the originally negatively-charged interface (due to the SDS head group) thereby depleting Ca^{2+} ions from the interface. The hydrophobic interactions between CTAB and SDS tails also help stabilize them at the interface. In addition to the disaggregation of cation bridging, propanol and CTAB also differently affect the H-bond between the SDS and H_2O. Propanol can form H-bonds with H_2O, and its density increases as the propanol interface concentration increases. Propanol barely interferes with the H-bond formation between SDS and H_2O, as they tend to accumulate in the spaces where there is no SDS. On the other hand, CTAB strongly affects the H-bond formation between SDS and water. As CTAB interface concentration increases, the SDS-H_2O H-bond density first increases and then decreases. The first increment of H-bond density is mainly due to the disaggregation of the cation bridging. Further decrement is mainly due to the SDS head groups being repelled from the water phase due to the high dense of CTAB distribution. This work suggests neutralizing the interface charge by combining cationic and anionic surfactants can repel the ion adsorption at the interface and further protect the surfactant efficiency under hard water conditions. Our work should provide important insight in designing surfactant formulas in application to chemical flooding under hard water reservoirs.

Chapter 4 : ROLE OF ALCOHOL AS A COSURFACTANT AT BRINE/OIL INTERFACE UNDER A TYPICAL RESERVOIR CONDITION

A version of this chapter has been published in *Langmuir*. (Nan *et al*.,2020) [56].

4.1 Introduction

Cosurfactant (or cosolvent), defined as a chemical used in combination with the primary surfactant, has a wide application in commercial products. For instance, in the formulation of products such as makeup remover[138], shampoo[139], bodywash[140], and washing powders[141], cosurfactants are used together with surfactants as active ingredients[136]. Specifically, in the petroleum industry, the usage of cosurfactants in chemical flooding during enhanced oil recovery (EOR) has a long history of more than 40 years[14-18]. An ideal chemical solution for chemical flooding should meet two basic requirements: First, it should be able to decrease the interfacial tension (IFT) of the brine/oil interface, thereby recovering the residual oils trapped by capillary forces[4-6]. Second, it should be stable during transportation over long distances (from wellhead to target strata) in a reservoir with low surfactant retention[142, 143]. Undoubtedly, the introduction of cosurfactants in chemical flooding should decrease IFT or stabilize the chemical solution in *in-situ* reservoirs.

As an important component in chemical flooding, understanding the roles of cosurfactants is of great significance. Many studies have been carried out to clarify their roles in the water/air or water/oil interface, such as theories[131], experiments[130, 144-148], and simulations[129, 136, 149] (**Table 4-1**). The most commonly used cosurfactants in chemical flooding are medium-chain alcohols[128], including propyl, butyl, and pentyl alcohols. As an amphiphilic chemical, one of the possible roles of these alcohols is to decrease interfacial energy by accumulating at the interface. A coarse-grained molecular dynamics (MD) simulation study from Dominguez *et al.*[129] stated that the alcohol (cosurfactant) molecules are located at the interface next to surfactant molecules at low alcohol (cosurfactant)-surfactant ratio, thereby decreasing IFT. On the other hand, Kahlweit *et al.*[130] reported that the effects of alcohols might be considered as co-solvents rather than cosurfactants, which increases surfactant solubility, because adding alcohols at a constant temperature may not always lower IFT. They also reported that for a system with a non-ionic surfactant, when the temperature is higher than the ternary temperature, the surfactant in the oil-rich phase will be gradually replaced by cosurfactants so that IFT increases continuously. Another interesting study by Dennes *et al.*[131] suggested that the major role of cosurfactants is to increase the local molecular fluidity in the interface region. They demonstrated that these small molecules can melt the liquid-crystalline and/or gel structures[150], which are unfavorable for long-term transportation, by penetrating into the surfactants. Though many interesting and suggestive studies have been reported previously, to our best knowledge, the roles of alcohols at the oil-water interface under reservoir conditions are still less clear.

Table 4-1 Literature on the cosurfactant study at different interfaces

Interface	Surfactant	Cosurfactant	Temperature (K)	Pressure (bar)	Methods	Ref.
Water/air	SDS	C12-Alcohol	296		MD	[136]
Brine (1-3 *wt.*% NaCl)/decane	SDS	Poly-oxyethylene dodecyl ether	308.15-333.15	Ambient	experiment	[144]
Brine (0-1.75 *wt.*% NaCl)/cyclo-hexane	SDS	n-C5-Alcohol	Ambient	Ambient	experiment	[146]
Water/air and Water/n-octane	Tetra-ethylene glycol mono-octyl ether	C4-Alcohol	288.15-343.15	Ambient	experiment	[130]
Water/isooctane	Octyl-phenol-ethoxylate	C(1-16)-Alcohols	298.15	Ambient	experiment	[147]
Water/cyclohexane or Water/decane	SDS or Decyl-tri-methyl-ammonium bromide	C(1-8)-Alcohols	298.15	Ambient	experiment	[148]
Brine (1 *wt.*% NaCl)/glycerol/Poly-ethylene-glycol/SDS			300	Ambient	experiment	[145]
					theory	[131]

Here, we report an MD simulation study exploring the roles of alcohols as cosurfactants at the brine/oil interface under a typical reservoir condition. More specifically, we study the cosurfactant distributions as well as their roles in terms of intermolecular interactions and the local fluidity in the interface region. Sodium dodecyl sulfate (SDS) combined with propane-1-ol[83], as commonly used formulate for chemical flooding, is chosen as the surfactant and the cosurfactant in this study. The brine and oil phases are represented by 12 *wt.*% NaCl solution[81] (a typical salinity in the reservoir) and n-decane, respectively. The temperature and pressure are set as 353 K and 200 bar[76] in order to reproduce the conditions in a typical reservoir.

4.2 Computational Methodology

4.2.1 Molecular model and simulation

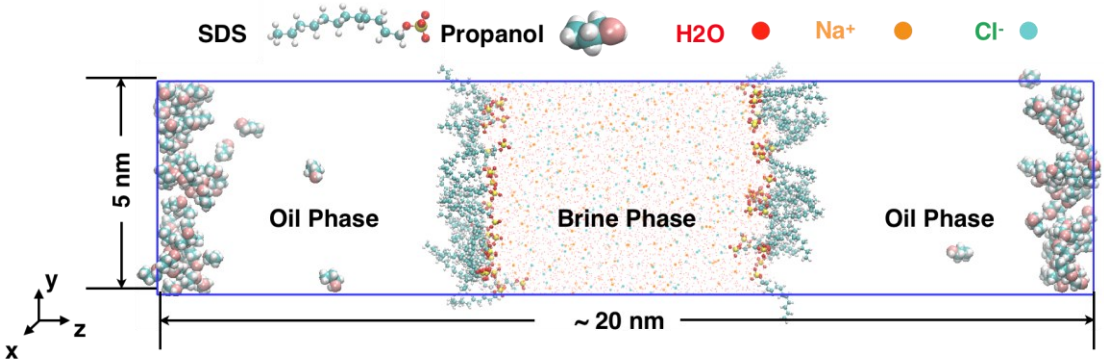

Figure 4-1 Schematic diagram of the initial configuration. n-decane molecules and hydrogen atoms in water molecules are omitted here for a better observation. The periodic boundaries are depicted by blue lines.

Table 4-2 System settings in each simulation run

	SDS	Propanol	Water	Na^+	Cl^-	n-Decane
SDS50_Prop0	50	0	5200	270	220	874
SDS50_Prop50	50	50	5200	270	220	874
SDS50_Prop100	50	100	5200	270	220	874
SDS50_Prop150	50	150	5200	270	220	874
SDS50_Prop200	50	200	5200	270	220	874
SDS50_Prop250	50	250	5200	270	220	874
SDS50_Prop400	50	400	5200	270	220	874
SDS50_Prop600	50	600	5200	270	220	874

We design a system in which a brine (12 *wt*.% NaCl solution) phase is sandwiched between two oil (decane) phases to study the oil-brine interfacial properties. We found that the SDS molecules incline to stay in the interface region, once they are trapped within. Therefore, in order to make the system symmetric, we artificially locate the same amount of SDS at the interfaces for the initial configuration. The propanol molecules (cosurfactants) are initially located in the oil phase. A schematic diagram of the initial configuration is depicted in **Figure 4-1**. Periodic boundary conditions (PBC) are applied in the *x*-, *y*-, and *z*-directions. The sizes of the simulation box are 5 nm, 5 nm, and about 20 nm in *x*-, *y*-, and *z*-directions, respectively. This size has been proven to be large enough to overcome the finite size effect[76]. A series of calculations with varying concentrations/numbers of cosurfactant (propanol) are studied to investigate the roles of cosurfactants. The selection of concentrations/numbers of the surfactant and cosurfactant in the system refers to the interfacial coverage of molecules from a previous experimental study[146]. The numbers of molecules in various systems are summarized in **Table 4-2**.

In this work, we use the CHARMM36[50] (an all-atom force field) combined with a modified TIP3P[99] forcefield, which has been reported as the best forcefield to study the structural properties of SDS among the commonly used forcefields (OPLSAA[44], OPLSUA[45, 46], and

GROMOS[48, 49] force field)[151]. A series of calibrations are conducted by comparing various physical properties (densities (pure n-decane, brine), IFT (pure water-decane)) with the experimental results. Our simulation study shows a good agreement with the experiments in terms of density[152] and interfacial tension[101, 102, 153] (see **Appendix A1)**.

4.2.2 Simulation Details

All simulations are conducted by GROMACS (version 2019.1)[154] software package. The equations of motions are integrated by the Leap-Frog algorithm[104] with a time step of 2 fs. After an energy minimization using the steepest descent algorithm until the maximum force is less than $1000\,kJ\,mol^{-1}nm^{-1}$, an equilibration run of 20 ns (*i.e.*, 0-20 ns) followed by a production run of 10 ns (*i.e.,* 20-30 ns) with NP_zT (*i.e.*, a fixed number of molecules, a constant pressure in the *z*-direction normal to the interfaces, and a constant temperature) algorithm is carried out at a constant pressure of 200 bar and temperature of 353 K. The system temperature is controlled by the velocity rescaling[105] and nose-hoover[106] thermostats with the relaxation time of 0.1 ps for the equilibration and production processes, respectively. System pressure is controlled by the Berendsen[107] and Parrinello-Rahman[108] barostats with a time constant of 0.1 ps for the equilibration and production processes, respectively. The atomic and molecular trajectories in the production stage are saved every 100 steps (200 fs) for data analysis.

The particle-mesh Ewald (PME) method[109] with a Fourier spacing of 0.12 nm and a 1.2 nm real-space cut-off are used to calculate the electrostatic interactions. Lennard Jones (LJ) forces are modified to decay smoothly to zero between 1.0 nm and 1.2 nm[154]. LJ interactions between unlike atoms are deducted from the conventional Lorentz-Berthelot mixing rules[110, 111]. The SETTLE algorithm[112] is used to constrain the bond length and angle of water molecules, while

the LINCS algorithm[113] is used to constrain the bond length for other molecules. The snapshots are presented by the Visual Molecular Dynamics (VMD) package[114].

4.3 Results and Discussion

In this section, we first present the density distributions of various molecules and some of their important functional groups. Then, we discuss the effects of the concentration/number of propanol on the interfacial properties in terms of IFT, the density of hydrogen bond, and radial distribution density. Finally, we discuss the effects of the concentration/number of propanol on the local fluidity in terms of the diffusion coefficient of SDS molecules.

4.3.1 Density Distribution

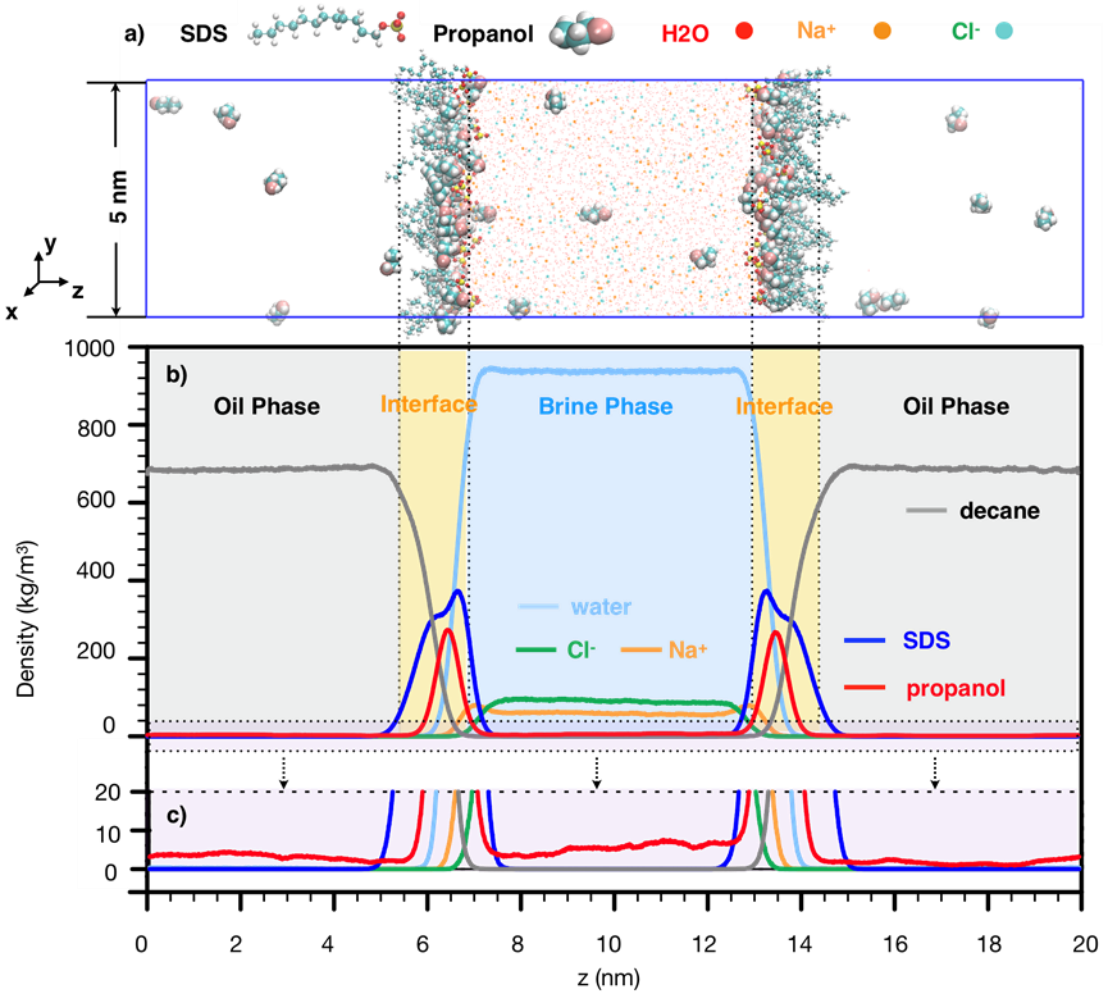

Figure 4-2 a) Snapshot of the SDS50_Prop100 system; b) density distributions of each molecule in the system, and c) its enlargement. n-decane molecules and hydrogen atoms in the water molecules are omitted in the snapshot (Figure 4-2 a) for a better observation. The dashed line represents the contact of the phases.

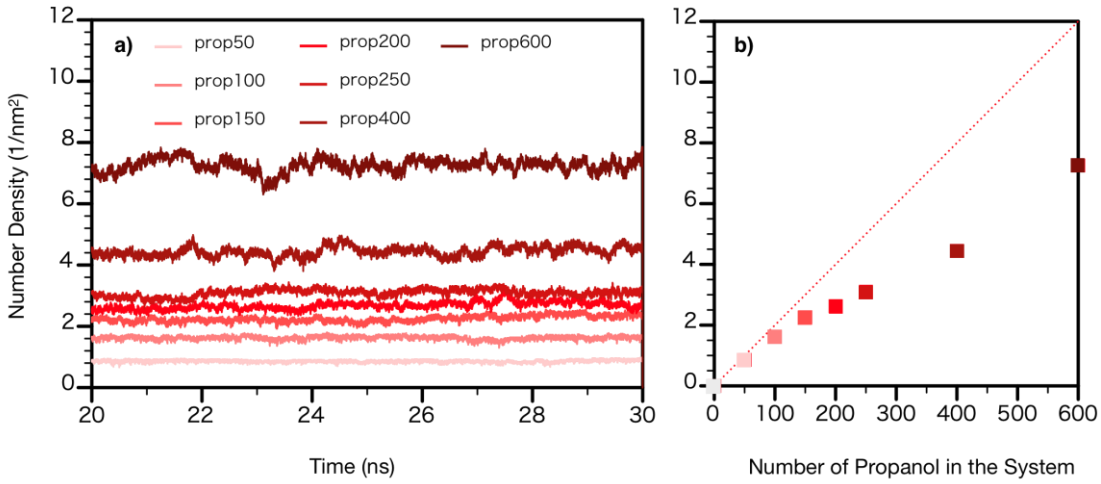

Figure 4-3 The propanol number density in the interfaces a) over simulation time; b) time-averaged. The darker color indicates a higher concentration/number of propanol in the system. The dashed line is the propanol number density when all propanol molecules are located in the interface. The statistical error is smaller than the symbol size.

We present the mass density distributions of each component as well as its enlarged view in **Figure 4-2 b**, and **Figure 4-2 c** (SDS50_Prop100 as a representative). The density distributions of each component in other systems are presented in **Appendix C.2**. To better explain molecular distributions, we present a snapshot of the equilibrated SDS50_Prop100 system in **Figure 4-2 a**. The "90-90" criterion[115], in which oil or water content is 90% of their own bulk value, is used to define the interfacial region (marked in **Figure 4-2 b)**). The snapshot in **Figure 4-2 a** clearly shows that all SDS molecules are trapped in the oil-water interfaces. On the other hand, the propanol molecules are distributed in the oil phase, interface, and brine phase. The greater part of the propanol was distributed in the interface while some of which were distributed in the oil and brine phase under equilibration; despite all propanol being originally distributed in the oil phase for the initial configuration **Figure 4-1**. This indicates that propanol, as a cosurfactant, can be transferred from the oil phase to the interface and brine phase. The dislocation of propanol, as a

dynamic process, is a good indicator to monitor the system to ensure that it reaches an equilibrium. Therefore, we use the propanol density at the interface as a parameter to determine the equilibration of the system. **Figure 4-3 a** depicts the propanol number density in the interfaces for the production run (trajectory from 20-30 ns). It shows that the system is under equilibration between 20 ns and 30 ns. We present the time-averaged propanol number density in the interfaces in **Figure 4-3 b**. The propanol density in the interfaces increases as propanol concentration/number increases. As shown in **Figure 4-3 b**, more and more propanol molecules are located in the brine and oil phases as propanol concentration increases.

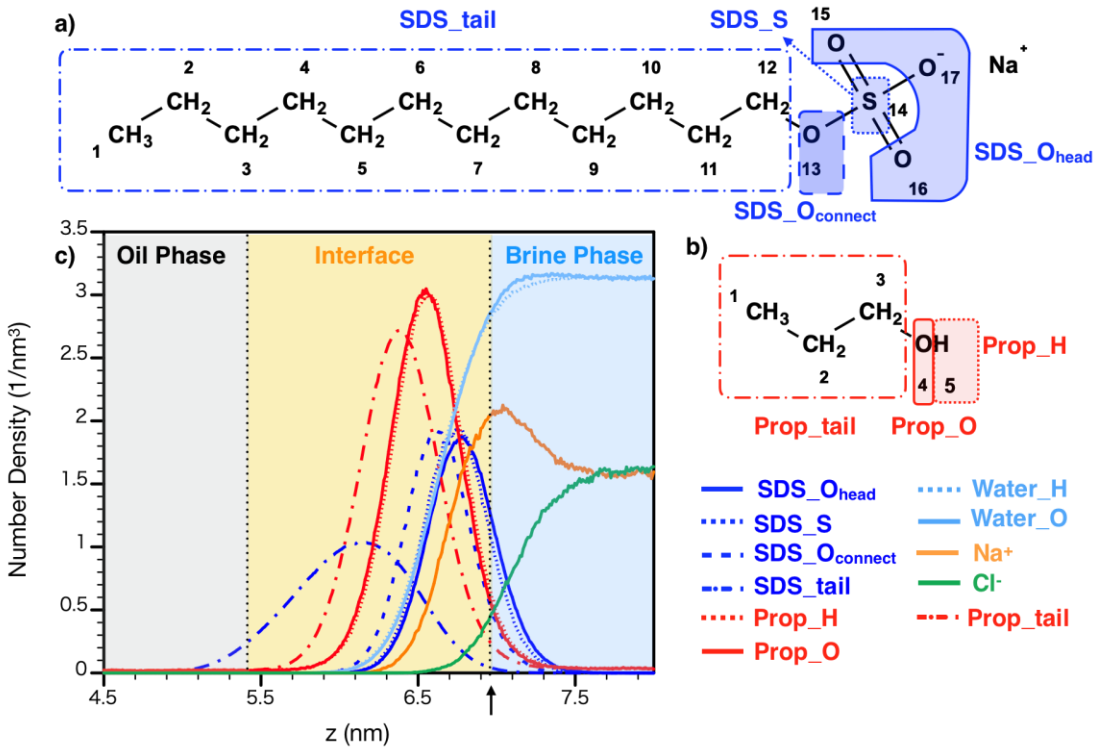

Figure 4-4 Molecular structure of a) SDS; b) propanol. c) number density distribution of functional groups in the interfaces. The oil phase, interface, and water phase have been represented using gray, yellow, and blue colors, respectively. The dashed line represents the contact of the phases. For clarity, water density is scaled down by 10 times in Figure 4-4 c.

As amphiphilic molecules, SDS and propanol, have functional groups with different affinities for solvent and salt ions as highlighted in **Figures 4-4 a** and **b**. To further investigate the distributions of these functional groups in the interface regions, we depict their number density distributions in **Figure 4-4 c** (SDS50_Prop100 as a representative). We classify the atoms in SDS molecules into four distinct groups (SDS_O_{head}, SDS_S, SDS_$O_{connect}$, and SDS_tail) based on their affinity to water (**Figure 4-4 a**). Similarly, the atoms in propanol molecules are classified into three distinct groups (Prop_H, Prop_O, and Prop_tail) (**Figure 4-4 b**). Here, we note that the entire group is counted as one (not the number of atoms in the group). As shown in **Figure 4-4 c**, the order of the peak positions from the brine phase is SDS_O_{head}, SDS_S, SDS_$O_{connect}$, Prop_H, Prop_O, Prop_tail, and SDS_tail. This indicates that propanol molecules reside after SDS molecules. This observation is in line with Dominguez *et al.* [136]. The peak position of the SDS_tail is farther than that of Prop_tail from the brine phase. This is because the length of the SDS tail group is longer than that of the propanol tail group.

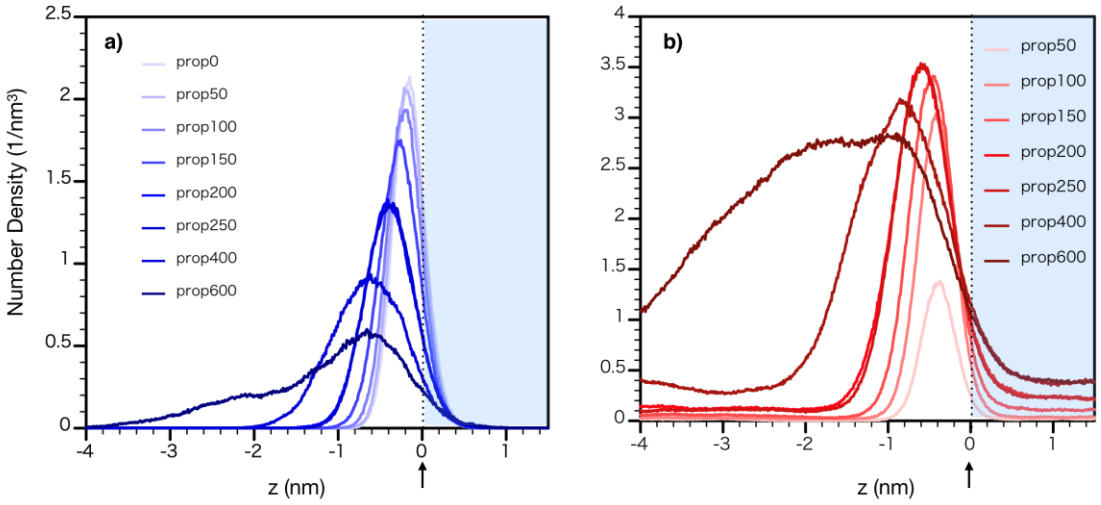

Figure 4-5 The number density of a) SDS_S; b) Prop_O under varying propanol concentrations/numbers. The darker color indicates the concentration of the propanol is high. The dashed line represents the contact between the interface and the brine phase.

We present SDS_S and Prop_O number density distributions under varying propanol concentrations/numbers in **Figure 4-5**. For a better comparison, we artificially reset the value of the *z*-axis at the contact of the interface and brine phase (marked in the figure) as zero. The peak in the SDS_S distributions shifts away from the brine phase as propanol concentration increases. Namely, SDS is supplanted by propanol as its concentration increases. Furthermore, the shape of SDS_S density distributions becomes broader as propanol concentration increases. It indicates that SDS is more dispersed along the *z*-direction as propanol concentration increases. On the other hand, as propanol concentration increases, the peak position of Prop_O distributions shifts away from the brine phase. However, we note that this phenomenon does not necessarily indicate that the number of propanol molecules in contact with water decreases as its concentration increases. In fact, as propanol concentration increases, its density at the interfaces increases gradually and reaches a plateau and the peak value of its distributions first increases and then decreases after reaching an inflection point. This maximum value (~3.5 $1/nm^3$) is observed in the system SDS50_Prop250.

4.3.2 Interfacial Interactions

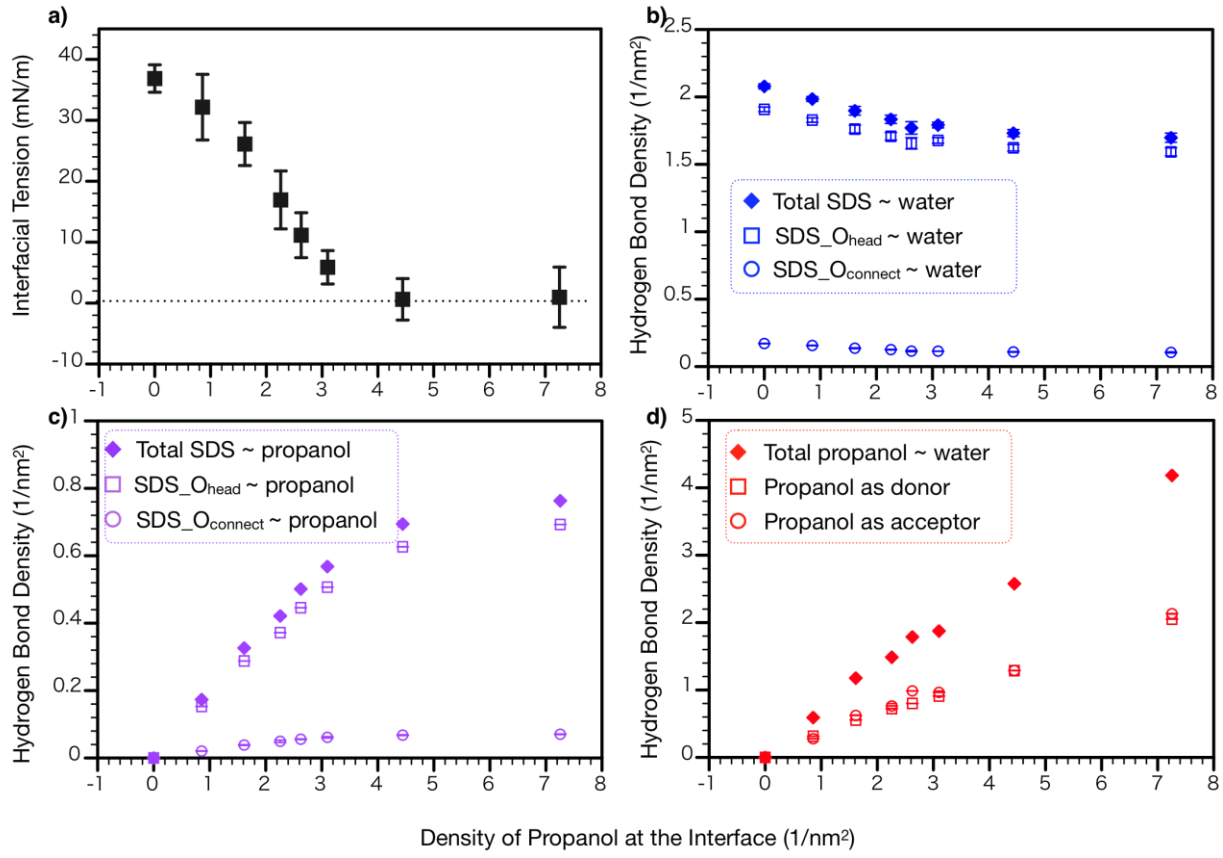

Figure 4-6 a) Interfacial tension; Hydrogen bond density between b) SDS and water; c) SDS and propanol; d) propanol and water.

The interfacial tension (IFT) of the system is calculated using the following equation described in **Chapter 1**, **Section 1.4.4.3**. IFT with varying propanol concentrations is depicted in **Figure 4-6 a**. We observe that IFT decreases as propanol concentration increases. Is such a phenomenon due to the reason that propanol helps SDS to form hydrogen bonds with water? Or is it because propanol can form hydrogen bonds with water? Does propanol form hydrogen bonds with SDS? In order to answer these questions, we analyze hydrogen bond (H-bond) densities between different combinations of these molecules.

We analyze the density of H-bonds between SDS and water, propanol and water, and SDS and propanol, respectively. In this study, we use a cut-off distance of 3.0 nm and an angle of 150 degrees to dictate H-bonds[155] (**Chapter 1**, **Section 1.4.4.5**). **Figure 4-6 b** represents the H-bond density formed by SDS and water. In order to better understand the contributions of different functional groups to H-bond formation, we analyze the density of H-bond formed by different functional groups separately. The H-bond density of SDS_O_{head} and water, SDS_$O_{conncet}$ and water, and their summation are also shown in **Figure 4-6 b**. It reveals that the H-bond density between SDS and water decreases as propanol concentration increases. The majority of the H-bonds between SDS and water are contributed by SDS_O_{head}, while there exist fewer H-bonds between SDS_$O_{connect}$ and water. Propanol can not only form H-bonds with water but also form H-bonds with SDS. The H-bond density between propanol and SDS is presented in **Figure 4-6 c**. The H-bond density increases as propanol concentration increases. Again, most H-bonds are contributed by SDS_O_{head} in contrast to SDS_$O_{connect}$. We also depict the H-bond density between propanol and water in **Figure 4-6 d**. When forming H-bond with water, propanol can act as either a donor (open square) or an accepter (open circle). The ratio of such roles (donor: accepter) is around 1 to 1. The H-bond density between propanol and water increases as propanol concentration increases. The increase in propanol concentration can decrease the formation of an H-bond between SDS and water. The decrease in IFT is due to the increasing number of H-bonds between propanol and water.

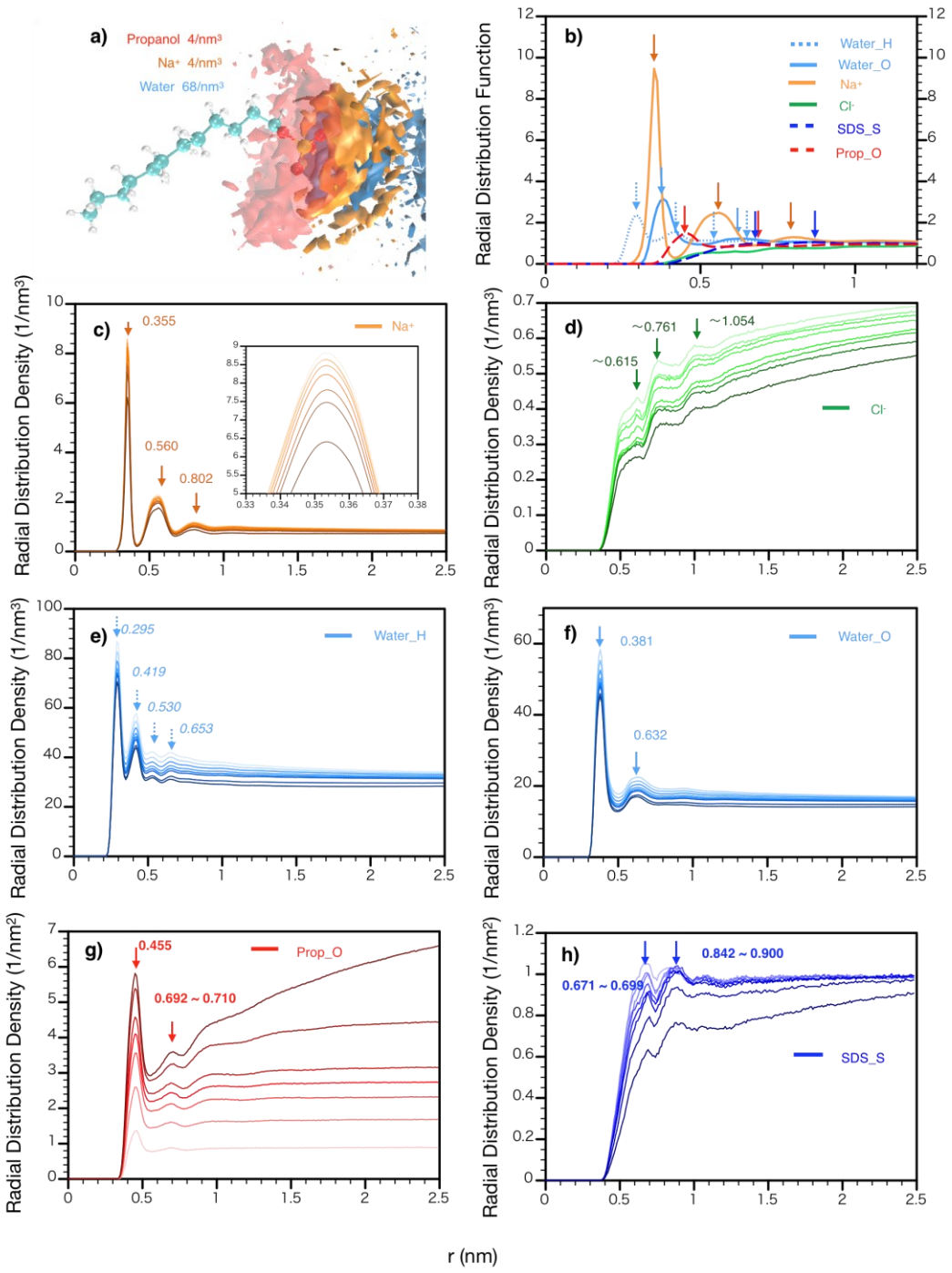

Figure 4-7 a) Spatial distribution functions; radial distribution densities of b) Na^+; c) Water_H; d) Water_O; e) Prop_O; f) SDS_S around SDS_S. A darker color corresponds to a higher concentration of propanol.

In order to further investigate the effect of propanol on SDS distributions, we present spatial and radial distribution functions/densities around SDS_S in **Figure 4-7**. A cylindrical-like iso-density surface was observed for the propanol around the SDS, while the hemispheres were monitored for the Na+ and the water molecules as shown in **Figure 4-7 a.** Since the system we are studying is heterogeneous as shown in **Figure 4-2 b,** and **Figure 4-7 a**, we used two different formulas to calculate the radial distribution densities (two different formulas for radial distribution functions correspondingly) for the molecules mainly distributed in the bulk (water_H, water_O, Na^+, Cl^-) and molecules mainly distributed in the interfaces (prop_O, SDS_S) (**Chapter 1**, **Section 1.4.4.1)**. The radial distribution functions of the molecules are depicted in **Figure 4-7 b**. Some of the peaks in **Figure 4-7 b**, which are not distinguishable, can be found in **Figures 4-7 c**, **d**, **e**, **f, g,** and **h**. Water_H is located nearest to the SDS_S, followed by Na^+ ion, water_O, and Prop_O. We use radial distribution density, instead of the radial distribution function in **Figures 4-7 c**, **d**, **e**, **f**, **g,** and **h**, when the converged densities which are dictated at a large radial distance (*i.e.*, $2 \le r \le 2.5\,\text{nm}$) are different from the system to system due to the introduction of propanol. Therefore, the radial distribution function, which is scaled down by this value, can not quantitively represent the density difference of the molecules system by system. All components, except for Prop_O, show density decrement as propanol concentration increases. It indicates that the introduction of propanol not only affects the interaction between water and SDS, but also the interaction between SDS and Na^+ as well as among SDS itself. Three distinct peaks are observed in the Na^+ distribution, while four peaks in water_H distributions and two peaks in water_O distributions are observed. This observation is in line with the previous report[65].

4.3.3 Local Fluidity

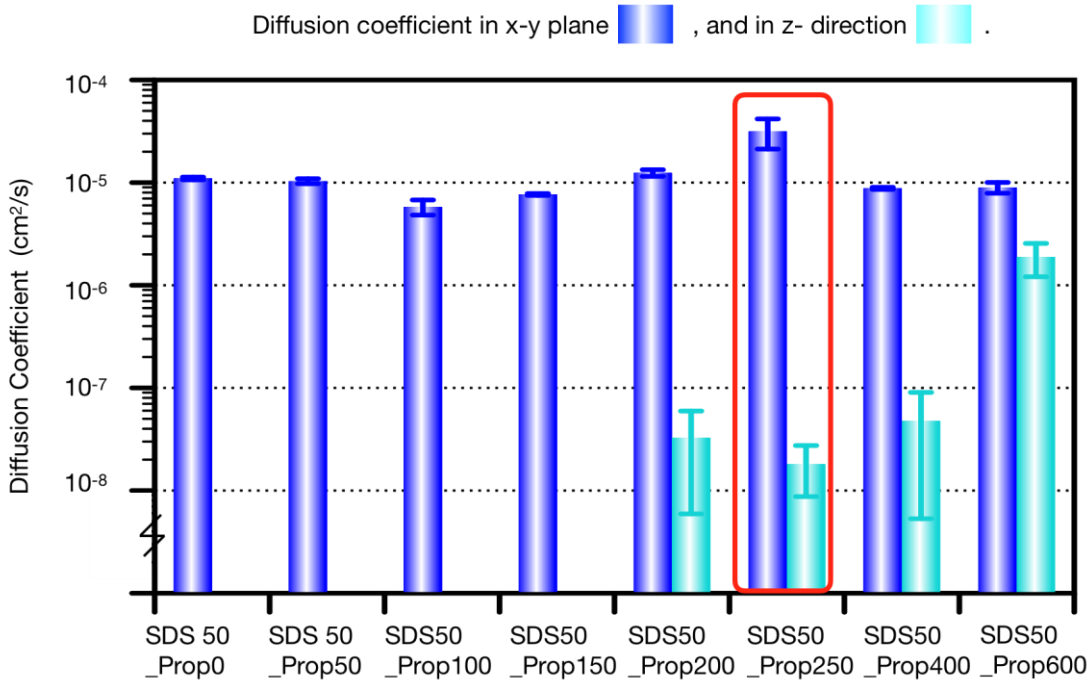

Figure 4-8 The diffusion coefficient of SDS in the *x*-*y* plane and the *z*-direction. The diffusion coefficient lower than 10^{-8} is not presented. The system with a maximum diffusion coefficient (SDS50_Prop250) is marked out using a red rectangle.

Previous studies demonstrated that molecular local fluidity mainly depends on molecular diffusion[156-158]. In order to investigate the effect of propanol on the local fluidity of SDS, we present the self-diffusion coefficient of SDS. The equations to calculate the diffusion coefficient are shown in **Chapter 1**, **Section 1.4.4.6**. The diffusion coefficients in the *x*-*y* planes are significantly higher than those in the *z*-direction. It reveals that the motion of the SDS molecule in the interfacial regions is dominated by the diffusion in the *x*-*y* plane. The diffusion coefficient in the *z*-direction becomes comparable to those in the *x*-*y* plane at high propanol concentration. The increase in propanol concentration does not always increase the diffusion coefficient of SDS. The

maximum diffusion coefficient is observed in the system of SDS50_Prop250. Interestingly, this is also the system in which we observe the maximum peak value from the propanol functional group density profile as shown in **Figure 4-5 b**. Thus, we hypothesize that the local fluidity is related to the molecular local packing in the interfaces.

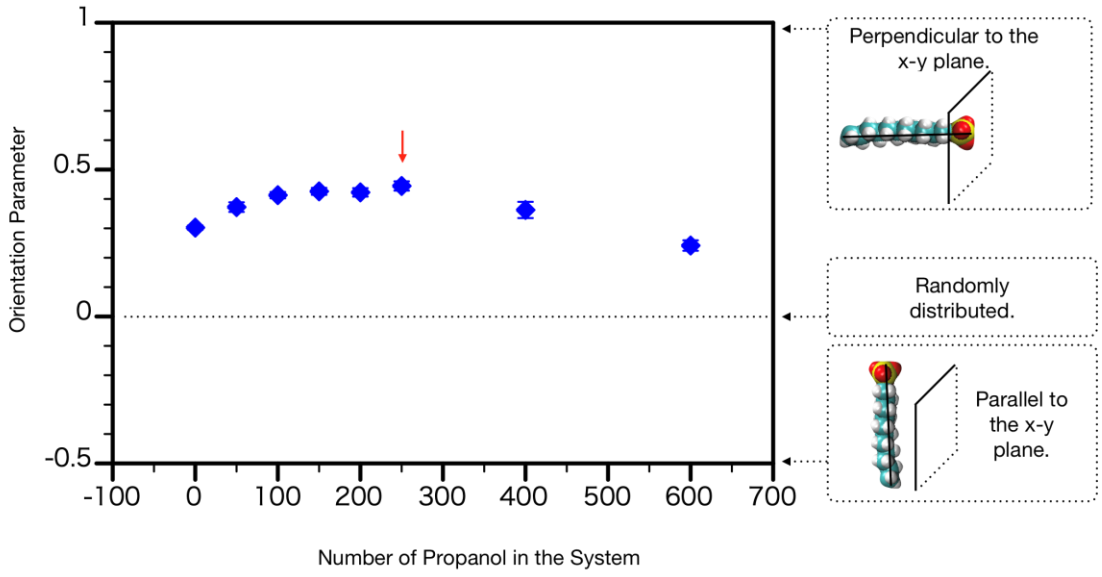

Figure 4-9 Orientation parameter of the SDS. The system with the maximum orientation parameter (SDS50_Prop250) is marked out using a red arrow.

We further investigate the effect of SDS orientation on its local fluidity. The orientation parameter[63, 159, 160] is given in **Chapter 1**, **Section 1.4.4.4**. The value of the orientation parameter can vary from -0.5 to 1. When the molecules are completely parallel to the plane, the calculated orientation parameter is -0.5; the orientation parameter of 1 indicates that the molecules are fully perpendicular to the *x-y* plane; the value of the orientation parameter is zero when the molecules are randomly distributed. As shown in **Figure 4-9**, SDS molecules incline to be more perpendicular to the *x-y* plane. The orientation parameter first increases and then decreases after a

local maximum. Again, this local maximum point is observed in the system SDS50_Prop250. Based on the above-stated observations, we hypothesize that propanol, penetrated into the SDS molecules, helps orientate the SDS molecules at low concentrations. However, it disorients the SDS molecules at high concentrations. Thus, the increment of local fluidity of SDS molecules is related to such transition.

4.4 Summary

The distribution and role of propanol as a cosurfactant under a typical reservoir condition were studied by using MD simulations. We found that propanol is distributed all over the system (oil phase, interface, brine phase), while they are mainly stood in the interfaces. The functional groups of propanol are stood after those of SDS. The interfacial tension decreases as propanol concentration increases. This is because propanol can form hydrogen bonds with water, while it harms the formation of H-bonds between water and SDS. The interactions between SDS_S and all molecules (Na^+ ion, water_O, water_H, and Prop_O) are affected by propanol. The introduction of the propanol does not always increase the local fluidity of SDS. When the orientation parameter is at the local maximum, the local fluidity of SDS is also the highest.

Chapter 5 : ETHANOL BLENDING TO IMPROVE REVERSE-MICELLE DISPERSITY IN SUPERCRITICAL CO_2: A MOLECULAR DYNAMICS STUDY

A version of this chapter has been published in *J. Phys. Chem. B*. (Nan *et al*.,2021) [161].

5.1 Introduction

Tight oil has been playing an increasingly important role in supplying global energy consumption[162]. Tight reservoirs generally have extremely low permeability (0.1~0.001 mD)[163]. As a result, the secondary and tertiary recoveries[164], often deployed in the conventional reservoirs to further recover the residual oils by injecting water and surfactants, have had limited success in the enhanced oil recovery (EOR) in tight reservoirs[32]. The supercritical CO_2 ($scCO_2$), as an environmentally friendly and inexpensive chemical, has moderate critical constants (T_c= 304.1 K, P_c=7.38 MPa)[20] with good injectivity[21], and is an excellent alternative solvent to carry surfactants. In addition, the $scCO_2$ flooding in tight reservoirs benefits from the generally sterling miscibility between CO_2 and oils[21-24] and promotes oil swelling and viscosity reduction, which are favorable for EOR. On the other hand, as one of several geological carbon sequestration (GCS) schemes[25-28], CO_2 injection into tight formations can help mitigate carbon emissions. However, CO_2 flooding in tight formations is subject to gas channeling which can adversely impact the efficacy of EOR[29]. Therefore, surfactants are usually added to $scCO_2$ injection to facilitate CO_2 foam formation[22, 29] which can eliminate the early breakthrough and viscous fingering due to the heterogeneous pore distributions[30]. In addition, surfactants can

further decrease the minimum miscible pressure (MMP) of the oil which is favorable for EOR[31, 32].

Unfortunately, in general, surfactants that are commonly used in oil reservoirs (*e.g.*, sodium bis(2-Ethylhexyl) sulfosuccinate (AOT) and sodium dodecyl sulfate (SDS)) have limited solubility in $scCO_2$[32]. Namely, surfactants precipitate in $scCO_2$, which significantly limits their delivery efficiency to the target zone. Therefore, extensive efforts have been dedicated to improving surfactant solubility and dispersity in $scCO_2$. These efforts can be generally classified into two approaches: the first one is to optimize surfactant structures to form relatively stable reverse micelles (RMs)[33-38], in which the head groups of surfactants distribute in the core with their tail groups immersed in the solvent. The second method is to introduce some chemical additives (such as alcohols) to the solvent to improve the RM dispersity[29, 32, 38-42]. The latter approach can be conveniently applied in actual oil fields, as one can readily use highly effective surfactants for EOR.

A few experimental and simulation studies have been carried out to study the role of alcohols in increasing the surfactant dispersity and solubility in $scCO_2$. An experimental study by Shi *et al*.[38] studied the efficacy of alcohols with various tail lengths (*i.e.*, ethanol, butanol, hexanol, octanol, and decanol) to improve the dispersity of Triton X-45 (TX-45) in $scCO_2$. They found that hexanol is the most efficient one among these alcohols and hypothesized that hexanol molecules can hinder the surfactant-surfactant interactions by inserting themselves in between the surfactant tails. Similar results are obtained by McFann *et al.*[165]. Chennamsetty *et al*.[166] used lattice Monte Carlo simulation to study the effect of the alcohols in the aggregation of $H\text{-}(CH_2)_{12}\text{-}(O\text{-}CH_2\text{-}CH_2)_5\text{-}O\text{-}(CH\text{-}(CH_3)\text{-}CH_2\text{-}O)_4\text{-}H$ (LS-54) in $scCO_2$. They demonstrated that alcohols can distribute at the core/corona interfaces, leading to a substantial decrease in the aggregate size. On

the other hand, Zhang *et al.*[167] reported a very promising performance of using ethanol to improve the solubility of AOT in $scCO_2$. They also used molecular dynamics (MD) simulations to investigate the role of ethanol by analyzing AOT-AOT and AOT-CO_2 radial distribution functions. They found that the ethanol molecules can decrease the head-head interactions among the AOTs in $scCO_2$, thereby increasing AOT dispersity. While their MD analysis is helpful to explain the underlying mechanism, a comprehensive understanding about the structural and thermodynamic properties of AOT RMs in $scCO_2$ and the role of ethanol still remains elusive.

Therefore, in this work, we use molecular dynamics (MD) simulations to study the role of ethanol in increasing AOT solubility and RM dispersity in the $scCO_2$ to provide an in-depth understanding from atomistic and molecular scales. The temperature and pressure are set as 333 K and 200 bar, respectively, to represent a typical reservoir condition[167]. We design two different systems: System A consists of AOT and $scCO_2$; System B consists of AOT, $scCO_2$, and 10 *wt*.% ethanol. After equilibrium, the AOT molecules aggregate together and form large rod-like RMs in System A. In contrast, AOT molecules form several small sphere-like RMs in System B. In System A, Na^+ ions aggregate in the cores of RMs, while they are bonded to the head groups of AOT molecules. By introducing ethanol (system B), Na^+ ions can be solvated by the ethanol molecules, which prevents further AOT aggregations. The potential of mean force (PMF) calculations also reveals that small clusters of AOT molecules attract each other in $scCO_2$, while they repel each other when ethanol is introduced. Our work should provide important insights into the role of alcohols in improving AOT solubility and dispersity in $scCO_2$, which can aid the design of $scCO_2$ soluble surfactant formulas in tight oil recovery.

The remainder of this paper is organized as follows. In **Computational Methodology**, we introduce the simulation methods and define molecular models. In **Results and Discussion**, we

first investigate the aggregation process in the systems without ethanol. Then, we study systems containing ethanol. Finally, we compare these two systems. In **Conclusion**, we summarize key findings and discuss potential implications.

5.2 Computational Methodology

5.2.1 Simulation Systems

We design two systems to study the ethanol effect on the spontaneous aggregation of AOTs in $scCO_2$: System A includes 40 randomly distributed AOT molecules (~4 *wt*.%) and 10000 CO_2 molecules; System B contains additional 955 ethanol molecules (~10 wt.%) beyond System A. Selection of AOT and ethanol concentration rely on the experimental reports[32] and simulation trials, of which condition can well explain the role of ethanol in solubility increment (see **Appendix D.2**). The initial simulation box size for both systems is $11\times11\times11$ nm^3. In both Systems A and B, the molecules are randomly inserted into the simulation box for the initial configurations. To test the effect of initial configurations, 20 and 5 different replicas are constructed for systems A and B, respectively.

Four additional systems (Systems C, D, E, and F) are designed to study the free energy profile of AOT self-aggregations. Systems C and D investigate the interactions between a single AOT molecule and a cluster (formed by 4 AOT molecules) at various separation distances in CO_2 and CO_2 with 10 *wt*.% ethanol, respectively. We pull one of the AOT molecules away from the cluster formed by 5 AOT molecules in Systems C and D, to generate the initial configurations for umbrella sampling windows with the center of mass (COM) of Na^+ ions in the cluster sequentially moving 0.1-0.2 nm between adjacent windows. Interactions between two clusters with each of them formed by 4 AOT molecules are studied in Systems E and F: System E contains two clusters in

CO_2; System F is similar to System E but in CO_2 with 10 *wt*.% ethanol. In Systems E and F, we push one cluster gradually close to the other from their initial Na^+ COM separation distance of 2.5 nm to ~0.5 nm, to generate the initial configurations for umbrella sampling windows. The cluster consisting of 4 AOT molecules is chosen based on the following considerations: 1) The 4-AOT cluster is the most common one (see **Figure 5-4 h**) based on the spontaneous aggregation process in System B; 2) the 4-AOT cluster is a sphere-like RM, which eliminates the effect of approaching directions in the umbrella sampling.

5.2.2 Computational Details

All simulations are conducted by GROMACS (version 2019.1)[103] software package. The equations of motions are integrated by the Leap-Frog algorithm[104] with a time step of 2 fs. The system energy is first minimized until the maximum force is less than $1000\,kJ\,mol^{-1}nm^{-1}$ using the steepest descent algorithm. The particle-mesh Ewald (PME) method[109] with a Fourier spacing of 0.12 nm and a 1.2 nm real-space cut-off is used to calculate electrostatic interactions. Lennard Jones (LJ) forces are modified to decay smoothly to zero between 1.0 nm and 1.2 nm[103]. LJ interactions between the unlike-atoms are obtained from the conventional Lorentz-Berthelot mixing rules[110, 111]. The LINCS algorithm[113] is used to constrain the bond length for all the molecules. The temperature and pressure are set as 333 K and 200 bar, respectively[76], to represent a typical reservoir condition. At this condition, CO_2 is in a supercritical state. Three-dimensional (3-D) periodic boundary conditions (PBCs) are applied in all cases. We employ the CHARMM forcefield[50, 168] for surfactants and the rigid EPM2[169] for CO_2 as shown in **Appendix D.1**. The snapshots are presented by the Visual Molecular Dynamics (VMD) package[114].

For spontaneous aggregation processes, 600-ns *NPT* (*i.e.*, a fixed number of molecules, a constant pressure, and a constant temperature) ensemble simulations are carried out with velocity rescaling[105] with a relaxation time of 0.1 ps and the Berendsen barostats[107] with a time interval of 0.2 ps for system temperature and pressure control, respectively. The atomic and molecular trajectories are saved every 100 steps (200 fs) for data analysis.

For umbrella sampling, the system in each window is conducted by the *NPT* ensemble with a constant pressure of 200 bar and temperature of 333 K with a 10-ns equilibration run followed by a 10-ns production run. Velocity rescaling[105] and Nose-Hoover thermostats[106] with a relaxation time of 0.1 ps are employed to control the system temperature for the equilibration and production processes, respectively. Berendsen[107] and Parrinello-Rahman[108] barostats with a time interval of 0.2 ps are used to control the system pressure for the equilibration and production processes, respectively. Harmonic position restraints with a force constant ranging from $1000\,kJ\,mol^{-1}nm^{-2}$ to $5000\,kJ\,mol^{-1}nm^{-2}$ are employed to restrain the distance between two desired structures (cluster or molecule). The weighted histogram analysis method[57] is used to obtain PMF curves among the sampled windows. The resulting PMF curves are adjusted by subtracting the entropic contribution of increased accessible phase space due to the volume increment[58], which is given as

$$\mathrm{V}_{\mathrm{PMF}}(r) = -(n_{\mathrm{c}} - 1)k_{\mathrm{B}}T\log(r) \tag{5-1}$$

where $n_c = 3$ is the number of dimensions in the reaction coordinate r. The PMF curves are further adjusted by a parallel movement in the *y*-axis to ensure their values vanish at the place where the reaction coordinate is large (2 nm).

5.3 Results and Discussion

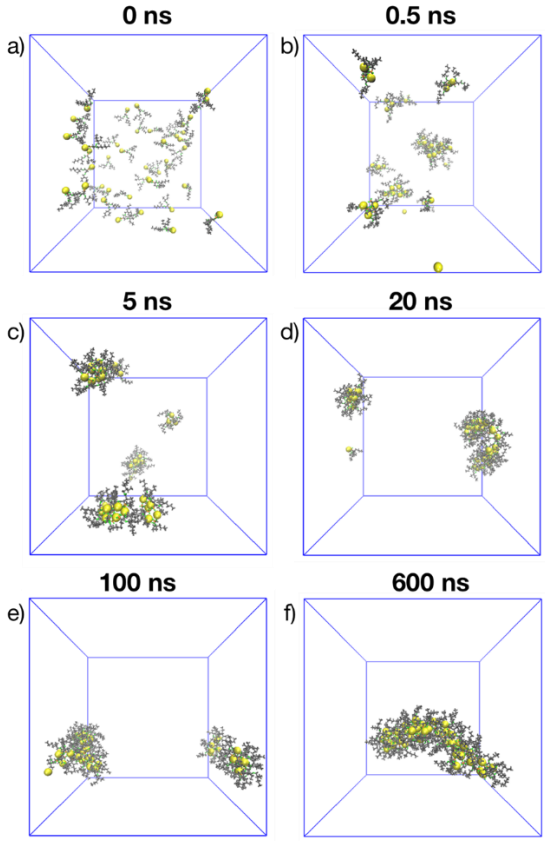

Figure 5-1 Formation of RMs and their evolution (0, 0.5, 5, 20, 100, and 600 ns) in System A. The yellow spheres represent the Na^+ ions in AOT, while other atoms in AOT are depicted by sticks. For clarity, CO_2 is not shown here.

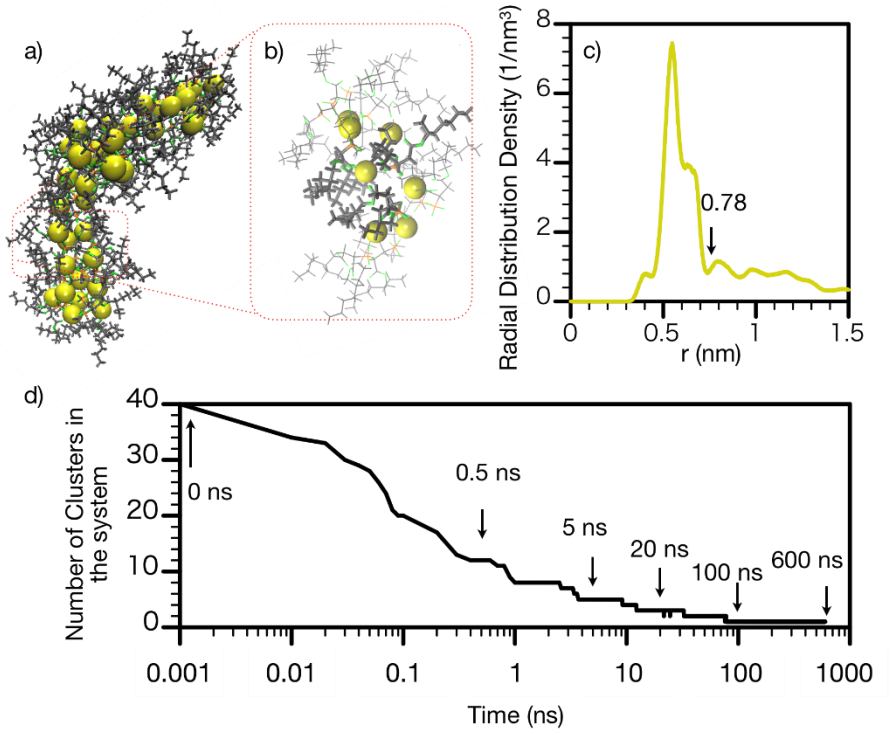

Figure 5-2 a) Snapshot of RM in System A; b) its enlargement; c) Na^+-Na^+ radial distribution density; d) Evolution of cluster number in System A.

In **Figure 5-1**, we present the formation of RMs and their evolution in system A for one specific simulation run. The AOT molecules barely dissociate in the $scCO_2$ with all the Na^+ ions strongly bound to the respective AOT head groups. This result is in line with Zhang *et al.*[167]. We observe spontaneous aggregations of AOT molecules forming large rod-like RMs after around 100 ns. The close-up RM structure is shown in **Figures 5-2 a** and **b**. The RM core consists of Na^+ ions, which are bounded by the AOT head groups, while the AOT tail groups are immersed in the $scCO_2$ phase. Since there is no dissociation of Na^+ ions from AOT head groups, the position of the first local minimum in the radial distribution density (RDD) of Na^+ ions around the Na^+ ions, 0.78 nm (**Figure 5-2 c**), is used to identify AOT clusters. Namely, any Na^+ ions within 0.78 nm are

treated as the same cluster. In addition, the Number of AOTs in one cluster is defined as the cluster size for clarity. The evolution of cluster number in System A obtained by the GROMACS analysis tool gmx_clustsize is presented in **Figure 5-2 d**. The time points illustrated in **Figure 5-1** are highlighted by the black arrows in **Figure 5-2 d**. The cluster number is 40 for the initial state, as 40 AOT molecules are randomly inserted and distributed. The decreasing trend in the cluster number indicates the gradual aggregation of AOT molecules. A single RM appears for the first time at 87 ns and remains stable thereafter. The general trend in the cluster number versus time is similar in the other 19 replicas, as shown in **Appendix D.3**. The spontaneous AOT aggregation is independent of the initial configurations. On the other hand, the cluster number after the 600-ns runs can be 2 or 3 in some replicas. The averaged cluster sizes (number of AOTs in a cluster) at the end of 600-ns runs from 20 replicas are presented in **Appendix D.3**. It is observed that 35 % of the systems (7 out of 20) end up with a single cluster. On the other hand, all other cluster sizes possess similar probabilities, which indicates that this spontaneous aggregation is randomly driven without any preference in forming a specific size.

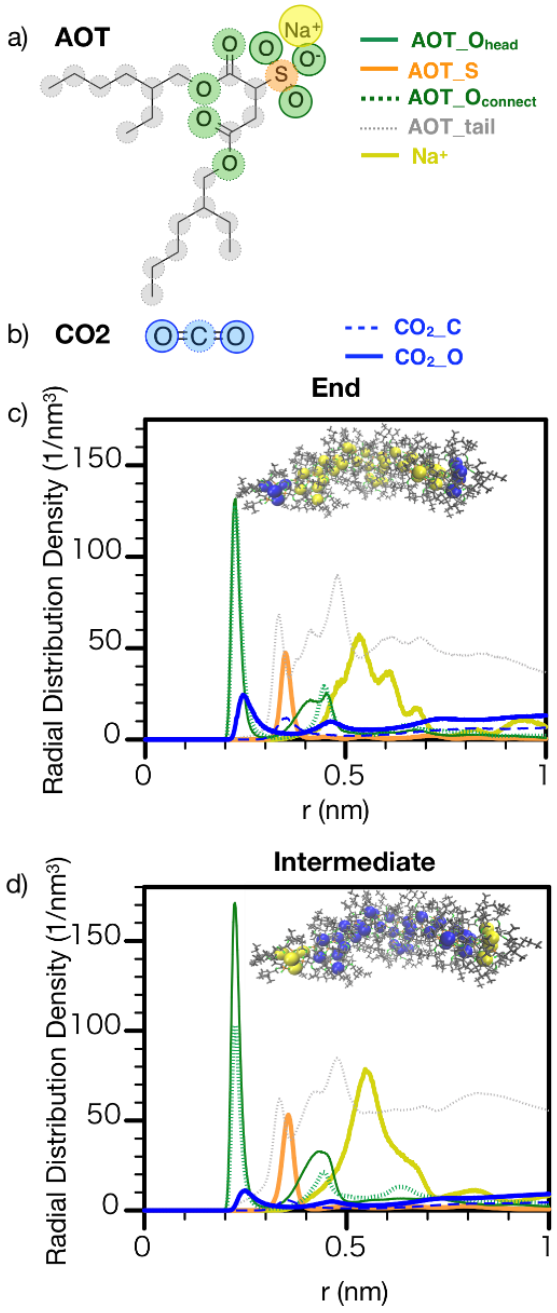

Figure 5-3 Molecular structures and the classifications of their functional groups in a) AOT; b) CO_2; RDD of the functional groups around Na^+ ions at c) the end; d) the intermediate. The reference Na^+ ions to obtain RDD are highlighted using blue color in the corresponding illustrations.

We present the aggregation process of two AOT clusters in **Video V1 (**see original paper [161]**)**. The Na^+ ions at the ends of these two clusters are highlighted by using red and blue colors, respectively. Two clusters repel each other when they approach each other side-to-side, while finally forming a stable single cluster when they approach each other end-to-end. The RDDs of the functional groups around Na^+ ions distributed in the end and intermediate are presented in **Figure 5-3**. Only the trajectories which form a single cluster (*i.e.,* 100 ns - 600 ns) are used in the RDD calculation for convenience. **Figures 5-3 a** and **5-3 b** depict the molecular structures of AOT and CO_2, and their classifications into several functional groups: Na^+, AOT_O_{head}, AOT_S, AOT_$O_{connect,}$ and AOT_tail for AOT; CO_2_O and CO_2_C for CO_2, respectively. The RDDs of these functional groups around the end Na^+ ions (highlighted by blue color in the inset) are shown in **Figure 5-3 c**. We observe that the AOT_O_{head} and AOT_$O_{connect}$ groups distribute closest to the Na^+ ions with strong peaks, followed by an enrichment of CO_2. The CO_2 enrichment might be due to the entropic effect[170, 171], as the apolar CO_2 possesses a low solvating power for Na^+ ions. The AOT_tail group is distributed after that of AOT_O_{head} and AOT_$O_{connect}$. In general, peak positions in the RDDs of functional groups around the intermediate Na^+ ions (highlighted by blue color in the inset) are similar to that of at the end, as shown in **Figure 5-3 d**. An obvious decrement in CO_2 density is observed in **Figure 5-3 d** in contrast to **Figure 5-3 c**, indicating that the Na^+ ions at the end have more exposure to CO_2 and are solvated by them. These CO_2 solvating the end Na^+ ions can be readily replaced by the polar molecules (*i.e.*, AOT). Therefore, cluster aggregation occurs rather end-to-end.

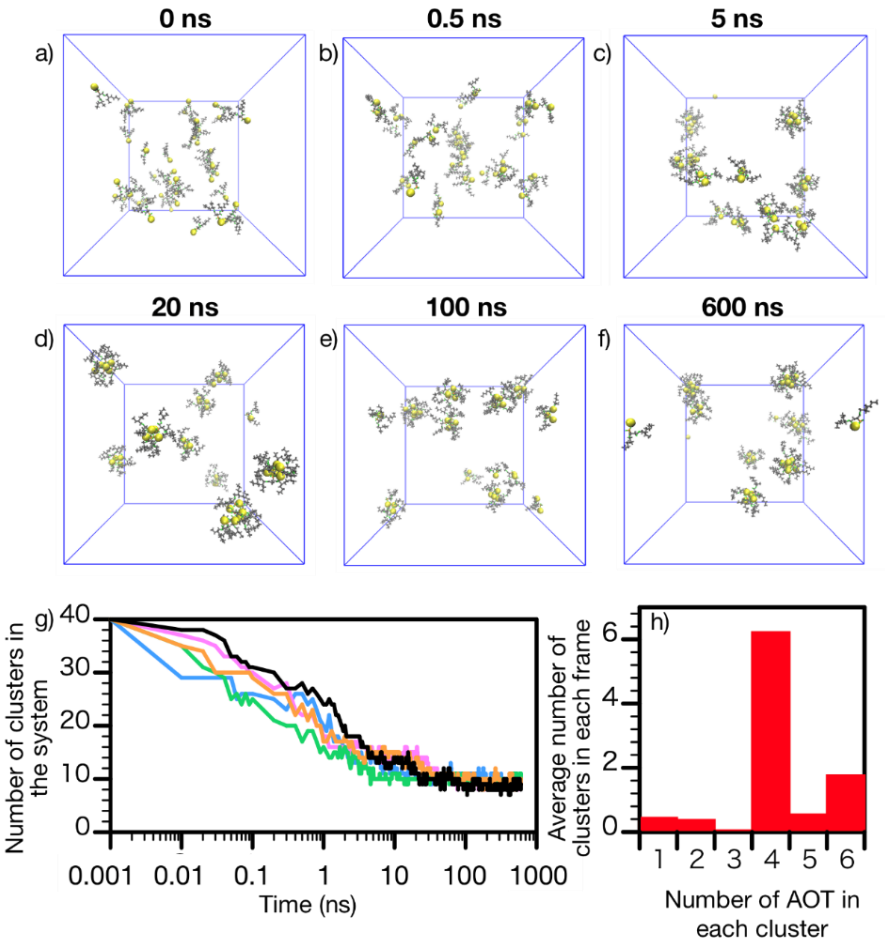

Figure 5-4 a)-f) Formation of RMs and their evolution (0, 0.5, 5, 20, 100, and 600 ns) in System B. The yellow spheres represent the Na^+ ions in AOT, while other atoms in AOT are depicted by sticks. For clarity, CO_2 and ethanol are not shown here; g) Evolution of cluster number in System B; h) average number of clusters in each frame.

The presence of ethanol can drastically alter the RM size and dispersity as shown in **Figure 5-4**. The AOT molecules first aggregate and become stable thereafter with several relatively smaller clusters dispersed in the simulation box. The cluster criterion is the same as that in System A since the RDD between Na^+ and Na^+ has the same local minimum (see **Appendix D.4**). The evolution of cluster number in System B with 5 replicas is shown in **Figure 5-4 g**, where the replica

of the snapshots shown in **Figures 5-4 a-f** is highlighted by the black line. The cluster number gradually decreases in all replicas and finally stabilizes at ~10. The cluster size distributions from these 5 replicas (based on the trajectories between 100 ns and 600 ns) are shown in **Figure 5-4 h**. In contrast to **Appendix D.3**, the cluster sizes are much smaller than those in System A, with the most common cluster size as 4 (cluster formed by 4 AOTs). These small RMs remain stable, which is favorable to form a stable colloidal solution containing surfactants in $scCO_2$[32]. This result is in line with the experimental observations[32], which suggested that the introduction of ethanol increases the dispersity of AOT and reduces the size of RMs, thereby enhancing their "solubility" in $scCO_2$.

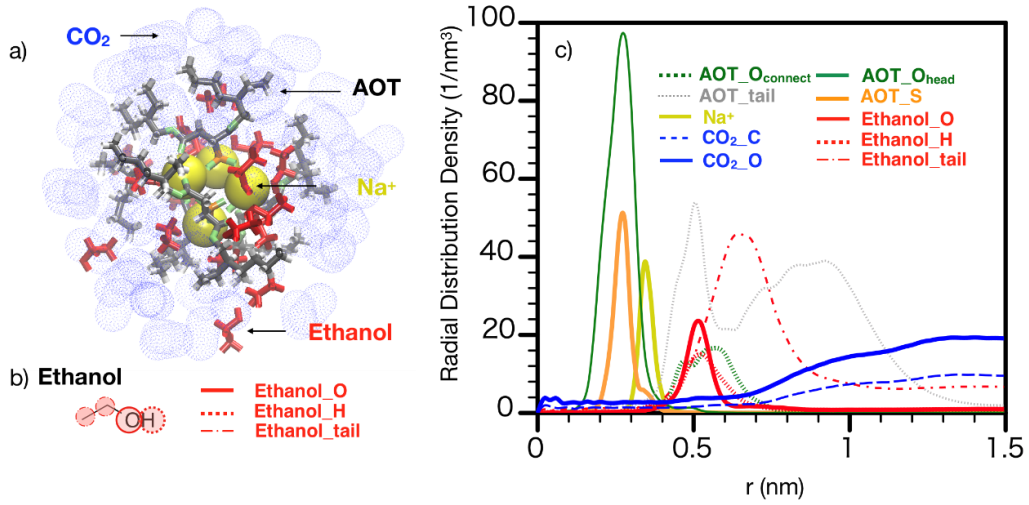

Figure 5-5 a) Snapshot of a typical 4-AOT RM in System B; b) molecular structure and its classification of ethanol; c) RDD of the functional groups around COM of Na^+ ions in the 4-AOT RM.

Further analysis is conducted to investigate the structural properties of 4-AOT RMs in System B. **Figure 5-5 a** depicts the snapshot of a typical 4-AOT RM in System B. We observe that the

Na^+ ions and AOT head groups are distributed at the center to constitute the core structure of the 4-AOT RM, surrounded by AOT tails and ethanol molecules. In contrast, CO_2 molecules are depleted from the center of RM. The RDD of the functional groups around the COM of 4 Na^+ ions in the 4-AOT RM is depicted in **Figure 5-5 c**. A single distinct peak in the RDD of Na^+ ions at ~0.35 nm indicates that the distances of the four Na^+ ions from the COM are similar. Namely, these four Na^+ ions form a tetrahedron-like structure in the 4-AOT RM. AOT_O_{head} and AOT_S functional groups as well as the Na^+ ions form the core structure, as shown in **Figures 5-5 c** and **a**. Enrichments of Ethanol_O and Ethanol_H groups are observed after AOT_O_{head}, AOT_S, and Na^+ ions, followed by Ethanol_tail group immersed in CO_2. Unlike AOT, the ethanol functional group densities converge to non-zero constant values where the distance from the COM is large (~1.5 nm), revealing that the ethanol molecules are distributed as a continuous phase in System B (*i.e.*, co-solvent). Interestingly, a small number of CO_2 molecules are distributed at the COM of Na^+ ions, while their density gradually increases and reaches a plateau as the distance increases, indicating that the CO_2 is generally depleted from the RM. The radius of this 4-AOT RM is around 1.5 nm, which is defined by the position where the AOT_tail distribution reaches zero. This value is smaller than the radius of RMs formed by AOK (a similar structure to AOT)/water/scCO_2 (~ 2.3 nm)[172], which is obtained from the experimental SANS data, while still in a reasonable range considering that there is no water core in the RMs in our study.

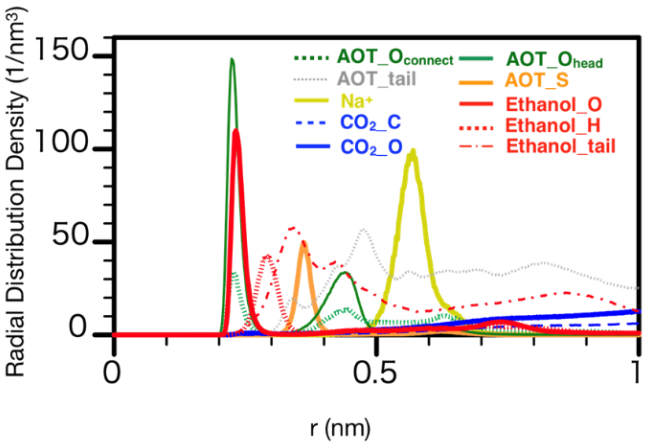

Figure 5-6 RDDs of various functional groups in AOT, CO_2, and ethanol as well as Na^+ ions around the Na^+ ions in the 4-AOT RM.

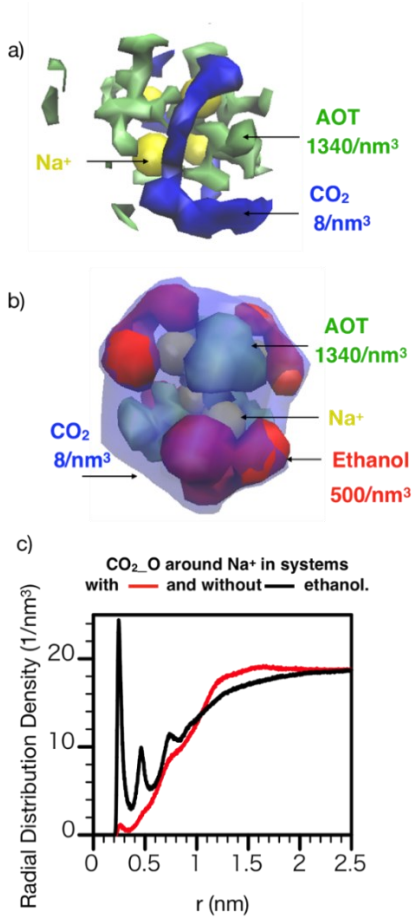

Figure 5-7 SDFs of a) AOT (1340/nm^3) and CO_2 (8/nm^3) around the end Na^+ ions in System A; b) AOT (1340/nm^3), CO_2 (8/nm^3), and ethanol (500/nm^3) around Na^+ ions in the 4-AOT RM in System B; c) RDD of CO_2_O around the end Na^+ ions in System A and the Na^+ ions in the 4-AOT RM in System B.

The functional group distributions around the Na^+ ions in the 4-AOT RM in System B are revealed in **Figure 5-6**. We do not further classify the end or intermediate Na^+ ions in the RDD calculations in System B. In addition to the polar groups in AOT (*i.e.*, AOT_$O_{connect}$, AOT_O_{head}, and AOT_S), the Ethanol_O group has a strong enrichment around the Na^+ ions as well. In contrast to System A (**Figure 5-3 c**), CO_2 is generally depleted from the Na^+ ions in System B. This is because, CO_2 molecules are replaced by ethanol molecules in the vicinity of Na^+ ions, which has

a stronger affinity to Na^+ ions. The affinity comparison is studied by calculating the PMF of CO_2 and ethanol around the Na^+ ion, as shown in **Appendix D.5**. The spatial distribution functions (SDFs), which depict the iso-density distributions of the target molecules in the three-dimensional space are depicted in **Figure 5-7**. **Figure 5-7 a** depicts the SDFs of AOT and CO_2 around the end Na^+ ions (highlighted by the blue color in **Figure 5-3 c**) in System A, while **Figure 5-7 b** represents the SDFs of AOT, CO_2, and ethanol molecules around the Na^+ ions in the 4-AOT RM in System B. The Na^+ ions are surrounded by AOT and CO_2 molecules in System A, which is in line with the functional group distributions depicted in **Figure 5-3 c**. On the other hand, the AOT and ethanol molecules occupy the inner shells around Na^+ ions, while CO_2 molecules are distributed in the outer shells in System B, which agrees well with the results shown in **Figures 5-5 a, c,** and **5-6**. Direct comparison between the RDD of CO_2_O around the Na^+ ions in System A (the end Na^+ ions) and System B (the Na^+ ions in 4-AOT RM) in **Figure 5-7 c** also confirms the high efficacy of ethanol molecules replacing the CO_2 molecules around the Na^+ ions.

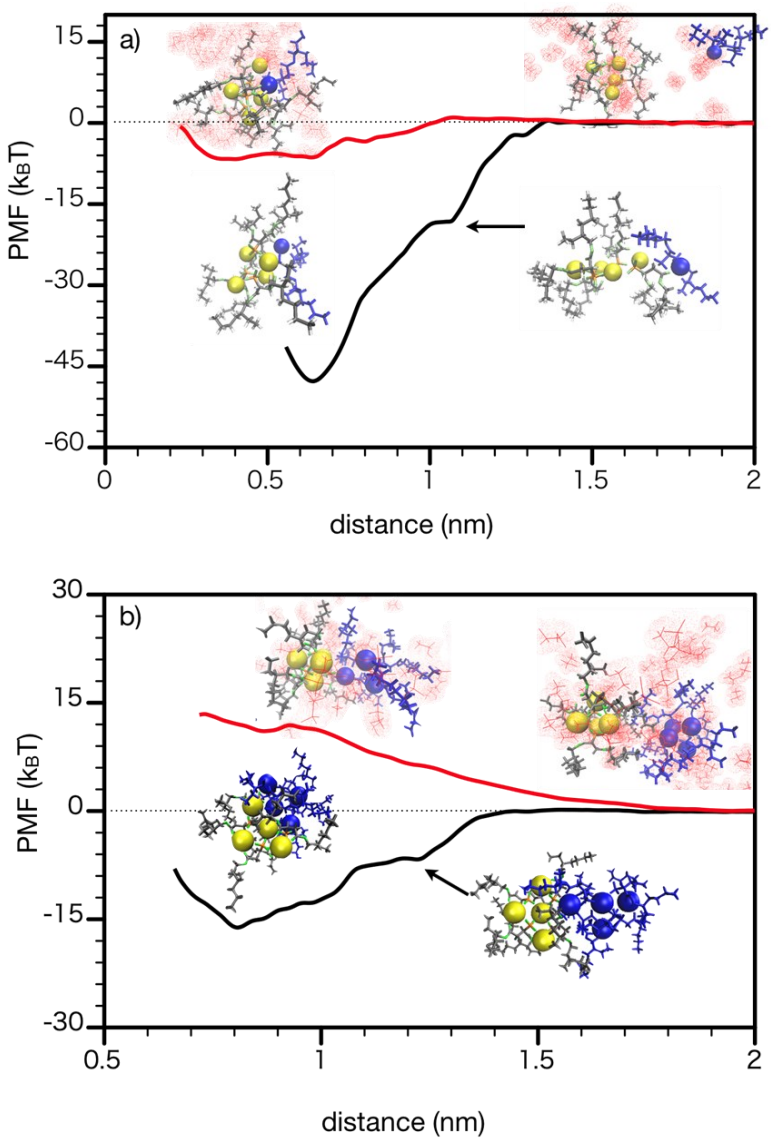

Figure 5-8 PMF between a) a 4-AOT cluster and an AOT; b) two 4-AOT clusters. Red and black lines indicate the systems with and without ethanol, respectively.

Umbrella sampling is employed to determine PMF for the systems with/without ethanol. Two different scenarios are considered: 1) one AOT (highlighted by blue color) molecule is gradually pulled out from the cluster formed by a 5-AOT cluster (Systems C and D), as shown in **Figure 5-8 a**) one 4-AOT cluster (highlighted by blue color) gradually approaches another 4-AOT cluster

(Systems E and F), as shown in **Figure 5-8 b**. The *x*-axis (the reaction coordinate) is the distance from the COM of 4 Na^+ ions in one cluster to the other. Both System C and D reveal a negative PMF when the separation distance is small, indicating that aggregation is thermodynamically favorable. Spontaneous aggregation in System C is also in line with the observation shown in **Figure 5-1**. The minimum value in the PMF is more negative in System C, indicating that the driving force for aggregation is stronger without ethanol. Although the 4-AOT cluster is the most common one in System B (*i.e.*, with ethanol), the spontaneous aggregation between one single AOT and a 4-AOT cluster can still be favorable, as shown in **Figure 5-8 a**. In fact, the clusters formed by 5 or 6 AOTs can be observed in **Figure 5-4 h**. Furthermore, the aggregation process is not always adding a single AOT to the cluster. In contrast, it can occur between two existing clusters or among a few clusters. On the other hand, the PMFs between two 4-AOT clusters with/without ethanol reveals a drastically different phenomenon: it is negative without ethanol, while positive with ethanol. This result clearly indicates that the presence of ethanol can make the aggregation of 4-AOT clusters which are the most common ones in System B thermodynamically unfavorable, while without ethanol such a cluster-cluster aggregation can occur spontaneously.

5.4 Summary

In this work, we use MD simulations to explore the role of ethanol in improving the AOT solubility and RM dispersity in $scCO_2$. We find that without ethanol, the AOT molecules spontaneously aggregate to form large rod-like RMs with the Na^+ ions and the AOT head groups at the core. This aggregation occurs when the two clusters approach each other end-to-end, rather than side-to-side. We demonstrate that this might be because the end Na^+ ions are more exposed to and solvated by CO_2 molecules, which can be readily replaced by AOT molecules. On the other hand, the system forms several small sphere-like RMs which are well dispersed in the presence of

ethanol. This result is in line with Zhang *et al*.[167], which reported that alcohols can increase the AOT dispersity and solubility in $scCO_2$. The number of AOTs in the most common cluster is 4 with its radius of around 1.5 nm. Further analysis of this typical 4-AOT RM structure suggests that ethanol molecules enrich the Na^+ ions by replacing CO_2 molecules, inhibiting further aggregation. The PMF calculations also suggest that in the presence of ethanol, the aggregation of 4-AOT RMs is thermodynamically unfavorable.

This work provides an atomic and molecular scale understanding of the surfactant (AOT) aggregation process in $scCO_2$, as well as the working mechanism of ethanol in surfactant dispersity increment. These fundamental understandings can potentially help design the surfactant formula with high "solubility" in $scCO_2$, which is highly desirable in CO_2 flooding for EOR in tight reservoirs. On the other hand, injecting the CO_2 into the reservoir, as one of the geological carbon sequestration (GCS) schemes[25-27], stores the CO_2 underground thereby reducing the CO_2 content in the atmosphere. Our work provides a theoretical foundation for an effective CO_2 utilization and storage scheme.

Chapter 6 : EFFECTS OF ALCOHOL CHAIN LENGTH ON CO_2 FOAM FLOODING, ROLE AS COSURFACTANTS

A version of this chapter will be submitted to *ACS Symposium Series* (Nan and Jin, 2022).

6.1 Introduction

CO_2 flooding has emerged as one of the most effective enhanced oil recovery (EOR) methods. In contrast to air, nitrogen, or methane, CO_2 has excellent miscibility with oil under relatively low pressures (*i.e*., low minimum miscible pressure (MMP))[21-24, 173]. In addition, CO_2 can effectively swell oil and reduce its viscosity[174, 175]. Furthermore, CO_2 injection into the underground can reduce carbon emission, while CO_2-EOR is one of the common forms of CO_2 utilization[25-28]. In practical applications, CO_2 foam flooding is often employed to prevent CO_2 fingering and/or overriding[176-179]. Foam is a mixture, formed by trapping pockets of gas in liquid or solid. In the underground porous media, foam acts as a more viscous fluid in high permeability regions than in low permeability regions, also known as selective mobility reduction (SMR)[180, 181]. SMR can smooth the front of displacement and prevent the early breakthrough caused by CO_2 fingering. In addition, foam also alleviates the gravity segregation (gas overriding), by shifting the competition between viscous and gravity forces[182].

Co-injection or alternate injection of surfactant solution and CO_2 can generate *in-situ* foam in reservoirs. CO_2 foam generation with surfactant solution (water as solvent) has been extensively investigated in both experimental and theoretical studies[176-179]. Several successful field applications have been reported as well[183-185]. Unfortunately, field experiences have shown

that the conventional foam generation with surfactant solution has some notable limitations[186]. One of the biggest drawbacks is the extensive surfactant loss due to their adsorption on reservoir rocks (especially the anionic surfactant loss in carbonate reservoirs)[186]. Simultaneously injecting surfactants dissolved in CO_2 into the reservoir, as an alternative method, has attracted much attention[167]. Experimental studies with core flooding proved that this method can generate *in-situ* foam with omnipresent water[29, 187]. Dissolving surfactants in the CO_2 phase can not only minimize the surfactant retention but also make surfactant available for foam generation wherever CO_2 is flowing, rather than relying on CO_2 flow into the same portions of formation invaded by previously-injected aqueous surfactant solution[188]. In addition, directly injecting surfactant-containing CO_2 can eliminate the alternate injections of water and CO_2, making it more convenient from an operational perspective[188].

CO_2 is usually under a supercritical state (critical temperature $T_c = 304.1$ K and critical pressure $P_c = 7.38$ MPa)[20] under CO_2 foam flooding conditions. Unfortunately, supercritical CO_2 ($scCO_2$), as an apolar solvent, barely dissolves ionic surfactants[32]. Extensive efforts have been dedicated to increasing the surfactant solubility in the $scCO_2$ phase[29, 32-42]. Among them, simply blending co-solvents (*e.g.*, alcohols) in the $scCO_2$ phase has been proven to be an effective and economically-viable method[29, 32, 38-42]. An experimental study by Zhang *et al.* [167] reported that ethanol can improve the bis(2-ethylhexyl) sulfosuccinate (AOT) solubility in $scCO_2$. Our previous simulation study[161] also demonstrated that ethanol can improve AOT and its reverse micelle dispersity in $scCO_2$. In addition, alcohols with different carbon chain lengths (C_2-C_{10}) can also increase the Triton X-45 (TX-45) solubility in $scCO_2$[38].

While alcohols are originally introduced as a co-solvent to increase the surfactant solubility in $scCO_2$, they can also function as co-surfactants to further improve foam properties. The effect of alcohols on foam (not limited to $scCO_2$ as gas phase) generation and stability have been studied both from experimental and simulation perspectives. Lower interfacial tension (IFT) is favorable to generate the foams[189]. It is also noted that foamability can be affected by the foaming strategy: shaking or air bubbling[190]. Foam stability can be attributed to several factors, IFT, surface viscosity, solution viscosity, temperature, and pressure. In general, foams with lower IFT, higher surface viscosity, higher solution viscosity, higher pressure, and lower temperature are more stable[189]. We also note that foams are not thermodynamically stable; they will collapse eventually[191]. Experimental work by Patist *et al*.[190] suggested that $C_{12}OH$ can increase water/SDS/air foamability (air bubbling through a single capillary) and foam stability (increasing bubble lifetime) Similarly, Miyashita *et al*.[192] reported that long-chain alcohol $C_{14}OH$ can increase the foam (water/SDS/air) interface stability by increasing surface viscosity. Zhang *et al*.[167] demonstrated that the foaming time of water/AOT/$scCO_2$ foam is reduced by ~ 3 times by blending ethanol with $scCO_2$. They also observed a significant increase in foam half-life time in the systems with ethanol. Molecular simulation is a powerful tool to shed light on molecular configurations at the interface (origin of different IFT and interface viscosity) and provide theoretical support for experimental observations. Domínguez *et al*.[136] reported that the SDS tail group is more orientated in the systems with $C_{12}OH$ compared to $C_{16}OH$ for well-mixed SDS and alcohol at the air/water interface, due to mismatching tail length of $C_{16}OH$ and SDS. Higher orientation would result in denser surfactant packing at the interface, which helps in decreasing IFT and increasing surface viscosity. decreasing Zhang *et al*. [167] demonstrated that ethanol can stabilize the water/AOT/$scCO_2$ interface by stabilizing the AOT tail at the interface. These works

are informative and suggestive, however, a comprehensive understanding of the alcohol tail length and concentration on the water/$scCO_2$ interfacial properties, which further affects foamability and foam stability is still lacking. This is particularly true for the effect of alcohols on the double chain surfactant, AOT. In addition to alcohol's effect on interfacial properties, their partitioning in different phases (water, interface region, and $scCO_2$ phases) also needs to be considered in industrial applications. In $scCO_2$ foam flooding, in particular, alcohols with less partitioning in the water phase would preferable. Because their loss in the abundant amount of reservoir water would cause material retention. It is noted that C_2-C_6OH are soluble in pure $scCO_2$under 333K 200 bar[193, 194]. C_2OH and C_3OH are soluble in water under ambient conditions. Alcohol solubility in pure $scCO_2$ and pure water decreases as tail length increases[195, 196]. In the meantime, the existence of water also might affect alcohol solubility in the $scCO_2$ phase[197].

Herein, we use molecular dynamics (MD) simulations to study the effect of alcohol tail length and concentration on water/AOT/$scCO_2$ interfacial properties at 333 K and 200 bar. AOT, as a popular surfactant that can be dissolved in $scCO_2$ with alcohols[29, 167], is chosen as the primary surfactant. Various alcohols with different tail lengths (C_2OH, C_3OH, C_4OH, C_8OH, C_{12}OH, and C_{16}OH) with varying concentrations are used. We first explore alcohol partitioning in different phases (water, interface region, and $scCO_2$) by fixing their concentration in the $scCO_2$ phase. We find that alcohol tail length significantly affects alcohol partitioning in the water phase. Alcohols with shorter tail lengths have a higher tendency to diffuse into the water phase, causing a severe chemical loss in actual field applications. Important interfacial properties, including interfacial tension (IFT), interfacial diffusion, and orientation parameters of surfactants and alcohols are investigated as well. We demonstrate that the alcohol tail length has a negligible effect on IFT reduction for a given alcohol concentration in the $scCO_2$ phase under low alcohol concentration

conditions. Nevertheless, as alcohol concentration further increases, the long-chain alcohols easily reach the inflection point in the IFT curve, resulting in higher lowest IFT. This might be attributed to the strong tail-tail interactions in long-chain alcohols resulting in narrower surfactant and cosurfactant distribution in the *z*- direction, making the interface saturated (reason for the inflection point) under lower concentration. The short-chain alcohols (C_2OH and C_3OH) slightly disorientate or have a negligible effect on the AOT tail as their concentration increases, while the long-chain alcohols (C_8OH and $C_{16}OH$) can orientate the AOT tail more perpendicular to the interface. Our work should provide a theoretical foundation and guidance for surfactant formula design for CO_2 foam flooding.

The remainder of this paper is organized as follows. In **Computational Methodology**, we introduce simulation methods and define molecular models. In **Result and Discussion**, we first discuss the alcohol tail length on their partitioning in various phases. Then, the effect of alcohol tail length and concentration on water/scCO_2 interfacial properties as well as surfactant and alcohol molecular configurations are studied. In **Conclusion**, we summarize key findings and discuss potential implications.

6.2 Computational Methodology

6.2.1 Simulation System

A sandwich-like double-layer film module is employed as in our previous studies[56, 64]: one ~10 nm water slab sandwiched between two ~ 15 nm CO_2 slabs, as shown in **Figure 6-1**. The simulation box sizes in the *x*- and *y*-directions are set as 5 nm, while the dimension in the *z*-directions varies from ~40 nm to ~45 nm depending on the systems. AOT concentration at the interface is fixed as 0.2/nm^2, lower than its saturation adsorption concentration (1.2/nm^2 under

298.15 K[198]). In all systems, AOT, Na^+, H_2O, and CO_2 molecule numbers are identical, which are 10, 10, 8086, and 8000, respectively. A series of systems with various alcohol concentrations of different tail lengths (C_2OH, C_3OH, C_4OH, C_8OH, $C_{12}OH$, and $C_{16}OH$) are designed to comprehensively study the alcohol chain length effect. The number of alcohol molecules and corresponding alcohol concentrations in $scCO_2$ phase are listed in **Table 6-1**. We define the system name by alcohol specie and alcohol concentration in $scCO_2$ phase. For example, a system containing 87 ethanol molecules with alcohol concentration in scCO2 phase of 0.035/nm^3 is defined as AOT10_C_2OH (0.035); a system containing 48 hexadecane-1-ol molecules is defined as AOT10_$C_{16}OH$ (0.042). Alcohols can distribute in $scCO_2$, interface, and water phases. Two sets of systems (highlighted with italic and underline (*0.038 ± 0.003 /nm³*) and bold italic underline (***0.282 ± 0.014 /nm³***) in **Table 6-1**) with similar alcohol concentrations in CO_2 phases are explicitly studied for a better comparison of different tail length alcohols. AOT molecules are separated into two interfaces, considering their high barrier to relocating between the phases. Alcohols are originally set in the $scCO_2$ phase, in line with operational protocol, in which alcohols are introduced from the $scCO_2$ phase. The initial configuration for system AOT10_C_2OH (0.035) is presented in **Appendix E.1**, as a representative. Three-dimensional (3-D) periodic boundary conditions (PBCs) are applied in all cases. We employ the CHARMM forcefield[50, 168] for AOT and alcohol molecules (**Appendix D.1**), the rigid EPM2[169] for CO_2, and modified TIP3P for water molecules. EPM2 and TIP3P can well reproduce condensed phase density of pure $scCO_2$ and water at 333 K and 200 bar, as shown in **Appendix E.2**. Nevertheless, the water concentration in the $scCO_2$ phase and the IFT between water and $scCO_2$ slightly deviates from experimental results. Such deviation might be attributed to the fact that water force fields are developed for polar water solution, while CO_2 dipole moment is much smaller than water[199]. In fact, some efforts

have been dedicated to adjusting the CO_2 (EPM2)-water (SPC/E) LJ potentials to match the water solubility and IFT results from experimental measurement[199]. We still choose forcefield combinations described above according to the following considerations: First, the focus of this study is on the effect of alcohol on interfacial properties, not the water solubility in the CO_2 phase. The water concentration in the CO_2 phase is extremely small, which has a negligible effect on interfacial properties. Second, switching the water force field from the modified TIP3P to SPC/E might affect surfactant-water interaction, while the CHARMM forcefield is designed to be compatible with the modified TIP3P. Despite some limitations on the forcefield combinations, we believe that they can still reliably capture interfacial properties of water/scCO_2 with AOT and alcohols.

Table 6-1 Number of alcohol molecules and corresponding alcohol concentration in the $scCO_2$ phase in each system*

C_2OH		C_3OH		C_4OH		C_8OH		$C_{12}OH$		$C_{16}OH$	
#of Alcohol	Alcohol concentration in $scCO_2$ ($1/nm^3$)	#of Alcohol	Alcohol concentration in $scCO_2$ ($1/nm^3$)	#of Alcohol	Alcohol concentration in $scCO_2$ ($1/nm^3$)	#of Alcohol	Alcohol concentration in $scCO_2$ ($1/nm^3$)	#of Alcohol	Alcohol concentration in $scCO_2$ ($1/nm^3$)	#of Alcohol	Alcohol concentration in $scCO_2$ ($1/nm^3$)
0	0	50	0.031	*50*	*0.039*	*48*	*0.038*	*48*	*0.039*	*48*	*0.042*
50	0.020	*55*	*0.038*	100	0.082	68	0.059	71	0.057	71	0.052
87	*0.035*	100	0.063	200	0.184	100	0.085	100	0.079	100	0.079
100	0.043	150	0.109	***319***	***0.288***	200	0.189	200	0.180	200	0.169
150	0.059	200	0.146	500	0.479	***309***	***0.305***	***309***	***0.281***	***309***	***0.264***
200	0.089	***364***	***0.288***	800	0.756	500	0.480	500	0.423		
300	0.131	500	0.399	1000	0.931						
500	0.226	800	0.682								
578	***0.268***	1000	0.882								
800	0.399	1500	1.306								
1000	0.625										
1500	1.110										

* Systems with similar alcohol concentrations in scCO2 phases are highlighted with italic and underline (*0.038 ± 0.003 /nm³*) and bold italic underline (***0.282 ± 0.014 /nm³***).

6.2.2 Simulation Details

All simulations are conducted using GROMACS (version 2019.1)[103] software package. We first minimize the system energy using the steepest descent algorithm until the maximum force is less than $1000\ kJ \cdot mol^{-1} \cdot nm^{-1}$. We conduct 120-ns NP_zT ensemble simulations, with 2 fs time steps to integrate equations of motions using the Leap-Frog algorithm[104]. Nosé-Hoover[106] thermostat and the Parrinello-Rahman[108] barostat with relaxation times of 0.1 and 0.2 ps, respectively, are employed for the NP_zT ensemble. The last 60 ns trajectories are saved every 500 steps (1 ps) for further analysis.

LJ potential and electrostatic interaction are truncated at a cut-off distance of 1.2 nm in the real space. The long-range electrostatic interaction is calculated using the particle-mesh Ewald (PME) method[109] beyond the real space. The long-range dispersion correction is applied for energy and pressure. LJ interactions between the unlike atoms, which are separated by more than three bonds or in different molecules, are obtained from the conventional Lorentz-Berthelot[110, 111] mixing rules. SETTLE[112] algorithm is employed to constrain the bond length and angle of H_2O and the LINCS[113] algorithm is used to constrain the H-X (X for any atom) bond length for other molecules. All snapshots are presented by the Visual Molecular Dynamics (VMD) package[114].

6.3 Results and Discussion

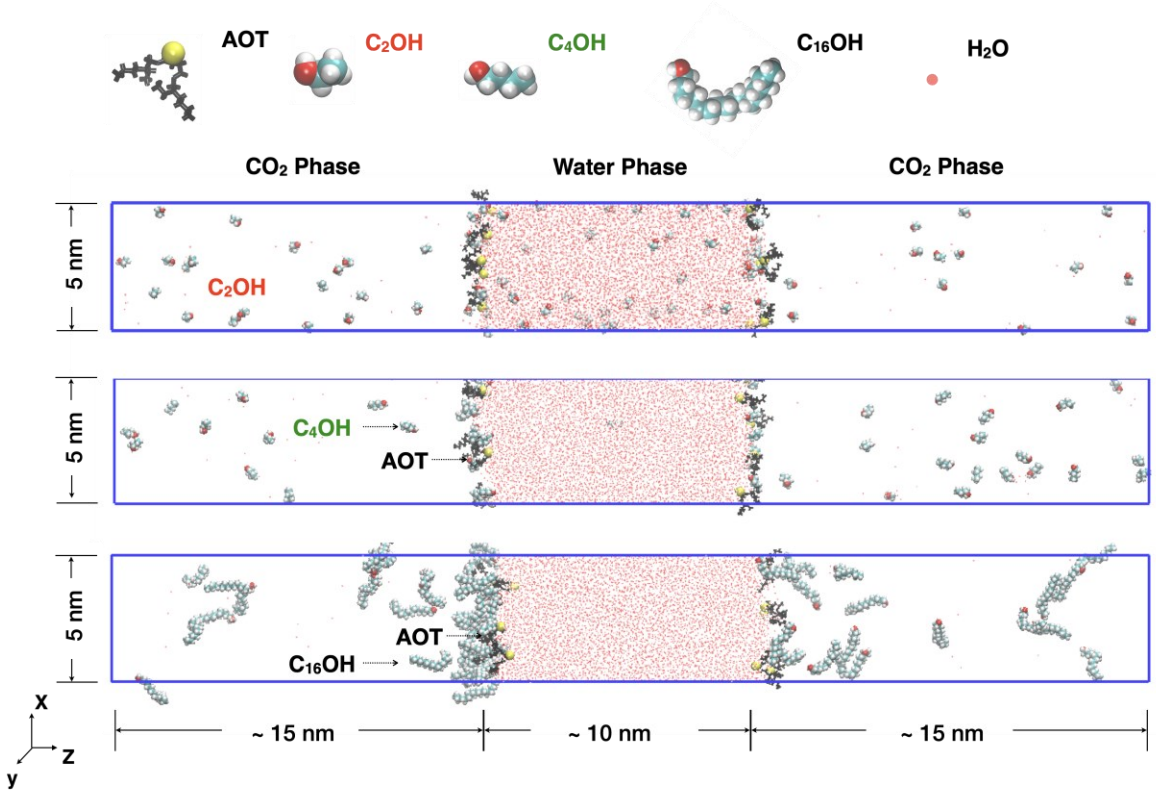

Figure 6-1 Molecular configurations at equilibrium in a) system AOT10_C_2OH (0.035); b) system AOT10_C_4OH (0.039); c) AOT10_$C_{16}OH$ (0.042). CO_2 molecules are not shown for clarity. The periodic boundaries are depicted by the blue rectangular. Values in brackets in the system names are the alcohol concentration in the scCO_2 phase with a unit of 1/nm^3.

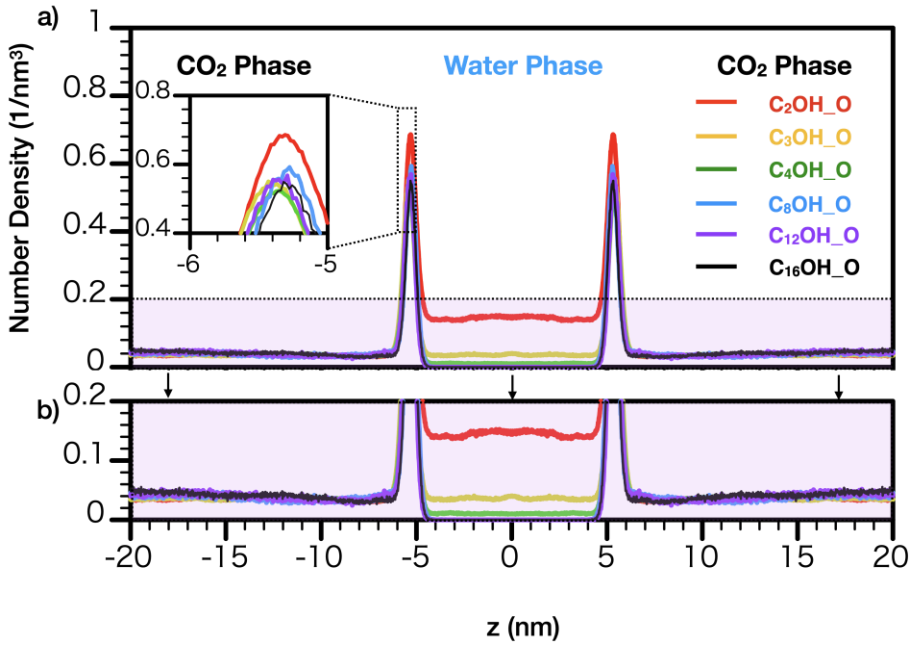

Figure 6-2 a) Number density distribution of Alcohol_O in systems AOT10_C_2OH (0.035), AOT10_C_3OH (0.038), AOT10_C_4OH (0.039), AOT10_C_8OH (0.038), AOT10_C_{12}OH (0.039), and AOT10_C_{16}OH (0.042). b) The enlargement of Figure 6-2 a. Values in brackets in the system names are the alcohol concentration in the scCO_2 phase with a unit of 1/nm^3.

Figures 6-1 a, b, and **c** depict the snapshots of systems AOT10_C_2OH (0.035), AOT10_C_4OH (0.039), and AOT10_C_{16}OH (0.042) after 120-ns NP_zT run, respectively. CO_2 molecules are omitted from snapshots for a better observation. All AOT molecules are distributed at the water/scCO_2 interfaces, with their head groups pointing toward the water phase and tail groups immersed in the scCO_2 phase. Alcohols can distribute in water (not necessarily for long-chain alcohols), interface, and scCO_2 phases. Their partitioning in various phases is dependent on the alcohol chain length. C_2OH concentration in the water phase is much higher than that of C_4OH and C_{16}OH. It is in line with the fact that alcohol affinity to water decreases as their tail length increases[196]. In **Figure 6-2**, we present the Alcohol_O (O element in alcohols) density

distributions in the *z*-direction for various alcohols (systems AOT10_C_2OH (0.035), AOT10_C_3OH (0.038), AOT10_C_4OH (0.039), AOT10_C_8OH (0.038), AOT10_C_{12}OH (0.039), and AOT10_C_{16}OH (0.042)) with a similar alcohol concentration in $scCO_2$ phase (0.038 ± 0.003 /nm^3). For all systems, alcohols are mainly distributed at the water/$scCO_2$ interfaces. Among all alcohols, C_2OH has the highest peak at the interfaces. The differences in peak values for other alcohols are negligible as highlighted in **Figure 6-2 a**. The short- and medium-chain alcohols (C_2OH, C_3OH, and C_4OH), have considerable distributions in the water phase, while the long-chain alcohols (C_8OH, C_{12}OH, and C_{16}OH) barely diffuse into the water phase. This result is in line with the snapshots in **Figure 6-1**. We note that the alcohol adsorption and desorption at the interface region is a dynamic process. Alcohol number density at the interface fluctuates around a certain value for the trajectories from 60 ns to 120 ns (**Appendix E.3**).

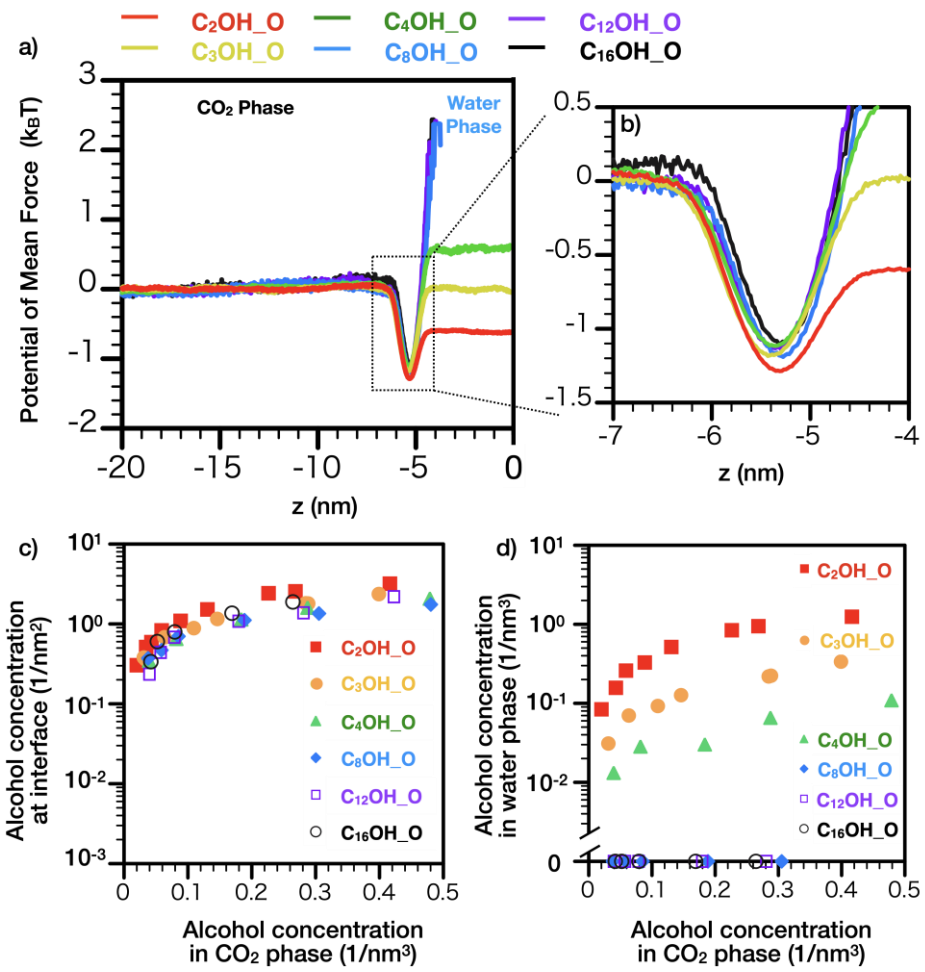

Figure 6-3 a) PMF distributions of Alcohol_O in systems AOT10_C_2OH (0.035), AOT10_C_3OH (0.038), AOT10_C_4OH (0.039), AOT10_C_8OH (0.038), AOT10_C_{12}OH (0.039), and AOT10_C_{16}OH (0.042); b) their enlargements in the corresponding systems. Alcohol concentration c) at interface d) in the water phase as their concentration in the CO_2 phase increases. Values in brackets in the system name are the alcohol concentration in the scCO_2 phase with a unit of 1/nm^3.

As discussed in the introduction part, injected chemicals (alcohol, surfactant, and scCO_2) meet the formation water and generate *in-situ* foam in the practical applications of alcohol-assisted scCO_2 foam flooding. Alcohol partitioning in different phases (water, interface, or scCO_2) is of great importance from a chemical-recycling perspective. Alcohols in the scCO_2 phase can be

recycled from the production well, while that dissolved in the water phase might cause a permanent loss in the reservoirs. Considering abundant formation water in the underground reservoirs, alcohol loss in the water phase is not only economically inviable but also contaminates (except for environmentally-benign ethanol) the groundwater. Therefore, alcohols with a higher partitioning in the $scCO_2$ phase and at the interfaces are preferable. The potential of mean force (PMF) is employed to study the alcohol partitioning in various phases as depicted in **Figure 6-3**, which is given as[59]

$$W(z) = -k_B T \ln \frac{\rho(z)}{\rho_{bulk}} \tag{6-1}$$

where k_B is the Boltzman constant and T is the system temperature; $\rho(z)$ and ρ_{bulk} are the local density and bulk density of the Alcohol_O in the $scCO_2$ phase, respectively. The left half side of the PMF curve is studied as representative. A lower PMF value indicates the higher tendency of a molecule to distribute at a certain position. From the CO_2 phase to the water phase, the PMF value first decreases (approaching the interface region) and then increases (in the water phase) for all alcohols. A local minimum is observed at z ~ -5.5 nm (**Figure 6-3 b**), where are the contact of water and $scCO_2$ phase (interface region). In line with the result from the density profile (**Figure 6-2**), where alcohols are priorly distributed at the interface. The PMF value in the water phase is lower than that in the $scCO_2$ phase in system AOT10_C_2OH (0.035) system. Indicating ethanol prefers to distribute in the water phase compared to the $scCO_2$ phase. C_3OH (propanol) possesses a similar tendency to distribute in the water and $scCO_2$ phases. The barrier to transmitting from the interface region to the water phase further increases, as alcohol tail length increases. The PMF value for the long-chain alcohols (C_8OH, C_{12}OH, and C_{16}OH) in the water phase is missing because they barely transmit to the water phase, which made it difficult to calculate PMF from the

density profile. A more intuitive observation of alcohol partitioning in the interface region and water phase under varying alcohol concentrations in the $scCO_2$ phase is represented in **Figures 6-3 c** and **d**. **Figure 6-3 c** illustrates alcohol concentrations in the interface region. The interface region is defined as the region in between where $scCO_2$ and water concentration are reduced to 90% of their respective bulk concentration (see **Appendix E.4**). This definition is also known as the 90-90 criteria. The alcohol concentration at the interface increases as their concentration in the CO_2 phase increases for all systems as shown in **Figure 6-3 c**. Alcohol tail length has a negligible effect on their partitioning at the interface when the alcohol concentration in the $scCO_2$ phase is fixed. On the other hand, alcohol tail length has a significant effect on alcohol participation in the water phase, as shown in **Figure 6-3 d**. The concentration of C_2OH in the water phase is about 1 order magnitude higher than that of C_4OH under certain alcohol concentrations in the $scCO_2$ phase. In the meantime, long-chain alcohols (C_8OH, $C_{12}OH$, and $C_{16}OH$) concentration in the water phase is around $0/nm^3$. In conclusion, from a material retention perspective, longer chain alcohols (C_nOH, $n \geq 4$) with less portioning in the water phase are more sounding for real industrial applications.

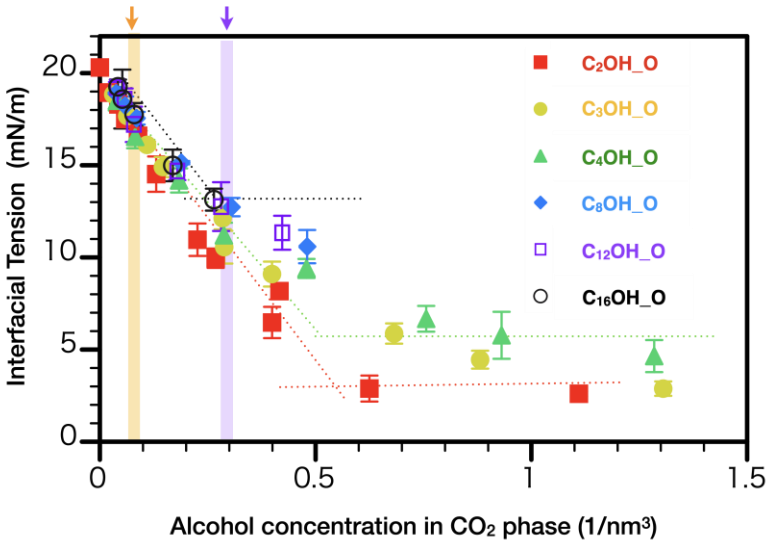

Figure 6-4 IFT of water/scCO$_2$ interface with varying alcohol concentration systems. The dotted lines are for eye guidance. Orange and purple sticks highlight the regions with alcohol concentration in the CO$_2$ phase with 0.038 ± 0.003 /nm^3 and 0.282 ± 0.014 /nm^3, respectively.

The ability to generate foams and foam stability are also important indexes in designing scCO$_2$ foam flooding. In general, lower IFT is preferred to generate and stabilize the foam. **Figure 6-4** illustrates water/AOT/scCO$_2$ IFT changes as alcohol concentration in scCO$_2$ increases with varying alcohol systems. The formula to calculate IFT is given in **Chapter 1**, **Section 1.4.4.3**. Overall, all alcohols can stand at the interface region (**Figure 6-2**), and decrease the IFT, as shown in **Figure 6-4**. The IFT decreases as alcohol concentrations in the scCO$_2$ phase increase. Under relatively low alcohol concentrations (before reaching the inflection point in the IFT curve), different tail length alcohols have a similar ability in decreasing IFT. This might be because alcohol adsorption at the interface is similar for different tail length alcohols under the same concentration in the scCO$_2$ phase, as shown in **Figure 6-3 c**. IFT curves reach the inflection point (which determines the lowest available IFT) as the alcohol concentration in the scCO$_2$ phase further increases. Longer chain alcohols reach inflection points under lower alcohol concentration in the

$scCO_2$ phase, resulting in higher lowest available IFT, correspondingly. For example, the inflection point of C_2OH (ethanol) is observed when an alcohol concentration is ~ 0.65 nm^3 in the $scCO_2$ phase, having the lowest IFT of ~ 3 mN/m. On the other hand, for long-chain $C_{16}OH$, the inflection point occurred at ~ 0.3 nm^3, with the lowest IFT of ~ 13 mN/m. This result suggests that for the application with lower alcohol concentration in $scCO_2 < 0.3$ nm^3, all alcohols studied in the current work (C_2-$C_{16}OH$) have similar effects in reducing IFT. However, for the systems that require higher alcohol concentration, lower chain alcohols might be beneficial, since they can further reduce IFT. It is also noted that the above-stated discussion is based on the calculation under 333 K and 200 bar. The inflection points might be different under other temperature and pressure conditions. Therefore, explicit studies are recommended for real applications.

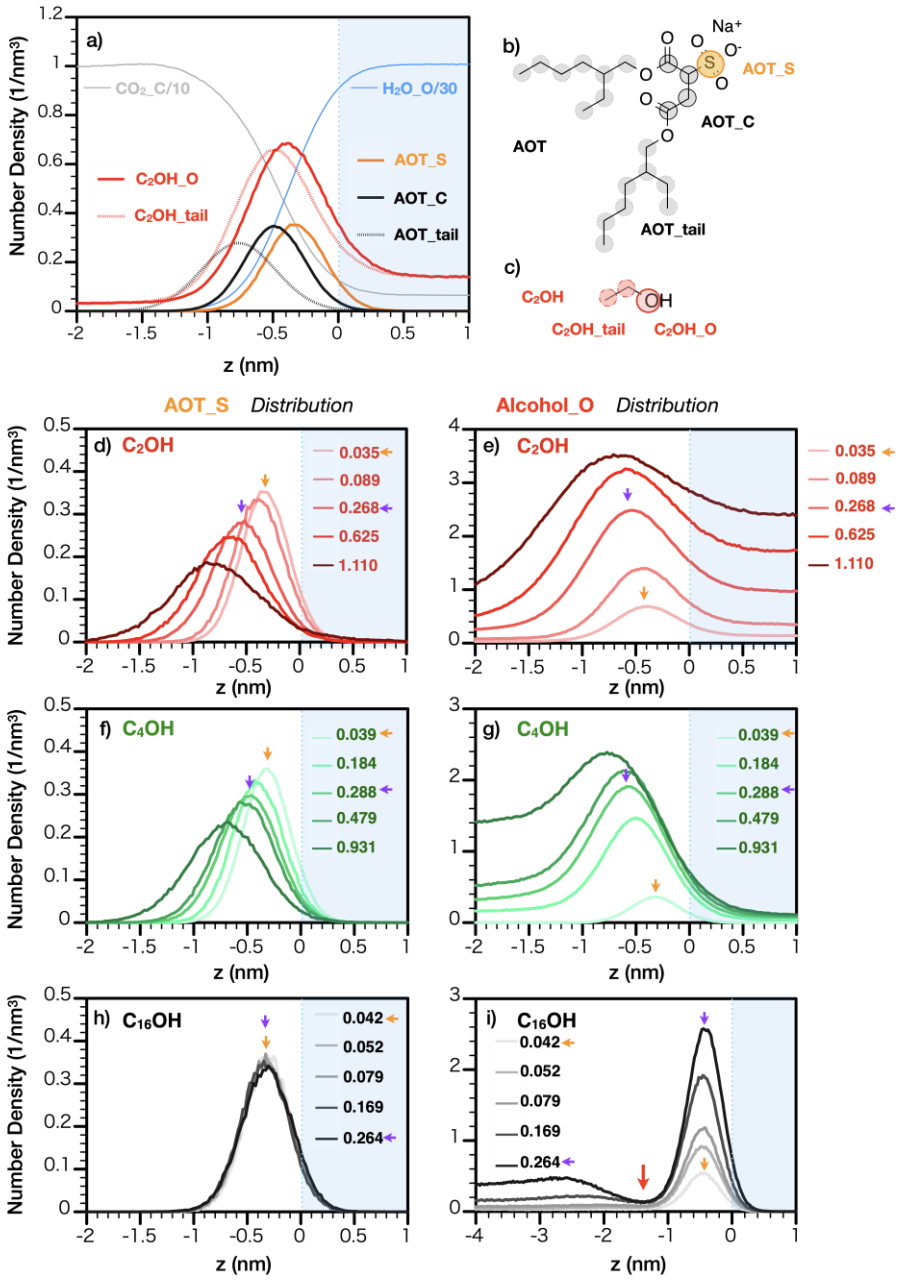

Figure 6-5 a) Functional group distribution in system AOT10_C_2OH (0.038). Molecular structure and definitions for functional groups for b) AOT and c) C_2OH. AOT_S functional group distribution with varying alcohol concentrations for systems containing d) C_2OH; f) C_4OH; h) $C_{16}OH$. Alcohol_O functional group distribution with varying alcohol concentrations for systems containing e) C_2OH; g) C_4OH; i) $C_{16}OH$. The Blue dotted line represents the contact between water and the interface region. The water phase is colored with light blue color. In figures d-i) deeper

color indicates higher alcohol concentration; values after labels are the alcohol concentration in the $scCO_2$ phase.

The inflection point from IFT is related to the molecular saturation at the interface. Before going further discussion, we first chose system AOT10_ C_2OH (0.035) as a representative to provide a general understanding of functional group distributions in **Figure 6-5 a**. AOT and C_2OH molecules are classified into several functional groups (AOT_S, AOT_C, AOT_tail, C_2OH _O, and C_2OH _tail) based on their affinity to water and chemical environment, (see **Figures 6-5 b** and **c**). AOT, C_2OH, H_2O, and CO_2 functional group distributions are shown in **Figure 6-5 a**. For a better illustration, density profiles of H_2O_O (oxygen element from water) and CO_2_C (carbon element from CO_2) are reduced by 30 and 10 times, respectively. The position of water density reduced to 90% of its respective bulk density is used to define the contact between the water phase and interface region. We artificially set the origin of the *z*- axis as the contact of the water phase and interface region (highlighted using blue dashed lines) and colored the water phase using light blue. Overall, water and CO_2 molecules are repelled from the interface; AOT and ethanol molecules are mainly distributed at the interface. Both AOT and alcohol groups are arranged with the head group towards the water phase and the tail group penetrating the CO_2 phase. C_2OH_O group distributes slightly after that of the AOT_S group.

In the rest of **Figure 6-5** (**Figures 6-5 d-i**), we use AOT_S and Alcohol_O distribution to study the effect of alcohol tail length and concentration on AOT and alcohol distribution. We chose short- (C_2OH), mid- (C_4OH), and long- ($C_{16}OH$) chain alcohols, as representatives for further study. **Figures 6-5 e**, **g**, and **i** illustrate the Alcohol_O distribution in systems containing C_2OH, C_4OH, and $C_{16}OH$, respectively. The deeper color indicates higher alcohol concentration, numbers after labels are the number of alcohols in the system. The Alcohol_O peaks intensity increase as

the number of alcohols increases. As C_2OH concentration increased, C_2OH _O density curve became wider and gradually shifted away from the water phase. A wide peak shape from the density profile indicates broad distribution in the *z*-direction. This result indicates that C_2OH can expand its distribution in the z- direction when the *x*-*y* plane is crowded. In addition, C_2OH density in the water and $scCO_2$ phase increases as their concentration in the system increase. In line with the previous discussion on the high participation of C_2OH in the water phase in **Figure 6-3**. A similar trend is observed in the systems containing C_4OH (see **Figure 6-5 g**). Peak from C_4OH_O density profile became wider and shifted away from water phase as C_4OH concentration increased. Different from C_2OH, the C_4OH molecules' density in the water phase is much lower. It is interesting to find that the $C_{16}OH$_O density distribution is entirely different from C_2OH_O and C_4OH_O distribution, as shown in **Figure 6-5 i**. Increasing $C_{16}OH$ concentration increases peak intensity, without affecting peak width, which suggests $C_{16}OH$ is not able to expand its distribution in the *z*- direction. This might be the main reason for reaching the inflection point under lower alcohol concentration in $C_{16}OH$-containing systems in **Figure 6-4**. A local minimum, highlighted using the red arrow in **Figure 6-5 i**, is observed in system AOT10_ $C_{16}OH$ (0.364). This local minimum might be caused by the dense space occupation of the $C_{16}OH$_tail group, which supplanted $C_{16}OH$_O from further approaching the water phase. The snapshot of system AOT10_ $C_{16}OH$ (0.364) in the *y*-*z* plane (**Figure 6-8 c**) clearly shows low $C_{16}OH$_O distribution where high dense of $C_{16}OH$ tail molecules is distributed. **Figures 6-5 d**, **f**, and **h** depict the AOT_S distribution in systems containing C_2OH, C_4OH, and $C_{16}OH$, respectively. In systems containing C_2OH and C_4OH, AOT_S functional group distribution in the *z*-direction became broader as alcohol concentration increased, as shown in **Figures 6-5 d** and **f**. In addition, peak positions gradually shifted away from the water phase as alcohol concentration increased. In contrast, alcohol

concentration has a negligible effect on the AOT_S functional group distribution in $C_{16}OH$-containing systems. Namely, $C_{16}OH$ barely affects AOT distribution at the interface region.

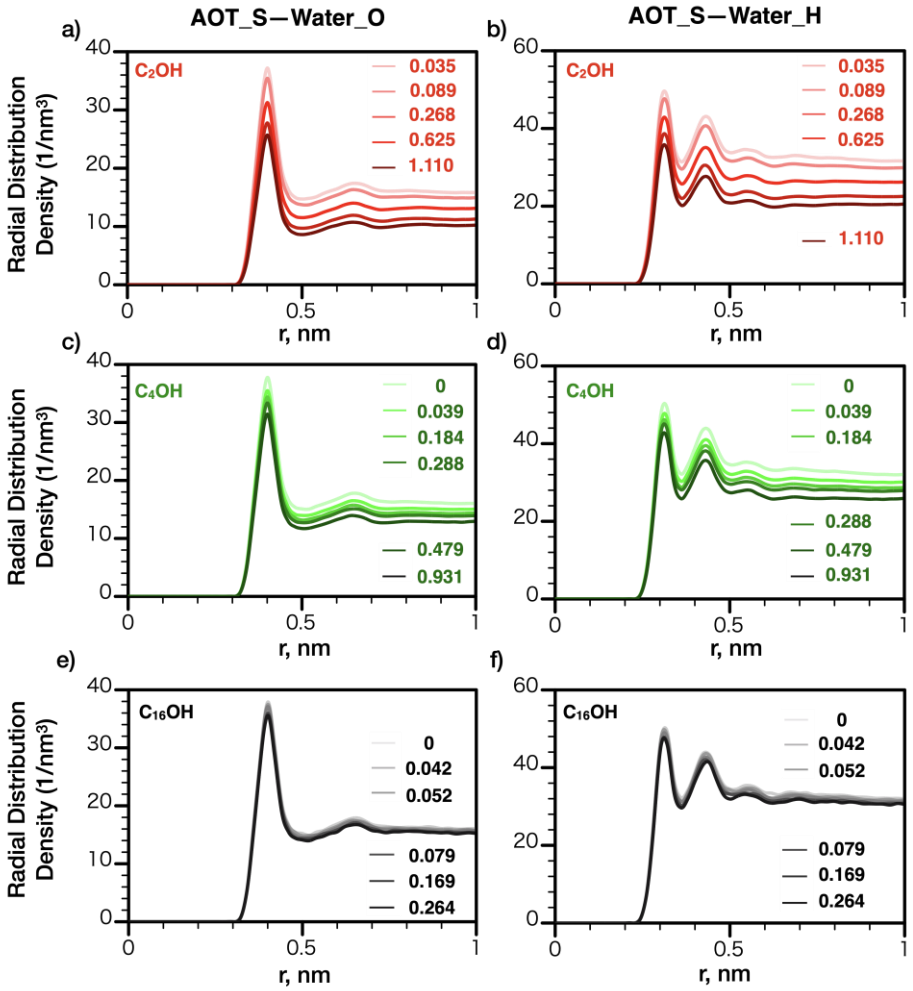

Figure 6-6 Radial distribution densities (RDDs) of AOT_S-Water_O with varying alcohol concentrations for systems containing a) C_2OH; c) C_4OH; e) $C_{16}OH$. Radial distribution densities (RDDs) of AOT_S-Water_H with varying alcohol concentrations for systems containing b) C_2OH; d) C_4OH; f) $C_{16}OH$. The deeper color indicates higher alcohol concentration; values after labels are the alcohol concentration in the $scCO_2$ phase.

AOT_S functional group distribution at the interface further affects their hydration structure. Radial distribution densities (RDDs) of H_2O_O and H_2O_H around AOT_S are shown in **Figure**

6-6. Similar to **Figure 6-5**, we chose C_2OH, C_4OH, and $C_{16}OH$, as representatives for further discussion. The deeper color indicates higher alcohol concentration. RDD shapes are similar for all alcohols with varying concentrations. Peak intensity from both H_2O_O-AOT_S and H_2O_H-AOT_S RDDs decreased as C_2OH concentration in the system increased, as shown in **Figures 6-6 a** and **b**. A similar trend is observed in systems containing C_4OH (see **Figures 6-6 c** and **d**). The decrement of water distribution around AOT_S is because the AOT_S functional group is repelled from the water phase as discussed in **Figures 6-5 d** and **f**. On the other hand, $C_{16}OH$ concentration barely affects the hydration intensity around AOT_S, as shown in **Figures 6-6 e** and **f**. This result is expected from previous observation in density profile, which suggested $C_{16}OH$ barely affects AOT_S distribution at the interface region in **Figure 6-5 h**.

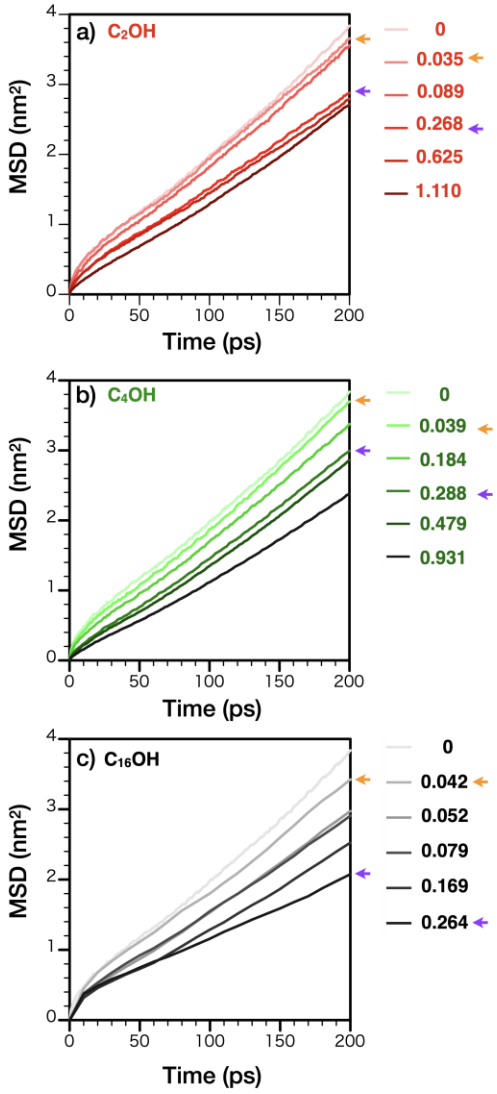

Figure 6-7 Mean squared displacement (MSD) of AOT with varying alcohol concentrations for systems containing a) C_2OH; b) C_4OH; c) $C_{16}OH$. The deeper color indicates higher alcohol concentration; values after labels are the alcohol concentration in the $scCO_2$ phase. Orange and purple arrows highlight the systems with alcohol concentration in the CO_2 phase with 0.038 ± 0.003 /nm^3 and 0.282 ± 0.014 /nm^3, respectively.

Other than IFT, AOT, and alcohol distribution in the *z*-direction, and AOT_S hydration structure, alcohols also affect the surfactant diffusion, which might further influence the foam stability. **Figures 6-7 a-c** depict the mean squared displacement (MSD) of the AOT_S functional

group by time for systems containing C_2OH, C_4OH, and $C_{16}OH$ with varying alcohol concentrations. The deeper color indicates higher alcohol concentration. In all the systems, MSD decreases as alcohol concentration increases, indicating alcohol obstacles to AOT diffusion. Such an obstacle effect increases as alcohol concentration increases. Systems with similar alcohol concentrations in the $scCO_2$ phase are highlighted using orange (systems: AOT10_ C_2OH (0.035), AOT10_ C_4OH (0.039), and AOT10_ $C_{16}OH$ (0.042)) and purple (systems: AOT10_ C_2OH (0.268), AOT10_ C_4OH (0.288), and AOT10_ $C_{16}OH$ (0.264)) arrows, respectively, for a better comparison. C_2OH and C_4OH have a similar effect in decreasing AOT MSD, while the $C_{16}OH$ has a more significant effect on MSD decrement. This result immediately suggests stronger tail-tail interaction between $C_{16}OH$ and AOT than that of short-chain alcohols. Snapshot in Figures 6-8 e and f also shows high dense of $C_{16}OH$_tail distribution around AOT molecules in system AOT10_ $C_{16}OH$ (0.264). In contrast, C_2OH_tail and C_4OH_tail distribution are relatively low in systems AOT10_ C_2OH (0.268) and AOT10_ $C_{16}OH$ (0.264), as depicted in Figures 6-8 a-d.

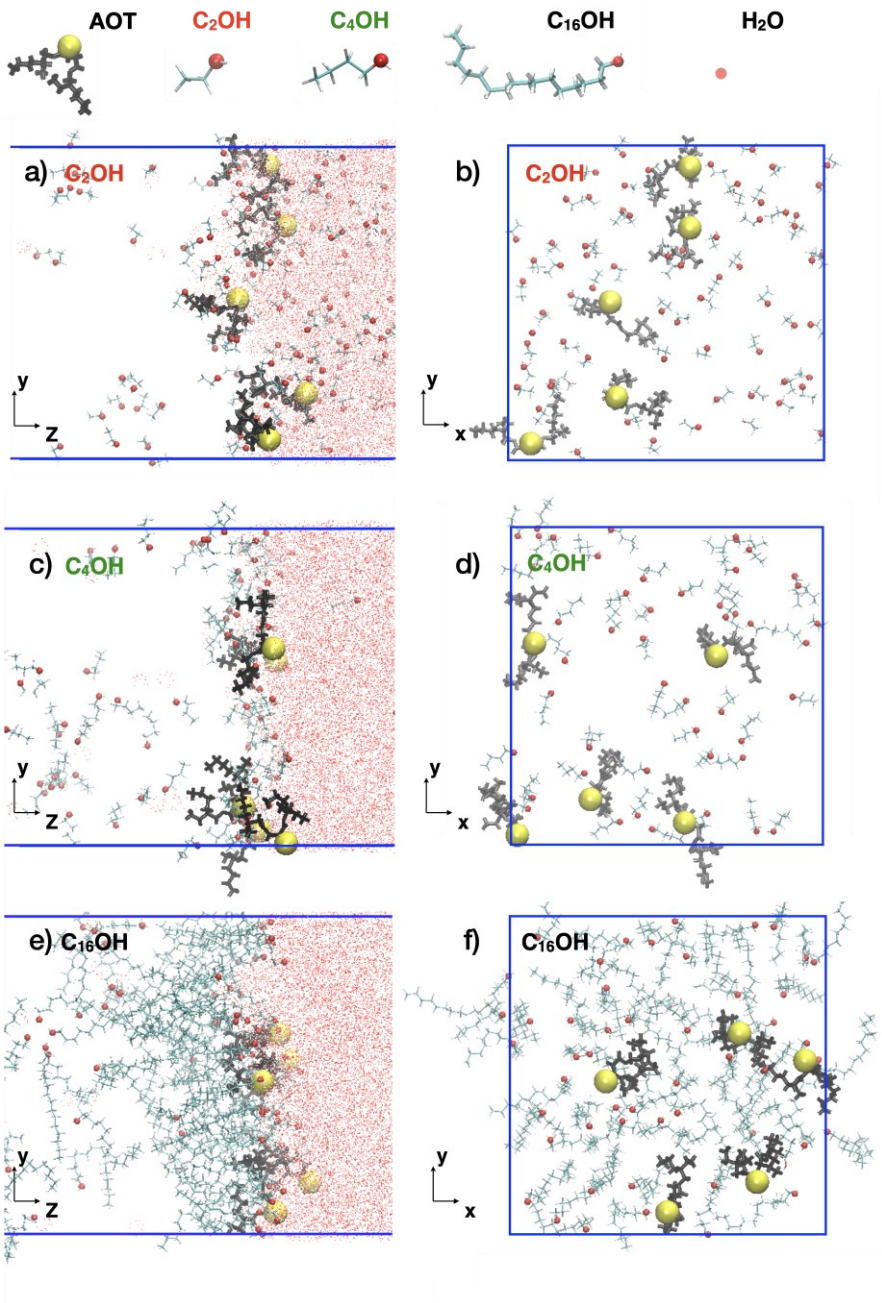

Figure 6-8 Snapshots of the *y-z* plane of systems a) AOT10_C_2OH (0.268); b) AOT10_C_4OH (0.288); c) AOT10_$C_{16}OH$ (0.264). Snapshots of the *x-y* plane of systems a) AOT10_C_2OH (0.268); b) AOT10_C_4OH (0.288); c) AOT10_$C_{16}OH$ (0.264). PBCs are depicted using blue colors. Values in brackets in the system name are the alcohol concentration in the $scCO_2$ phase with a unit of $1/nm^3$.

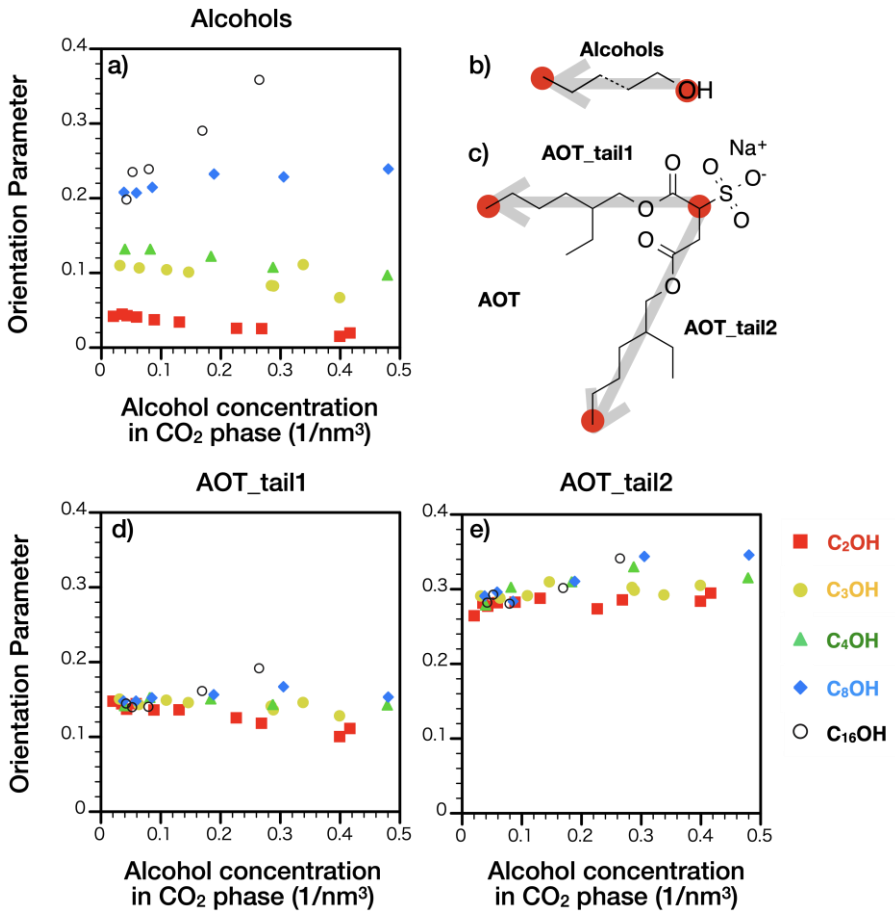

Figure 6-9 Orientation parameters of a) alcohols; d) AOT_tail1; e) AOT_tail2 with varying alcohol tail length and concentration. Molecular structure and definition for tails axis of b) alcohols and c) AOT.

Strong $C_{16}OH$-$C_{16}OH$ and AOT-$C_{16}OH$ tail-tail interactions can further affect the alcohol and AOT orientation at the interface. **Figures 6-9 a**, **d**, and **e** show the orientation parameter of alcohols and two tail groups from AOT, respectively. The function to calculate the orientation parameter is given in **Chapter 1**, **Section 1.4.4.4**. Detailed definitions on the alcohol and AOT tails axis are highlighted using black arrows in **Figures 6-9 b** and **c**, respectively. The value of the orientation parameter can vary from -0.5 to 1. The orientation parameter of -0.5, 0, and 1 indicates for a molecule is fully parallel to the *x*-*y* plane, randomly distributed, and fully perpendicular to the *x*-*y*

plane, respectively. Longer chain alcohols distribute more perpendicular to the *x-y* plane as shown in **Figure 6-9 a**. The orientation parameter of alcohol increases as their concentration in the CO_2 phase increases for long-chain alcohols (C_8OH and $C_{16}OH$). On the other hand, the alcohol orientation parameter slightly decreases for short and mid-chain alcohols (C_2OH, C_3OH, and C_4OH) as their concentration increases. AOT is a surfactant with two tail groups: AOT_tail1 and AOT_tail2 (see **Figure 6-9 c**). We explicitly study the orientation parameters of these two tails in **Figures 6-9 d** and **e**, respectively. AOT_tail1 arranged more perpendicular to the *x-y* plane as C_8OH and $C_{16}OH$ concentrations increased. In contrast, the AOT_tail1 orientation parameter slightly decreased as C_2OH, C_3OH, and C_4OH concentrations increased. AOT_tail2 orientation parameters are slightly increased as alcohol concentration increases, as shown in **Figure 6-9 e**. Such an increment effect is more significant in systems containing longer chain alcohols. Integrating orientation parameter change in both tails (AOT_tail1 and AOT_tail2), long-chain alcohols (C_8OH and $C_{16}OH$) can help the AOT tail group more perpendicular to the *x-y* plane, while short and mid-chain alcohols (C_2OH, C_3OH, and C_4OH) might have a negligible effect on AOT tail group orientation.

6.4 Summary

In this work, we use MD simulations to study the alcohol tail length and concentration effect on the water/scCO_2 interfacial properties under typical reservoir conditions (333 K and 200 bar). Alcohols can distribute in water, interface region, and scCO_2 phases. The alcohol tail length has a negligible effect on their participation at the interface when their concentrations in the scCO_2 phase are the same. On the other hand, alcohol participation in the water phase is highly affected by the alcohol tail length. Alcohol density in the water phase increases as its tail length decreases. Notably, C_2OH concentration in the water phase is one order higher than that of C_4OH under the

same alcohol concentration in the $scCO_2$ phase. The high alcohol concentration in the water phase results in high alcohol retention in the reservoir water. This is not only economically inefficient but also contaminates the underground water (except for ethanol). When the alcohol concentration is relatively low (before reaching the inflection point in IFT), different chain length alcohols possess similar abilities in decreasing IFT. It is also noted that higher tail length alcohols reach the inflection point in IFT under lower alcohol concentration in $scCO_2$, which needs to be considered for high alcohol concentration $scCO_2$ foam flooding. Strong tail-tail interaction in long-chain alcohols might be the main reason for a different inflection point in IFT. AOT_S and Alcohol_O distribute more widely in the *z*-direction as alcohol concentration increases providing more space in the *z*-direction, for short-chain alcohols. On the other hand, increasing alcohol concentration only increases AOT_S and Alcohol_O peak intensity without changing the width in the *z*-direction, resulting in saturation of the interface region under lower alcohol concentration. All of the alcohols decrease AOT diffusion at the interface, while long-chain alcohol ($C_{16}OH$) has a more significant effect than short-chain alcohols (C_2OH and C_3OH). In addition, long-chain alcohols can also help orientate the AOT tail group to be more perpendicular to the *x*-*y* plane. This work should provide important insight into alcohol's effect on water/$scCO_2$ interfacial properties in application to $scCO_2$ foam flooding.

Chapter 7 : CONCLUSIONS, LIMITATIONS, AND FUTURE WORKS

7.1 Conclusions

The effects of amphiphilic chemical additives on the enhanced oil recovery process are studied using molecular dynamics simulation. Formation brine contains omnipresent ions (*e.g.*, Na^+, K^+, Ca^{2+}, Mg^{2+}, Cl^-, SO_4^{2-}, CO_3^{2-}, *etc.*), which significantly affect anionic surfactant efficacy in the chemical flooding process. Effect of ion valency and concentration on SDS (anionic surfactant) efficacy at brine-decane interface is studied. Ca^{2+} has a significant effect on the SDS in-plane distribution by forming cation bridging. Introducing cationic surfactant CTAB can disaggregate such cation bridging, while nonionic propanol barely affects cation bridging density. Propanol can relocate through the phases (brine, interface region, oil), and such relocation is a dynamic process. In addition, propanol can form H-bonds with water molecules at the interface, while CTAB can't. Alcohols are also often employed as a cosolvent in the $scCO_2$ flooding to increase the surfactant solubility in the $scCO_2$ phase. The working mechanism of ethanol on increasing AOT dispersity in $scCO_2$ is studied. We demonstrate that ethanol can better solvate Na^+ in AOT, thereby inhibiting further aggregation of AOT. The alcohols are originally introduced as a cosolvent in $scCO_2$ foam flooding, while they also work as cosurfactants at the foam interface (water/$scCO_2$ interface). Effects of different tail length alcohols on the water/$scCO_2$ are studied as well. Key findings in each chapter are listed below.

In Chapter 2, we report a molecular dynamics (MD) study to investigate the ion valency and concentration effect on the structural and thermodynamic properties of brine-decane interfaces with anionic surfactant (SDS), under typical reservoir conditions (353 K and 200 bar). We use two

different cations (Na^+ and Ca^{2+}) and a wide range of ion concentrations (up to 3.96 M) to simulate typical reservoir conditions. We find that ion valency has a significant effect on the molecular configurations, which further influences the thermodynamic properties. Ca^{2+} ions can have strong adsorption at the interface due to the strong electrostatic interactions between Ca^{2+} ions and SDS, which also results in the Cl^- ion enrichment at the interface. Furthermore, Ca^{2+} ions can form pentagon-like SDS-Ca^{2+} complexes through SDS-Ca^{2+}-SDS cation bridging, which renders a non-uniform distribution of SDS at the interface. On the other hand, the cation bridging density monotonically increases as ion concentration increases for the systems without Ca^{2+} ions, while first increases, then decrease for the systems with Ca^{2+} ions. This is because the accumulation of Cl^- ions at the interface at high salt concentrations can melt SDS-Ca^{2+} complexes. This work should provide new insights into the structural and thermodynamic properties of brine-oil interfaces with anionic surfactant which can facilitate the optimization of chemical flooding processes.

In Chapter 3, we report a molecular dynamics (MD) study to investigate the molecular arrangement and possible applications of surfactant blending in hard-water resistant chemical flooding for oil recovery. We chose commonly used anionic surfactants, Sodium dodecyl sulfate (SDS), as primary surfactants. The non-ionic (propanol) and cationic (cetrimonium bromide (CTAB)) surfactants with a wide range of concentrations are introduced to the primary system. We demonstrate that CTAB can disaggregate the cation bridging when their concentration is above a certain threshold. This threshold value is related to the surfactant and cosurfactant surface charge in the interface region. The cation bridging density is maintained at a low level when the sum of surfactants and cosurfactant interface charge is neutral or positive. On the other hand, propanol barely disaggregates the cation bridging. When propanol concentration is above a certain value, it even facilitates the cation bridging formation. Both propanol and CTAB can further decrease the

oil-brine interfacial tension (IFT) while having different efficacies (IFT decrement rate is different as their interface concentration increases). More rapid IFT decrement is observed when cation bridging is disaggregated (*i.e.*, in the systems with high CTAB concentrations). Increasing propanol concentration barely affects hydrogen-bond (H-bond) formation between SDS and H_2O, because of low propanol distribution around SDS. On the other hand, the first increase and then decrease trend in H-bond density between SDS and H_2O is observed as CTAB concentration increases. Our work should provide important insights in designing chemical formulas for chemical flooding applications.

In Chapter 4, we report a molecular dynamics simulation study to explore the role of alcohol (propanol) as a cosurfactant at the brine/oil interface in chemical flooding under a typical reservoir condition (353K, 200 bar). We demonstrate that propanol, as a cosurfactant, can transport through the oil and brine phases; such a dislocation of propanol in the system is a dynamic process. Propanol is distributed after surfactant at the interfaces. The interfacial tension between brine and oil decreases as propanol concentration in the system increases. This is because, propanol can form hydrogen bonds with water molecules, while it decreases the density of hydrogen bonds formed between surfactant and water. The introduction of propanol does not always increase the local fluidity of surfactants at the interfaces. A local maximum fluidity was observed when surfactants are more perpendicular to the interfaces. Our work should provide important insights into the design of the surfactant formulas.

In Chapter 5, we report a molecular dynamics simulation study to investigate the role of alcohols in the solubility increment of AOT in $scCO_2$ under typical tight oil reservoir conditions (333 K and 200 bar). We randomly inserted AOT molecules in two different systems (A, and B) as initial configurations: System A consists of AOT and $scCO_2$; System B consists of AOT, $scCO_2$,

and 10 *wt*.% ethanol. After 600-ns runs, the AOT molecules aggregate together and form rod-like reverse-micelles (RMs) in System A. On the other hand, AOT molecules form several small sphere-like RMs in System B. In System A, Na^+ ions aggregate in the cores of RMs, while they are bounded to the head groups of AOT molecules. By introducing ethanols (system B), the Na^+ ions are exposed to and solvated by the ethanol molecules, which prevent further AOT aggregations. The potential of mean force (PMF) calculation also reveals that small clusters formed by 4 AOT molecules attract each other in System A, while the opposite is true in System B. Our work should provide important insights into the design of $scCO_2$ soluble surfactant formulas and chemical blending for EOR and GCS.

In Chapter 6, we use the molecular dynamics (MD) simulation to study the alcohol effect on the foam interface properties. Alcohols with varying tail lengths (C_2OH-$C_{16}OH$) under a wide range of concentrations are introduced to water/AOT/$scCO_2$ interface systems to study their effects. Temperature and pressure are set as typical reservoir conditions (333K, 200 bar). We demonstrate that alcohol can distribute in water, interface region, and $scCO_2$ phases, and their participation in phases is affected by the alcohol tail length. Alcohols' tail length has a negligible effect on alcohol distribution at the interface when their concentration in the $scCO_2$ phase is fixed. On the other hand, alcohol concentration in the water phase increase as tail length decrease. The ability in decreasing interfacial tension (IFT) is similar for different tail length alcohols when alcohol concentration is relatively low (before reaching the inflection point). Longer chain alcohols reach an inflection point under lower alcohol concentration. In other words, the lowest available IFT increases as alcohol chain length increases. Alcohols not only can reduce the IFT, but also can decrease the AOT diffusion at the interface. MSD of AOT decreases as alcohol concentration increases, and such a decrement trend is more significant in systems with long-chain alcohols. In

addition, long-chain alcohols also help orientate the AOT tail group, while a negligible change in the AOT orientation tail is observed for the systems with short- and mid-tail alcohols.

7.2 Limitations and Recommendations for Future Works

In this section, we first discuss the general limitations of the current MD simulations and then point out limitations and recommended future works for this dissertation in specific.

MD simulation is a strong tool to study molecular behavior with atomic precision while having its limitations. **First**, the MD study is depending on the forcefields. An appropriate and accurate forcefield is the basis for a convincing and rigorous molecular simulation study. Non-polarizable forcefields are the most commonly used forcefields. However, they could not fully reflect the ion polarizability, which might significantly change ion distribution. It is noted that scientists are actively developing polarizable force fields nowadays. **Second**, MD simulation is computationally expensive. This is particularly true to applying them in real industrial applications with large systems for a long processing time. Take oil production, for example, the oil recovery process could last for ~ months or years. It would not be problematic on using MD simulation to study the equilibrium properties. However, to study the dynamic properties, it is almost impossible to conduct such a long-time MD simulation. We also note that scientists are also dedicating themselves to solving this problem, either using machine learning (ML) or coarse-grained (CG) models. It would be exciting to be able to calculate the ~ months MD simulations in the future.

Limitations and recommended future works based on this dissertation are listed below.

- **Forcefields**

Though we strive to choose and validate the force fields in our studies, there still exist some limitations in currently available forcefields. For example, we employed the general forcefield in Chapters 2, 3, and 4 which contain systems with high ion concentrations. It is noted that ion polarizability, which could not be considered from the general force field, might affect the surfactant and ion distribution at the interface[200-203]. In addition, as discussed in Chapter 6, the

compatibility of water and $scCO_2$ forcefields (developed under different solution polarity) needs to be improved.

- **Non-equilibrium Simulation**

As discussed in Chapter 6, foam is not thermodynamically stable. In our simulation, we study the equilibrated systems by artificially stabilizing the foam interface (fix simulation box size in the *x*- and *y*- directions). In the real application of foam flooding, foam generation and propagation can be affected by foam dynamic properties. Future works on investigating the surfactant and cosurfactant dynamic properties at the foam (water/$scCO_2$ interface) are highly recommended.

- **Oil Model**

We employed n-decane, which contains the same carbon number as the recommended crude (light) oil equivalent alkane carbon number (EACN)[94-97], to represent the oil phase for simplicity. Nevertheless, it should be noted that actual crude oil is composed of thousands of components. Oil components with different chemical structures (with/without an aromatic ring or branch chains) also might further affect the surfactant arrangement and efficacy at the brine-oil interface. We recommend future works to explore the oil component effect on the surfactant arrangements at the brine-oil interface.

- **Launching Experiments**

A unique pentation-like structure is observed in the SDS-Ca^{2+} complex from the molecular simulation study in Chapters 2 and 3. It would be exciting to find such a structure from experimental measurements to verify our simulation findings.

Bibliography

1. Dale, S. and B. Fattouh, *Peak oil demand and long-run oil prices.* Energy Insight, 2018. **25**.
2. Carpenter, N.L., *Method and apparatus for tertiary recovery of oil*. 1980, Google Patents.
3. Bera, A. and A. Mandal, *Microemulsions: a novel approach to enhanced oil recovery: a review.* Journal of Petroleum Exploration and Production Technology, 2015. **5**(3): p. 255-268.
4. Cayias, J., R.S. Schechter, and W. Wade, *The utilization of petroleum sulfonates for producing low interfacial tensions between hydrocarbons and water.* Journal of Colloid and Interface Science, 1977. **59**(1): p. 31-38.
5. Nazar, M., S. Shah, and M. Khosa, *Microemulsions in enhanced oil recovery: a review.* Petroleum science and technology, 2011. **29**(13): p. 1353-1365.
6. Rocha De Farias, M.L., et al. *A comparative study of emulsion flooding and other IOR methods for heavy oil fields*. in *SPE Latin America and Caribbean Petroleum Engineering Conference*. 2012. Society of Petroleum Engineers.
7. Lee, J., T. Babadagli, and R. Giesbrecht, *Impact of Divalent Ions on Heavy Oil Recovery by in situ Emulsification.* Journal of Surfactants and Detergents, 2019. **22**(6): p. 1371-1385.
8. Zhu, Y., M. Lei, and Z. Zhu. *Development and performance of salt-resistant polymers for chemical flooding*. in *SPE Middle East Oil & Gas Show and Conference*. 2015. Society of Petroleum Engineers.
9. Shiau, B.J.B., et al. *Recovery of oil from high salinity reservoir using chemical flooding: from laboratory to field tests*. in *SPE Enhanced Oil Recovery Conference*. 2013. Society of Petroleum Engineers.
10. Kang, M. and R.B. Jackson, *Salinity of deep groundwater in California: Water quantity, quality, and protection.* Proceedings of the National Academy of Sciences of the United States of America, 2016. **113**(28): p. 7768-7773.
11. Bachu, S. and D.B. Bennion, *Dependence of CO2-brine interfacial tension on aquifer pressure, temperature and water salinity.* Energy Procedia, 2009. **1**(1): p. 3157-3164.
12. Aggelopoulos, C.A., et al., *CO2/CaCl2 solution interfacial tensions under CO2 geological storage conditions: influence of cation valence on interfacial tension.* Advances in Water Resources, 2010. **33**(6): p. 691-697.
13. Thomas, S., *Enhanced oil recovery-an overview.* Oil & Gas Science and Technology-Revue de l'IFP, 2008. **63**(1): p. 9-19.
14. Chiang, M.Y. and D.O. Shah, *The effect of alcohol on surfactant mass transfer across the oil/brine interface and related phenomena*, in *Surface Phenomena in Enhanced Oil Recovery*. 1981, Springer.
15. Falls, A.H., et al., *Field test of cosurfactant-enhanced alkaline flooding.* SPE Reservoir Engineering, 1994. **9**(03): p. 217-223.
16. Jones, S. and K. Dreher, *Cosurfactants in micellar systems used for tertiary oil recovery.* Society of petroleum engineers journal, 1976. **16**(03): p. 161-167.
17. Iglauer, S., et al., *Alkyl polyglycoside surfactant–alcohol cosolvent formulations for improved oil recovery.* Colloids and Surfaces A, 2009. **339**(1-3): p. 48-59.
18. Puig, J., et al., *Roles of co-surfactant and co-solvent in surfactant waterflooding.* Chemical Engineering Communications, 1988. **65**(1): p. 169-185.

19. Kulkarni, M.M., *Multiphase mechanisms and fluid dynamics in gas injection enhanced oil recovery processes*. 2005: Louisiana State University and Agricultural & Mechanical College.
20. Lemmon, E., *Thermophysical Properties of Fluid Systems, NIST chemistry WebBook, NIST standard reference database number 69.* http://webbook. nist. gov., 2005.
21. Zhou, X., et al., *Performance evaluation of CO2 flooding process in tight oil reservoir via experimental and numerical simulation studies.* Fuel, 2019. **236**: p. 730-746.
22. Burrows, L.C., et al., *A literature review of CO2, natural gas, and water-based fluids for enhanced oil recovery in unconventional reservoirs.* Energy & Fuels, 2020. **34**(5): p. 5331-5380.
23. Zhang, K., et al., *Millimeter to nanometer-scale tight oil–CO2 solubility parameter and minimum miscibility pressure calculations.* Fuel, 2018. **220**: p. 645-653.
24. Czarnota, R., et al., *Minimum miscibility pressure measurement for CO2 and oil using rapid pressure increase method.* Journal of CO2 utilization, 2017. **21**: p. 156-161.
25. Psarras, P., et al., *Methane and CO2 adsorption capacities of kerogen in the Eagle Ford shale from molecular simulation.* Accounts of chemical research, 2017. **50**(8): p. 1818-1828.
26. Bui, M., et al., *Carbon capture and storage (CCS): the way forward.* Energy & Environmental Science, 2018. **11**(5): p. 1062-1176.
27. Lal, R., *Carbon sequestration.* Philosophical Transactions of the Royal Society B: Biological Sciences, 2008. **363**(1492): p. 815-830.
28. Lackner, K.S., *A guide to CO2 sequestration.* Science, 2003. **300**(5626): p. 1677-1678.
29. Zhang, C., et al., *Enhancing sodium bis (2-ethylhexyl) sulfosuccinate injectivity for CO2 foam formation in low-permeability cores: dissolving in CO2 with ethanol.* Energy & fuels, 2018. **32**(5): p. 5846-5856.
30. Cuthiell, D., et al., *Viscous fingering effects in solvent displacement of heavy oil.* Journal of Canadian Petroleum Technology, 2006. **45**(07).
31. Elsharkawy, A., F. Poettmann, and R. Christiansen. *Measuring minimum miscibility pressure: slim-tube or rising-bubble method?* in *SPE/DOE enhanced oil recovery symposium*. 1992. OnePetro.
32. Zhang, C., et al., *A novel system for reducing CO2-crude oil minimum miscibility pressure with CO2-soluble surfactants.* Fuel, 2020. **281**: p. 118690.
33. Fan, X., et al., *Oxygenated hydrocarbon ionic surfactants exhibit CO2 solubility.* Journal of the American Chemical Society, 2005. **127**(33): p. 11754-11762.
34. Newman, D., et al., *Phase behavior of fluoroether-functional amphiphiles in supercritical carbon dioxide.* The Journal of Supercritical Fluids, 1993. **6**(4): p. 205-210.
35. Hutton, B.H., et al., *AOT reverse microemulsions in scCO2—a further investigation.* Colloids and surfaces A: Physicochemical and engineering aspects, 2001. **189**(1-3): p. 177-181.
36. Hoefling, T., R. Enick, and E. Beckman, *Microemulsions in near-critical and supercritical carbon dioxide.* The Journal of Physical Chemistry, 1991. **95**(19): p. 7127-7129.
37. Liu, J., et al., *Solubility of Ls-36 and Ls-45 surfactants in supercritical CO2 and loading water in the CO2/water/surfactant systems.* Langmuir, 2002. **18**(8): p. 3086-3089.
38. Shi, Q., et al., *Solubility of nonionic hydrocarbon surfactants with different hydrophobic tails in supercritical CO2.* Journal of Chemical & Engineering Data, 2015. **60**(8): p. 2469-2476.

39. Hutton, B.H., et al., *Investigation of AOT reverse microemulsions in supercritical carbon dioxide.* Colloids and surfaces A: Physicochemical and engineering aspects, 1999. **146**(1-3): p. 227-241.
40. Yu, W., et al., *Phase behavior of supercritical CO2 microemulsions with surfactant Ls-36 and selective solubilization of propane-1, 3-diol.* Journal of chemical & engineering data, 2013. **58**(3): p. 814-820.
41. Ji, M., et al., *Synthesizing and dispersing silver nanoparticles in a water-in-supercritical carbon dioxide microemulsion.* Journal of the American Chemical Society, 1999. **121**(11): p. 2631.
42. Liu, J., et al., *Effect of cosolvent on the phase behavior of non-fluorous Ls-54 surfactant in supercritical CO2.* Fluid phase equilibria, 2003. **211**(2): p. 265-271.
43. Frenkel, D. and B. Smit, *Understanding molecular simulation: from algorithms to applications*. Vol. 1. 2001: Elsevier.
44. Jorgensen, W.L., D.S. Maxwell, and J. Tirado-Rives, *Development and testing of the OPLS all-atom force field on conformational energetics and properties of organic liquids.* Journal of the American Chemical Society, 1996. **118**(45): p. 11225-11236.
45. Kaminski, G., et al., *Free energies of hydration and pure liquid properties of hydrocarbons from the OPLS all-atom model.* The Journal of Physical Chemistry, 1994. **98**(49): p. 13077-13082.
46. Stubbs, J.M., J.J. Potoff, and J.I. Siepmann, *Transferable potentials for phase equilibria. 6. United-atom description for ethers, glycols, ketones, and aldehydes.* The Journal of Physical Chemistry B, 2004. **108**(45): p. 17596-17605.
47. Martin, M.G. and J.I. Siepmann, *Transferable potentials for phase equilibria. 1. United-atom description of n-alkanes.* The Journal of Physical Chemistry B, 1998. **102**(14): p. 2569-2577.
48. Oostenbrink, C., et al., *A biomolecular force field based on the free enthalpy of hydration and solvation: the GROMOS force‐field parameter sets 53A5 and 53A6.* Journal of computational chemistry, 2004. **25**(13): p. 1656-1676.
49. Horta, B.A., et al., *New interaction parameters for oxygen compounds in the GROMOS force field: Improved pure-liquid and solvation properties for alcohols, ethers, aldehydes, ketones, carboxylic acids, and esters.* Journal of chemical theory and computation, 2011. **7**(4): p. 1016-1031.
50. Huang, J. and A.D. MacKerell Jr, *CHARMM36 all‐atom additive protein force field: Validation based on comparison to NMR data.* Journal of computational chemistry, 2013. **34**(25): p. 2135-2145.
51. Berendsen, H.J., et al., *Interaction models for water in relation to protein hydration*, in *Intermolecular forces*. 1981, Springer. p. 331-342.
52. Berendsen, H., J. Grigera, and T. Straatsma, *The missing term in effective pair potentials.* Journal of Physical Chemistry, 1987. **91**(24): p. 6269-6271.
53. Jorgensen, W.L., et al., *Comparison of simple potential functions for simulating liquid water.* The Journal of chemical physics, 1983. **79**(2): p. 926-935.
54. Horn, H.W., et al., *Development of an improved four-site water model for biomolecular simulations: TIP4P-Ew.* The Journal of chemical physics, 2004. **120**(20): p. 9665-9678.
55. Mahoney, M.W. and W.L. Jorgensen, *A five-site model for liquid water and the reproduction of the density anomaly by rigid, nonpolarizable potential functions.* The Journal of chemical physics, 2000. **112**(20): p. 8910-8922.

56. Nan, Y., W. Li, and Z. Jin, *Role of Alcohol as a Cosurfactant at the Brine–Oil Interface under a Typical Reservoir Condition.* Langmuir, 2020. **36**(19): p. 5198-5207.
57. Hub, J.S., B.L. De Groot, and D. Van Der Spoel, *g_wham · A Free Weighted Histogram Analysis Implementation Including Robust Error and Autocorrelation Estimates.* Journal of chemical theory and computation, 2010. **6**(12): p. 3713-3720.
58. Janke, J.J., W.D. Bennett, and D.P. Tieleman, *Oleic acid phase behavior from molecular dynamics simulations.* Langmuir, 2014. **30**(35): p. 10661-10667.
59. Nalaparaju, A., J. Wang, and J. Jiang, *Enhancing water permeation through alumina membranes by changing from cylindrical to conical nanopores.* Nanoscale, 2019. **11**(20): p. 9869-9878.
60. Kirkwood, J.G. and F.P. Buff, *The statistical mechanical theory of surface tension.* The Journal of Chemical Physics, 1949. **17**(3): p. 338-343.
61. Yang, X. and C. Zhang, *Structure and diffusion behavior of dense carbon dioxide fluid in clay-like slit pores by molecular dynamics simulation.* Chemical physics letters, 2005. **407**(4-6): p. 427-432.
62. Singh, S.K., et al., *Vapor− liquid phase coexistence, critical properties, and surface tension of confined alkanes.* The Journal of Physical Chemistry C, 2009. **113**(17): p. 7170-7180.
63. Jin, Z. and A. Firoozabadi, *Methane and carbon dioxide adsorption in clay-like slit pores by Monte Carlo simulations.* Fluid Phase Equilibria, 2013. **360**: p. 456-465.
64. Nan, Y., W. Li, and Z. Jin, *Ion Valency and Concentration Effect on the Structural and Thermodynamic Properties of Brine–Decane Interfaces with Anionic Surfactant (SDS).* The Journal of Physical Chemistry B, 2021. **125**(33): p. 9610-9620.
65. Yan, H., et al., *Effect of Ca2+ and Mg2+ ions on surfactant solutions investigated by molecular dynamics simulation.* Langmuir, 2010. **26**(13): p. 10448-10459.
66. Allen, M. and D. Tildesley, *Computer simulation of liquids. 1987.* New York: Oxford, 1989. **385**.
67. Rosen, M.J. and J.T. Kunjappu, *Surfactants and interfacial phenomena*. 2012: John Wiley & Sons.
68. Taylor, S.E. and H.T. Chu, *Metal Ion Interactions with Crude Oil Components: Specificity of Ca2+ Binding to Naphthenic Acid at an Oil/Water Interface.* Colloids and Interfaces, 2018. **2**(3): p. 40.
69. Anachkov, S.E., et al., *Adsorption of linear alkyl benzene sulfonates on oil–water interface: Effects of Na+, Mg2+ and Ca2+ ions.* Colloids and Surfaces A: Physicochemical and Engineering Aspects, 2015. **466**: p. 18-27.
70. Jamaloei, B.Y. and M. Rafiee. *Effect of monovalent and divalent ions on macroscopic behaviour of surfactant flooding*. in *Canadian International Petroleum Conference*. 2008. Petroleum Society of Canada.
71. Jha, N.K., S. Iglauer, and J.S. Sangwai, *Effect of monovalent and divalent salts on the interfacial tension of n-heptane against aqueous anionic surfactant solutions.* Journal of Chemical & Engineering Data, 2017. **63**(7): p. 2341-2350.
72. Robertson, E.J., D.K. Beaman, and G.L. Richmond, *Designated drivers: The differing roles of divalent metal ions in surfactant adsorption at the oil–water interface.* Langmuir, 2013. **29**(50): p. 15511-15520.

73. Badakshan, A. and P. Bakes, *The influence of temperature and surfactant concentration on interfacial tension of saline water and hydrocarbon systems in relation to enhanced oil recovery by chemical flooding.* 1990.
74. Sedghi, M., M. Piri, and L. Goual, *Atomistic molecular dynamics simulations of crude oil/brine displacement in calcite mesopores.* Langmuir, 2016. **32**(14): p. 3375-3384.
75. de Lara, L.S., M.F. Michelon, and C.R. Miranda, *Molecular dynamics studies of fluid/oil interfaces for improved oil recovery processes.* The Journal of Physical Chemistry B, 2012. **116**(50): p. 14667-14676.
76. Li, W., et al., *Effects of Salinity and N-, S-, and O-Bearing Polar Components on Light Oil–Brine Interfacial Properties from Molecular Perspectives.* The Journal of Physical Chemistry C, 2019. **123**(38): p. 23520-23528.
77. Alejandre, J., et al., *The short range anion-H interaction is the driving force for crystal formation of ions in water.* The Journal of chemical physics, 2009. **130**(17): p. 174505.
78. Wen, B., et al., *Ionic hydration-induced evolution of decane–water interfacial tension.* Physical Chemistry Chemical Physics, 2017. **19**(22): p. 14606-14614.
79. Zhao, J., et al., *Molecular dynamics simulation of the salinity effect on the n-decane/water/vapor interfacial equilibrium.* Energy & Fuels, 2018. **32**(11): p. 11080-11092.
80. Badizad, M.H., et al., *How do ions contribute to brine-hydrophobic hydrocarbon Interfaces? An in silico study.* Journal of colloid and interface science, 2020. **575**: p. 337-346.
81. Li, W. and Z. Jin, *Effect of ion concentration and multivalence on methane-brine interfacial tension and phenomena from molecular perspectives.* Fuel, 2019. **254**: p. 115657.
82. Riccardi, E. and T. Tichelkamp, *Calcium ion effects on the water/oil interface in the presence of anionic surfactants.* Colloids and Surfaces A: Physicochemical and Engineering Aspects, 2019. **573**: p. 246-254.
83. Bera, A., et al., *Screening of microemulsion properties for application in enhanced oil recovery.* Fuel, 2014. **121**: p. 198-207.
84. Benjamin, l., *Mechanism and dynamics of ion transfer across a liquid-liquid interface.* Science, 1993. **261**(5128): p. 1558-1560.
85. Kikkawa, N., L. Wang, and A. Morita, *Microscopic barrier mechanism of ion transport through liquid–liquid interface.* Journal of the American Chemical Society, 2015. **137**(25): p. 8022-8025.
86. Karnes, J.J., N. Villavicencio, and I. Benjamin, *Transfer of an erbium ion across the water/dodecane interface: Structure and thermodynamics via molecular dynamics simulations.* Chemical Physics Letters, 2019. **737**: p. 136825.
87. Yan, H., et al., *Molecular dynamics study of the effect of calcium ions on the monolayer of SDC and SDSn surfactants at the vapor/liquid interface.* Langmuir, 2011. **27**(10): p. 5762-5771.
88. Chen, M., et al., *Specific counterion effects on the atomistic structure and Capillary-waves fluctuation of the water/vapor interface covered by sodium dodecyl sulfate.* The Journal of Physical Chemistry C, 2014. **118**(33): p. 19205-19213.
89. Müller, P., et al., *Ionic Surfactants at Air/Water and Oil/Water Interfaces: A Comparison Based on Molecular Dynamics Simulations.* The Journal of Physical Chemistry B, 2021. **125**(1): p. 406-415.

90. Kunieda, M., et al., *Self-accumulation of aromatics at the oil− water interface through weak hydrogen bonding.* Journal of the American Chemical Society, 2010. **132**(51): p. 18281-18286.
91. Mohammed, S. and G.A. Mansoori, *Molecular insights on the interfacial and transport properties of supercritical CO2/brine/crude oil ternary system.* Journal of Molecular Liquids, 2018. **263**: p. 268-273.
92. Gao, F., et al., *Molecular dynamics simulation: the behavior of asphaltene in crude oil and at the oil/water interface.* Energy & fuels, 2014. **28**(12): p. 7368-7376.
93. Wan, W., et al., *Characterization of crude oil equivalent alkane carbon number (EACN) for surfactant flooding design.* Journal of Dispersion Science and Technology, 2016. **37**(2): p. 280-287.
94. Antón, R., N. Garcés, and A. Yajure, *A correlation for three-phase behavior of cation1C surfactant-oil-water systems.* Journal of dispersion science and technology, 1997. **18**(5): p. 539-555.
95. Baran Jr, J.R., et al., *Microemulsion formation with mixed chlorinated hydrocarbon liquids.* Journal of colloid and interface science, 1994. **168**(1): p. 67-72.
96. Bouton, F.o., et al., *A QSPR model for the prediction of the "fish-tail" temperature of C i E4/water/polar hydrocarbon oil systems.* Langmuir, 2010. **26**(11): p. 7962-7970.
97. Wu, B., et al., *Formulating microemulsion systems for a weathered jet fuel waste using surfactant/cosurfactant mixtures.* Separation Science and Technology, 2000. **35**(12): p. 1917-1937.
98. Chattoraj, D., *Adsorption and the Gibbs surface excess*. 2012: Springer Science & Business Media.
99. Pastor, R. and A. MacKerell Jr, *Development of the CHARMM force field for lipids.* The journal of physical chemistry letters, 2011. **2**(13): p. 1526-1532.
100. Lemmon, E., et al., *NIST chemistry WebBook, Nist standard reference database number 69.* National Institute of Standards and Technology, Gaithersburg, 2011.
101. Rehfeld, S.J., *Adsorption of sodium dodecyl sulfate at various hydrocarbon-water interfaces.* The Journal of Physical Chemistry, 1967. **71**(3): p. 738-745.
102. Mitrinović, D.M., et al., *Noncapillary-wave structure at the water-alkane interface.* Physical review letters, 2000. **85**(3): p. 582.
103. Abraham, M.J., et al., *GROMACS User Manual version 2019.1.*
104. Hockney, R.W., S. Goel, and J. Eastwood, *Quiet high-resolution computer models of a plasma.* Journal of Computational Physics, 1974. **14**(2): p. 148-158.
105. Bussi, G., D. Donadio, and M. Parrinello, *Canonical sampling through velocity rescaling.* The Journal of chemical physics, 2007. **126**(1): p. 014101.
106. Evans, D.J. and B.L. Holian, *The nose–hoover thermostat.* The Journal of chemical physics, 1985. **83**(8): p. 4069-4074.
107. Berendsen, H.J., et al., *Molecular dynamics with coupling to an external bath.* The Journal of chemical physics, 1984. **81**(8): p. 3684-3690.
108. Parrinello, M. and A. Rahman, *Polymorphic transitions in single crystals: A new molecular dynamics method.* Journal of Applied physics, 1981. **52**(12): p. 7182-7190.
109. Essmann, U., et al., *A smooth particle mesh Ewald method.* The Journal of chemical physics, 1995. **103**(19): p. 8577-8593.
110. Lorentz, H., *Ueber die Anwendung des Satzes vom Virial in der kinetischen Theorie der Gase.* Annalen der physik, 1881. **248**(1): p. 127-136.

111. Berthelot, D., *Sur le mélange des gaz.* Compt. Rendus, 1898. **126**: p. 1703-1706.
112. Miyamoto, S. and P.A. Kollman, *Settle: An analytical version of the SHAKE and RATTLE algorithm for rigid water models.* Journal of computational chemistry, 1992. **13**(8): p. 952-962.
113. Hess, B., et al., *LINCS: a linear constraint solver for molecular simulations.* Journal of computational chemistry, 1997. **18**(12): p. 1463-1472.
114. Humphrey, W., A. Dalke, and K. Schulten, *VMD: visual molecular dynamics.* Journal of molecular graphics, 1996. **14**(1): p. 33-38.
115. Jang, S.S., et al., *Molecular dynamics study of a surfactant-mediated decane− water interface: Effect of molecular architecture of alkyl benzene sulfonate.* The Journal of Physical Chemistry B, 2004. **108**(32): p. 12130-12140.
116. Wu, J., et al., *A classical density functional theory for interfacial layering of ionic liquids.* Soft Matter, 2011. **7**(23): p. 11222-11231.
117. Sammalkorpi, M., M. Karttunen, and M. Haataja, *Ionic surfactant aggregates in saline solutions: sodium dodecyl sulfate (SDS) in the presence of excess sodium chloride (NaCl) or calcium chloride (CaCl2).* The Journal of Physical Chemistry B, 2009. **113**(17): p. 5863-5870.
118. Fainerman, V. and R. Miller, *Surface tension isotherms for surfactant adsorption layers including surface aggregation.* Langmuir, 1996. **12**(25): p. 6011-6014.
119. Sresht, V., et al., *Combined Molecular Dynamics Simulation–Molecular-Thermodynamic Theory Framework for Predicting Surface Tensions.* Langmuir, 2017. **33**(33): p. 8319-8329.
120. Zargartalebi, M., R. Kharrat, and N. Barati, *Enhancement of surfactant flooding performance by the use of silica nanoparticles.* Fuel, 2015. **143**: p. 21-27.
121. Nan, Y., W. Li, and Z. Jin, *Molecular Dynamics Studies on Effective Surface-Active Additives: Toward Hard Water-Resistant Chemical Flooding for Enhanced Oil Recovery.* Langmuir.
122. Miyazaki, N., et al., *Screening of the effective additive to inhibit surfactin from forming precipitation with divalent cations for surfactin enhanced oil recovery.* Energies, 2020. **13**(10): p. 2430.
123. Barnes, J.R., et al. *Development of surfactants for chemical flooding at difficult reservoir conditions*. in *SPE Symposium on Improved Oil Recovery*. 2008. Society of Petroleum Engineers.
124. Elraies, K.A., *The effect of a new in situ precipitation inhibitor on chemical EOR.* Journal of Petroleum Exploration and Production Technology, 2013. **3**(2): p. 133-137.
125. Zhang, J., et al., *Mechanisms of enhanced natural imbibition with novel chemicals.* SPE reservoir evaluation & engineering, 2009. **12**(06): p. 912-920.
126. Flaaten, A., et al. *A systematic laboratory approach to low-cost, high-performance chemical flooding*. in *SPE Symposium on Improved Oil Recovery*. 2008. Society of Petroleum Engineers.
127. Liu, Z., et al., *Interactions of divalent and trivalent metal counterions with anionic sulfonate gemini surfactant and induced aggregate transitions in aqueous solution.* The Journal of Physical Chemistry B, 2016. **120**(17): p. 4102-4113.
128. Date, A.A. and V.B. Patravale, *Microemulsions: applications in transdermal and dermal delivery.* Critical Reviews in Therapeutic Drug Carrier Systems, 2007. **24**(6).

129. Méndez-Bermúdez, J.G. and H. Dominguez, *Structural changes of a sodium dodecyl sulfate (SDS) micelle induced by alcohol molecules.* Journal of molecular modeling, 2016. **22**(1): p. 33.
130. Kahlweit, M., R. Strey, and G. Busse, *Effect of alcohols on the phase behavior of microemulsions.* The Journal of Physical Chemistry, 1991. **95**(13): p. 5344-5352.
131. De Gennes, P. and C. Taupin, *Microemulsions and the flexibility of oil/water interfaces.* The Journal of physical chemistry, 1982. **86**(13): p. 2294-2304.
132. Kume, G., M. Gallotti, and G. Nunes, *Review on anionic/cationic surfactant mixtures.* Journal of Surfactants and Detergents, 2008. **11**(1): p. 1-11.
133. Rosen, M. and X. Hua, *Synergism in binary mixtures of surfactants: II. Some experimental data.* Journal of the American Oil Chemists' Society, 1982. **59**(12): p. 582-585.
134. Rajkhowa, S., S. Mahiuddin, and K. Ismail, *An assessment of the aggregation and adsorption behavior of the sodium dodecylsulfate–cetyltrimethylammonium bromide mixed surfactant system in aqueous medium.* Journal of Solution Chemistry, 2017. **46**(1): p. 11-24.
135. Van Der Spoel, D., et al., *GROMACS: fast, flexible, and free.* Journal of computational chemistry, 2005. **26**(16): p. 1701-1718.
136. Domínguez, H., *Computer studies on the effects of long chain alcohols on sodium dodecyl sulfate (SDS) molecules in SDS/dodecanol and SDS/hexadecanol monolayers at the air/water interface.* The Journal of Physical Chemistry B, 2006. **110**(26): p. 13151-13157.
137. Li, W., et al., *CO2 solubility in brine in silica nanopores in relation to geological CO2 sequestration in tight formations: Effect of salinity and pH.* Chemical Engineering Journal, 2021. **411**: p. 127626.
138. Brissonnet, J.P. and V. Burnier, *Makeup remover/skin cleanser compositions comprising quaternary phosphates and peg diesters*. 1997, Google Patents.
139. Tarasov, A. and H.S. Koenig, *Clear shampoo formulation*. 1976, Google Patents.
140. Traynor, D.H., et al., *Bodywashes containing additives*. 2006, Google Patents.
141. Lange, B., et al., *Process for the production of washing powders of stabilized or enhanced appearance which contain fluorescent whitening agents*. 1981, Google Patents.
142. Hill, H., J. Reisberg, and G. Stegemeier, *Aqueous surfactant systems for oil recovery.* Journal of petroleum technology, 1973. **25**(02): p. 186-194.
143. Gogarty, W., *Status of surfactant or micellar methods.* Journal of Petroleum Technology, 1976. **28**(01): p. 93-102.
144. Aramaki, K., K. Ozawa, and H. Kunieda, *Effect of temperature on the phase behavior of ionic–nonionic microemulsions.* Journal of colloid and interface science, 1997. **196**(1): p. 74-78.
145. Maugey, M. and A. Bellocq, *Effect of adsorbed and anchored polymers on membrane flexibility: a light scattering study of sponge phases.* Langmuir, 2001. **17**(21): p. 6740-6742.
146. Verhoeckx, G., P. De Bruyn, and J.T.G. Overbeek, *On understanding microemulsions: I. Interfacial tensions and adsorptions of SDS and pentanol at the cyclohexanewater interface.* Journal of colloid and interface science, 1987. **119**(2): p. 409-421.
147. Graciaa, A., et al., *Improving solubilization in microemulsions with additives. 2. Long chain alcohols as lipophilic linkers.* Langmuir, 1993. **9**(12): p. 3371-3374.
148. Stilbs, P., K. Rapacki, and B.r. Lindman, *Effect of alcohol cosurfactant length on microemulsion structure.* J. Colloid Interface Sci.;(United States), 1983. **95**(2).

149. Poghosyan, A.H., et al., *Molecular dynamics simulations of inverse sodium dodecyl sulfate (SDS) micelles in a mixed toluene/pentanol solvent in the absence and presence of poly (diallyldimethylammonium chloride)(PDADMAC).* Journal of colloid and interface science, 2011. **358**(1): p. 175-181.
150. Abe, M., et al., *Microemulsion formation with branched tail polyoxyethylene sulfonate surfactants.* Journal of colloid and interface science, 1986. **114**(2): p. 342-356.
151. Tang, X., P.H. Koenig, and R.G. Larson, *Molecular Dynamics Simulations of Sodium Dodecyl Sulfate Micelles in Water · The Effect of the Force Field.* The Journal of Physical Chemistry B, 2014. **118**(14): p. 3864-3880.
152. LINSTORM, P., *NIST chemistry webbook, NIST standard reference database number 69.* J. Phys. Chem. Ref. Data, Monograph, 1998. **9**: p. 1-1951.
153. Aveyard, R. and D. Haydon, *Thermodynamic properties of aliphatic hydrocarbon/water interfaces.* Transactions of the Faraday Society, 1965. **61**: p. 2255-2261.
154. E. Lindahl, M.A., B. Hess, D. van der Spoel and the GROMACS development team,, *GROMACS User Manual version 2019.1.*
155. Dočkal, J., et al., *A general hydrogen bonding definition based on three-dimensional spatial distribution functions and its extension to quantitative structural analysis of solutions and general intermolecular bonds.* Journal of Molecular Liquids, 2019. **281**: p. 225-235.
156. Baumler, S., T.M. Reidy, and G. Blanchard, *Diffusional motion as a gauge of fluidity and interfacial adhesion. Supported alkylphosphonate monolayers.* Journal of colloid and interface science, 2016. **468**: p. 145-155.
157. Singh, P., et al., *Unraveling the Role of Monoolein in Fluidity and Dynamical Response of a Mixed Cationic Lipid Bilayer.* Langmuir, 2019. **35**(13): p. 4682-4692.
158. Ma, J., et al., *Molecular Dynamics Simulation Insight into Interfacial Stability and Fluidity Properties of Microemulsions.* Langmuir, 2019. **35**(42): p. 13636-13645.
159. Bitsanis, I. and G. Hadziioannou, *Molecular dynamics simulations of the structure and dynamics of confined polymer melts.* The Journal of chemical physics, 1990. **92**(6): p. 3827-3847.
160. Zhan, S., et al., *Effect of water film on oil flow in quartz nanopores from molecular perspectives.* Fuel, 2020. **262**: p. 116560.
161. Nan, Y., et al., *Ethanol Blending to Improve Reverse Micelle Dispersity in Supercritical CO2: A Molecular Dynamics Study.* The Journal of Physical Chemistry B, 2021. **125**(33): p. 9621-9628.
162. Mills, R.M., *The myth of the oil crisis: overcoming the challenges of depletion, geopolitics, and global warming*. 2008: Greenwood Publishing Group.
163. Wei, B., et al., *Adsorptive behaviors of supercritical CO2 in tight porous media and triggered chemical reactions with rock minerals during CO2-EOR and-sequestration.* Chemical Engineering Journal, 2020. **381**: p. 122577.
164. Sheng, J.J., *Modern chemical enhanced oil recovery: theory and practice*. 2010: Gulf Professional Publishing.
165. McFann, G.J., K.P. Johnston, and S.M. Howdle, *Solubilization in nonionic reverse micelles in carbon dioxide.* AIChE journal, 1994. **40**(3): p. 543-555.
166. Chennamsetty, N., et al., *Cosurfactant and cosolvent effects on surfactant self-assembly in supercritical carbon dioxide.* The Journal of chemical physics, 2005. **122**(9): p. 094710.

167. Zhang, C., et al., *Ethanol enhanced anionic surfactant solubility in CO2 and CO2 foam stability: MD simulation and experimental investigations.* Fuel, 2020. **267**: p. 117162.
168. Abel, S., et al., *Molecular modeling and simulations of AOT− water reverse micelles in isooctane: structural and dynamic properties.* The Journal of Physical Chemistry B, 2004. **108**(50): p. 19458-19466.
169. Harris, J.G. and K.H. Yung, *Carbon dioxide's liquid-vapor coexistence curve and critical properties as predicted by a simple molecular model.* The Journal of Physical Chemistry, 1995. **99**(31): p. 12021-12024.
170. Yu, Y.-X. and J. Wu, *Structures of hard-sphere fluids from a modified fundamental-measure theory.* The Journal of Chemical Physics, 2002. **117**(22): p. 10156-10164.
171. Jin, Z. and J. Wu, *Hybrid MC−DFT Method for Studying Multidimensional Entropic Forces.* The Journal of Physical Chemistry B, 2011. **115**(6): p. 1450-1460.
172. Eastoe, J., S. Gold, and D.C. Steytler, *Surfactants for CO2.* Langmuir, 2006. **22**(24): p. 9832-9842.
173. Mathiassen, O.M., *CO2 as injection gas for enhanced oil recovery and estimation of the potential on the Norwegian continental shelf.* Trondheim, Norway, 2003.
174. Jarrell, P.M., et al., *Practical aspects of CO2 flooding*. Vol. 22. 2002: Society of Petroleum Engineers Richardson, TX.
175. Li, C., H. Pu, and J.X. Zhao, *Molecular simulation study on the volume swelling and the viscosity reduction of n-alkane/co2 systems.* Industrial & Engineering Chemistry Research, 2019. **58**(20): p. 8871-8877.
176. Wang, G. *A laboratory study of CO2 foam properties and displacement mechanism*. in *SPE Enhanced Oil Recovery Symposium*. 1984. OnePetro.
177. Di Julio, S. and A. Emanuel, *Laboratory study of foaming surfactant for CO2 mobility control.* SPE Reservoir Engineering, 1989. **4**(02): p. 136-142.
178. Du, D., P.L.J. Zitha, and M.G. Uijttenhout, *Carbon dioxide foam rheology in porous media: a CT scan study.* SPE Journal, 2007. **12**(02): p. 245-252.
179. Talebian, S.H., et al., *Foam assisted CO2-EOR: A review of concept, challenges, and future prospects.* Journal of Petroleum Science and Engineering, 2014. **120**: p. 202-215.
180. Tsau, J.-S. and J. Heller. *Evaluation of surfactants for CO2-foam mobility control*. in *Permian Basin Oil and Gas Recovery Conference*. 1992. OnePetro.
181. Tsau, J.-S. and J.P. Heller. *How can selective mobility reduction of CO2-foam assist in reservoir floods?* in *Permian Basin Oil and Gas Recovery Conference*. 1996. OnePetro.
182. Wellington, S. and H. Vinegar. *CT studies of surfactant-induced CO2 mobility control*. in *SPE Annual Technical Conference and Exhibition*. 1985. OnePetro.
183. Qingfeng, H., et al. *Studies on foam flooding EOR technique for Daqing reservoirs after polymer flooding*. in *SPE Improved Oil Recovery Symposium*. 2012. OnePetro.
184. Wang, D., et al. *Sweep improvement options for the Daqing oil field*. in *SPE/DOE symposium on improved oil recovery*. 2006. OnePetro.
185. Patzek, T.W., *Field applications of steam foam for mobility improvement and profile control.* SPE Reservoir Engineering, 1996. **11**(02): p. 79-86.
186. Lawson, J. *The adsorption of non-ionic and anionic surfactants on sandstone and carbonate*. in *SPE symposium on improved methods of oil recovery*. 1978. OnePetro.
187. Le, V.Q., Q.P. Nguyen, and A. Sanders. *A novel foam concept with CO2 dissolved surfactants*. in *SPE symposium on improved oil recovery*. 2008. OnePetro.

188. Talebian, S.H., et al. *Foam assisted CO2-EOR; concepts, challenges and applications*. in *SPE Enhanced Oil Recovery Conference*. 2013. OnePetro.
189. Renpu, W., *Measures for Putting a Well into Production.* Advanced Well Completion Engineering. Gulf Professional Publishing, 2011. **8**: p. 417-523.
190. Patist, A., T. Axelberd, and D.O. Shah, *Effect of long chain alcohols on micellar relaxation time and foaming properties of sodium dodecyl sulfate solutions.* Journal of colloid and interface science, 1998. **208**(1): p. 259-265.
191. Sheng, J.J., *Foams and their applications in enhancing oil recovery*, in *Enhanced Oil recovery field case studies*. 2013, Elsevier. p. 251-280.
192. Miyashita, M., et al., *Improving foam stability of ethanol/water mixture with anionic surfactant and long-chain alcohol.* Chemistry Letters, 2020. **49**(5): p. 453-456.
193. Elizalde-Solis, O., et al., *Vapor–liquid equilibria and critical points of the CO2+ 1-hexanol and CO2+ 1-heptanol systems.* Fluid phase equilibria, 2003. **210**(2): p. 215-227.
194. Hsieh, C.-M. and J. Vrabec, *Vapor–liquid equilibrium measurements of the binary mixtures CO2+ acetone and CO2+ pentanones.* The Journal of Supercritical Fluids, 2015. **100**: p. 160-166.
195. Yau, J.S. and F.N. Tsai, *Solubilities of 1-hexadecanol and 1-octadecanol in subcritical and supercritical carbon dioxide.* Journal of Chemical and Engineering Data, 1992. **37**(3): p. 285-287.
196. Amidon, G., S.H. Yalkowsky, and S. Leung, *Solubility of nonelectrolytes in polar solvents II: solubility of aliphatic alcohols in water.* Journal of pharmaceutical sciences, 1974. **63**(12): p. 1858-1866.
197. Iwai, Y., et al., *Measurement of entrainer effects of water and ethanol on solubility of caffeine in supercritical carbon dioxide by FT-IR spectroscopy.* The Journal of supercritical fluids, 2006. **38**(3): p. 312-318.
198. Aono, K., et al., *Relationship between air-water interfacial dilational viscoelasticity and foam property in aqueous solutions of sodium alkylsulfates with different hydrocarbon chains.* Journal of Dispersion Science and Technology, 2021. **42**(8): p. 1218-1224.
199. Vlcek, L., A.A. Chialvo, and D.R. Cole, *Optimized unlike-pair interactions for water–carbon dioxide mixtures described by the SPC/E and EPM2 models.* The Journal of Physical Chemistry B, 2011. **115**(27): p. 8775-8784.
200. Jungwirth, P. and D. Tobias, *Ions at the air/water interface.* The Journal of Physical Chemistry B, 2002. **106**(25): p. 6361-6373.
201. Jungwirth, P. and D.J. Tobias, *Specific ion effects at the air/water interface.* Chemical reviews, 2006. **106**(4): p. 1259-1281.
202. Garrett, B.C., *Ions at the air/water interface.* Science, 2004. **303**(5661): p. 1146-1147.
203. Levin, Y., A.P. Dos Santos, and A. Diehl, *Ions at the air-water interface: an end to a hundred-year-old mystery?* Physical review letters, 2009. **103**(25): p. 257802.
204. Lemmon, E., et al., *Thermophysical Properties of Fluid Systems.* in NIST Chemistry WebBook, NIST Standard Reference Database Number 69, Eds. P.J. Linstrom and W.G. Mallard, National Institute of Standards and Technology, Gaithersburg MD, 20899, https://doi.org/10.18434/T4D303, (retrieved April 23, 2020).
205. Menger, F.M. and S.A. Rizvi, *Relationship between surface tension and surface coverage.* Langmuir, 2011. **27**(23): p. 13975-13977.
206. Wang, X., et al., *Cation bridging studied by specular neutron reflection.* Langmuir, 2013. **29**(18): p. 5520-5527.

207. Gerold, C.T. and C.S. Henry, *Observation of dynamic surfactant adsorption facilitated by divalent cation bridging.* Langmuir, 2018. **34**(4): p. 1550-1556.
208. Allen, F.J., et al., *Potassium, calcium, and magnesium bridging of AOT to mica at constant ionic strength.* Langmuir, 2019. **35**(17): p. 5753-5761.
209. Span, R. and W. Wagner, *A new equation of state for carbon dioxide covering the fluid region from the triple‐point temperature to 1100 K at pressures up to 800 MPa.* Journal of physical and chemical reference data, 1996. **25**(6): p. 1509-1596.
210. Wagner, W. and A. Pruß, *The IAPWS formulation 1995 for the thermodynamic properties of ordinary water substance for general and scientific use.* Journal of physical and chemical reference data, 2002. **31**(2): p. 387-535.
211. Wang, Z., et al., *Determination of water solubility in supercritical CO2 from 313.15 to 473.15 K and from 10 to 50 MPa by in-situ quantitative Raman spectroscopy.* Fluid Phase Equilibria, 2018. **476**: p. 170-178.
212. Duan, Z. and R. Sun, *An improved model calculating CO2 solubility in pure water and aqueous NaCl solutions from 273 to 533 K and from 0 to 2000 bar.* Chemical geology, 2003. **193**(3-4): p. 257-271.
213. Pereira, L.M., et al., *Study of the impact of high temperatures and pressures on the equilibrium densities and interfacial tension of the carbon dioxide/water system.* The Journal of Chemical Thermodynamics, 2016. **93**: p. 404-415.

Appendix A

A.1. Force Field Calibration

Table A-1 The density of pure n-Decane

Condition	Our simulation (kg/m^3)	NIST chemistry webbook[204] (kg/m^3)	Relative error
300 K, 1 bar	710.38	725.09	-2.03%
353 K, 200 bar	695.41	703.37	-1.13%

Table A-2 Density of brine

Condition	Our simulation (kg/m^3)	NIST chemistry webbook[204] (kg/m^3)	Relative error
353 K, 200 bar	1064.99	1067.07	-0.19%

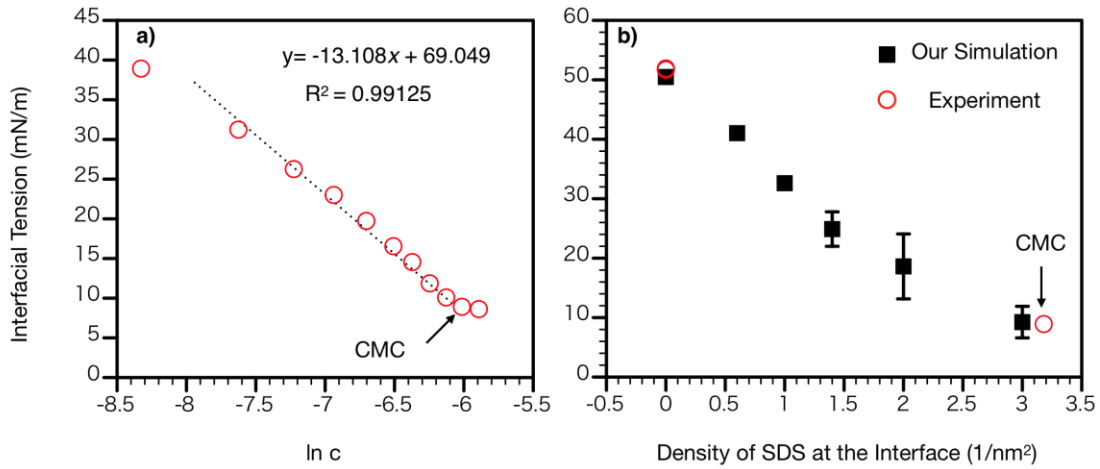

Figure A-1. a) Interfacial tension as a function of ln c. b) Comparison of interfacial tension obtained from experiment[101] and our simulation under ambient conditions (298.15 K, 1bar).

To compare experimental results with our simulation, we analyzed the surface coverage of SDS at critical micelle concentration (CMC) in **Fig. A-1.** using the Gibbs equation[205],

$$\Gamma = -\frac{d\gamma / d(\ln c)}{RT}, \tag{A-1}$$

where the Γ is the surface excess (equivalent to the interfacial concentration in units of 1/nm^2), γ is the interfacial tension, c is the surfactant concentration, R is the gas constant. The SDS concentration at the interfaces at CMC condition is around 3.18/nm^2, with the corresponding interfacial tension as ~8.91 mN/m.

A.2. Density Profiles in Varying Salt Concentrations

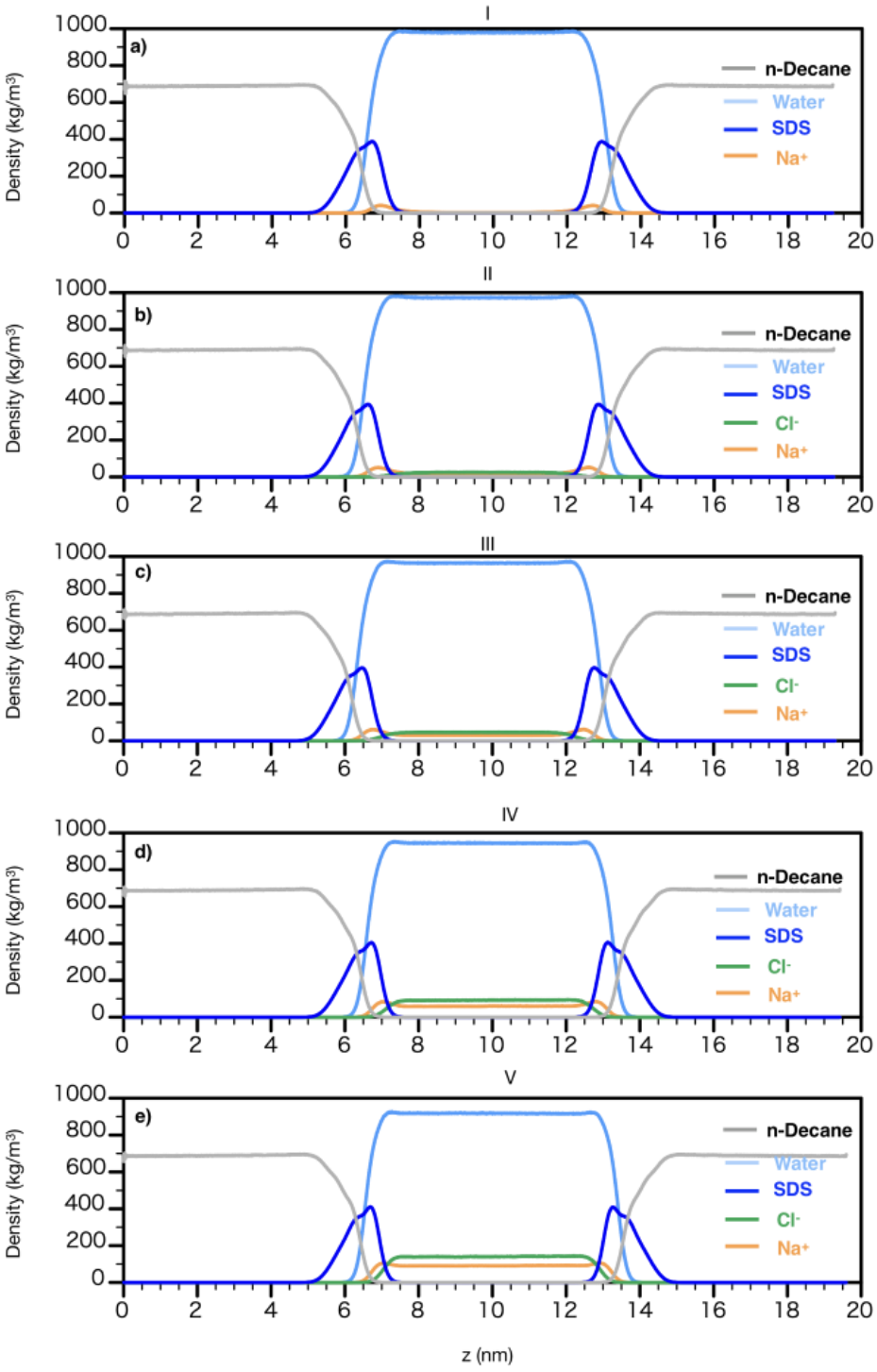

Figure A-2 The density distribution of each component with various concentrations of salts for the systems with SDS only and monovalent ions.

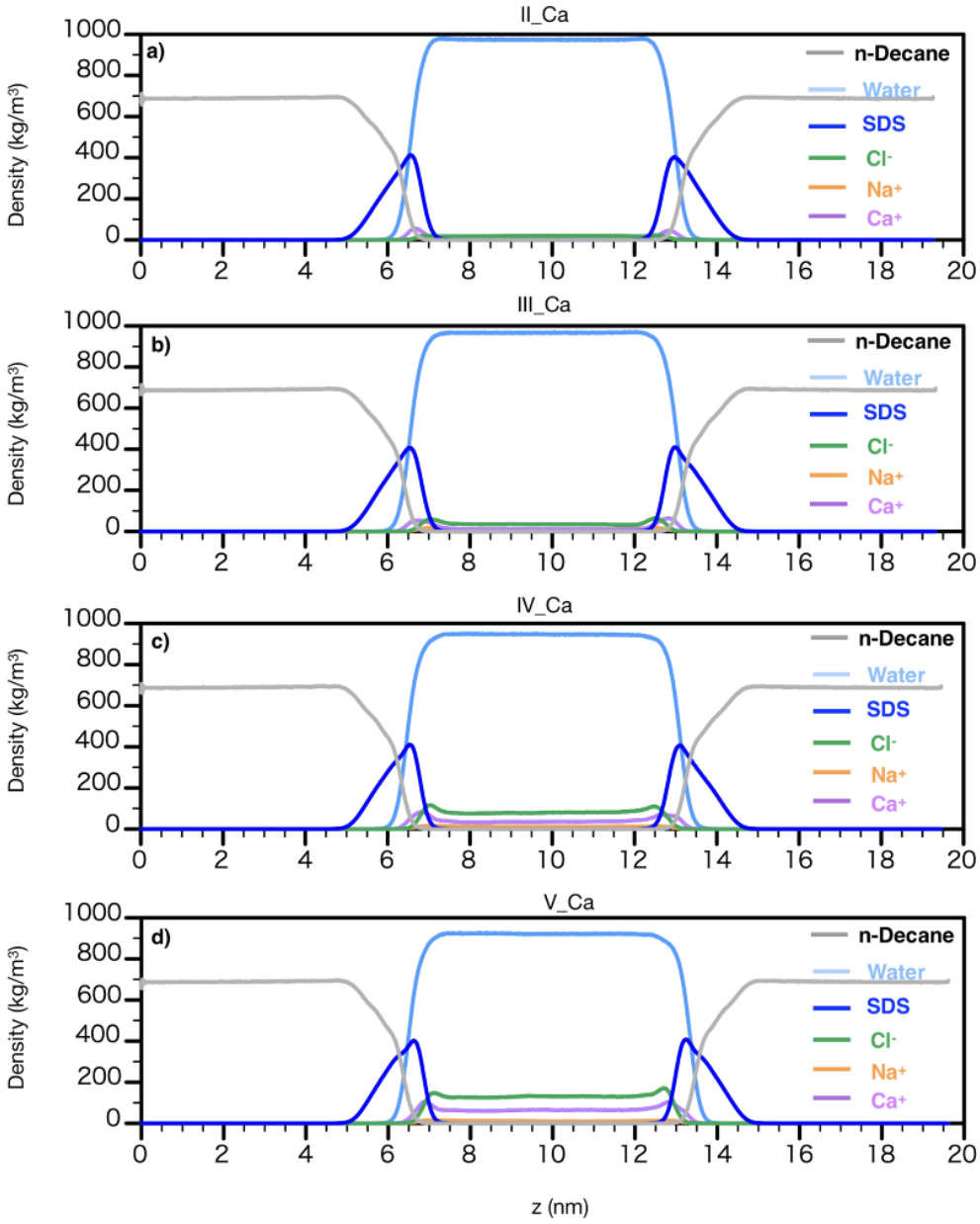

Figure A-3 The density distribution of each component with various concentrations of salts for the systems with SDS only and divalent ions.

A.3. Density Distributions of ions in the Systems without SDS

Table A-3. Number of molecules in the systems without SDS

System	Water	Na^+	Cl^-	Ca^{2+}	n-Decane
a	5200	50	0	0	874
b	5200	100	50	0	874
c	5200	152	102	0	874
d	5200	270	220	0	874
e	5200	402	352	0	874
b_Ca	5200	50	50	25	874
c_Ca	5200	50	102	51	874
d_Ca	5200	50	220	110	874
e_Ca	5200	50	352	176	874

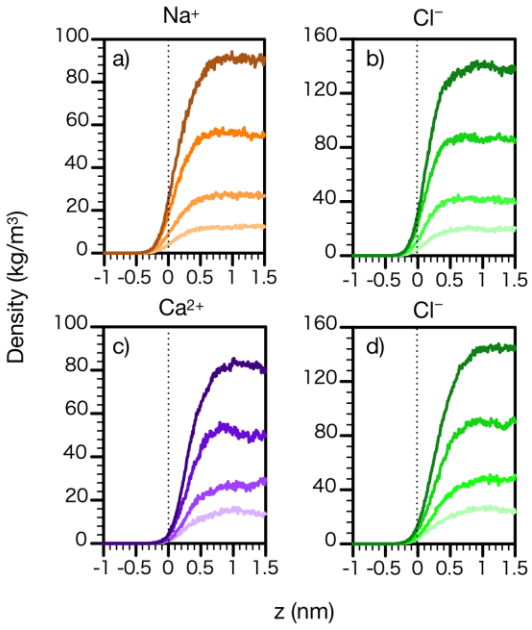

Figure A-4 Density distributions of a) Na^+ ions; b) Cl^- ions; for systems a, b, c, d, and e. Density distributions of c) Ca^{2+} ions; d) Cl^- ions; for systems b_Ca, c_Ca, d_Ca, and e_Ca. The darker color indicates higher salinity. The dotted lines represent the contact between the interface and the brine phase.

A.4. Criteria and Calculations for the Cation Bridging

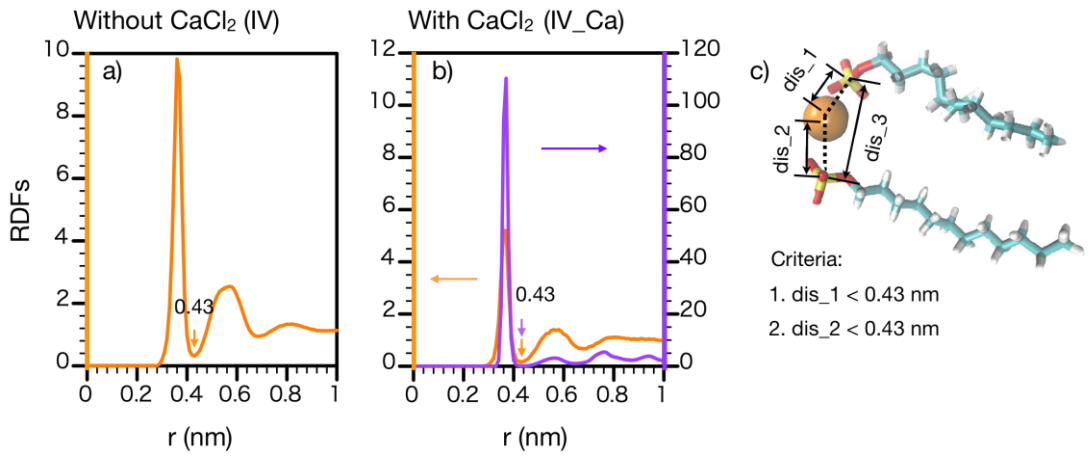

Figure A-5 RDFs of Na^+ (orange), and Ca^{2+} (purple) around SDS_S for a) system IV; b) system IV_Ca. c) Criteria for cation bridging.

One restriction is applied to define the cation bridging as shown in **Fig. A-5. c)**: the distance between SDS_S and one cation (Na^+ or Ca^{2+}) is less than 0.43 nm. This value (0.43 nm) is obtained from the RDFs in **Fig. A-5**, which is the distance of SDS_S and cation when the RDF is at the first local minimum.

The cation bridging distribution is given as

$$\rho_{CB}(r) = \left\langle \frac{N(r)}{A_{xy}} \right\rangle, \tag{A-2}$$

where $N(r)$ is the number of cation bridging with SDS_S-SDS_S distance within r to $r+\Delta r$; A_{xy} is the cross-sectional area in the *x*-*y* plane; $\langle ... \rangle$ implies averaging over time and molecules.

Total cation bridging density is given as

$$\rho_{T,CB} = \int_0^\infty \rho_{CB}(r)\, dr \tag{A-3}$$

where $\rho_{CB}(r)$ is the cation bridging density profile.

A.5. Effect of Forcefield

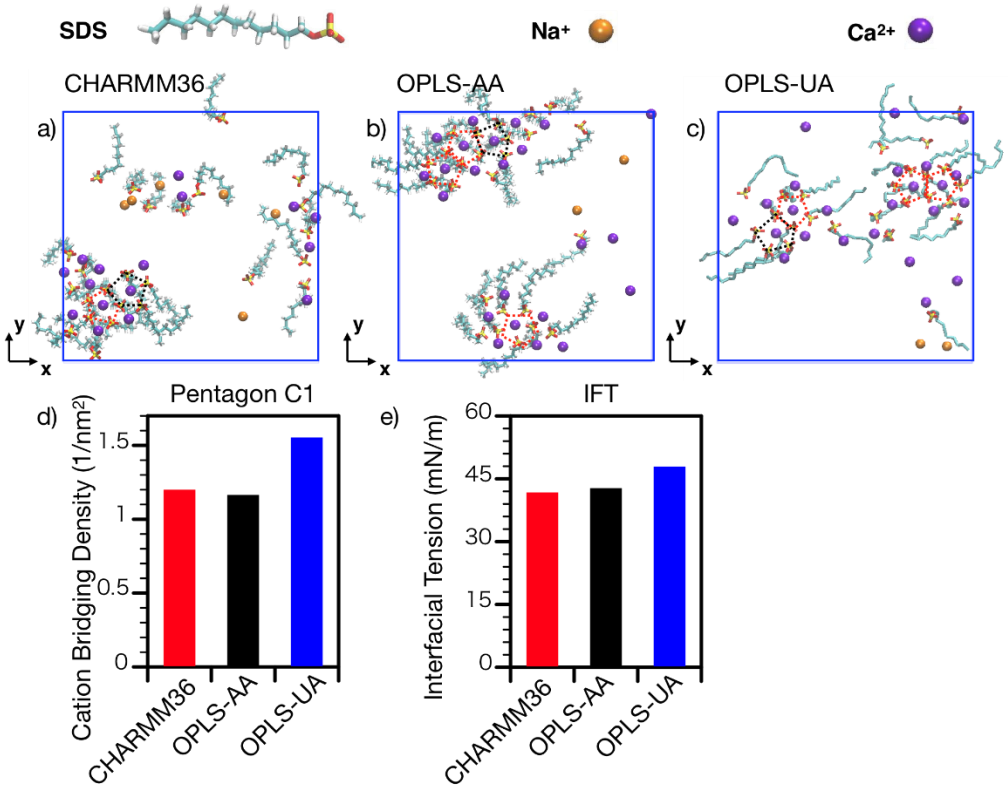

Figure A-6 The snapshots in the *x-y* plane with forcefield a) CHARMM36; c) OPLS-AA; d) OPLS-UA. The black dashed lines enclose the structures satisfying Pentagon_C1 but not qualifying as Pentagon_C2. The red dashed lines enclose the structures satisfying Pentagon_C2. d) cation bridging density and e) IFT calculated from different forcefields.

The pentagon-like structures are still observed with OPLS-AA and OPLS-UA forcefields. The cation-bridging density originated from the pentagon-like structure is also in the same order from different forcefields.

A.6. Analysis on the Pentagon-like Structures

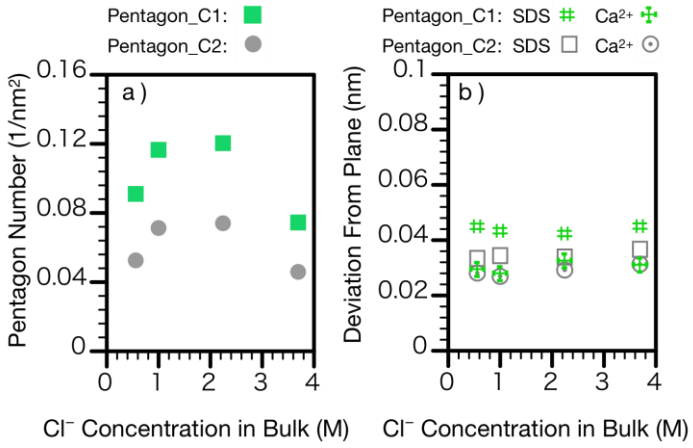

Figure A-7 a) Criteria for pentagon-like structure; b) Pentagon_C1 and Pentagon_C2 number densities in different systems; c) standard deviation distances of SDS_S and Ca^{2+} ion from the optimized plane.

A.7. Mass Density Profile of Molecules at the Interface Region

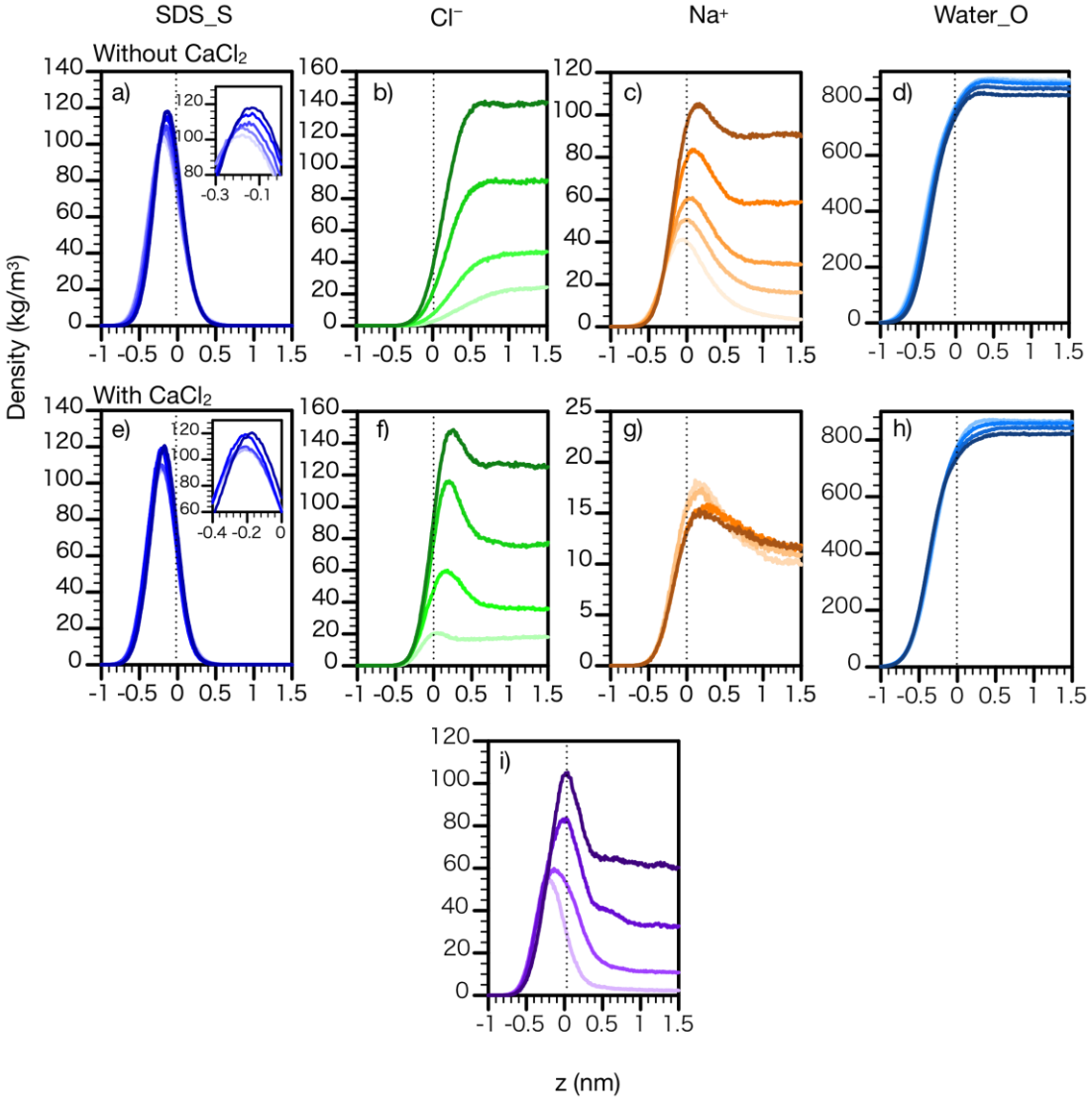

Figure A-8 Density distributions of a) SDS; b) Cl^- ions; c) Na^+ ions; d) O atom in water (Water_O) for systems I, II, III, IV, and V. Density distributions of e) SDS; f) Cl^- ions; g) Na^+ ions; h) Water_O; i) Ca^{2+} ions for systems II_Ca, III_Ca, IV_Ca, and V_Ca. The darker color indicates higher salinity. The dotted lines represent the contact between the interface and the brine phase.

A.8. Comparison of Cation Bridging Density for System IV_Ca and V_Ca

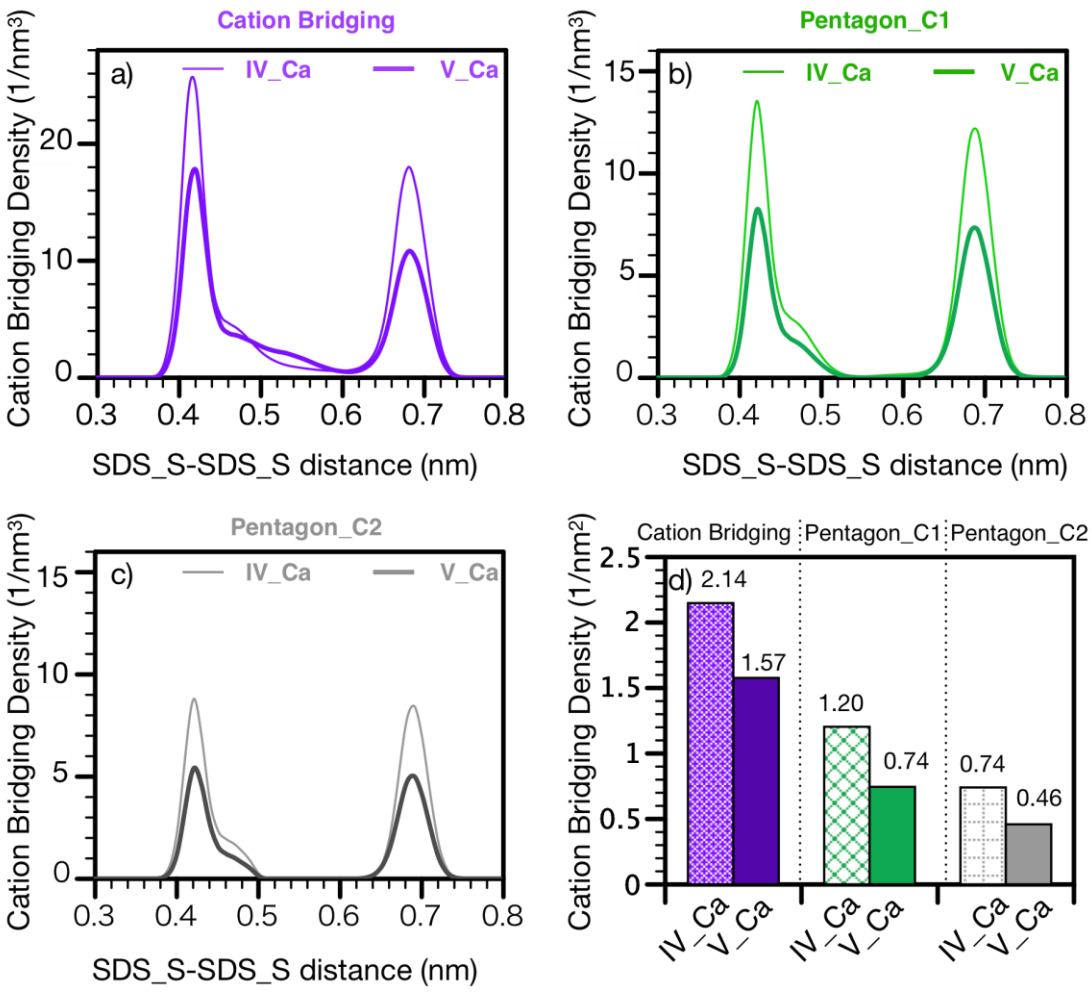

Figure A-9 a-c) Cation bridging distributions in system IV_Ca and system V_Ca in different scenarios; d) Cation bridging density in system IV_Ca and V_Ca in different scenarios, respectively.

A.9. RDDs of Molecules around SDS_S

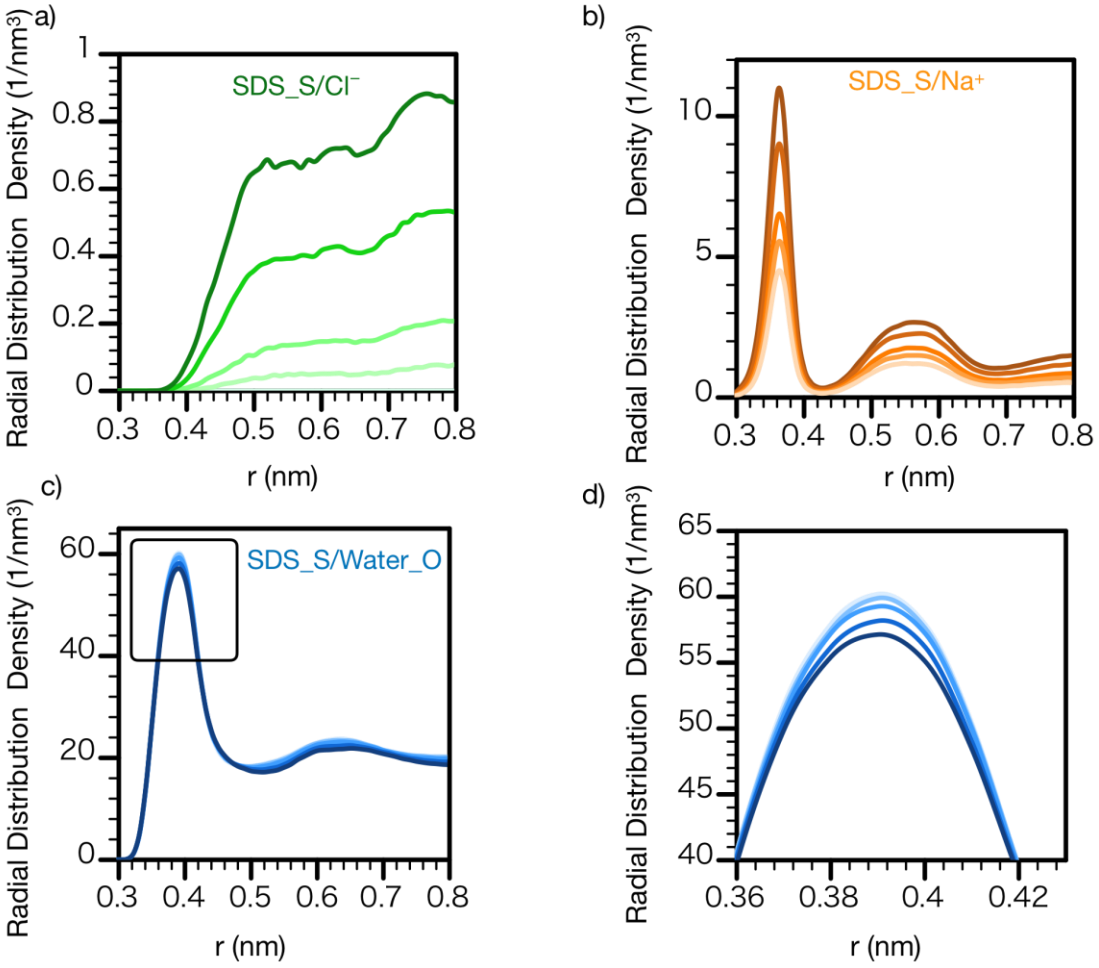

Figure A-10. RDDs of a) Cl^-, b) Na^+ ,and c) Water_O around SDS_S; and d) enlargement of c).

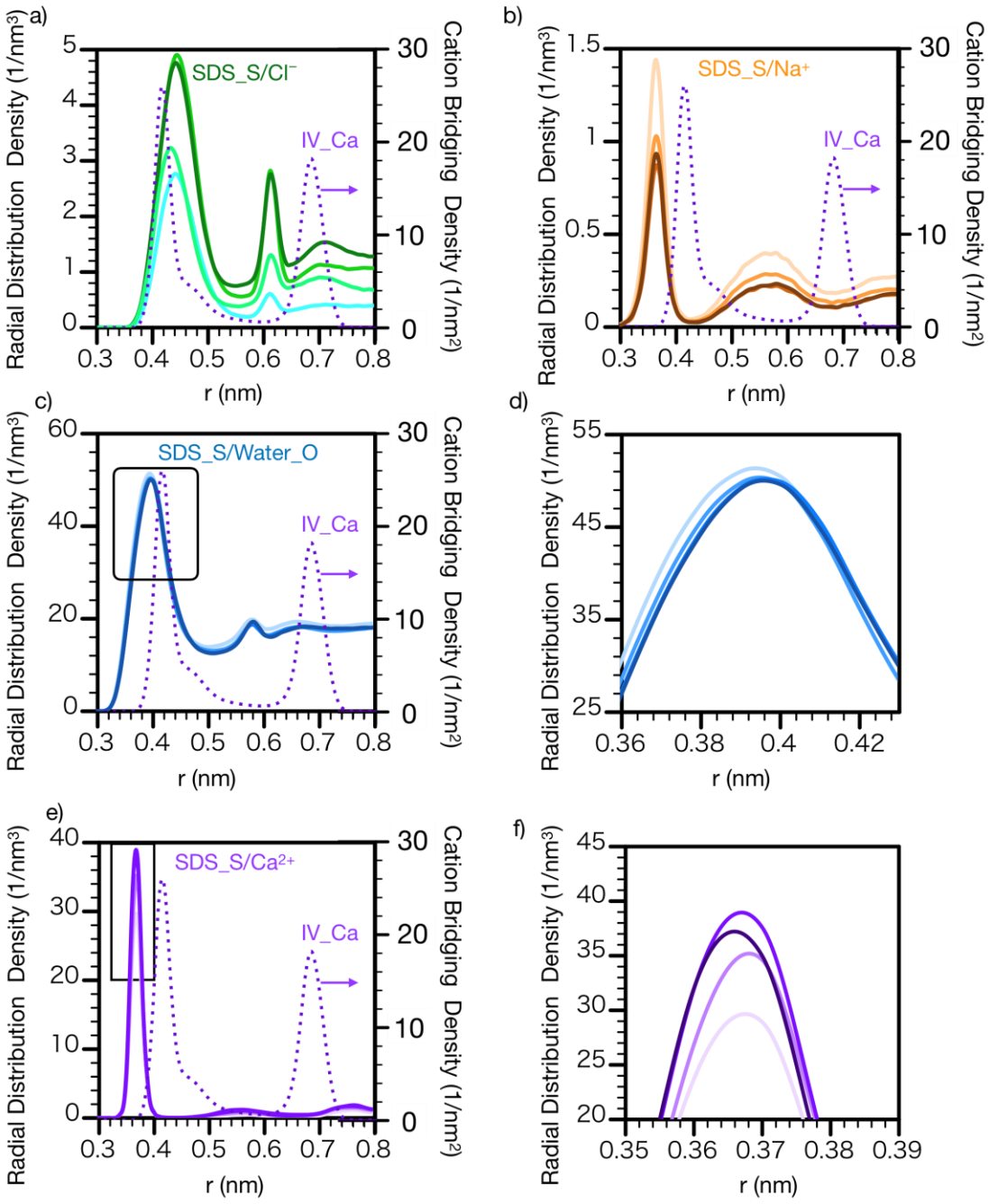

Figure A-11 RDDs of a) Cl^- ions; b) Na^+ ions; c) Water_O; e) Ca^{2+} ions around SDS_S; and d) enlargement of c); f) enlargement of e).

A.10. Orientation Parameter of SDS in all the Systems

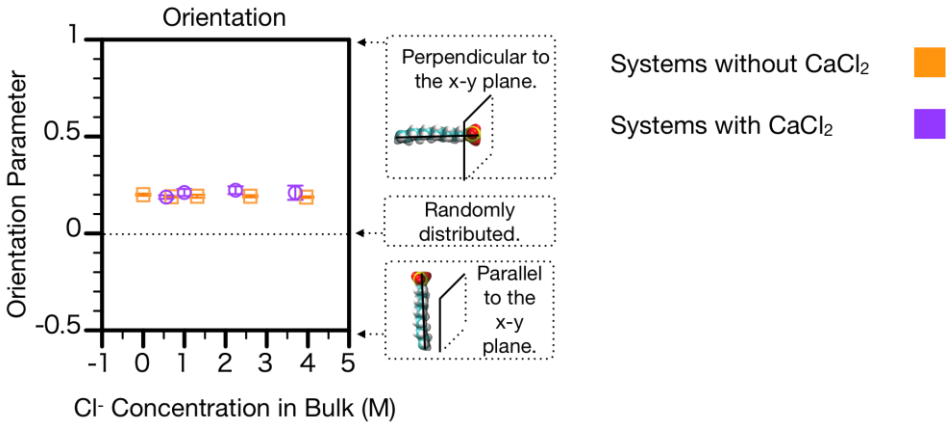

Figure A-12 Orientation parameter of SDS for the systems without (orange, I, II, III, IV, and V) and with (purple, II_Ca, III_Ca, IV_Ca, and V_Ca) Ca^{2+} ions at various salt concentrations.

A.11. Under Ambient Conditions

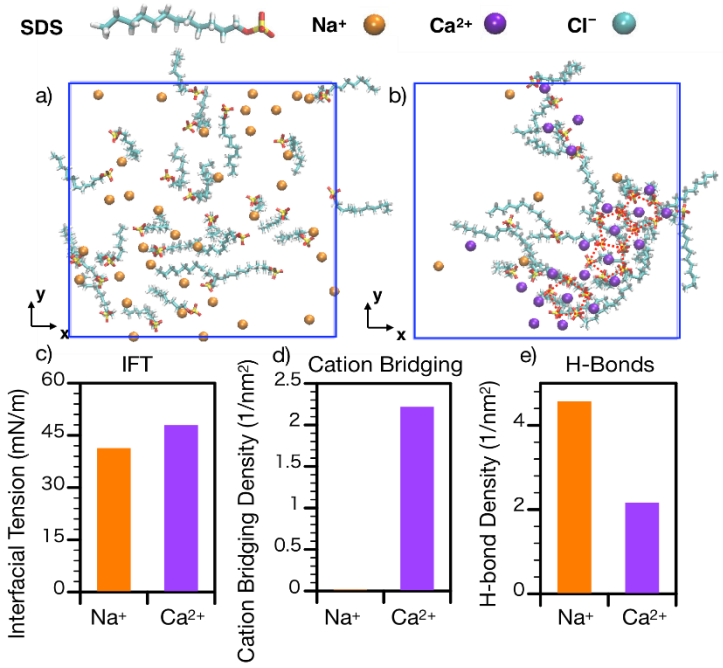

Figure A-13 a) The snapshots in the *x*-*y* plane for a) system IV; b) system IV_Ca; under ambient conditions (298.15 K, 1 bar). c) Interfacial tension; d) cation bridging density; e) H-bond densities of systems IV and IV_Ca under ambient conditions (298.15 K, 1 bar).

A.12. Ion Size Effect on Interfacial Properties

Table A-4 σ parameters in forcefield CHARMM

Ion type	σ (nm)
Na^+	0.24357
Ca^{2+}	0.25137
K^+	0.31426
Mg^{2+}	0.21114

Table A-5 Number of molecules in the systems

System	SDS	Water	Na^+	Cl^-	Ca^{2+}	K^+	Mg^{2+}	n-Decane
IV	50	5200	270	220	0	0	0	874
IV_Ca	50	5200	50	102	51	0	0	874
IV_K	50	5200	50	220	0	220	0	874
IV_Mg	50	5200	50	220	0	0	110	874

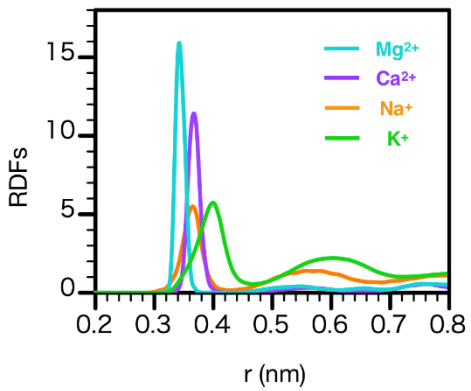

Figure A-14 Radial distribution functions of the cations around SDS_S in systems IV, IV_Ca, IV_K, and IV_Mg.

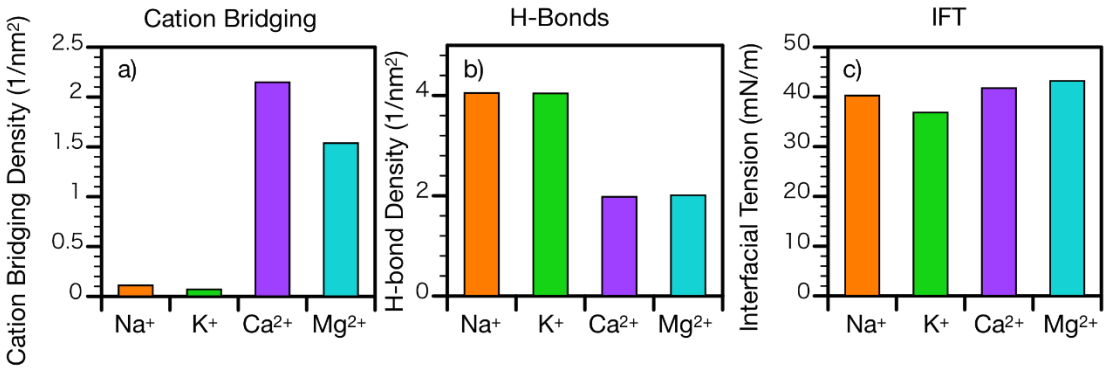

Figure A-15 a) Cation bridging densities; b) H-bond densities; c) interfacial tension for systems IV, IV_K, IV_Ca, and IV_Mg, respectively.

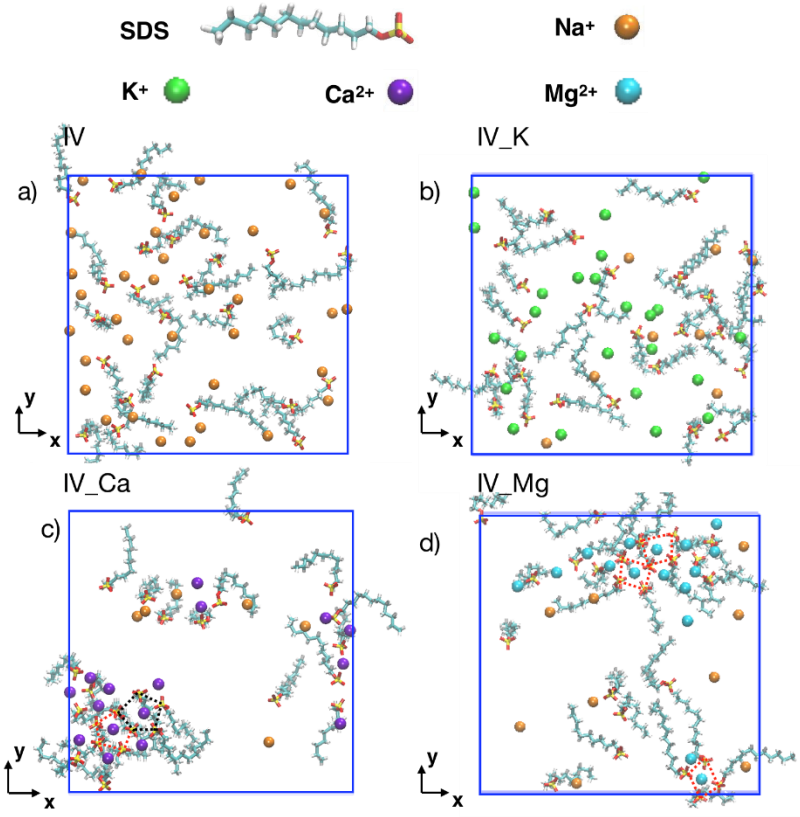

Figure A-16 The snapshots in the *x-y* plane for a) system IV; b) system IV_K; c) system IV_Ca; e) system IV_Mg. Red and black dotted lines are the eye guidance for the special structures formed by SDS and cations.

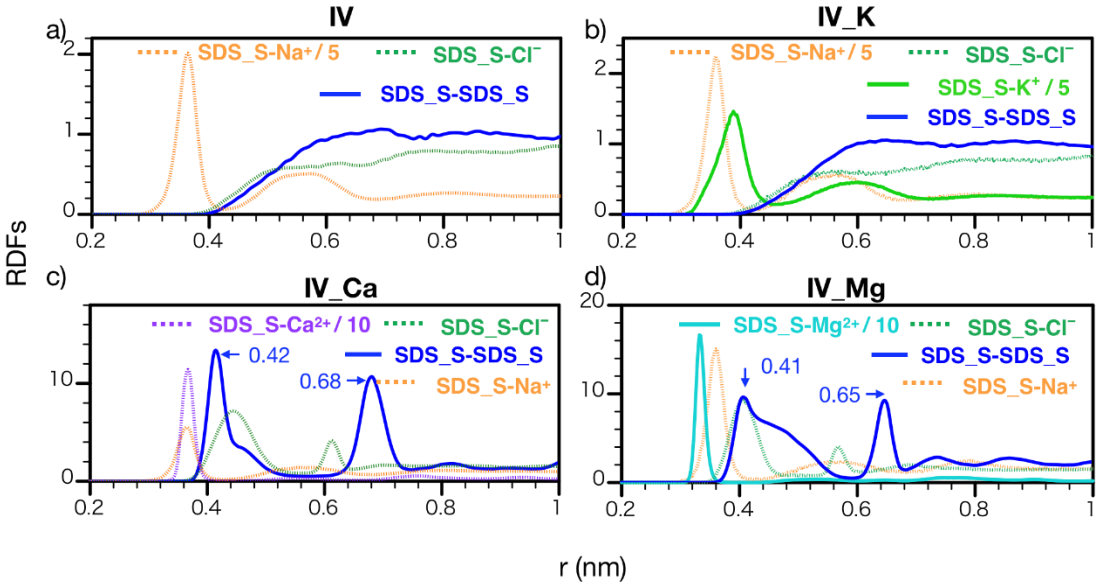

Figure A-17 RDFs of SDS_S and ions around SDS_S in a) system IV; b) system IV_K; c) system IV_Ca; d) system IV_Mg.

Appendix B

B.1. Literatures on Studies on Cation Bridging

Table B-1 Literatures on studies on cation bridging

Phase 1	Phase2	Surfactant	Temperature (K)	Pressure (bar)	Methods	Ref.
Brine (~ 0.33M Ca^{2+})	Air	SDS	298.15	1	MD	[87]
Brine (up to ~1.8 M Ca^{2+})	n-decane	SDS	333.15	200	MD	[64]
Brine (~ 1.5 M Ca^{2+}/Mg^{2+})	/	SDS/SDSn	298.15	1	MD	[65]
Water	/	Ca $(AOT)_2$	Ambient	Ambient	experiment	[206]
Brine (~ 1 mM Ca^{2+})	polydimethylsiloxane (PDMS) surface	2-naphthoate	Ambient	Ambient	experiment	[207]
Brine (~ up to 6.25 mM Ca^{2+}/ Mg^{2+}/Na^{+}/K^{+})	Mica surface	AOT	Ambient	Ambient	experiment	[208]

B.2. Initial Configurations

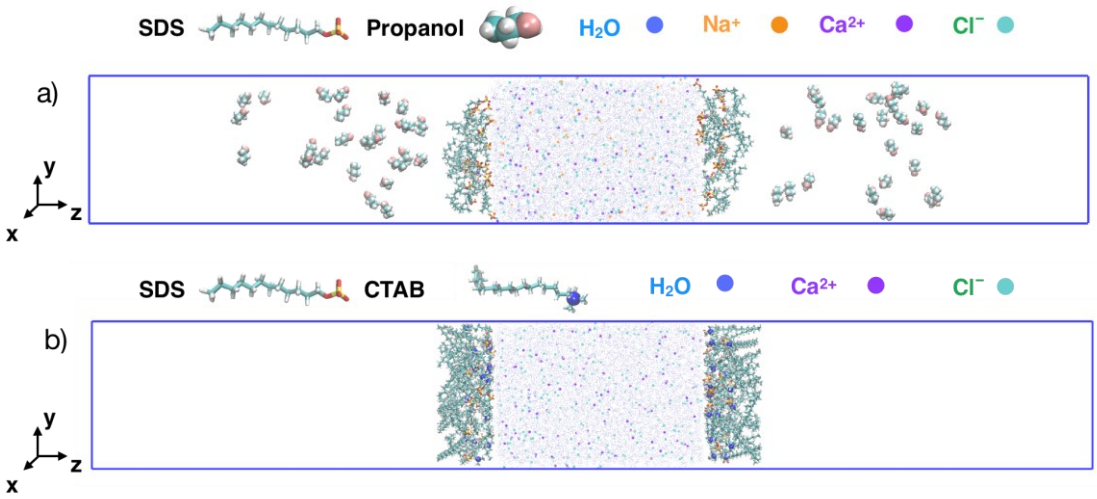

Figure B-1 Initial configuration of simulation in a) system SDS50_Prop50; b) system SDS50_CTAB50. Oil phases are not shown for clarity. The periodic boundaries are depicted by the blue rectangular.

B.3. Radial Distribution Functions (RDFs) of Molecules around CTAB_N

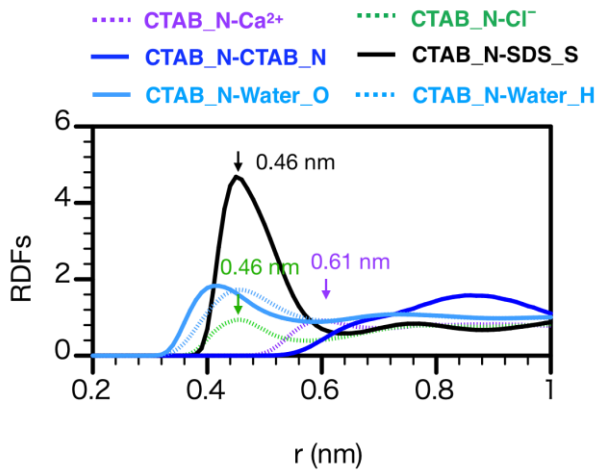

Figure B-2 RDFs of Ca^{2+}, Cl^{-}, CTAB_N, SDS_S, Water_O, and Water_H around CTAB_N in system SDS50_CTAB50.

B.4. Radial Distribution Functions (RDFs)

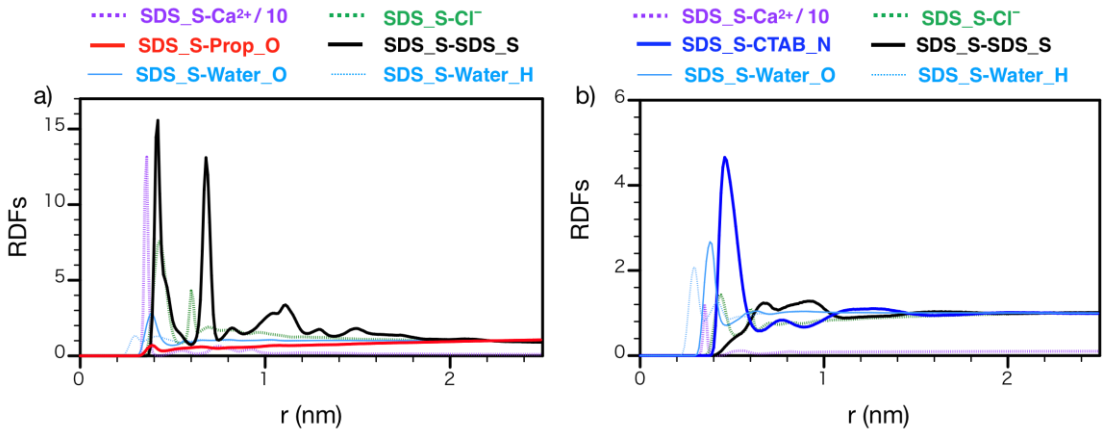

Figure B-3 RDFs of SDS_S, Prop_O, CTAB_N, water, and salt ions around SDS_S in a) system SDS50_Prop50; b) system SDS50_CTAB50. To clarify, SDS_S-Ca^{2+} RDFs are scaled down by 10 times for a better observation.

It is noted that we use two different formulas to calculate the radial distribution densities (RDDs) of the molecules mainly distributed in bulk (water and ions) (B-1) and the interface (surfactants and cosurfactants) (B-2)

$$\rho_{\mathrm{d,b}}(r) = \frac{\langle N(r) \rangle}{4\pi r^2 \Delta r}, \tag{B-1}$$

$$\rho_{\mathrm{d,i}}(r) = \frac{\langle N(r) \rangle}{2\pi r \Delta r}, \tag{B-2}$$

where $N(r)$ is the number of the molecules placed in the distance of r to $r + \Delta r$. $\langle \ldots \rangle$ implies averaging over time and molecules.

Correspondingly, two different formulas are used to calculate the radial distribution functions (RDFs) of the molecules mainly distributed in bulk (water and ions) (B-3) and the interface (surfactants and cosurfactants) (B-4).

$$\rho_{\mathrm{b}}(r) = \frac{\langle N(r) \rangle}{4\pi r^2 \Delta r \rho_{\mathrm{d,b,2\text{-}2.5}}(r)}, \tag{B-3}$$

$$\rho_{i}(r) = \frac{\langle N(r) \rangle}{2\pi r \Delta r \rho_{\mathrm{d,i,2\text{-}2.5}}(r)}, \tag{B-4}$$

where $\rho_{\mathrm{d,b,2\text{-}2.5}}(r)$ and $\rho_{\mathrm{d,i,2\text{-}2.5}}(r)$ are the average of $\rho_{\mathrm{d,b}}(r)$ and $\rho_{\mathrm{d,i}}(r)$ when $2 \le r \le 2.5\,\mathrm{nm}$, where the number density converges to a constant value.

B.5. Spatial Distribution Functions (SDFs)

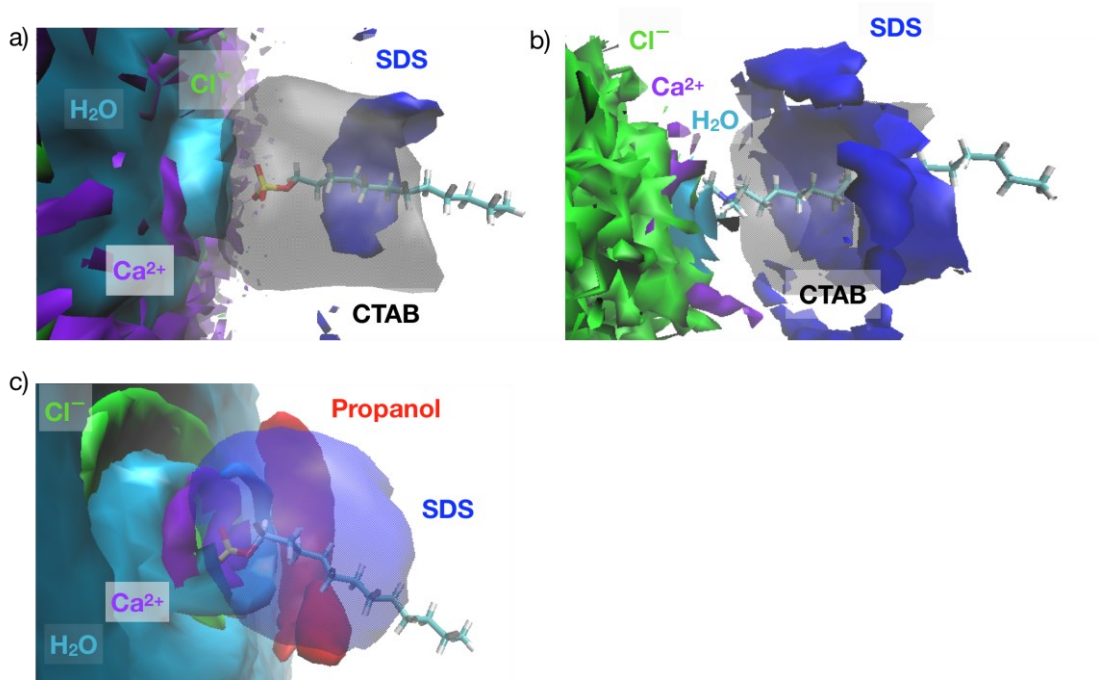

Figure B-4 Spatial distribution functions (SDFs) of a) water (50/nm^3), SDS (140/nm^3), CTAB (200/nm^3), Ca^{2+} (200/nm^3), and Cl^- (25/nm^3) around SDS molecule in system SDS50_CTAB50; b) water (50/nm^3), SDS (800/nm^3), CTAB (500/nm^3), Ca^{2+} (200/nm^3), and Cl^- (15/nm^3) around CTAB molecule in system SDS50_CTAB50; c). water (60/nm^3), SDS (1200/nm^3), propanol (500/nm^3), Ca^{2+} (1500/nm^3), and Cl^- (100/nm^3) around SDS molecule in system SDS50_Prop50.

B.6. Radial Distribution Functions (RDFs) of Ca^{2+} around SDS_S

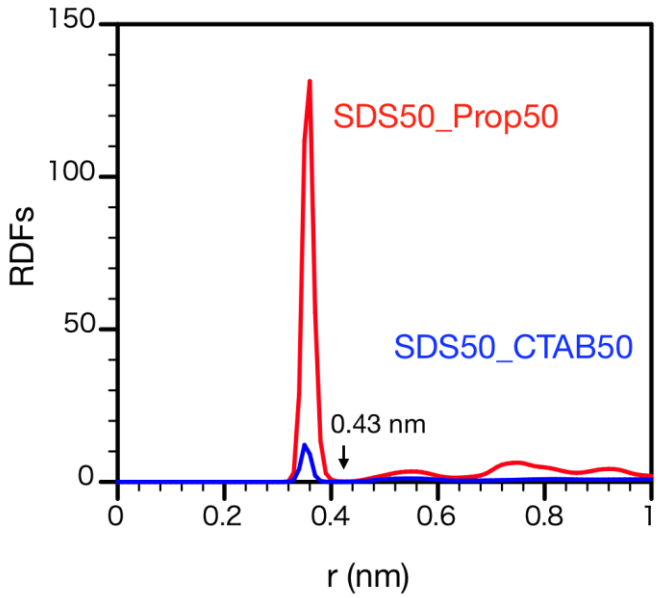

Figure B-5 RDFs of Ca^{2+}around SDS_S in systems SDS50_Prop50 and SDS50_CTAB50.

B.7. Fraction of Cation Bridging Oriented from Pentagon-Like Structure

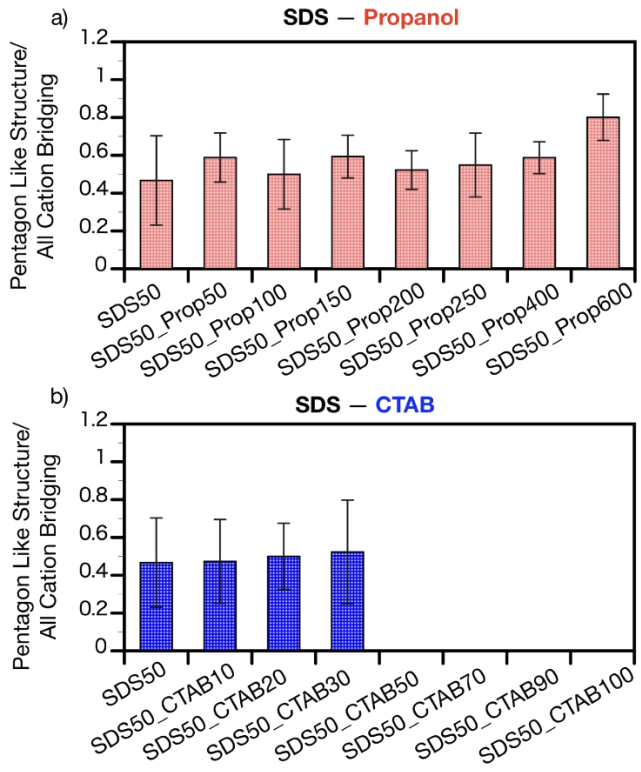

Figure B-6 Ratio of cation bridging densities in a) ASNC systems; b) ASCS systems

B.8. Criteria for H-bond (SDS, CTAB, and Propanol)

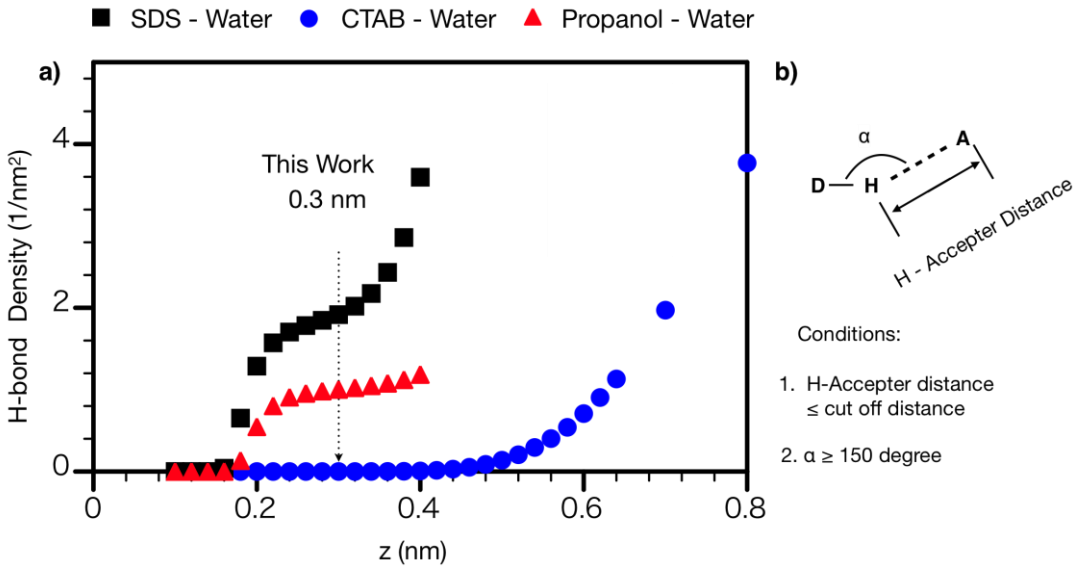

Figure B-7 Criteria for hydrogen bonding. H-bond densities of SDS-water and propanol-water in system SDS50_Prop50, and CTAB-water in system SDS50_CTAB50.

H-bond density between SDS and water increases rapidly as cut-off distance > 0.3 nm. This further increment should not be counted as hydrogen bonds, because it is contributed by water molecules from the second shell[65]. CTAB-water H-bond density is low when the cut-off distance is small (< ~ 0.4 nm), which is caused by the steric effect of the methyl groups. Further increment at large cut-off distances (> ~0.4 nm) should not be counted as the hydrogen bonds.

B.9. Water Solvation Structures around CTAB_N and SDS_S

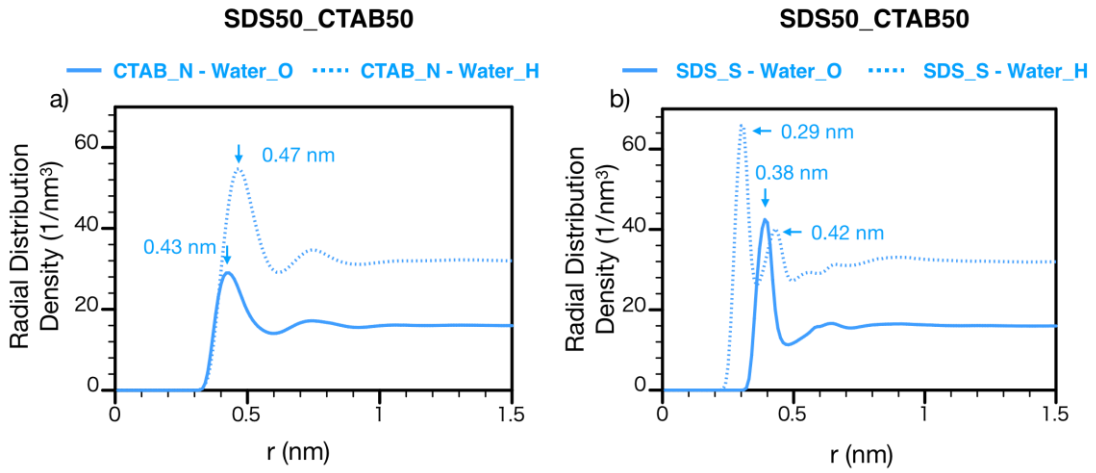

Figure B-8 Radial distribution densities of H and O elements from H_2O around a) CTAB_N; b) SDS_S in SDS50_CTAB50.

B.10. Water Solvation Structures under Varies CTAB and Propanol Concentrations

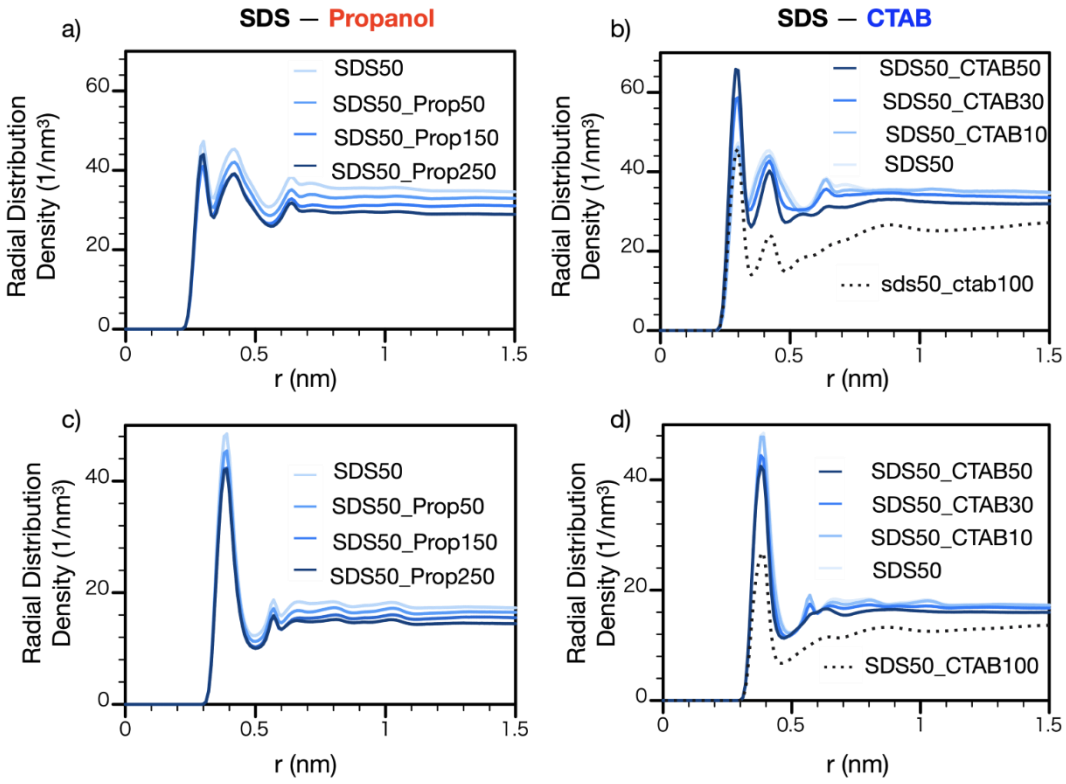

Figure B-9 The radial distribution density of H atom from H_2O around SDS_S in a) ASNC systems; b) ASCS systems. c); d): The same as a); b) but for O atom in H_2O around SDS_S.

B.11. SDS and CTAB Head Group Density Distributions in ASCS Systems

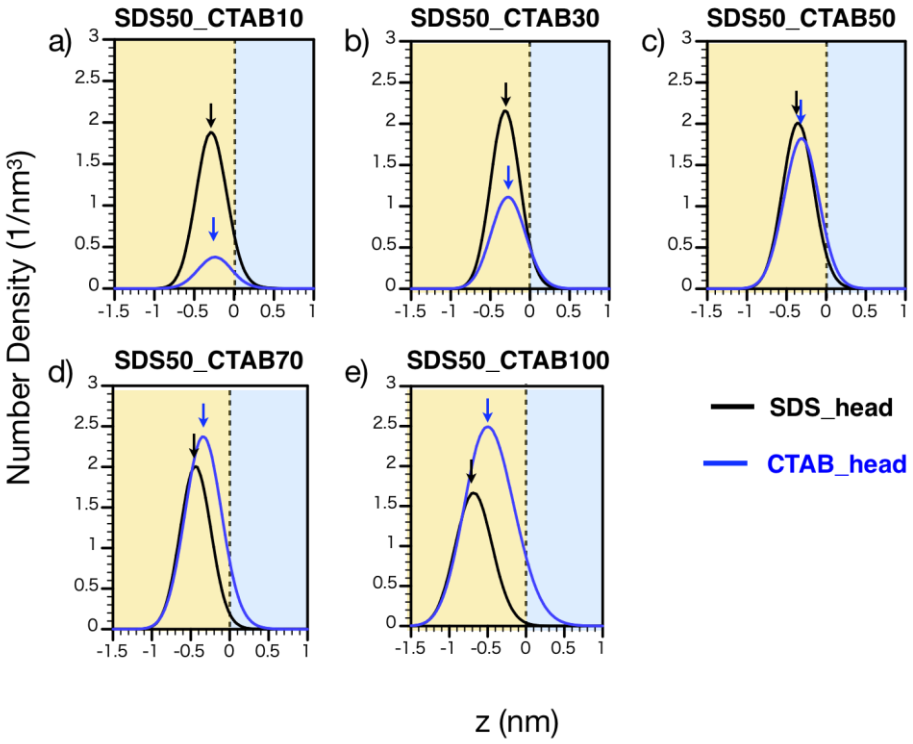

Figure B-10 SDS_head and CTAB_head density distributions in ASCS systems a) SDS50_CTAB10; b) SDS50_CTAB30; c) SDS50_CTAB50; d) SDS50_CTAB70; e) SDS50_CTAB100 . The entire functional group is counted as one unit; the black dashed lines represent the contact between the brine phase and the interface region. The brine phase and the interface region are represented by blue and yellow colors.

B.12. SDS and Propanol Hydrophobic Connector Distribution

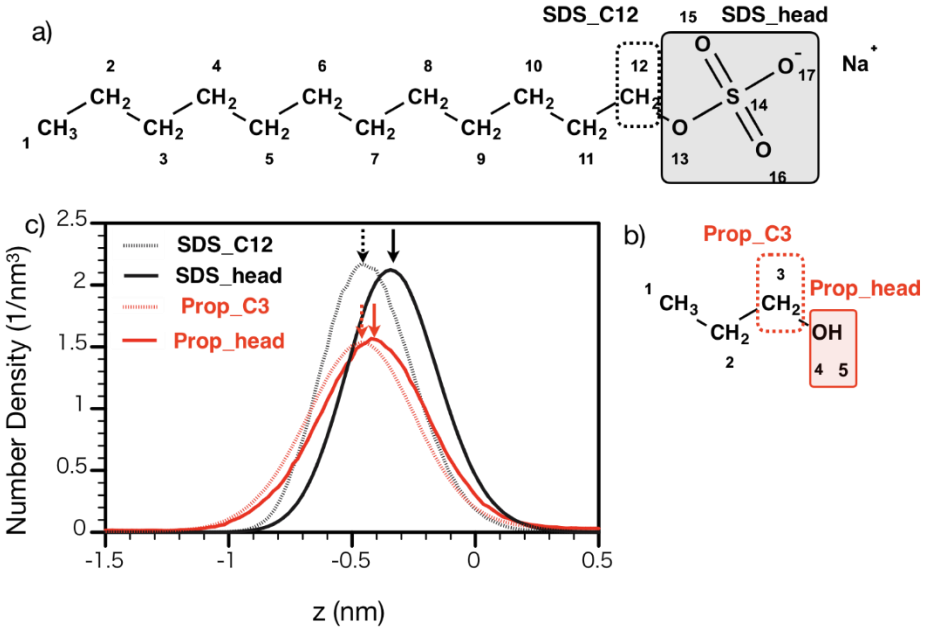

Figure B-11 Molecular structures of a) SDS; b) propanol. Number density distributions of functional groups in the interface region in c) system SDS50_Prop50. The entire functional group is counted as one unit".

B.13. Effect of Thermostats on IFT and Cation Bridging Density

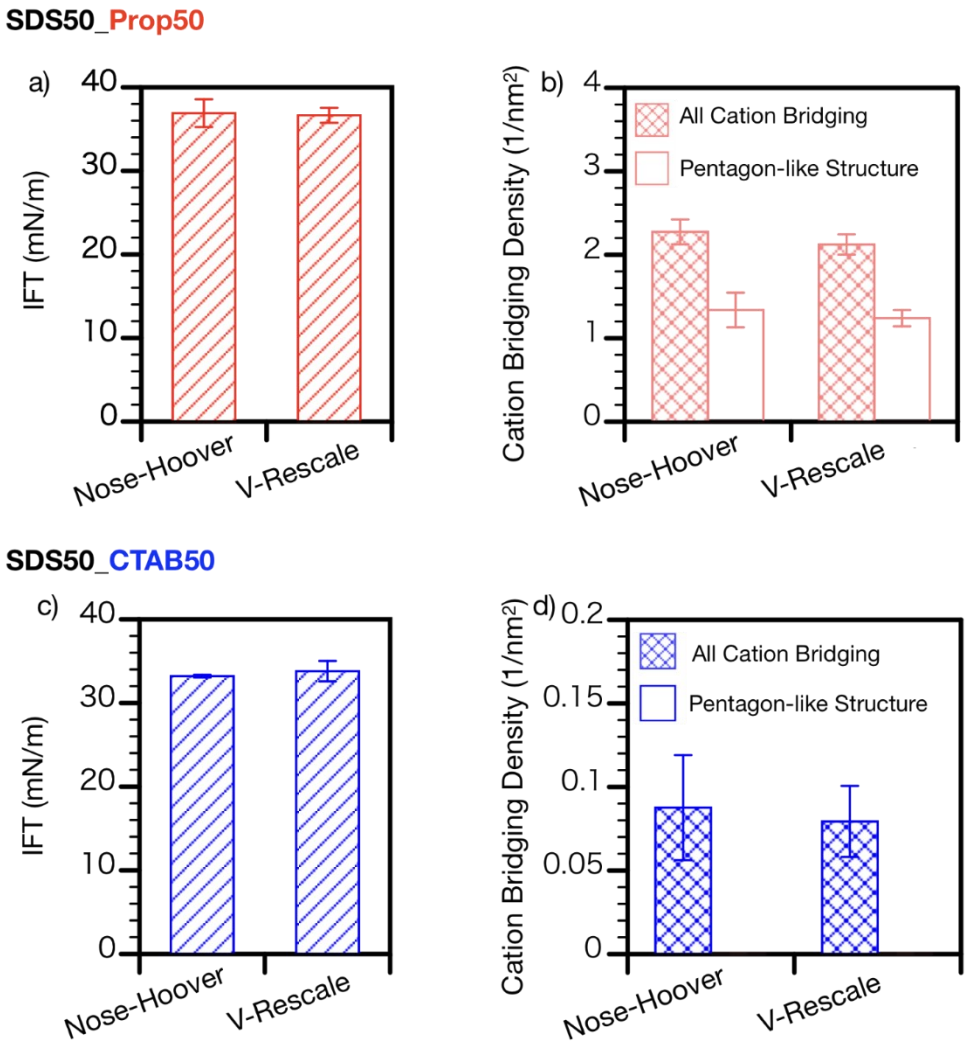

Figure B-12 Interfacial tension by using the different thermostats in systems a) SDS50_Prop50 and c) SDS50_CTAB50; cation bridging density by using different thermostats in systems b) SDS50_Prop50 and d) SDS50_CTAB50.

B.14. H-bond Formation Per SDS Molecule

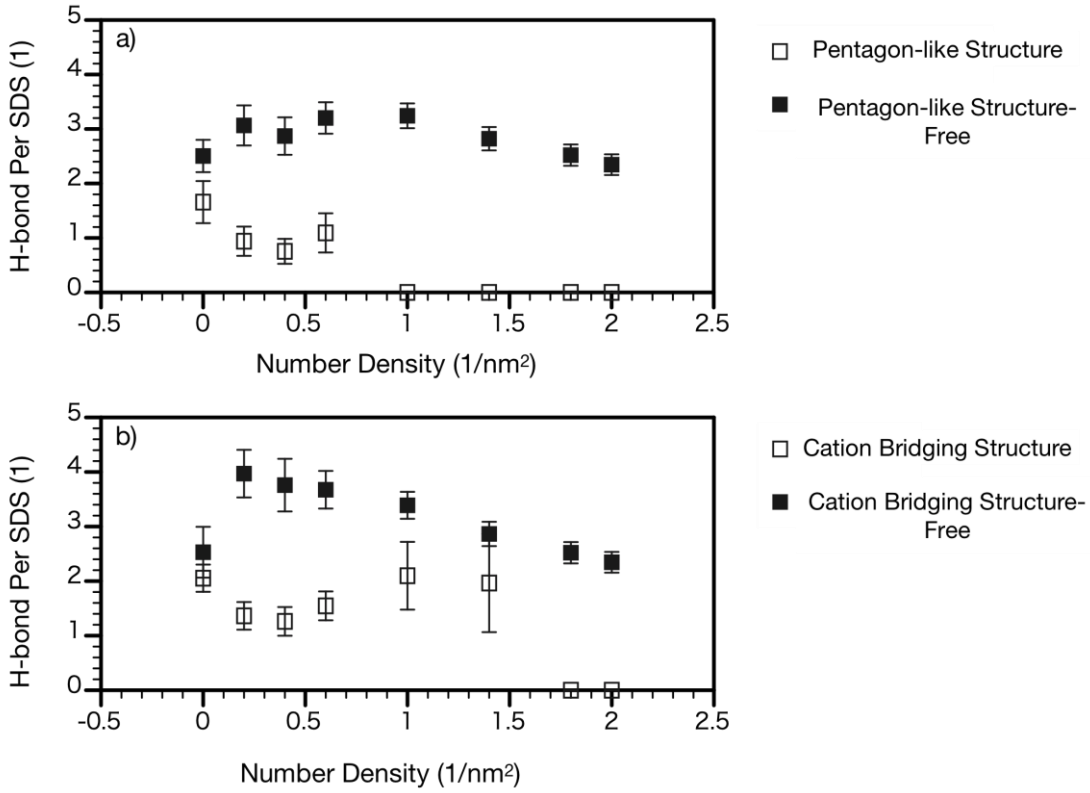

Figure B-13 H-bond formation number per SDS in systems ASCS from different structures a) pentagon-like and pentagon-like free structures; b) cation bridging and cation bridging free structures. the *x*-axis is the number density of CTAB molecules at the interface.

B.15. Radial Distribution Densities (RDDs) of CTAB around SDS

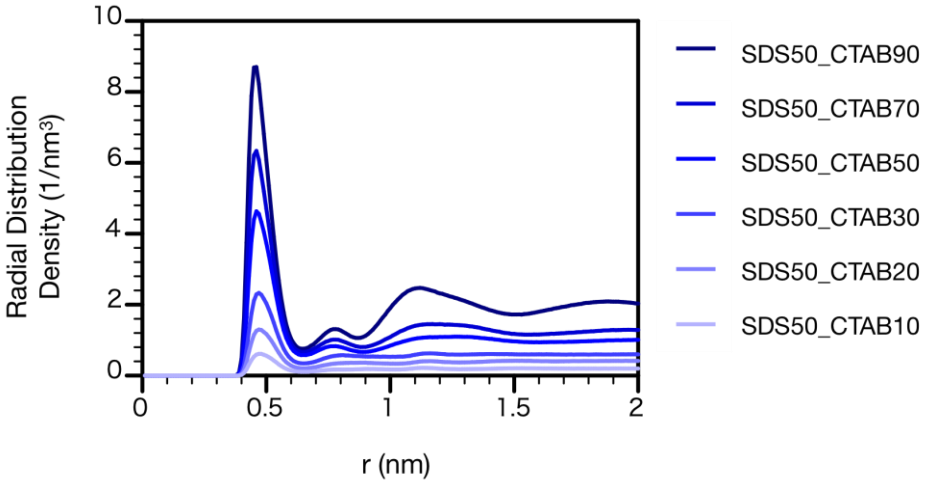

Figure B-14 Radial distribution densities of CTAB_N around SDS_S in ASCS systems.

Appendix C

C.1. Potential Energies of the Systems

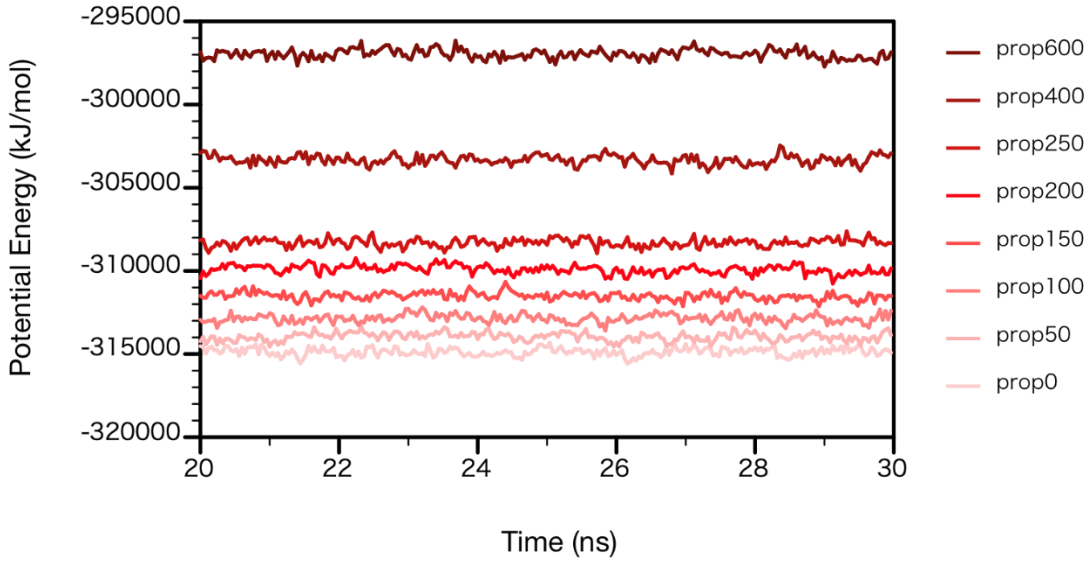

Figure C-1 Potential energies of different systems.

C.2. Systems with Varying SDS Concentrations

We also conducted some simulations with varying SDS concentrations at the interfaces as shown in **Fig. C-2** and **C-3**. Most propanol molecules are distributed at the interfaces, while some are dispersed in the oil and brine phases. As SDS concentration increases, the distribution of propanol becomes less enriched at the interface, and Na^+ ions gradually show an accumulation at the interface as well. In addition, the diffusion coefficient of SDS is independent of its concentration (**Fig. C-2.)**, while the brine-oil interfacial tension declines as SDS concentration increases (**Fig. C-3**.).

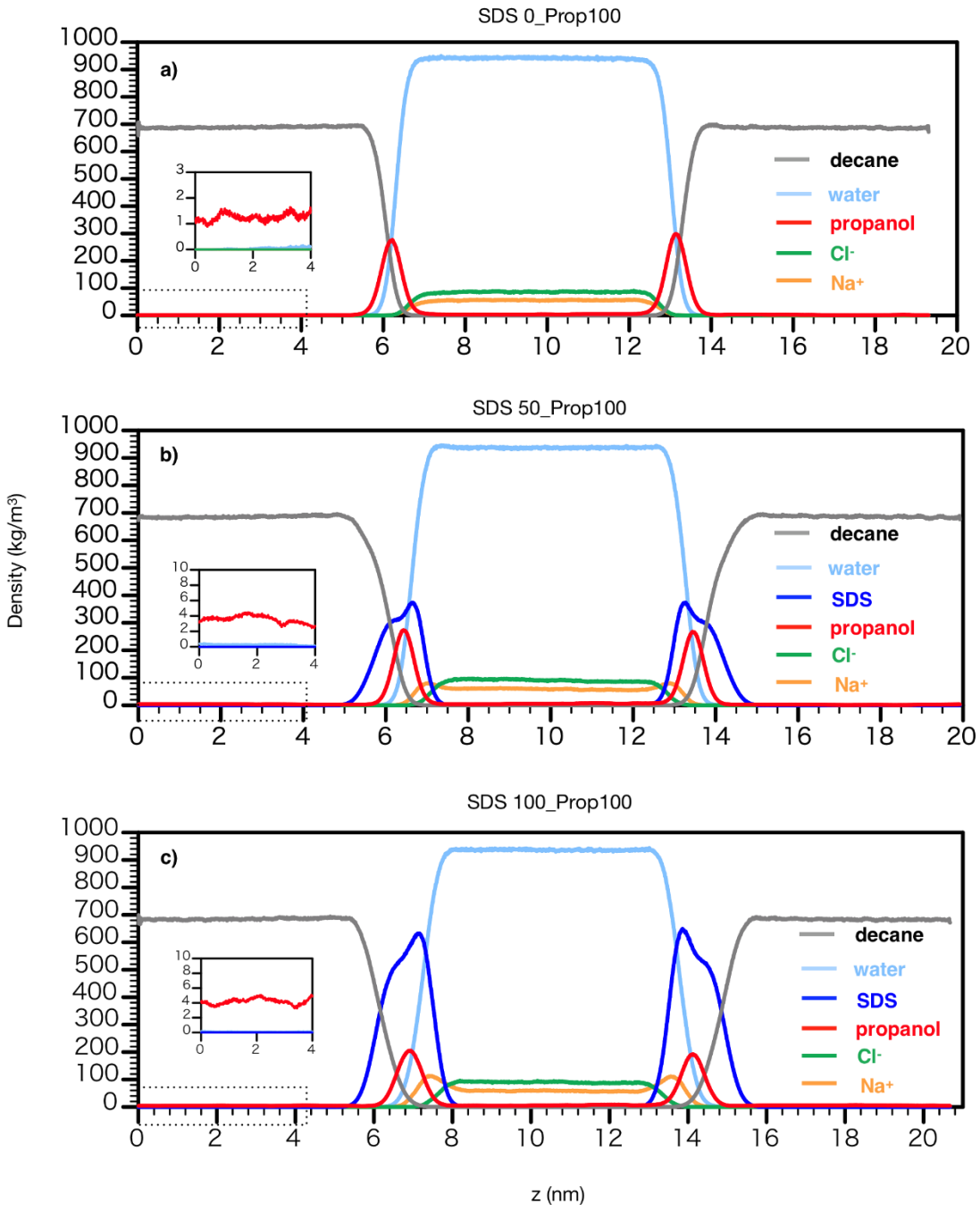

Figure C-2 Density profile of each molecule for SDS concentration at the interface of (a) 0 nm^{-2}; (b) 1 nm^{-2}; (c) 2 nm^{-2} with 100 propanol molecules.

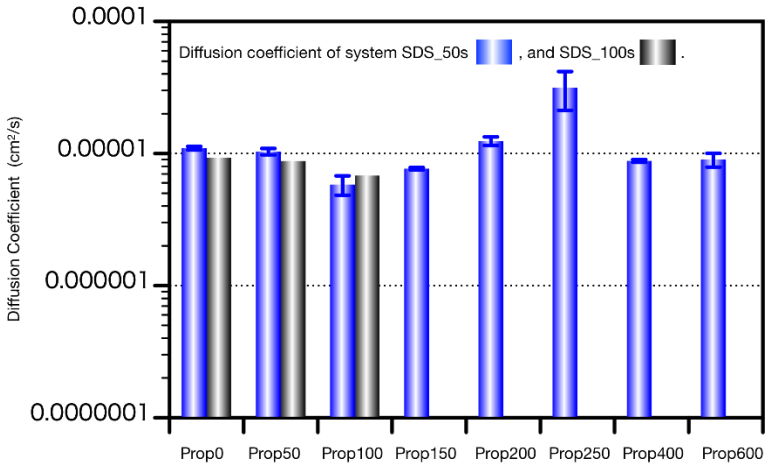

Figure C-3 The diffusion coefficient of SDS in the *x*-*y* plane.

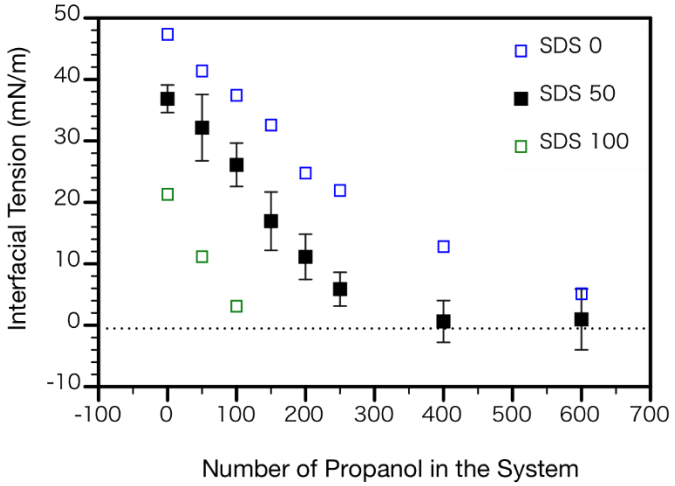

Figure C-4 Interfacial tension of system with various SDS and propanol concentrations.

C.3. Density Profiles in Varying Propanol Concentrations

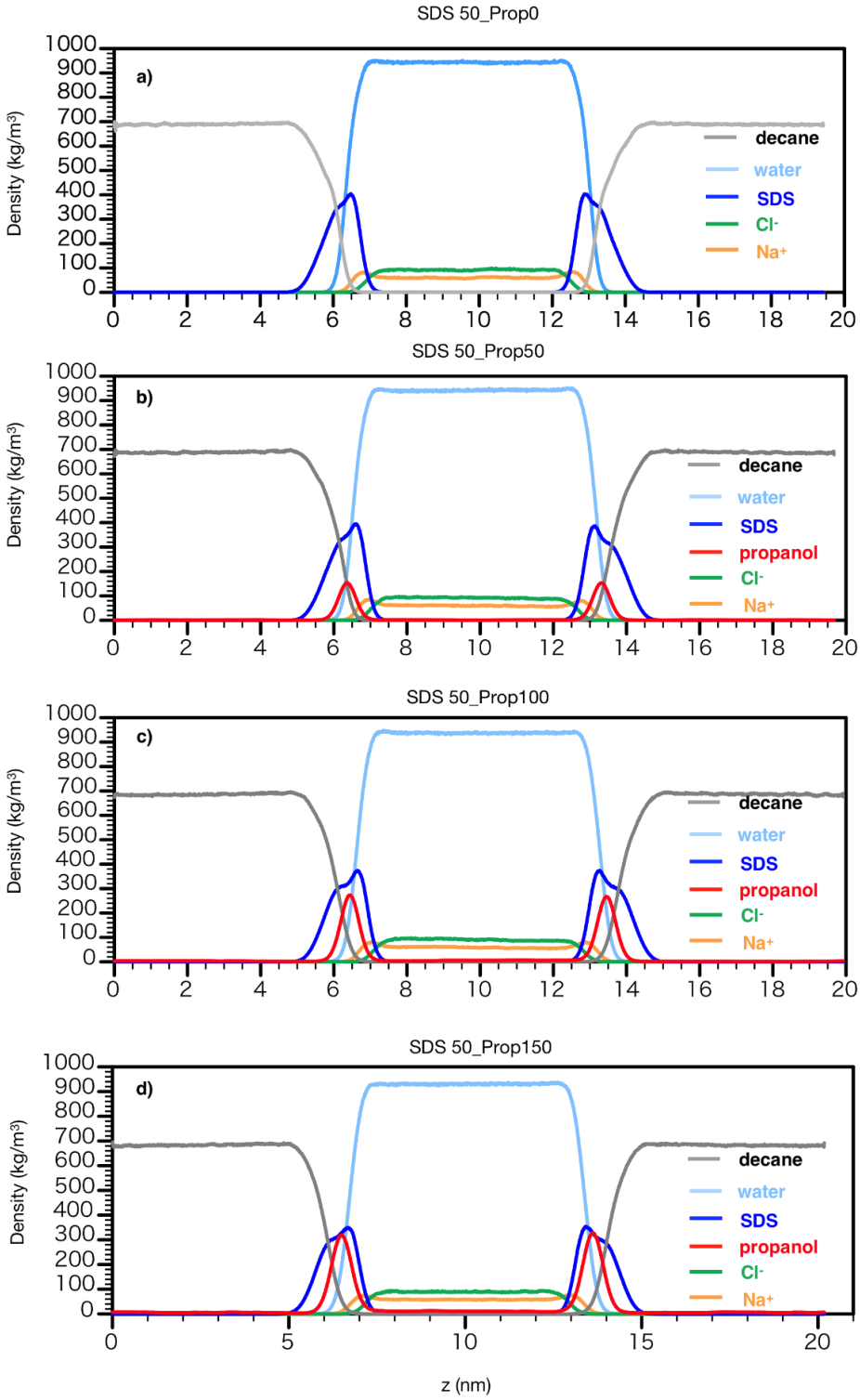

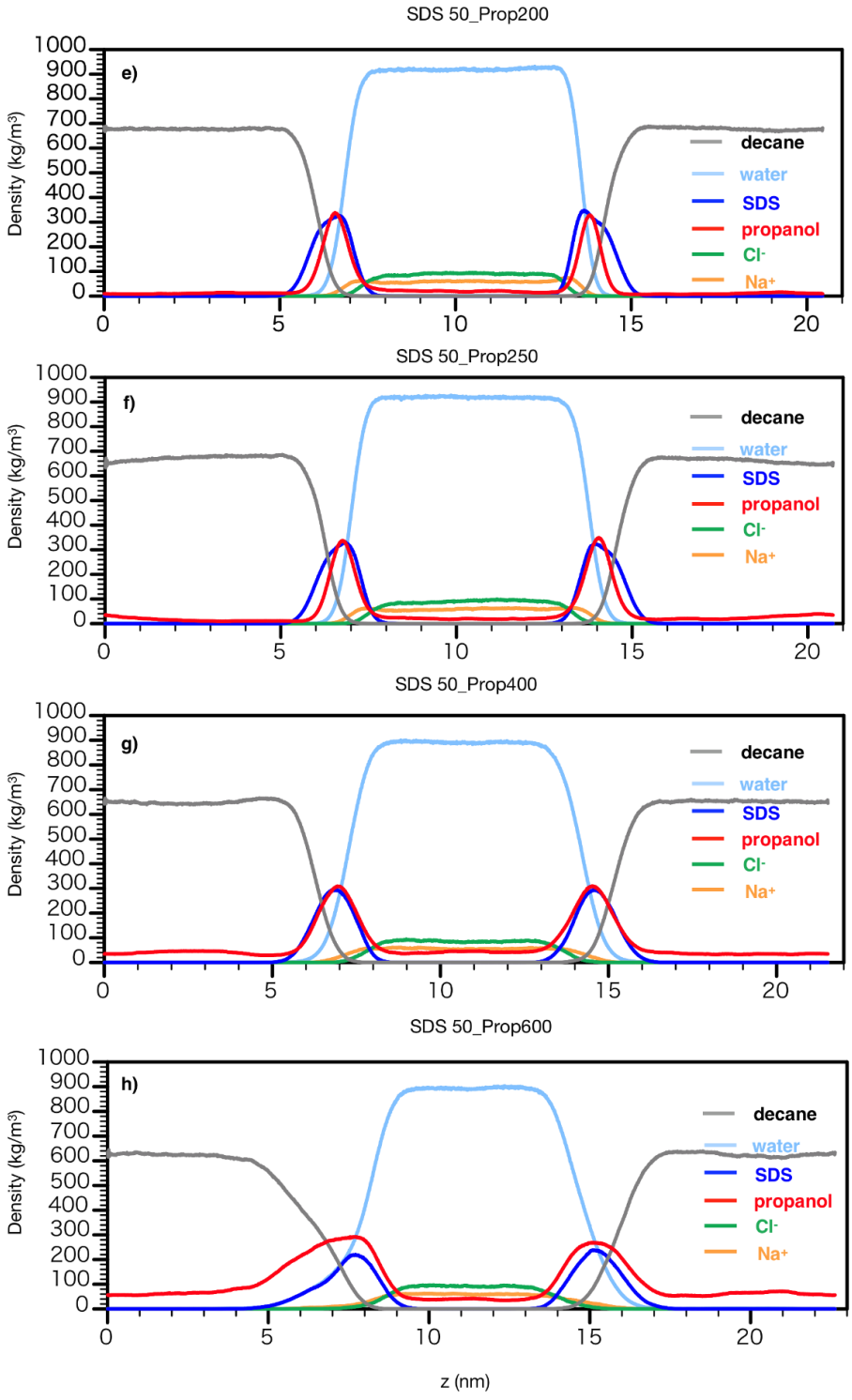

Figure C-5 The density distribution of each components in the system with the number of propanol as (a) 0 ; (b) 50; (c) 100; (d) 150; (e) 200; (f) 250; (g) 400; and (h) 600.

C.4. Effect of Propanol Concentration on Decane and Water Distribution

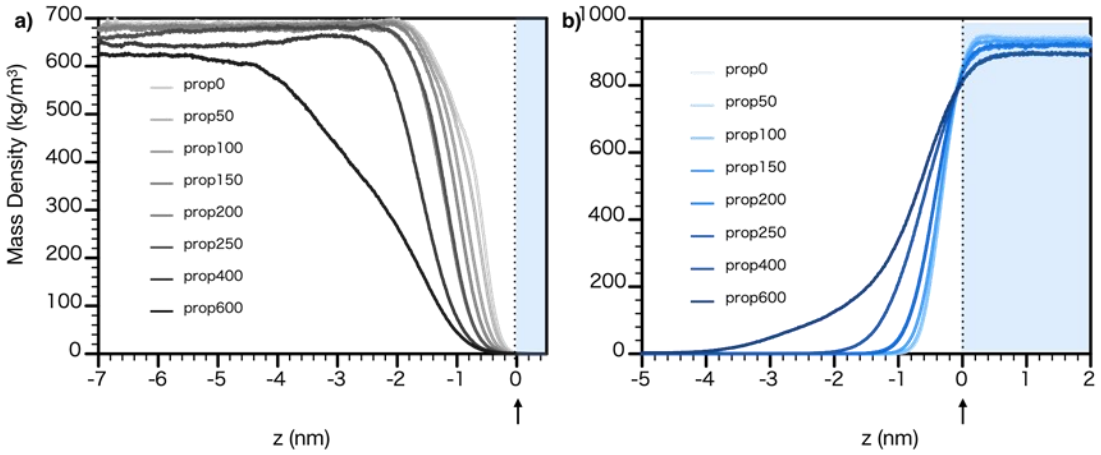

Figure C-6 The mass density distributions of a) n-decane; b) water under varying propanol concentrations/numbers. The darker color indicates that propanol concentration is higher. The dotted lines represent the location where water density is equal to 90% of its bulk value.

Bulk densities of n-decane and water decrease as propanol concentration increases. In addition, as propanol concentration increases, the interfacial thickness increases, and the slopes of n-decane and water density distributions at the interfaces decrease.

Appendix D

D.1. Force field

Table D-1 Force field parameters for CO_2

	Atom Type	σ (nm)	ε (kJ/mol)	q (e)
CO_2_EPM2	**C**	0.275700	0.233878	0.65120
	O	0.303300	0.669373	−0.32560

l_{bond} (C=O bond) = 1.16 Å

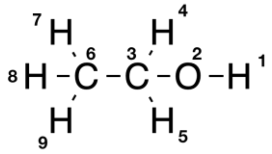

Table D-2 force field parameters for ethanol

Atom parameters			
$E_{\mathrm{vdW}} = 4\varepsilon\left[\left(\frac{\sigma}{r}\right)^{12} - \left(\frac{\sigma}{r}\right)^{6}\right]$ $E_{coulomb} = \frac{1}{4\pi\varepsilon_0}\frac{q_i q_j}{\varepsilon_r r_{ij}}$			
Atom Type (index)	σ (nm)	ε (kJ/mol)	q (e)
H (1)	0.040001	0.192460	0.41900
O (2)	0.314487	0.803750	−0.64900
C (3)	0.358141	0.234300	0.04900
H (4, 5)	0.238761	0.146440	0.09000
C (6)	0.365268	0.326350	-0.26900
H (7, 8, 9)	0.238761	0.100420	0.09000

Bond parameters		
$E_{bond} = \frac{1}{2}k_{ij}\left(r_{ij} - b_{ij}\right)^2$		
Bond Type (index)	b (nm)	k (kJ/mol/nm^2)
H (1) − O (2)	0.096000	456056.00
O (2) − C (3)	0.142000	358150.40
C (3) − C (6)	0.152800	186188.00
C (3) − H (4, 5)	0.111100	258571.20
C (6) − H (7, 8, 9)	0.111100	269449.60
Angle parameters		
$E_{angle} = \frac{1}{2}k_{ijk}^{\theta}\left(\theta_{ijk} - \theta_{ijk}^{0}\right)^2 + \frac{1}{2}k_{ijk}^{UB}\left(r_{ik} - r_{ik}^{0}\right)^2$		

Angle Type (index)	θ_{ijk}^{0} (deg)	k_{ijk}^{θ} (kJ/mol/rad^2)	r_{ik}^{0} (nm)	k_{ijk}^{UB} (kJ/mol/nm^2)
H (1) − O (2) − C (3)	106.00	418.400000	0.000000	0.00
O (2) − C (3) − H (4, 5)	108.89	384.091200	0.000000	0.00
O (2) − C (3) − C (6)	110.10	633.457600	0.000000	0.00
H (4, 5) − C (3) − H (4, 5)	109.00	297.064000	0.180200	4518.72
H (4, 5) − C (3) − C (6)	110.10	289.532800	0.217900	18853.10
H (7, 8, 9) − C (6) − H (7, 8, 9)	108.40	297.064000	0.180200	4518.72
C (3) − C (6) − H (7, 8, 9)	110.10	289.532800	0.217900	18853.10
Dihedral Parameters				
$E_{dihedral} = k_{\phi}\left(1+\cos\left(\mathrm{n}\phi - \phi_s\right)\right)$				
	ϕ_s (deg)	k_{ϕ} (kJ/mol)	n	
O (2) − C (3) − C (6) − H (7, 8, 9)	0.00	0.669440	3	
H (4, 5) − C (3) − O (2) − H (1)	0.00	0.753120	3	
C (6) − C (3) − O (2) − H (1)	0.00	4.727920	1	
C (6) − C (3) − O (2) − H (1)	0.00	0.585760	2	
C (6) − C (3) − O (2) − H (1)	0.00	1.004160	3	
H (4, 5) − C (3) − C (6) − H (7, 8, 9)	0.00	0.669440	3	

D1.2 Force Field for AOT

The force field for AOT is as same as that described in the SI of reference [168].

D.2. Results from Various AOT Concentrations

Table D-3 Results from various AOT concentrations

AOT concentration (*wt*.%)	Number of Clusters after 600 ns run (Without ethanol)	Number of Clusters after 600 ns run (With 10 *wt*.% ethanol)	Computational time using one GPU node (wall clock) for 600 ns run (h)
40	1	5	~ 32
20	1	6	~ 43
4 (*this work*)	1~3	9~10	~ 70
2	1~3	9~10	~ 100
1	1~3	10	~ 200

In the current manuscript, we chose the ethanol and AOT concentration to be ~10 *wt*.% and ~ 4 *wt*.%, respectively. Relatively high ethanol concentration (~10 *wt*.%) is conducted to observe the more significant effect in solubility increment. As for AOT concentration, we tried the systems with various AOT concentrations (40 *wt*.%, 20 *wt*.%, 4 *wt*.%, 2 *wt*.%, and 1 *wt*.%) and chose the concentration which can well explain the role of ethanol while possessing reasonable computational expense (**Table D-3**). In all the systems, the number of AOT molecules is kept constant while the CO_2 number is adjusted to study the AOT concentration effect. After 600 ns run, systems with 4 *wt*.%, 2 *wt*.%, and 1 *wt*.% ended up with similar cluster numbers in both with and without ethanol systems. With the Consideration of our objective (to provide a molecular-level understanding of the role of the ethanol), as well as the computational cost, we chose the 4 *wt*.% AOT concentration for further study in the main text. It is noted that the AOT concentration we chose (~ 4 *wt*.%) is a little higher than the experimental report (~ 1 *wt*.%)[167]. There might be several reasons for this quantitative difference in AOT solubility. One is the limitation of forcefield, which might not reproduce the quantitative solubility of the AOT. Another might be

the different standards in defining the “solubility” from experiments and simulation. In the experiments, the solubility is defined visually at the concentration where the could-point first observed[38, 167], however, the molecular dispersity is the benchmark in the simulations.

D.3. Cluster Analysis on 20 Replicas in System A

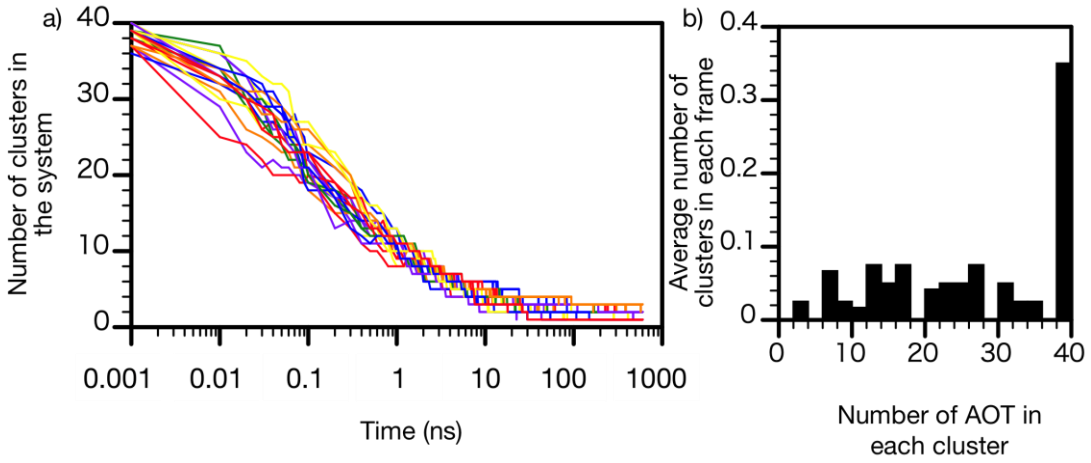

Figure D-1 a) Evolution of cluster number from 20 replicas in System A; b) Average number of clusters in each frame.

D.4. RDD of Na^+ around Na^+ in System B

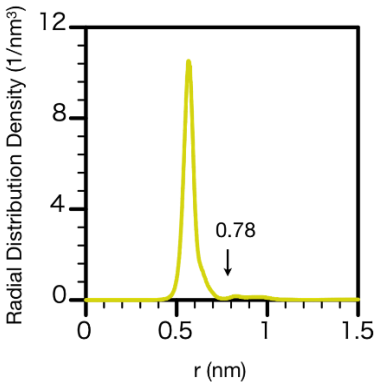

Figure D-2 Na^+-Na^+ radial distribution density profile in System B.

D.5. PMFs of CO_2 and Ethanol around Na^+ ion from AOT

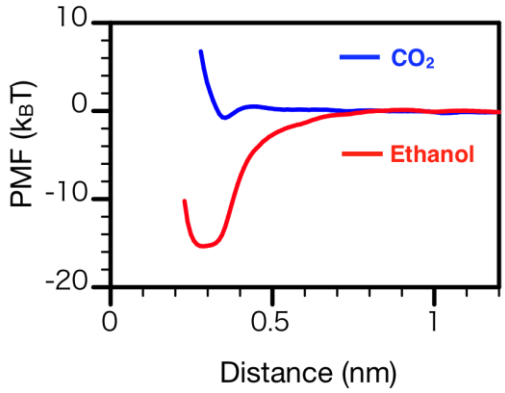

Figure D-3 PMFs of CO_2 and ethanol around Na^+ ion from AOT.

We explicitly designed two systems (Systems G and H) to compare the affinity of the CO_2 and ethanol to the Na^+ ion from AOT. System G contains one AOT molecule and 2000 CO_2 molecules. We gradually pull one CO_2 molecule distributed around the Na^+ ion (from AOT) away to generate the initial configurations for umbrella samplings. System H contains one AOT, one ethanol, and 2000 CO_2 molecules. Initial configuration generation for System H is similar to that of System G but pulling one ethanol molecule away. The potential of mean force in **Figure D-3** shows that ethanol has a stronger affinity to the Na+ ions than CO_2.

Appendix E

E.1. Initial Configuration

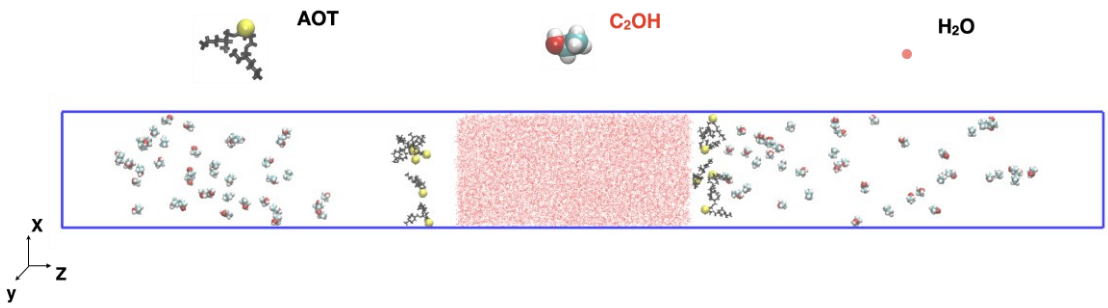

Figure E-1 Initial configuration of system AOT10_C_2OH (0.035). The periodic boundaries are depicted by the blue rectangular.

E.2. Force Field Calibration

Table E-1 Force field calibration under 333K, 200 bar

	Experiment	Our Simulation	Relative Error
scCO2 density (kg/m3)	724.63[209]	704.17	-2.83%
Water density (kg/m3)	992[210]	996	0.40%
Water solubility in $scCO_2$	0.0129[211] (333.15K, 200 bar) or 0.0089[212] (333.15 K, 200 bar)	0.0041	-
Water/$scCO_2$ IFT (mN/m)	28.13[213](333.2 K, 212 bar)	22.93	-18.49%

E.3. Time Evolution of Alcohol Adsorption at Interface

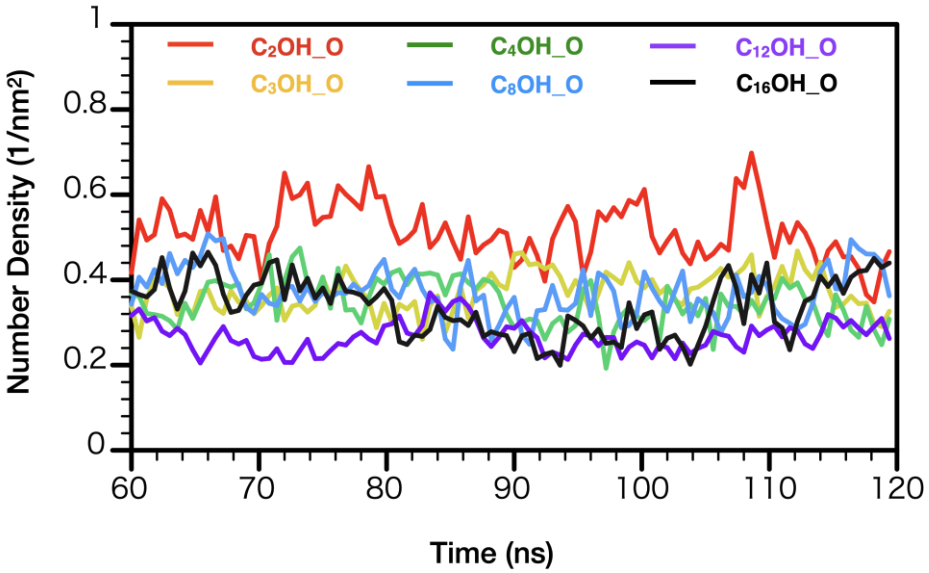

Figure E-2 Time evolution of different tail length alcohol adsorption at the interface region. The interface region is defined using 90-90 criteria.

E.4. Density Profile in System AOT10_C_2OH (0.035)

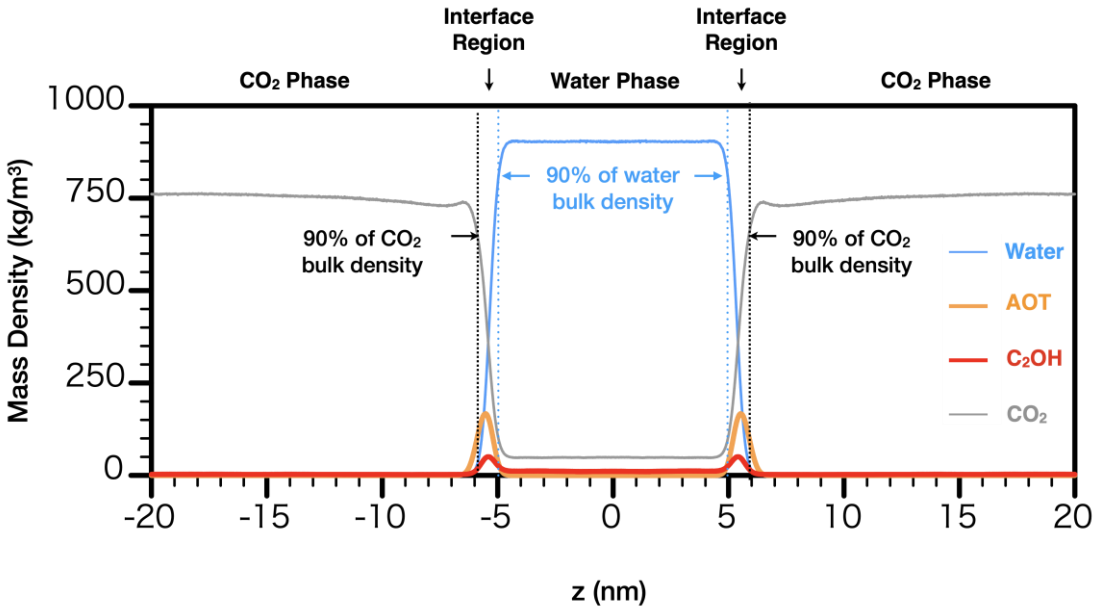

Figure E-3 Mass density distribution of molecules in system AOT10_C_2OH (0.035). Contact between the CO_2 phase and interface region is depicted using black dashed lines; contact between the interface region and the water phase is depicted using blue dotted lines.